Synthetic modelling study of marine controlled-source electromagnetic data for hydrocarbon exploration

by

©Mariella Nalepa

A Thesis submitted to the School of Graduate Studies in partial fulfillment of the requirements for the degree of

Master of Science

Department of Earth Sciences

Memorial University of Newfoundland

May 2016

St. John's, Newfoundland and Labrador

Abstract

The marine controlled-source electromagnetic method (CSEM) is a geophysical technique for mapping subsurface electrical resistivity structure in the offshore environment. It has gained ground in recent years as a tool for remote detection and mapping of hydrocarbon reservoirs as it serves as an independent yet complementary method to seismic acquisition. While CSEM data contains useful information about the subsurface, modelling and inversion are required to convert data into interpretable resistivity images. Improvement of modelling tools will assist in closing the gap between acquisition and interpretation of CSEM data. The primary focus of this study was to explore the limits of our present modelling capabilities in the context of marine electromagnetic scenarios. Software based on the three-dimensional CSEM finite-element forward code CSEM3DFWD (Ansari and Farquharson, 2014; Ansari et al., 2015) was employed in this study. While testing of this software had been expanded to models of relevance to mineral exploration, its performance for models which are representative of marine geologic environments, in particular those which are encountered in offshore oil and gas exploration, had not yet been investigated. In this study, marine models of increasing complexity were built and tested, with the ultimate goal of synthesizing marine CSEM data for three-dimensional earth models which were complete in their description of the subsurface. Computed responses were compared to results existing in the literature, when available. To investigate the capability of the code in modelling realistic scenarios, forward solutions were computed for a marine reservoir model based on the real-life North Amethyst oil field, located in the Jeanne d'Arc Basin, offshore Newfoundland. When the capability of modelling realistic earth models is fully realized, forward modelling may be used to assess the utility of the marine CSEM method as a tool for hydrocarbon detection and delineation in specific offshore scenarios.

Acknowledgements

First and foremost, I would like to thank my thesis supervisor, Dr. Colin Farquharson, for his enduring encouragement and optimism and always having time to chat, despite his ever-expanding research group at MUN. I am grateful for his support in my academic and professional development and for providing me the opportunity to explore my interests in geophysics. Dr. SeyedMasoud Ansari was equally important as my mentor in the subject of geophysical EM modelling and as the developer of CSEM3DFWD, without which this project would not exist. I am very grateful for his patience in explaining concepts related to numerical methods, as well as his direction in navigating the difficulties of unstructured meshes. Further, I greatly benefited from having a peer with which to discuss problems and ideas related to my research. Funding for my project was provided by Husky Energy, with additional financial support obtained through an NSERC Canada Graduate Scholarship, a Chevron Canada Limited Rising Star Award, and a SEG–Chevron Graduate Scholarship.

There are many others to thank and acknowledge for their support and contributions to this project. Dr. Peter Lelièvre provided essential model-building and mesh and data manipulation programs; I very much appreciate his willingness to collaborate in the development of programs tailored to my research. I am also grateful to Dr. Alison Leitch for serving on my supervisory committee and for providing feedback that served to strengthen and clarify various aspects of my thesis. Dr. Christoph Schwarzbach provided finite-element solutions for the seafloor topography model of Section 5.3, which were used for verification of my own results. The DIPOLE1D code written by Dr. Kerry Key was used in Section 5.4 for verification of the 1D solutions computed using MARDIP1D for a finite-water depth marine halfspace model; I thank Dr. Kerry Key and the Marine EM Laboratory at the Scripps Institution of Oceanography for making the DIPOLE1D code available for public use.

Finally, thank you to friends who made studying in beautiful St. John's such a pleasure,

and to my family, particularly Drew, for their encouragement in continuing my work, and putting into perspective what a great life I've had so far as a student.

Table of Contents

List of Tables

List of Figures

Chapter 1

Introduction

1.1 Marine CSEM in hydrocarbon exploration

The marine controlled-source electromagnetic (CSEM) method is a geophysical technique for mapping subsurface electrical resistivity structure in the offshore environment. Resistivity is a useful measurement in offshore hydrocarbon exploration because it is largely influenced by pore fluid content, and thus may be useful in distinguishing between conductive brine-saturated and resistive oil- or gas-saturated reservoirs. For example, seafloor sediments saturated with brine or saline fluids have typical resistivities of about 1 ohm-m, whereas sediments saturated with hydrocarbons may have resistivities of up to 100 ohm-m or higher (Constable, 2006). Because of the sensitivity of the method to pore fluid properties, it is viewed as a complementary tool to conventional seismic methods in offshore exploration and development for detection and delineation of hydrocarbons (Danielsen and Bekker, 2011). The seismic reflection method excels in imaging subsurface structure, but only provides a qualitative, and often ambiguous, interpretation of pore fluid properties (Vieira da Silva et al., 2012; MacGregor and Tomlinson, 2014). Seismic attributes that may indicate the presence of hydrocarbons, such as local high-amplitude anomalies known as

“bright spots" and characteristic amplitude-variation-with-offset (AVO) responses, may be explained by other changes in rock and fluid properties (Vieira da Silva et al., 2012). Interpretation of pore fluid content from CSEM-derived resistivity alone can also be misleading since variations in the earth’s electrical structure reflect not only pore fluid composition, but also lithology, temperature, porosity, and permeability. Not all resistive anomalies encountered in the offshore exploration environment are associated with the presence of hydrocarbons (Key, 2003; MacGregor and Tomlinson, 2014). For example, evaporites, volcanics, carbonates, and freshwater-saturated sands can exhibit high electrical resistivity relative to their surroundings, and even variations in bathymetry or host rock resistivity may cause anomalies (Constable, 2006; Srnka et al., 2006). Further, non-economic targets may occur as thin horizons, thus disguising themselves as potential hydrocarbon reservoirs. By integrating CSEM data with geophysical and geological data obtained via independent methods, whether through simple co-rendering or computationally demanding joint inversion, subsurface structure may be interpreted with greater confidence.

Many papers provide extensive reviews of the history of the CSEM method and its application in hydrocarbon exploration (e.g., Constable and Srnka, 2007; Constable, 2010; Key, 2012b). While the marine CSEM method has existed as an academic technique for the study of oceanic lithosphere since the late 1970s, its adaptation for commercial use within the oil and gas industry did not begin until the early 2000s. This transformation from academic to commercial application was driven in large part by the expansion of hydrocarbon exploration into deep water ($>$1000 m depth) and the associated technical and economic challenges of the environment (Constable, 2006; Srnka et al., 2006; Constable and Srnka, 2007). The marine CSEM method is well-suited to the deepwater environment as a result of preferential electrical coupling of transmitted fields to the subseafloor and the low electromagnetic (EM) noise level due to the filtering effect of the water column (Srnka et al., 2006). Its application in shallow water is more challenging due to the dominance of the

response by signal that has interacted with the atmosphere, often referred to as the *airwave* (Constable and Weiss, 2006; Andréis and MacGregor, 2007). The airwave problem has been well-studied and several solutions have been developed to mitigate its effect in shallow water (e.g. Amundsen et al., 2006; MacGregor et al., 2006; Andréis and MacGregor, 2008; Chen and Alumbaugh, 2011).

Since the early successes of marine CSEM field trials held by Statoil and Exxonmobil offshore West Africa (described in Ellingsrud et al., 2002; Srnka et al., 2006; Constable and Srnka, 2007), surveys have been conducted worldwide in both under-explored and highly developed basins representing a diversity of geological environments and water depths (e.g., Carazzone et al., 2008; Alcocer et al., 2012; Bouchrara et al., 2012; Gist et al., 2013; Colombo et al., 2014). Beyond hydrocarbon mapping, the marine CSEM method has been applied in petroleum exploration and development for geohazard screening in the shallow subsurface and structural imaging in environments which are ill-suited to conventional seismic methods (e.g., Weitemeyer and Constable, 2010; Alcocer et al., 2012; Colombo et al., 2014). As industry use of the method has become more widespread, acquisition and data processing techniques have matured and companies have been motivated to develop in-house software and expertise for CSEM integration and interpretation (Danielsen and Bekker, 2011).

1.2 Electric and magnetic properties of sedimentary rocks

Three physical properties characterize the EM behaviour of a medium: electrical conductivity (σ; unit: siemens per metre, S/m), or its reciprocal, resistivity (ρ; unit: ohm-metre, Ωm), electrical permittivity (ε; unit: farads per meter, F/m), and magnetic permeability (μ; unit: henries per meter, Hm^{-1}). Electrical resistivity is a measure of the opposition of a material to the flow of current. Electrical permittivity is related to electric susceptibility

χ_e, where $\varepsilon = (1+\chi_e)\,\varepsilon_0$ and ε_0 is the permittivity of free space, which is a measure of the polarization of a material in response to an applied electric field. Analogously, magnetic permeability is related to magnetic susceptibility χ_m, where $\mu = (1+\chi_m)\,\mu_0$ and μ_0 is the permeability of free space, which is a measure of the magnetization of a material in response to an applied magnetic field.

In consideration of low-frequency EM modelling, resistivity is the most important property for characterization of the earth's structure. Since displacement currents are negligible for the frequencies at which marine CSEM data is acquired (Section 2.1.6), the electric permittivity structure of the earth can be safely ignored (Chave et al., 1990). For reference, the relative permittivity ε_r ($\varepsilon_r = \varepsilon/\varepsilon_0 = 1+\chi_e$) of seawater is approximately 80 (Chave et al., 1990), and the relative permittivities of sedimentary rocks are typically in the range of 1–100 (permittivities between 10^{-9} and 10^{-11} F/m; Constable, 2010); since sedimentary rocks are not intrinsically polarizable, their permittivity depends primarily on pore fluid content (Chave et al., 1990). Martinez and Byrnes (2001) tabulate the bulk permittivities of common earth materials. Since magnetic mineral content is generally low for sedimentary rocks common to offshore oil and gas basins (Commer and Newman, 2008; Constable, 2010), the magnetic permeability μ is generally taken to be that of free space, i.e., $\mu = \mu_0 = 4\pi \times 10^{-7}$ H/m, for marine CSEM modelling.

Resistivity is a highly variable property among earth materials (Figure 1.1). While the resistivity of some lithologies is dictated by content of certain conductive or semiconductive minerals, e.g., native metals and metallic sulfides, most rock-forming minerals are insulators, and so in situ conduction of electrical current is primarily via electrolytic pore fluid (Kearey et al., 2002). The basic controls on rock resistivity are then pore fluid conductivity, pore fluid saturation, and volume and interconnectivity of pore space, i.e., porosity and permeability. Both dissolved salt content and temperature are important considerations because they influence pore water conductivity. The salinity of pore water reflects the

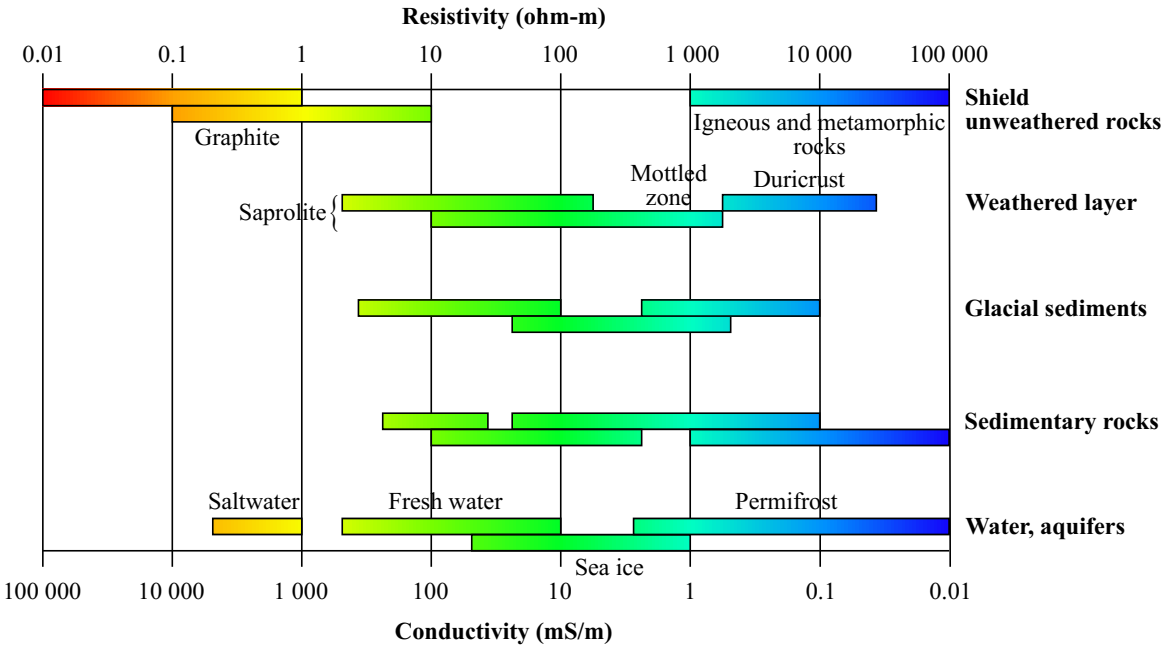

Figure 1.1. Typical resistivity ranges of some common earth materials. After Palacky (1988).

amount of ions available to conduct electricity, and temperature and ion size, determined by the minerals in solution, e.g., Na^{+}, Ca^{++}, and Mg^{++}, influence the mobility of ions in solution (Bassiouni, 1994; Keller, 1988).

For sedimentary rocks targeted in oil and gas exploration, the primary minerals – silicates, carbonates, and oxides – are insulators (Telford et al., 1990); it should however be noted that clay minerals, while not inherently conductive when dry, exhibit electrostatic surface charges which affects pore fluid conductivity via surface adsorption of cations. Because of this ion exchange capacity, clay content generally increases a rock's in situ conductivity (Keller, 1988). For most clean, i.e. low or zero clay content, sedimentary rocks, Archie's law (1942) provides a reasonable estimate of in situ electrical resistivity. This petrophysical law assumes that pore fluid is the only element contributing to a sedimentary rock's bulk resistivity. The bulk electrical resistivity ρ_b of a sedimentary rock is related empirically to its porosity ϕ and pore fluid content, expressed in terms of pore water saturation

Table 1.1. Parameters for Archie's Law for sedimentary rocks of different ages. After Keller (1988).

Sedimentary rock description	ϕ	a	m
Weakly cemented detrital rocks, usually Tertiary in age	25 – 45%	0.88	1.37
Moderately well-cemented sedimentary rocks, usually Mesozoic in age	18 – 35%	0.62	1.72
Well-cemented sedimentary rocks, usually Paleozoic in age	5 – 25%	0.62	1.95

S_w and pore water resistivity ρ_w, in the formula

$$\rho_b = a\phi^{-m} S_w^{-n} \rho_w, \tag{1.1}$$

where a, m, and n are empirical parameters known as the tortuosity factor, cementation exponent, and saturation exponent, respectively (MacGregor and Tomlinson, 2014). These parameters depend on rock type and mainly reflect pore geometry and degree of consolidation (Bassiouni, 1994). Laboratory measurements indicate wide ranges of possible parameter values. For sandstone formations, a has been found to range from 0.35 to 4.78, and m from 1.14 to 2.52 (Bassiouni, 1994). Table 1.1, after Keller (1988), illustrates standard values of a and m for sedimentary rocks of different ages. The parameter n is introduced when considering a rock with partial water saturation; values from 1 to 2.5 have been reported, with a value of 2 found to provide a good empirical fit for clean, consolidated sands (Bassiouni, 1994).

Archie's law reinforces the ambiguity of formation fluid interpretation based on resistivity alone since reasonable parameter ranges may account for variations of several orders of magnitude in bulk resistivity. Moreover, any given resistivity might be explained by various combinations of parameter values. For example, assuming invariable a, m, n, and ρ_w, a high in situ resistivity may indicate either a high-porosity, oil-saturated rock, or a low-porosity, water-saturated rock (MacGregor and Tomlinson, 2014). This again emphasizes

the importance of interpreting marine CSEM resistivity in context of other geophysical and geological information.

In the marine CSEM method, it is also important to consider the electrical structure of the water column. Seawater is highly conductive due to its salinity, with the mean conductivity of the Pacific Ocean at 3.2 S/m ($\approx$ 0.3 ohm-m), and that of the Atlantic Ocean at slightly higher (Chave et al., 1990). The electrical structure of the water column varies approximately linearly as a function of in situ temperature, with salinity and pressure exerting a weaker dependence (Chave et al., 1990). Since temperature in the shallow section is highly variable and can be anywhere from freezing temperature to greater than 30°C, the conductivity of seawater is also highly variable (Constable, 2013). Below the thermocline, which can occur at anywhere from 300 to 1000 m depth, temperature, and therefore conductivity, become relatively stable (Chave et al., 1990; Constable, 2013). Key (2009) illustrated through a series of one-dimensional (1D) inversions that incorrect representation of seawater as a homogeneous layer may generate spurious features within inverted electrical structure. For interpretation of real marine CSEM data, it is therefore advisable to measure the seawater resistivity profile at the survey location, as is possible with the use of a transmitter-mounted conductivity-temperature-depth sensor (Constable, 2013). The earth models constructed in this study, both synthetic and real world-based, represent the seawater as a homogeneous layer of 0.3 ohm-m resistivity, as is fairly common practice in the marine CSEM modelling literature. This must be acknowledged as an uncertainty when interpreting modelling results for real-world scenarios.

1.3 Introduction to geophysical EM modelling

1.3.1 Motivation

Geophysical methods exploit physical principles to gain information about the spatial distributions of one or more of the earth's physical properties through measurement of the related fields (West and Macnae, 1988; Zhdanov, 2002). The purpose of geophysical modelling is to use the governing mathematical relationships to transform between data, whether real or synthetic, and possible spatial distributions of the related physical property. Through modelling, we gain an understanding of what can be known about the directly unobservable subsurface from a limited number of observations made at or near the surface (Vieira da Silva et al., 2012).

The marine CSEM method uses the principles of electromagnetism, governed by Maxwell's equations (Section 2.1), to investigate the electrical structure of the earth. An artificial source transmits a time-varying EM signal into the earth, where it is modified in both amplitude and phase by the earth's electrical structure (Eidesmo et al., 2002; Constable, 2010). Through modelling, measurements made at the seafloor of the electric and magnetic fields can be related back to subsurface variations in electrical resistivity.

In pre-survey planning, modelling can be a crucial step for analysis of the sensitivity of the CSEM method to structures of interest and optimization of acquisition parameters for target resolution (MacGregor and Tomlinson, 2014). The sensitivity of the marine CSEM method to a particular target is determined not only by electrical structure, but also by survey considerations such as source-receiver offset, source configuration, and source frequency content (e.g. Constable and Weiss, 2006; Key, 2009). In the post-survey stage, modelling is essential for interpretation of observed data in terms of subsurface electrical structure. These applications involve the processes of both forward modelling and inver-

sion.

Commercial investment in marine CSEM technology has motivated the development of interpretation tools to realize the full potential of marine CSEM data. Accordingly, recent papers presenting new EM modelling methods frequently feature examples relevant to marine CSEM hydrocarbon exploration. In Chapter 2, methods for EM forward modelling will be reviewed, with a particular focus on developments relevant to the marine CSEM method. For models that make simplistic assumptions about the earth's structure, analytic or semi-analytic (i.e., numerically evaluated analytic) forward solutions for the electric and magnetic fields may be derived; in the case of earth models with arbitrary complexity, numerical approximation techniques such as the finite-difference or finite-element methods are required for computation of the fields.

1.3.2 The forward and inverse problems

Forward modelling predicts geophysical data for a particular physical property distribution or earth model. Conceptually, the forward problem involves mapping from the model space $\mathscr{M}$ to the data space $\mathscr{D}$, that is (Zhdanov, 2002)

$$\mathbf{G} : \mathscr{M} \rightarrow \mathscr{D} \tag{1.2}$$

$$\mathbf{d} = \mathbf{G}(\mathbf{m}), \tag{1.3}$$

where $\mathbf{G}$ is the forward operator that describes the mathematical relationship between the set of model parameters $\mathbf{m} \in \mathscr{M}$ and observed data $\mathbf{d} \in \mathscr{D}$. The forward problem has a unique solution, meaning that for any given physical property distribution, a unique geophysical response exists. Given a preliminary, best-estimate earth model, forward modelling can be used to determine the sensitivity of geophysical data to a target of interest and the optimal acquisition parameters for detection of an anomalous response. It can also be

used post-survey to validate potential earth models; if predicted data agree well with measured data, we might assume that the earth resembles our model. This is the foundation of the inverse problem, which seeks to estimate a physical property distribution or earth model from observed data.

The inverse problem can be conceptualized as the mapping (Zhdanov, 2002)

$$\mathbf{G}^{-\mathbf{1}} : \mathscr{D} \rightarrow \mathscr{M} \tag{1.4}$$

$$\mathbf{m} = \mathbf{G}^{-\mathbf{1}}(\mathbf{d}), \tag{1.5}$$

where $\mathbf{G}^{-\mathbf{1}}$ is the inverse operator. In contrast to the forward problem, the inverse problem typically has non-unique solutions, i.e., an infinite number of models may fit the observed data equally well. For many inverse problems, the issue of non-uniqueness arises in the attempt to recover a continuous physical property distribution, or a discrete distribution with an arbitrary large number of degrees of freedom, from a limited number of observations (Hohmann and Raiche, 1988; Snieder and Trampert, 1999). In general, the number of data or observations does not equal the number of model parameters, and so $\mathbf{G}$ is non-square and does not have a formal inverse. Since there is not enough information to uniquely determine the solution to this type of inverse problem, we say that it is under-determined. This is the general case for geophysical methods due to discrete sampling of the earth's fields. The inverse problem is therefore recast as an optimization problem that seeks to minimize the difference between observed data and predicted data (Sen and Stoffa, 1995).

For EM problems, forward modelling requires solving Maxwell's equations (Section 2.1) in the time or frequency domain. The EM behaviour of earth materials is defined completely by three physical properties: electrical conductivity σ (or the reciprocal quantity, electrical resistivity ρ), permittivity ε, and magnetic permeability μ. The EM forward

problem can thus be symbolically described by the operator equation (Zhdanov, 2002)

$$\{\mathbf{E},\mathbf{H}\} = \mathbf{G}\left(\{\sigma,\varepsilon,\mu\}\right) \tag{1.6}$$

where $\mathbf{G}$ is the forward operator derived from Maxwell's equations, and $\mathbf{E}$ and $\mathbf{H}$ are the electric and magnetic fields (specifically, the electric field intensity and magnetic field intensity) computed for an earth model defined by parameters σ, ε, and μ. For EM induction methods, electrical conductivity is the most relevant of the three physical properties that define the earth model (West and Macnae, 1988).

1.4 Thesis objective and overview

The focus of this study was to investigate the limits of our present three-dimensional (3D) CSEM modelling capabilities, specifically in the context of marine CSEM hydrocarbon exploration scenarios. Marine CSEM data for 3D earth models and survey parameters of relevance to offshore hydrocarbon exploration were simulated using the 3D finite-element forward code CSEM3DFWD (Ansari and Farquharson, 2011, 2013, 2014; Ansari, 2014; Ansari et al., 2015). The finite element method is readily applied to boundary-conforming unstructured meshes which provide more accurate representation of complex boundaries associated with subsurface geology than rectilinear meshes. While the accuracy of the electric and magnetic fields computed using the CSEM3DFWD code has been verified for a number of simple earth models, its application to models representative of marine sedimentary environments, and more realistic models in general, has been limited. This study extended application of the code to marine models of increasing complexity, with the ultimate goal of synthesizing marine CSEM data for 3D earth models complete in their description of the subsurface. Crucial to CSEM forward modelling is the construction of meshes which are suitable in terms of mesh refinement and quality. A progression of

increasingly complex models allowed challenges associated with different model aspects (e.g., thin, laterally extensive subsurface bodies and topographic or stratigraphic surfaces) to be individually investigated and addressed.

In summary, the purposes of this study were three-fold: (1) to contribute to the continued development of the CSEM3DFWD code by extending its application to marine CSEM scenarios; (2) to address the challenges of incorporating different realistic model aspects, e.g., finite subsurface bodies and topographic or stratigraphic boundaries; and (3) to ultimately generate synthetic data for a real-world model that was detailed in its description of the subsurface, such that forward modelling could be used for practical application, e.g., feasibility studies to assess the utility of marine CSEM data for specific offshore hydrocarbon exploration and development scenarios.

The division of this thesis is as follows. In Chapter 2, the mathematics and physics governing geophysical EM phenomena are presented, as well as numerical methods for their simulation. In Chapter 3, the marine CSEM method is reviewed in more detail to provide context to the modelling scenarios. In Chapter 4, the general procedure for numerical modelling is discussed, including earth model construction, mesh generation, problem formulation, and finite element discretization, the latter two of which constitute the methodology of the CSEMFWD forward code. In Chapter 5, numerical solutions for halfspace and simple 3D models are presented and validated against semi-analytic and numerical solutions existing in the literature. Finally, in Chapter 6, a realistic marine reservoir model based on the real-life North Amethyst oil field, located in the Jeanne d'Arc Basin, offshore Newfoundland, is presented. This model provided the opportunity to identify and attempt to address some of the challenges involved in modelling real-life earth structure with unstructured meshes, both in terms of accuracy in representation of structure and management of limited computational resources.

Chapter 2

Geophysical EM modelling

2.1 Governing equations

Maxwell's equations form the basis of classical electrodynamics and govern geophysical EM phenomena. They comprise two scalar and two vector partial differential equations in five vector fields (**e**, **b**, **h**, **d**, and **j**) that describe the generation and dynamics, or time evolution, of the electric and magnetic fields due to charges, currents, and time-varying fields. The two vector partial differential equations, representative of Faraday's and Ampère's laws, may be coupled through constitutive relations that describe the interaction of fields with matter. In the following sections, Maxwell's equations will be introduced in the time domain and subsequently transformed to their frequency-domain or time-harmonic form suitable for discussion of frequency-domain EM induction methods. The presentation and development closely follows Ward and Hohmann (1988).

2.1.1 Time domain

Maxwell's equations describe the relationships between the EM fields and fluxes at position **r** and time t. For a region free of applied sources, Maxwell's equations may be expressed

in differential, time-domain form as

$$\nabla \times \mathbf{e} = -\frac{\partial \mathbf{b}}{\partial t}, \quad \text{(Faraday's law)} \tag{2.1a}$$

$$\nabla \times \mathbf{h} = \frac{\partial \mathbf{d}}{\partial t} + \mathbf{j}, \quad \text{(Ampère's law)} \tag{2.1b}$$

$$\nabla \cdot \mathbf{d} = \rho, \quad \text{and} \quad \text{(Gauss's law)} \tag{2.1c}$$

$$\nabla \cdot \mathbf{b} = 0, \quad \text{(Gauss's law for magnetism)} \tag{2.1d}$$

where

$\mathbf{e}$ is the electric field intensity in volts per metre (V/m),

$\mathbf{b}$ is the magnetic flux density in webers per square metre or teslas (Wb/m^2 or T; 1 T = 1 Wb/m^2),

$\mathbf{d}$ is the electric displacement field in coulombs per square metre (C/m^2),

$\mathbf{h}$ is the magnetic field intensity in amperes per metre (A/m),

$\mathbf{j}$ is the free electric current density in amperes per square metre (A/m^2), and

ρ is the free electric charge density in coulombs per cubic metre (C/m^3).

For regions containing applied electric sources, Maxwell's equations take the inhomogeneous form (Ward and Hohmann, 1988; Haber, 2014)

$$\nabla \times \mathbf{e} = -\frac{\partial \mathbf{b}}{\partial t}, \tag{2.2a}$$

$$\nabla \times \mathbf{h} = \frac{\partial \mathbf{d}}{\partial t} + \mathbf{j} + \mathbf{j}_{\mathbf{e}}^{\mathbf{s}}, \tag{2.2b}$$

$$\nabla \cdot \mathbf{d} = \rho, \tag{2.2c}$$

$$\nabla \cdot \mathbf{b} = 0, \tag{2.2d}$$

where $\mathbf{j}_{\mathbf{e}}^{\mathbf{s}}$ is the applied electric current density.

The auxiliary fields **d** and **h** are introduced to account for macroscopic material effects due to bound charges and bound currents on the total electric and magnetic fields. When dielectric and/or magnetic materials are exposed to external electric and magnetic fields, they react to and in turn modify the total fields (Griffiths, 1999). This cyclical process describes the phenomena of polarization in dielectric material and magnetization in magnetic material, which produce macroscopic bound charges and macroscopic bound currents, respectively. With the introduction of the auxiliary fields, Maxwell's equations may be expressed solely in terms of free charge and free current. The **e** and **b** fields and auxiliary **d** and **h** fields are related through the linear and isotropic EM constitutive relations (Ward and Hohmann, 1988)

$$\mathbf{d} = \varepsilon \mathbf{e}, \tag{2.3a}$$

$$\mathbf{b} = \mu \mathbf{h}, \quad \text{and} \tag{2.3b}$$

$$\mathbf{j} = \sigma \mathbf{e}, \quad \text{(Ohm's law)} \tag{2.3c}$$

where $\varepsilon = \varepsilon(\mathbf{r})$, $\mu = \mu(\mathbf{r})$, and $\sigma = \sigma(\mathbf{r})$ represent the dielectric permittivity, magnetic permeability, and electrical conductivity, respectively. Equations (2.3a) – (2.3c) are empirical relations that describe a material's response to and affect on the electric and magnetic fields, as measured by the physical material properties ε, μ, and σ. In general, the constitutive relations are non-linear and anisotropic, where $\varepsilon = \tilde{\boldsymbol{\varepsilon}}$, $\mu = \tilde{\boldsymbol{\mu}}$, and $\sigma = \tilde{\boldsymbol{\sigma}}$ are tensors whose components may depend on position as well as field strength, frequency, time, temperature, and pressure. For most geophysical applications, earth materials are assumed to be isotropic and homogeneous, and to possess physical properties dependent on position only, i.e., $\sigma = \sigma(\mathbf{r})$, such that the relations may be approximated as linear (Ward and Hohmann, 1988).

Electrical structure is rarely so simple to be well approximated by an isotropic model; some degree of anisotropy is generally encountered due to spatial ordering of earth materials from the grain and fabric scale to the lithological bedding scale (Løseth and Ursin, 2007; Constable, 2010). For 3D CSEM imaging using multicomponent field data, any significant anisotropy must be taken into account not only to avoid artefacts and misinterpretation, but also to be able to simultaneously fit both inline and broadside data (Carazzone et al., 2008; Constable, 2010; Newman et al., 2010). Several methods for 3D CSEM modelling consider fully generalized anisotropy where resistivity is treated as a symmetric 3×3 tensor made up of six independent elements (e.g., Weiss and Newman, 2002; Løseth and Ursin, 2007). Transverse anisotropy is a relatively simple instance of anisotropy where conductivity in the horizontal bedding plane is constant but varies from conductivity in the vertical direction, i.e., (Puzyrev et al., 2013)

$$\tilde{\sigma} = \begin{pmatrix} \sigma_x & 0 & 0 \\ 0 & \sigma_y & 0 \\ 0 & 0 & \sigma_z \end{pmatrix},$$

where $\sigma_x = \sigma_y = \sigma_{horz}$ and $\sigma_z = \sigma_{vert}$. In offshore sedimentary basins where layering is primarily horizontal, electrical structure is often well approximated by transverse anisotropy, with conductivity in the horizontal direction generally being greater than that in the vertical direction, i.e., $\sigma_{horz} > \sigma_{vert}$ (Constable, 2010; Newman et al., 2010). The CSEM3DFWD code used in this study can only accommodate isotropic conductivity models at this time.

A mathematical statement about the local conservation of charge, known as the continuity equation (Griffiths, 1999), is contained within Maxwell's equations and may be derived by taking the divergence of equation (2.2b) and substituting equation (2.2c) in the resultant

expression to obtain*

$$\nabla \cdot \mathbf{j} = -\frac{\partial \rho}{\partial t} - \nabla \cdot \mathbf{j}_\mathbf{e}^\mathbf{s}. \tag{2.4}$$

Note that conservation of charge is a fundamental physical law that is independent from, but consistent with, Maxwell's equations. Since the source current density $\mathbf{j}_\mathbf{e}^\mathbf{s}$ is localized in space to the source location and all other regions of space are source-free, we have, more specifically,

$$\nabla \cdot \mathbf{j} = \begin{cases} -\dfrac{\partial \rho}{\partial t} - \nabla \cdot \mathbf{j}_\mathbf{e}^\mathbf{s} & \text{at source location, and} \\ -\dfrac{\partial \rho}{\partial t} & \text{everywhere else.} \end{cases} \tag{2.5}$$

2.1.2 Frequency domain

The time dependence of the EM fields, e.g., $\mathbf{e}(\mathbf{r},t)$, can be transformed to a frequency dependence, e.g., $\mathbf{E}(\mathbf{r},\omega)$, by computing the Fourier transforms of the EM fields. Taking the 1D Fourier transform of equations (2.2a) – (2.2d), we obtain Maxwell's equations in the frequency domain,

$$\nabla \times \mathbf{E} = -i\omega\mathbf{B}, \tag{2.6a}$$

$$\nabla \times \mathbf{H} = i\omega\mathbf{D} + \mathbf{J} + \mathbf{J}_\mathbf{e}^\mathbf{s}, \tag{2.6b}$$

$$\nabla \cdot \mathbf{D} = \rho, \quad \text{and} \tag{2.6c}$$

$$\nabla \cdot \mathbf{B} = 0, \tag{2.6d}$$

*The operators $\nabla\times$ and $\partial/\partial t$ may be interchanged provided that $\mathbf{d}$ is piecewise continuous and that its first and second derivatives exist and are continuous, based on Clairaut's or Schwarz' theorem for symmetry of second derivatives.

where we have made use of the Fourier transform pair (Hohmann, 1988)

$$\mathbf{F}(\mathbf{r},\omega) = \int_{-\infty}^{\infty} \mathbf{f}(\mathbf{r},t) e^{-i\omega t} dt \tag{2.7}$$

and

$$\mathbf{f}(\mathbf{r},t) = \frac{1}{2\pi} \int_{-\infty}^{\infty} \mathbf{F}(\mathbf{r},\omega) e^{i\omega t} d\omega. \tag{2.8}$$

Transformation of the EM equations to the frequency domain is equivalent to assuming a harmonic time dependence of $e^{i\omega t}$ for the EM fields (Hohmann, 1988). The continuity equation (2.5) becomes, in the frequency domain,

$$\nabla \cdot \mathbf{J} = \begin{cases} -i\omega\rho - \nabla \cdot \mathbf{J}_{\mathbf{e}}^{\mathbf{s}} & \text{at source location, and} \\ -i\omega\rho & \text{everywhere else.} \end{cases} \tag{2.9}$$

Many EM induction methods, specifically, frequency-domain EM methods, employ time-harmonic sources, that is, sources which vary sinusoidally in time at some specific yet arbitrary angular frequency ω; such time-harmonic sources generate time-harmonic, steady-state EM fields. For these methods, frequency-domain analysis of the EM fields is more convenient because the EM problem reduces from a four-dimensional problem in (x,y,z,t) space to a 3D problem in (x,y,z) space at a fixed, single frequency ω (Jin, 2014). Because Fourier analysis tells us that any well-behaved, time-varying function can be expressed in terms of time-harmonic components, frequency-domain solutions can be extended to transient time-domain EM methods as well. Rather than time-stepping directly in the time domain, it may be advantageous to instead approximate a transient response as a sum of Fourier-transformed, time-harmonic fields at discrete, sampled frequencies (Hohmann, 1988; Jin, 2014).

2.1.3 The EM Helmholtz equations

By substituting the frequency-domain form of the constitutive relations into equations (2.6a) and (2.6b), which describe the time evolution of the electric and magnetic fields, we obtain expressions solely in terms of **E** and **H**,

$$\nabla \times \mathbf{E} + i\mu\omega\mathbf{H} = 0 \tag{2.10}$$

and

$$\nabla \times \mathbf{H} - (\sigma + i\varepsilon\omega)\mathbf{E} = \mathbf{J}_\mathbf{e}^\mathbf{s}. \tag{2.11}$$

By making appropriate substitutions, these equations may be modified to expressions involving only the electric or the magnetic field. Solving for **H** in (2.10) and **E** in (2.11), we obtain

$$\mathbf{E} = \frac{1}{\tilde{\sigma}}\nabla \times \mathbf{H} - \frac{1}{\tilde{\sigma}}\mathbf{J}_\mathbf{e}^\mathbf{s} \tag{2.12}$$

and

$$\mathbf{H} = -\frac{1}{i\omega\mu}\nabla \times \mathbf{E}, \tag{2.13}$$

where

$$\tilde{\sigma} = \sigma + i\varepsilon\omega. \tag{2.14}$$

By substituting (2.12) into (2.10) and (2.13) into (2.11), we obtain two decoupled, second-order partial differential equations in **E** and **H** (Zhdanov, 2002),

$$\mu\nabla \times \left(\frac{1}{\mu}\nabla \times \mathbf{E}\right) + i\omega\mu\tilde{\sigma}\mathbf{E} = -i\omega\mu\mathbf{J}_\mathbf{e}^\mathbf{s} \tag{2.15}$$

and

$$\tilde{\sigma}\nabla \times \left(\frac{1}{\tilde{\sigma}}\nabla \times \mathbf{H}\right) + i\omega\mu\tilde{\sigma}\mathbf{H} = \tilde{\sigma}\nabla \times \left(\frac{1}{\tilde{\sigma}}\mathbf{J}_\mathbf{e}^\mathbf{s}\right). \tag{2.16}$$

For a homogeneous region within which the parameters ε, μ, and σ are constant, equations (2.15) and (2.16) become

$$\nabla \times \nabla \times \mathbf{E} + i\omega\mu\tilde{\sigma}\mathbf{E} = -i\mu\omega\mathbf{J}_{\mathbf{e}}^{\mathbf{s}} \tag{2.17}$$

and

$$\nabla \times \nabla \times \mathbf{H} + i\omega\mu\tilde{\sigma}\mathbf{H} = \nabla \times \mathbf{J}_{\mathbf{e}}^{\mathbf{s}}. \tag{2.18}$$

For source-free regions, the divergence of the electric and magnetic fields is zero, i.e., $\nabla \cdot \mathbf{E} = 0$ and $\nabla \cdot \mathbf{H} = 0$, and the vector identity $\nabla \times \nabla \times \mathbf{A} = \nabla\nabla \cdot \mathbf{A} - \nabla^2\mathbf{A}$ can be used to replace the curl-curl operators in equations (2.17) and (2.18) by Laplace operators to obtain (Ward and Hohmann, 1988; Zhdanov, 2002)

$$\nabla^2\mathbf{E} + \tilde{k}^2\mathbf{E} = i\mu_0\omega\mathbf{J}_{\mathbf{e}}^{\mathbf{s}} \tag{2.19}$$

and

$$\nabla^2\mathbf{H} + \tilde{k}^2\mathbf{H} = -\nabla \times \mathbf{J}_{\mathbf{e}}^{\mathbf{s}}, \tag{2.20}$$

where

$$\tilde{k}^2 = -i\mu\omega\tilde{\sigma} = -i\mu\omega(\sigma + i\varepsilon\omega) = -i\mu\sigma\omega + \mu\varepsilon\omega^2. \tag{2.21}$$

Equations (2.19) and (2.20) are inhomogeneous forms of the EM Helmholtz equations

$$\nabla^2\mathbf{E} + \tilde{k}^2\mathbf{E} = 0 \tag{2.22}$$

and

$$\nabla^2\mathbf{H} + \tilde{k}^2\mathbf{H} = 0, \tag{2.23}$$

which are the frequency-domain equivalents of the *lossy* or damped EM wave equations, that is, the wave equations featuring first-order, conductivity-governed loss terms, $-i\mu\sigma\omega\mathbf{E}$ and $-i\mu\sigma\omega\mathbf{H}$ (Haber, 2014). The EM Helmholtz equations describes a continuum of EM behaviour from static (e.g., the direct-current, DC, resistivity method), to quasi-static (e.g., induction methods; see Section 2.1.6), to wave-like behaviour (e.g., ground penetrating radar; Haber, 2014). The constant $\tilde{k}$, known as the propagation constant or wave number, can be written in complex form as (Zonge and Hughes, 1988)

$$\tilde{k} = \alpha - i\beta,$$

where the phase constant α is

$$\alpha = \omega \left[\frac{\mu\varepsilon}{2} \left(\sqrt{1 + \left(\frac{\sigma}{\varepsilon\omega} \right)^2} + 1 \right) \right]^{1/2}, \tag{2.24}$$

and the attenuation constant β is

$$\beta = \omega \left[\frac{\mu\varepsilon}{2} \left(\sqrt{1 + \left(\frac{\sigma}{\varepsilon\omega} \right)^2} - 1 \right) \right]^{1/2}. \tag{2.25}$$

2.1.4 Plane waves in a homogeneous earth

For a uniform plane wave propagating in the $+z$ or downward direction in a homogeneous earth, equations (2.22) and (2.23) reduce to (Ward and Hohmann, 1988; Zhdanov, 2009)

$$\frac{\partial^2 \mathbf{E}}{\partial^2 z} + \tilde{k}^2 \mathbf{E} = 0 \tag{2.26}$$

and

$$\frac{\partial^2 \mathbf{H}}{\partial^2 z} + \tilde{k}^2 \mathbf{H} = 0, \tag{2.27}$$

which have the plane-wave solutions (e.g., Zonge and Hughes, 1988; Zhdanov, 2009)

$$\mathbf{E} = \mathbf{E}^{+} e^{-i\tilde{k}z} + \mathbf{E}^{-} e^{i\tilde{k}z} \tag{2.28}$$

and

$$\mathbf{H} = \mathbf{H}^{+} e^{-i\tilde{k}z} + \mathbf{H}^{-} e^{i\tilde{k}z}, \tag{2.29}$$

where $\mathbf{E}^{+}$, $\mathbf{E}^{-}$, $\mathbf{H}^{+}$ and $\mathbf{H}^{-}$ are undetermined coefficients. Recalling the complex form of $\tilde{k}$, $\tilde{k} = \alpha - i\beta$, the solutions can be equivalently expressed as

$$\mathbf{E} = \mathbf{E}^{+} e^{-i\alpha z} e^{\beta z} + \mathbf{E}^{-} e^{i\alpha z} e^{-\beta z} \tag{2.30}$$

and

$$\mathbf{H} = \mathbf{H}^{+} e^{-i\alpha z} e^{\beta z} + \mathbf{H}^{-} e^{i\alpha z} e^{-\beta z}, \tag{2.31}$$

where the terms $e^{\pm i\alpha z}$ and $e^{\pm\beta z}$ respectively indicate phase oscillation and amplitude attenuation or growth with respect to z. The reason for description of α and β as the phase and attenuation constants, respectively, now becomes apparent. The phase constant α defines the rate of change in phase as the wave propagates and the attenuation constant β defines the rate of change in amplitude as the wave propagates. For a whole space, to avoid $\mathbf{E}, \mathbf{H} \to \infty$ as $z \to \infty$, $\mathbf{H}^{+}$ and $\mathbf{E}^{+}$ must be set to zero; in the more general case of a homogeneous-layered earth, $\mathbf{H}^{\pm}$ and $\mathbf{E}^{\pm}$ can be non-zero if boundaries are present which reflect a portion of the incident field (Zhdanov, 2009). We can define the distance over which the field amplitude has decayed to $1/e$ of its initial value, known as the skin depth δ, as the inverse of the attenuation constant β (Zonge and Hughes, 1988),

$$\delta = \frac{1}{\beta}. \tag{2.32}$$

Skin depth can be used as a quantitative measure of the amount of inductive attenuation experienced by an EM signal as it propagates with frequency ω through a background of conductivity σ.

2.1.5 Mode decomposition in a homogeneous earth

For a source-free, homogeneous region, the EM fields may be decomposed about an arbitrary axis into two orthogonally polarized modes of propagation known as the transverse electric (TE) and transverse magnetic (TM) modes, where 'transverse' refers to the direction normal to the reference axis (Chave and Cox, 1982; Ward and Hohmann, 1988). For a 1D earth in which structure varies in the vertical (z) direction, the reference axis is generally taken as the z-axis; with this choice of axis, there is no coupling between the TE and TM modes, i.e., the modes independently satisfy Maxwell's equations (Chave and Cox, 1982; Weidelt, 2007; Andréis and MacGregor, 2008; Chave, 2009). Mode decomposition theory is elaborated in Stamnes (1986).

In the TE mode, the electric field is restricted to the horizontal plane and there exists no vertical component of the electric field; current loops circle in the horizontal plane, and coupling between adjacent layers is purely inductive (see Section 3.2 for further explanation of inductive and galvanic coupling; Andréis and MacGregor, 2008; Chave, 2009). In the TM mode, the magnetic field is restricted to the horizontal plane, and there exists no vertical component of the magnetic field. Given the orthogonality of the electric and magnetic fields, the electric field, and hence current loops, are restricted to the vertical plane, and coupling between adjacent layers is both inductive and galvanic (Andréis and MacGregor, 2008; Chave, 2009). EM sources may produce one or a combination of the two modes (see Chave, 2009). In the near-zero frequency (DC) limit, the TE mode vanishes and the TM-mode response is exclusively galvanic (Chave and Cox, 1982). For optimal sensitivity to thin, resistive horizontal layers such as hydrocarbon targets, the CSEM source must

excite the TM mode of propagation; this issue will be discussed further in Section 3.2. In Appendix A, through the use of Schelkunoff potentials, it is demonstrated that an arbitrary field in a homogeneous, source-free region can be expressed as the sum of TE and TM modes.

2.1.6 Low-frequency EM wave propagation in conductive media

To better understand the intrinsic resolution of the CSEM method, and low-frequency EM methods in general, we revisit the EM Helmholtz equations. The physical description or behaviour of EM wave propagation is defined in different asymptotic limits of the EM Helmholtz equations. To review, the homogeneous EM Helmholtz equations are (equations 2.22 and 2.23)

$$\nabla^2\mathbf{E} + \tilde{k}^2\mathbf{E} = 0$$

and

$$\nabla^2\mathbf{H} + \tilde{k}^2\mathbf{H} = 0,$$

where

$$\tilde{k}^2 = -i\mu\omega\tilde{\sigma} = -i\mu\omega(\sigma + i\varepsilon\omega) = -i\mu\sigma\omega + \mu\varepsilon\omega^2.$$

In free space and air, where conductivity is approximately zero, i.e., $\sigma \approx 0$, the conductivity-governed loss term $-i\mu\sigma\omega$ disappears, the wavenumber k is real-valued, i.e., $k^2 = \mu\varepsilon\omega^2$, and the Helmholtz equations reduce to the frequency-domain equivalents of the lossless EM wave equations. In lossless wave propagation, which is often used to approximate seismic wave propagation, vertical resolution is proportional to frequency, energy loss is via geometric spreading only, and resolution at depth or distance from source is essentially the same as resolution at the near surface or near source (Constable, 2010). Physical phenomena described by wave propagation are easily visualized using ray-tracing techniques (West

and Macnae, 1988).

By contrast, in low-frequency EM methods where $\omega < 100$ kHz, the loss term $-i\mu\sigma\omega$ dominates since earth materials have conductivities of many orders of magnitude larger (typically 10^9) than their dielectric permittivity[†], and the inequality $\sigma \gg \varepsilon\omega$ holds (Zonge and Hughes, 1988; Constable, 2010). In this limit, the wavenumber k is completely imaginary, i.e.,

$$k^2 = -i\mu\omega\sigma, \tag{2.33}$$

and the phase and attenuation constants α and β reduce to

$$\alpha = \beta = \sqrt{\frac{\mu\sigma\omega}{2}}, \tag{2.34}$$

such that the skin depth δ becomes

$$\delta = \frac{1}{\beta} = \sqrt{\frac{2}{\mu\sigma\omega}}, \tag{2.35}$$

which for $\mu = \mu_0$, is approximately equal to

$$\delta \approx 503\sqrt{\frac{1}{f\sigma}} \quad \text{(SI units)}. \tag{2.36}$$

In this regime, the Helmholtz equations reduce to the frequency-domain equivalents of the diffusion equation. The regime in which diffusive EM behaviour arises is known as the quasi-static or quasi-stationary regime since the fields are varying sufficiently slowly such that in any region of non-vanishing conductivity, the system may be approximated to be in equilibrium or steady state at all times (Grant and West, 1965; Ward and Hohmann, 1988; Zhdanov, 2002).

[†]Earth materials typically have conductivities $\sigma > 10^{-4}$ S/m and permittivities $\varepsilon < 10^{-11}$ F/m (Zonge and Hughes, 1988).

The negligibility of terms related to $\varepsilon\omega$ indicates that the displacement current associated with a time-varying electric field is negligible compared to the conduction current associated with the flow of charge. In this limit, Ampère's law reduces to its pre-Maxwell form,

$$\nabla \times \mathbf{H} = \mathbf{J} + \mathbf{J}_{\mathbf{e}}^{\mathbf{s}}, \tag{2.37}$$

where we have included the source inhomogeneity $\mathbf{J}_{\mathbf{e}}^{\mathbf{s}}$. Consequently, it can be shown in the low-frequency case that the frequency-domain continuity equation reduces to

$$\nabla \cdot \mathbf{J} = \begin{cases} -\nabla \cdot \mathbf{J}_{\mathbf{e}}^{\mathbf{s}} & \text{at source location, and} \\ 0 & \text{everywhere else.} \end{cases} \tag{2.38}$$

Description of the behaviour of low-frequency EM fields in conductive media as propagative, which suggests wave-like behaviour, or diffusive is a contentious issue within the geophysical EM community. Løseth et al. (2006) demonstrate that both undamped wave propagation in nonconducting media and highly damped wave propagation in conducting media may be treated in a unified mathematical framework; both the time-domain hyperbolic wave and parabolic diffusion equations transform to the elliptic Helmholtz equation in the frequency domain, which has damped wave solutions. The behaviour of EM propagation, as described by the EM Helmholtz equations, is characterized by the position of the wavenumber k in the complex plane. There exists a continuum between undamped wave propagation, which corresponds to a real-valued k, and highly attenuated propagation or diffusion, which corresponds to an imaginary-valued k, and thus there is no clear cut-off between wave-like and diffusive behaviour (Løseth et al., 2006).

While a full wave treatment will lead to correct solutions for low-frequency EM propagation in conductive media, the diffusion equation affords simplification of the ensuing mathematics. Further, behaviour of low-frequency EM propagation is decidedly in the dif-

fusive limit, where wave propagation is both highly attenuated and highly dispersive. Solutions of the diffusion equation to a transient source are characterized by a smoothing of the fields in time toward equilibrium. Since many initial states tend toward the same final equilibrium state, an attempt to recover an earlier configuration from the final state constitutes an ill-posed problem. In contrast to the hyperbolic wave equation, which is time-reversal invariant, i.e., changing t to $-t$ leaves the equation unaltered, the parabolic diffusion equation is not. Diffusive EM fields evolve unidirectionally forward in time, that is, the fields at a given point (r',t') depend only on $t < t'$, which precludes the existence of reflections and refractions at interfaces (Chave, 2009). Further, propagation of a disturbance through space is theoretically instantaneous (information propagation speed is infinite along characteristic curves of constant time) and does not possess a wavefront, although an apparent speed may be interpreted from the time it takes for fields to reach their maxima at a given distance from source (Ward and Hohmann, 1988; Zhdanov, 2009).

In short, while low-frequency EM propagation in conductive media may be treated within a wave framework, its behaviour resembles diffusion, which provides an equally acceptable mathematical description.

2.2 1D EM modelling

The theory of EM field propagation in 1D media, i.e., media with properties varying in only one direction, is well developed (e.g. Harrington, 1961; Wait, 1962; Ward and Hohmann, 1988). Closed-form expressions for the EM fields in a layered earth are readily available, and several forward and inverse modelling codes have been written specifically for geophysical applications (e.g. Chave and Cox, 1982; Flosadóttir and Constable, 1996; Løseth and Ursin, 2007; Key, 2009). Due to the cylindrical symmetry of a layered earth, solutions for the EM fields take the form of two-dimensional (2D) spatial Fourier or Hankel transforms

that may be numerically evaluated using digital filter or quadrature methods (e.g. Anderson, 1982; Chave, 1983; Anderson, 1989; Key, 2012a). 1D solutions computed in this manner are often referred to as *semi-* or *quasi-analytic* because the closed-form expressions require numerical techniques for their evaluation.

1D modelling and inversion have often been used to cultivate an understanding of the performance of the marine CSEM method in different exploration scenarios. Variations on the so-called 1D canonical oil field or reservoir model are frequently featured in modelling studies to investigate the effects of the environment (e.g., water depth, reservoir burial depth, and reservoir thickness) and survey parameters (e.g., source frequency content and source-receiver offset) on the ability of the method to resolve thin, buried resistive layers (e.g., Constable and Weiss, 2006; Um and Alumbaugh, 2007; Key, 2009). The 1D canonical reservoir model consists of a 100 m-thick, 0.01 S/m (100 ohm-m) resistive layer buried at a depth of 1000 m within a 1 S/m (1 ohm-m) sediment halfspace, with an overlying 3.3 S/m (0.3 ohm-m) sea halfspace (Figure 2.1). This model was inspired by the Girassol oil field located offshore Angola, where the first marine CSEM field trial for industry was conducted by Statoil in 2000 with support from the Southampton Oceanography Centre and the Scripps Institution of Oceanography (Ellingsrud et al., 2002; Constable, 2010).

For structure that can be reasonably approximated by layers, 1D modelling provides a best-case estimate of target resolution as well as guidance in survey design (Hoversten et al., 2006). For complex structure where there is significant directional variation in resistivity, 2D or 3D modelling is required to properly account for the CSEM response. The downside of multidimensional modelling is that computation of the forward responses becomes much more demanding in terms of CPU time and memory usage (Hohmann, 1988). For this reason, 1D modelling and inversion continue to have relevance for the purpose of quick and simple interpretation of marine CSEM data. Moreover, while 3D CSEM surveys are becoming the standard for commercial applications (Danielsen and Bekker, 2011),

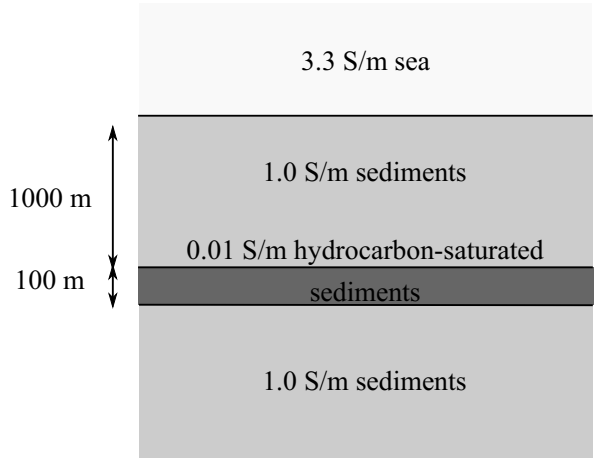

Figure 2.1. The 1D canonical oil field or reservoir model inspired by the Girassol deepwater field, offshore Angola. The model consists of a 100 m-thick, 0.01 S/m (100 ohm-m) reservoir embedded at a depth of 1000 m within a 1 S/m (1 ohm-m) sediment halfspace, with an overlying 3.3 S/m (0.3 ohm-m) sea halfspace.

circumstances may persist where collected data are insufficient, both in terms of data coverage and measured field components, to properly constrain multidimensional interpretation (Constable, 2010). Lastly, as will be demonstrated in this study, 1D modelling is an important tool for verifying the accuracy of multidimensional numerical solutions; 1D modelling is accurate for 3D tabular targets within lateral limits of the body (Constable and Weiss, 2006), and it can handle the large offsets and depths associated with large, computationally taxing finite-difference or finite-element schemes (Flosadóttir and Constable, 1996; Løseth and Ursin, 2007).

2.3 Numerical methods for multidimensional EM modelling

With the exception of a few simple geometries, easily computable analytic or semi-analytic forward solutions do not exist for arbitrary 2D or 3D earth models; instead, approximate numerical solutions are sought (Hohmann, 1988). Numerical solution of EM problems involves discretization of either the integral or differential form of Maxwell's equations on the computational domain Ω and application of appropriate boundary conditions at do-

main boundary Γ. The process of discretization involves replacement of the continuous governing equations by discrete approximations, thereby converting the original continuous boundary value problem with an infinite number of unknowns into a discrete problem with a finite number of unknowns (Saad, 2003; Jin, 2002). Discretization of the governing equations gives rise to a system of equations of matrix form

$$Au = b,$$

where A is the system matrix involving operators defined by the governing equations, and u and b are the solution and source vectors, respectively. Discretization is achieved by subdividing the model domain into a number of subdomains or cells. Physical property values are continuous functions of space within these subdomains and only allowed to be discontinuous along subdomain boundaries. The EM fields are assigned within each subdomain via interpolation from values computed at discrete elements of the mesh. The resultant mesh is a discrete approximation to the true earth model, and the corresponding numerical solution is an approximation to the true forward solution (Zhdanov, 2009). Construction of the mesh is non-trivial since it will ultimately affect memory requirements, computation time, and the accuracy and efficiency of the numerical solution (Jin, 2002; Avdeev, 2005). The importance of mesh quality will be discussed in Section 4.2.2.

There are several common techniques for discretization of Maxwell's equations, including the integral-equation method, the finite-difference method, and the finite-element method, the later two of which can be considered more generally as differential-equation methods. The integral-equation method is based on the scattering equation, a second-type Fredholm integral equation arising from decomposition of the EM fields into primary components associated with some background conductivity distribution and secondary (also known as anomalous or scattered) components arising from localized conductivity inho-

mogeneities (e.g. Raiche, 1974; Hohmann, 1975; Wannamaker et al., 1984). The formulation replaces the region of anomalous conductivity distribution with an equivalent volume of scattering current and requires calculation of the Green's functions for the background model of the earth. Because it is only necessary to solve for the scattering current within the anomalous body, the method requires discretization of only those regions of the model with anomalous conductivity distribution. This dramatically reduces the size of the system matrix and thus required memory for the integral-equation method as compared to other numerical schemes. There are however several drawbacks that limit its application to general geophysical EM problems. Firstly, calculation of the appropriate Green's function is only manageable for very simple (i.e., layered) background models of the earth (Avdeev, 2005; Zhdanov, 2009). Secondly, the integral-equation formulation gives rise to dense system matrices, that is, matrices in which most of the elements are nonzero. Lastly, any structure which deviates from the background model must be treated as a region of anomalous conductivity. Earth models with large-scale and complex variations in conductivity thus give rise to large, dense matrices (Avdeev, 2005; Zhdanov, 2009). In summary, while the integral-equation method can in principle handle any model, practical limitations restrict its use to compact bodies residing in a simple earth, and differential-equation methods are typically employed for models of arbitrary size and complexity (Newman and Alumbaugh, 1995; Alumbaugh et al., 1996; Zhdanov, 2009).

The finite-difference method is based on local approximation of the partial differential operators of Maxwell's equations by operators derived from Taylor series expansions (Saad, 2003). The finite-difference operators act on discrete values of the EM field arising from discretization of the model region using a structured mesh, i.e., a mesh with regular ordering of nodes and predictable connectivity of elements (Zhdanov, 2009). The simplicity and ease of implementation of finite-difference schemes make them a popular choice for 3D EM modelling. The structured meshes do however have limitations in the accuracy with which

they represent earth structure due to the staircasing of curvilinear boundaries. Moreover, because of the structured nature of the mesh, refinement cannot be localized and instead propagates in all three dimensions, leading to a mesh with a very large number of cells (Constable, 2010).

By contrast, the finite-element method is readily applied to unstructured meshes which are more flexible in their discretization, thus enabling more accurate representation of complex structure as well as localized mesh refinement (Ansari and Farquharson, 2014). Unlike structured meshes, where the ordering of nodes and cells is regular and predictable using simple arithmetic, unstructured meshes require explicit storage of neighbouring nodes or cells (Cheng et al., 2012). The division of the modelling domain into subdomains, or *finite elements*, is commonly accomplished in 2D and 3D using triangular and tetrahedral elements, respectively, of variable shape and size (Zhdanov, 2009). Within each element, the EM fields or potentials are represented as a sum of interpolation functions, also known as expansion or basis functions (Jin, 2002). The linear coefficients of the basis function expansion, that is, the degrees of freedom in the system, are typically associated with the nodes and/or edges of the element (Schwarzbach, 2009); the former scalar-valued type is known as a Lagrange nodal element, and the latter vector-valued type is known as a Nédélec edge element. Vector-valued edge elements are often preferred to scalar-valued nodal elements for discretization of the electric field because they conform to the requirement of continuity of the tangential electric field and discontinuity of the normal electric field, and enforce the zero-divergence electric field condition for a source-free cell (Schwarzbach et al., 2011; Vieira da Silva et al., 2012; Ansari and Farquharson, 2014). There are many variations on the finite-element method, depending on the choice of basis functions and technique for determining the coefficients of the basis function expansions (Jin, 2002; Avdeev, 2005; Zhdanov, 2009). The two most widely used methods to formulate the system of equations are the variational method and the method of weighted residuals (Jin, 2002). Both meth-

ods lead to weak formulations of the original boundary value problem, meaning that the problem is reduced to one in which the governing differential equations are only required to be satisfied in an average (integral) sense, rather than an absolute sense, over the global domain (Ansari and Farquharson, 2014).

In contrast to the integral-equation method, differential-equation methods require discretization of the entire model domain (Newman and Alumbaugh, 1995; Zhdanov, 2009). While this is a disadvantage in terms of overall problem size, the system matrices that arise are sparse, meaning that they have very few nonzero entries, and numerical solvers which are designed to exploit this matrix structure may be implemented to solve the system more efficiently (Saad, 2003). Due to the size and complexity of 3D EM problems, iterative solvers, in particular those based on Krylov subspace methods (e.g., the CG, BiCG, GMRES methods), are typically preferred to direct solvers (e.g., MUMPS) because they are computationally less expensive; solution requires only computation and storage of matrix-vector products (Avdeev, 2005; Streich, 2009; Vieira da Silva et al., 2012). Direct solvers for sparse linear systems are commonly based on LU factorization, which can be viewed as modified form of Gaussian elimination (Saad, 2003). In a finite and predictable number of operations, a numerical solution is obtained which could be considered exact in the absence of rounding errors. By contrast, iterative solutions generate successive, improving approximate solutions based on some initial guess, and arrive at an acceptable solution when the residual norm falls below a specified tolerance.

Iterative methods are less demanding than direct solvers in terms of storage requirements, but they are generally less robust to system ill-conditioning (Saad, 2003; Vieira da Silva et al., 2012). The linear systems arising from finite-element discretization using unstructured meshes are highly ill-conditioned, meaning that the output solution is highly sensitive to changes or errors in input (Newman, 2014). The rate of convergence of the iterative solver, or the number of iterations required to arrive at an acceptable approximate

solution, depends on the condition number of the system matrix. The successful application of iterative methods to EM problems depends on appropriate modification to the original matrix system, known as *preconditioning*, to make the problem more amenable to iterative methods (Saad, 2003). For finite-element solutions implementing iterative solvers, the quality of the mesh is very influential on the condition number of the system matrix and hence performance of the solver. The subject is further discussed in Section 4.2.2.

In addition to its robustness to ill-conditioning, a direct solver may be preferable to an iterative solver for efficient multisource simulation in moderately sized problems. For a system of the form $Ax = b$, given an invariable left-hand-side A, a one-time LU factorization of A may be used for solving the system for multiple values of right-hand side b. This initial matrix factorization involves many steps, but once completed, solutions for multiple source locations can be inexpensively achieved using the same left-hand-side factorization (Streich, 2009). To avoid the necessity of mesh refinement at all possible source locations, in such instances a primary-secondary formulation is appropriate to remove source singularities from discretization (e.g., Streich, 2009; Vieira da Silva et al., 2012, see Section 2.3.2.1).

2.3.1 2D EM modelling

2Dl modelling of marine CSEM refers to modelling in which the electrical structure of the subsurface is assumed to be invariable along geological strike. Because the EM source field is 3D, 2D forward algorithms collapse the source fields along-strike by Fourier transforming the governing equations into the spatial wavenumber domain with respect to the strike direction, i.e., the direction in which conductivity is invariable (Hohmann, 1988; Constable, 2010). For this reason, 2D modelling is sometimes referred to as a 2.5D problem (Unsworth et al., 1993).

One of the first 2D forward codes for frequency-domain EM modelling was the finite-

element code of Unsworth et al. (1993). Unsworth and Oldenburg (1995) implemented this forward code into a marine CSEM inversion code for application to mid-ocean ridge exploration, but this code has not largely featured in the literature (Constable, 2010). A modified version of the 2D finite-element code of Unsworth et al. (1993) was also used by MacGregor et al. (2001) in conjunction with the Occam's inversion algorithm of Constable et al. (1987) to invert a mid-ocean ridge CSEM data set, constituting the first 2D inversion of real CSEM data.

Li and Key (2007) developed a 2D adaptive finite-element code, MARE2DCSEM (Modeling with Adaptively Refined Elements for the 2D CSEM method), for forward modeling of marine CSEM in the frequency domain with adaptive mesh refinement. This code was developed at the Scripps Institution of Oceanography Marine EM Laboratory and is publicly available. The accuracy of the code was validated through comparison of its solution for the 1D canonical oil field model to that of Constable and Weiss (2006), and has also been demonstrated on several complex offshore structural models (e.g., Li and Key, 2007; Key, 2012c). In a companion paper by Li and Constable (2007), MARE2DCSEM was used to study the effects of variable seafloor topography on the marine CSEM response. Key and Ovall (2011) later parallelized MARE2DCSEM and substituted a dual-weighted residual method for the previous dual-error weighting method for a posteriori error estimation in adaptive mesh refinement (see Li and Key, 2007; Key and Ovall, 2011, for details). More recently, the forward algorithm was implemented along with the Occam inversion algorithm (Constable et al., 1987) in the MARE2DEM (Modelling with Adaptively Refined Elements for 2D Electromagnetics) code (Key, 2012c). The most recent version of code allows forward and inverse modelling for isotropic or triaxially anisotropic conductive media using electric dipole, magnetic dipole, or magnetotelluric sources.

Many other 2D forward and inversion codes have been applied to marine CSEM modelling. Abubakar et al. (2008) developed a 2D staggered-grid finite-difference inversion

code which allows for efficient simulation of multisource surveys through implementation of a multifrontal LU decomposition algorithm. This inversion code was used to invert CSEM data collected for an offshore Oregon gas hydrate mapping and characterization study (Weitemeyer, 2008; Weitemeyer et al., 2011). Streich et al. (2011) present a 2D finite-difference algorithm based on a primary-secondary electric field decomposition and enforce explicit divergence conditions to stabilize the finite-difference system at low frequencies. Kong et al. (2008) developed a 2D finite-element algorithm for marine CSEM modelling in stratified anisotropic media also based on a primary-secondary approach. The 2D finite-element code of Everett and Edwards (1993) was used in a modelling study of similar intent to this project (see Boyce, 1996), but computes the transient step-on response.

For marine CSEM survey data collected along single lines, 2D modelling and inversion may constitute a reasonable approach to data interpretation as the spatial density of such data is inadequate for 3D modelling. This idea was addressed in a CSEM sensitivity study conducted by Constable (2010). Constable (2010) used the 3D finite-volume code of Weiss and Constable (2006) to demonstrate that the inline horizontal electric and magnetic field components typically measured in a CSEM survey are primarily sensitive to structure beneath or between the source and receiver, and that changes in conductivity more than about half the source-receiver separation in the crossline (broadside) or vertical direction have little effect on the data. 2D modelling may be adequate for surveys involving a small to moderate volume of data. Moreover, full 3D inversion of EM data remains a challenge due to the significant computational requirements, as demonstrated by Commer et al. (2008).

2.3.2 3D EM modelling

Numerous numerical techniques have been employed for frequency-domain 3D modelling of marine CSEM, including the finite-difference method (e.g., Newman and Alumbaugh, 1995, 1997; Commer and Newman, 2008; Sasaki and Meju, 2009; Newman et al., 2010)

the finite-element method (e.g. Streich, 2009; Schwarzbach et al., 2011; Vieira da Silva et al., 2012; Puzyrev et al., 2013; Ansari and Farquharson, 2014), and to a lesser extent, the finite-volume method (e.g., Constable and Weiss, 2006; Weiss, 2013) and finite-integration technique (e.g., Plessix et al., 2007).

2.3.2.1 Finite-difference schemes

The finite-difference codes of Newman and Alumbaugh (1995) and Sasaki and Meju (2009) are implemented on Yee staggered rectangular grids (Yee, 1966), where the electric and magnetic field vectors are assigned to the centers of the cell edges and cell faces, respectively. This staggered scheme enforces conservation of electric current and a divergence-free magnetic field (Newman and Alumbaugh, 1995). All of the finite-difference codes mentioned above rely on a primary-secondary electric field decomposition wherein the frequency-domain Helmholtz equation is formulated in terms of the secondary or scattered electric field, i.e., (Newman and Alumbaugh, 1995; Sasaki and Meju, 2009),

$$\nabla \times \nabla \times \mathbf{E}_s + i\omega\mu_0\sigma\mathbf{E}_s = -i\omega\mu_0\left(\sigma - \sigma_p\right)\mathbf{E}_p, \tag{2.39}$$

where $\mathbf{E}_s$ is the secondary or scattered field, $\mathbf{E}_p$ is the primary field, and $\sigma_p = \sigma_p(\mathbf{r})$ is the background resistivity model, typically chosen to correspond to a homogeneous whole space or 1D layered halfspace. A primary-secondary decomposition removes the source singularity from discretization, thus avoiding the numerical difficulties associated with large and rapidly varying electric and magnetic field values, and the requisite mesh refinement, in the vicinity of the source. Since the scattered field varies more smoothly in space near the source than the total field, a coarser mesh may be employed without impacting accuracy (Streich, 2009). The electric field Helmholtz formulation has the advantage that the electric field is solved for directly, thus avoiding the errors associated with numerical dif-

ferentiation when a potential formulation is used (Weiss, 2013). The disadvantage of the formulation is that the associated system is ill-conditioned at low frequencies, where the second conductivity-related term tends to zero as $i\omega\mu_0\sigma \to 0$. In this limit, the system tends toward

$$\nabla \times \nabla \times \mathbf{E}_s = -i\omega\mu_0 (\sigma - \sigma_p) \mathbf{E}_p, \tag{2.40}$$

which is a singular system, and therefore possesses an infinite condition number and non-unique solutions (Aruliah et al., 2001). For ill-conditioned systems, an iterative solver may be slow or fail to converge without adequate preconditioning to deflate the non-trivial null-space of the curl-curl operator (Weiss, 2013).

In terms of practical usage, the finite-difference code of Newman and Alumbaugh (1995), further developed in Alumbaugh et al. (1996), Newman and Alumbaugh (1997), Commer and Newman (2008), and Newman et al. (2010), has been used extensively in the marine CSEM community for modelling of real-life offshore hydrocarbon reservoirs (e.g., Green et al., 2005; Carazzone et al., 2005; Hoversten et al., 2006; Commer and Newman, 2008; Newman et al., 2010). The non-linear conjugate gradient inversion code of Newman and Alumbaugh (1997) was notably employed by ExxonMobil for 3D CSEM imaging of realistic and challenging targets (e.g., Green et al., 2005; Carazzone et al., 2005). Data employed in these proof-of-concept studies were collected during ExxonMobil's extensive CSEM acquisition campaign offshore West Africa in the early 2000s. Green et al. (2005) present a case study where 3D modelling was successful in pre-drill prediction of hydrocarbons in an environment where electrical structure was complicated by the presence of salt and mixed lithology. Carazzone et al. (2005) used the code of Newman and Alumbaugh (1997) for both constrained and unconstrained inversions of marine CSEM data collected for a deepwater hydrocarbon reservoir located off West Africa. The finite-difference code of Sasaki and Meju (2009) has been used in several studies focussing on the effects of water depth and near-surface heterogeneities such as bathymetry, fizz gas, gas hydrates, gas

seepage alteration halos, and channel-fill deposits on the marine CSEM response for 3D rectilinear reservoir models.

2.3.2.2 Finite-element schemes

In recent years, a number of finite-element codes have been presented for EM modelling (Badea et al., 2001; Börner et al., 2008; Um et al., 2010; Vieira da Silva et al., 2012; Ansari and Farquharson, 2011). Finite-element techniques are more flexible than finite-difference techniques in terms of the geometry of the mesh that can be employed. Börner et al. (2008) and Um et al. (2010) present finite-element approaches for the time-domain which are applicable to time-domain EM methods rather than the frequency-domain CSEM method considered in this work.

Schwarzbach et al. (2011) present a 3D finite-element adaptive mesh refinement code, based on a primary-secondary electric field decomposition, which allows for use of higher order Nédélec elements for finite-element approximation on an unstructured tetrahedral mesh. For a two-halfspace, flat seafloor model, Schwarzbach et al. (2011) examine solution accuracy with varying polynomial degree for the finite-element expansion and found that higher order polynomials (in this instance, polynomials of order 2 and 3) provide better accuracy than polynomials of order 1 (i.e., linear edge elements). Use of higher order polynomials may not be feasible however for complex models that result in large meshes because of the associated increase in number of degrees of freedom in the system. For example, finite-element discretization of a seafloor bathymetry model in Schwarzbach et al. (2011) was limited to polynomials of order 2 because use of polynomials of order 3 exceeded available computational resources. Schwarzbach et al. (2011) also present solutions for a two-halfspace, seafloor topography model, the same topography model as that presented in Chapter 5, and for the canonical disk model of Weiss and Constable (2006).

Vieira da Silva et al. (2012) present a finite-element code which uses a primary-secondary electric field decomposition and Nédélec edge elements for discretization of the electric field, but implement their code on structured hexahedral meshes rather than unstructured tetrahedral meshes. Puzyrev et al. (2013) present a finite-element forward code for CSEM modelling in anisotropic media using a secondary potential formulation with the Coulomb gauge to ensure uniqueness of the vector potential. Nodal finite elements are employed for both the scalar and vector potentials. A parallelization strategy based on mesh-partitioning or substructuring is implemented to reduce the program execution time. Numerical solutions are validated for a two-halfspace, flat seafloor model and the canonical disk model. The performance of the code is also demonstrated on both isotropic and anisotropic versions of a realistic synthetic model.

2.4 Concluding remarks

Many semi-analytic and numerical codes have been developed which are applicable to simulation of frequency-domain marine CSEM data. For modelling of earth structure which varies arbitrarily in three dimensions, 3D numerical methods are required to appropriately capture the behaviour of EM fields. The finite-element method is readily applicable to unstructured meshes which provide flexibility in representation of complex boundaries; it may therefore be preferable to the finite-difference method which conventionally employs structured, rectilinear meshes. The CSEM3DFWD code (Ansari and Farquharson, 2014) employed in this study has several advantageous features: a total field formulation which does not require consideration of a primary solution; a vector-scalar potential ($\mathbf{A}$-ϕ) decomposition which circumvents numerical difficulties associated with formulation in terms of the electric field and, theoretically, allows investigation of inductive and galvanic contributions; and application of vector-valued edge element basis functions for expansion of

the magnetic vector potential **A**, which better conform to the physical behaviour of fields across conductivity boundaries than scalar-valued nodal element basis functions.

Many numerical solutions are presented in the literature for simple 3D marine earth models, but there exist few examples of application of 3D numerical methods to realistic or real-world earth models. Those that do exist mainly occur as industry case studies presented only in conference expanded abstracts, wherein the data and modelling software are proprietary. Specifically, there exist few examples of more realistic earth models discretized using unstructured meshes instead of the more common rectilinear meshes. This underscores the contribution of this thesis to the geophysical EM modelling literature in presentation of finite-element solutions for a realistic 3D earth model where unstructured meshes have been used for discretization of the model domain.

Chapter 3

The marine CSEM method

3.1 Overview of the method

The marine CSEM method commonly employs a deep-towed horizontal electric dipole (HED) source which transmits low-frequency EM energy to an array of multicomponent EM receivers deployed at or near the seafloor (Srnka et al., 2006; Li and Key, 2007). As the EM fields propagate or diffuse away from the dipole source, they are modified in both amplitude and phase by the resistivity structure of the earth, and the resultant, modified signal is recorded at the receiver array (Key, 2012b). Targets are often thin, resistive, hydrocarbon-saturated sedimentary layers embedded within the subsurface. Figure 3.1 illustrates the standard CSEM survey configuration. The HED is the most effective source orientation for detection of thin, horizontal to subhorizontal resistors due to the excitement of vertical currents, or TM-mode fields, in the earth (Srnka et al., 2006; Constable and Srnka, 2007). Reviews of less common CSEM acquisition systems can be found in MacGregor and Tomlinson (2014), Key (2012b), and Edwards (2005). Alternative systems include a linear array in which both source and receivers are towed on the same streamer, and a system in which both the source and receivers are vertical electric dipoles. The latter system exclusively

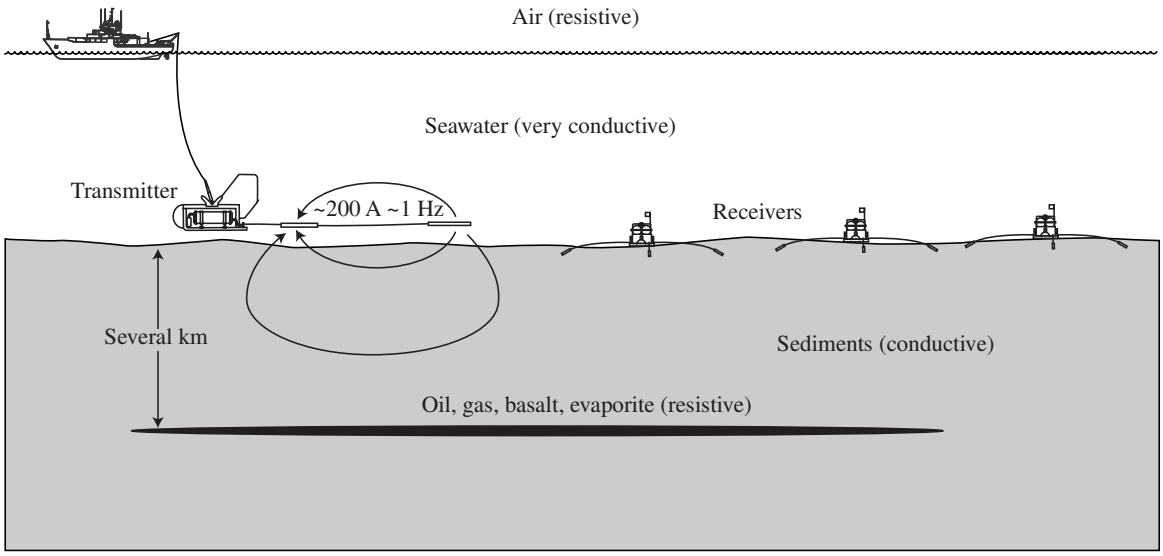

Figure 3.1. Schematic representation of the marine CSEM method. The HED transmitter is towed close to the seafloor to maximize coupling of the electric field to the subsurface. Current lines are indicated. This source configuration excites vertical currents normal to the horizontal or subhorizontal boundaries of a resistive target layer, thereby generating a galvanic perturbation in the electric field. The resultant electric and magnetic fields are recorded by receivers resting on the seafloor. Modified from Constable and Weiss (2006).

excites TM mode fields (Chave, 2009), allows detection of resistors at shorter offset, and potentially improves lateral resolution of seafloor structure, but is very sensitive to tilt angle since the vertical electric field is small in comparison to the horizontal component (MacGregor and Tomlinson, 2014).

Due to the conductive nature of the earth, CSEM soundings are heavily constrained by EM skin depth. In the marine environment, the highly conductive seawater has a shorter skin depth than the less conductive sedimentary subsurface, and so fields travelling through the subsurface experience less attenuation. Thus, for sufficient source-receiver offset, the CSEM response measured at the seafloor will be dominated by fields which have travelled through the subsurface (Constable and Srnka, 2007). Consider operation at 1 Hz in 3 S/m (0.3 ohm-m) seawater overlying a 1 S/m (1 ohm-m) sedimentary subsurface. Neglecting the effects of geometric spreading, over a distance of 5 km, fields propagating through the subsurface will have decayed by approximately 10 skin depths to about 0.004% of their

initial amplitude, while fields propagating through seawater will have decayed over 18 skin depths to about 0.000001% of their initial amplitude. If we consider propagation within a 0.01 S/m (100 ohm-m) layer, such as a hydrocarbon-saturated reservoir, over a distance of 5 km, fields will have decayed by only one skin depth, that is, to about 37% of their initial amplitude. The utility of the CSEM method for hydrocarbon applications therefore stems from the favourable ratio of skin depths between the relatively conductive seawater and relatively resistive subsurface (Constable and Srnka, 2007).

3.1.1 Source

The most commonly used source for marine CSEM acquisition is a HED, which excites both TE- and TM-mode fields, the latter of which provide particular sensitivity to thin, resistive layers. Chave (2009) presents 1D formulations for all four fundamental source geometries – the HED, the vertical electric dipole, the horizontal magnetic dipole, and the vertical magnetic dipole – and an analysis which provides insight into their suitability for marine CSEM hydrocarbon exploration.

The electric dipole transmits a high-current, low-voltage oscillatory waveform at a low fundamental frequency (Srnka et al., 2006). The physical transmitter consists of a neutrally buoyant streamer carrying two electrodes which comprise the ends of a grounded electric dipole (MacGregor and Tomlinson, 2014). Antenna length is typically from 100 to 300 m, currents employed may be in the range of 100–1500 A, and typical frequencies are in the range of 0.01–10 Hz (Constable, 2006; MacGregor and Tomlinson, 2014). Low frequencies are required to allow penetration of the signal to several kilometers depth below the seafloor, as dictated by EM skin depth (Srnka et al., 2006). The transmitter is towed at a speed of about 0.5–1.0 m/s (1–2 knots; Myer et al., 2011), with 25–100 m clearance to avoid obstructions on the seafloor. Towing the source close to the seafloor promotes maximal coupling of transmitted energy to the seafloor and minimal coupling to air (Constable and

Srnka, 2007; Constable, 2010; MacGregor and Tomlinson, 2014).

For frequency-domain EM, the source signal is typically a waveform customized to spread energy across several frequencies or harmonics of some fundamental frequency in the band of 0.1–10 Hz (Key, 2012b). Various oscillatory waveforms may be generated by switching a DC current between the two electrodes of the dipole (Constable, 2006). Design of the transmitter frequency spectrum is a compromise between penetration at low frequency and structural resolution at high frequency, as constrained by skin depth. Ideally, energy would be spread continuously across the frequency spectrum to promote sensitivity to both shallow and deep electrical structure, but there is a finite amount of energy to be allocated based on the source dipole moment (MacGregor and Tomlinson, 2014). Symmetric square waveforms were initially in common use by contractors, with fundamental frequencies of around 0.25 Hz and odd harmonics of decreasing current amplitude (Constable, 2006, 2010); current amplitude decreases as $1/n$, where n is the harmonic number (Myer et al., 2011). The square waveform has the advantage of transferring maximum energy to the subsurface because the source is always transmitting at peak amplitude, but has the disadvantage of concentrating most of the energy in the first harmonic (Mittet and Schaug-Pettersen, 2008). Since inductive attenuation increases with frequency, it is beneficial to distribute greater power to higher harmonics to counteract the loss of amplitude and boost signal-to-noise ratio. Further, processing and interpretation of marine CSEM data benefit from several high-power harmonics spaced over a large bandwidth (Constable, 2006; Mittet and Schaug-Pettersen, 2008; Key, 2009). The present standard is to use generalized binary (square pulse) waveforms with current amplitude spectra optimized for the environment and target (e.g., Lu and Srnka, 2009; Mittet and Schaug-Pettersen, 2008; Myer et al., 2011).

3.1.2 Receivers

The receiver array typically consists of 30 to 50 autonomous units placed along the seafloor pre-survey (Srnka et al., 2006). The receivers are allowed to free fall through the water column to their approximate planned positions on the seafloor; locations are selected with reference to seismic information or based on pre-survey modelling (Srnka et al., 2006). A typical commercial receiver consists of electric field-sensing dipoles and induction coil magnetometers and is similar in design to that illustrated in Figure 3.2 and described in Constable et al. (1998) and Constable (2013). The receivers are capable of recording up to three components of the electric and magnetic fields, although they are typically configured to record only the horizontal electric and magnetic fields in a survey (MacGregor and Tomlinson, 2014). Horizontal electric field measurements are made using a system consisting of low-noise and low-impedance silver-silver chloride electrodes mounted on the ends of 5 m-length dipole arms (Constable et al., 1998; Key, 2003). Magnetic field components are measured by lightweight and low-power induction coil magnetometers (Key, 2003). An acoustic unit is used to track the receiver through the water column during deployment and recovery, as well as for release of the unit from its anchor at the end of the recording period (Constable et al., 1998; Key, 2003). The unit rises to the surface with the help of glass flotation spheres. In addition to the controlled source signal, the receivers record the natural source magnetotelluric signal, although this is highly attenuated in deep water, as well as excitations due to seawater motion. These natural source signals have incoherent phases relative to the controlled source and may be suppressed using signal processing techniques (Srnka et al., 2006).

Receiver, source, and navigation data are recorded in the time-domain and must be converted to the frequency-domain for interpretation of CSEM data. Processing includes spectral decomposition of the receiver time series data, that is, transformation of the time

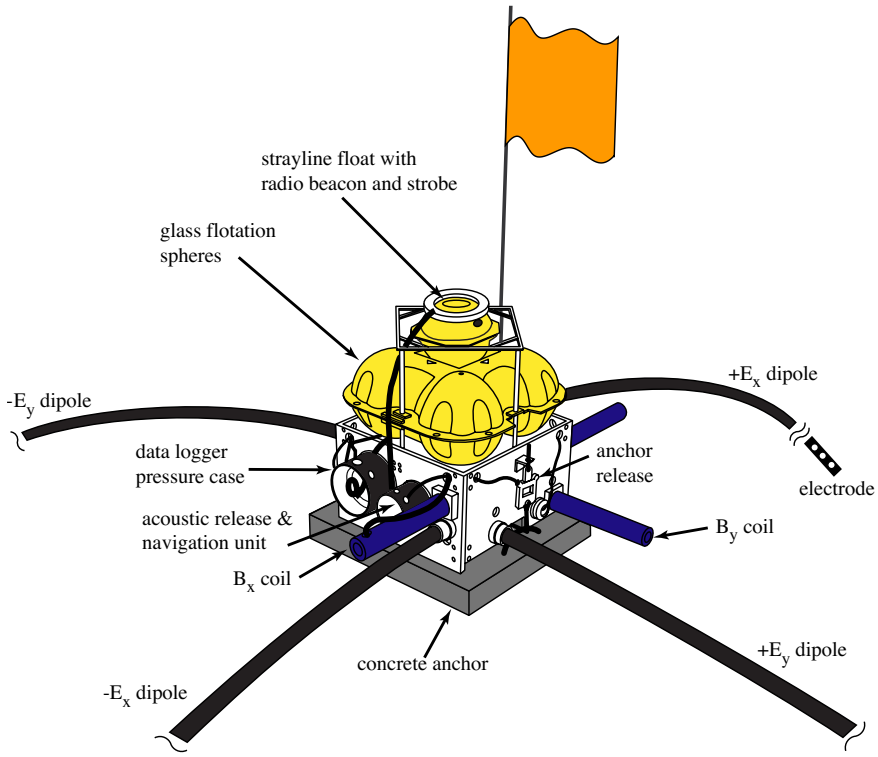

Figure 3.2. The Scripps Institution of Oceanography broadband EM receiver. The instrument can be used to collect both MT and CSEM data. From Key (2003).

series data to amplitude and phase data as a function of both source-receiver offset and frequency, normalization of the electric field amplitude with respect to source and receiver considerations, and reconstruction of source-receiver geometry from navigation data (Lu et al., 2006; Constable and Srnka, 2007). Transformation of time series data to frequency-domain amplitude and phase data is accomplished by division or *binning* of the time series into intervals corresponding to the transmitter period (Lu and Willen, 2011). Spectral decomposition is then performed on each time bin via Fourier transform or least-squares fit (Lu et al., 2006). Each bin is associated with a time, typically that at the center of the bin, which can be related to transmitter location or source-receiver offset based on navigation information (Lu and Willen, 2011). The electric field magnitude is normalized by the source dipole moment so that the amplitude is independent of dipole antenna length and source current. The normalized electric field amplitude is presented in units of V/m[/Am]

or V/Am^2 (e.g., Constable and Srnka, 2007). To emphasize amplitude anomalies associated with resistive target structure, it is common practice to further normalize the electric field amplitude by either a halfspace response or by a receiver response assumed to be off-target (Constable and Srnka, 2007).

3.2 Sensitivity of the method to hydrocarbon reservoirs

Low-frequency EM phenomena are difficult to visualize in terms of the underlying physical interactions. A harmonic source excites with the entire earth-sea-air system, and the response measured at a receiver can be understood as the convolution of the source signal with an attenuative, diffusive earth (Myer et al., 2011; see Ward and Hohmann, 1988, for discussion of Green's functions). In this manner, the response can be thought of as a spatial average of the system weighted by the sensitivity to each component of the system (Constable, 2010). Sensitivity to a particular component has numerous controls including resistivity, source-receiver offset, and various other geometric factors, e.g., orientation relative to source field, physical dimensions, and depth. The conventional CSEM method which employs a HED source is designed to optimize sensitivity to thin, horizontal to subhorizontal resistive bodies such as hydrocarbon reservoirs. The sensitivity of the method to hydrocarbon-saturated reservoirs has in turn been described in terms of galvanic and inductive interactions, TE and TM modes, and EM skin depth. An attempt is made here to clarify these descriptions by reviewing the physical interactions between the source fields and subsurface which modify the amplitude and phase of the EM fields.

3.2.1 Inductive and galvanic coupling

The EM fields excited by a harmonic source are modified not only in amplitude via $1/r^3$ geometric spreading, but also in amplitude via galvanic effects associated with the direct flow of

current, and in amplitude and phase via frequency-dependent inductive effects (Constable, 2010). Inductive and galvanic coupling between regions of differing electrical properties is governed by the EM boundary conditions. Requirement for the continuity of the tangential electric field component E^T across an interface results in inductive coupling, while requirement for the continuity of the normal current density component J^N across an interface results in galvanic coupling, the later of which is more important for anomaly generation in relation to thin, horizontal to sub-horizontal resistive bodies (Um and Alumbaugh, 2007).

Consider two adjacent regions with different conductivities σ_1 and σ_2. The boundary condition governing the inductive coupling between electric fields in adjacent regions is the requirement of continuity of the tangential electric field across the boundary separating the regions, i.e.,

$$E_1^T = E_2^T, \tag{3.1}$$

where the superscript T denotes the tangential component (Figure 3.3). Based on this condition, if there exists an electric field in medium 1 with a component parallel to the boundary separating the two regions, the generation of parallel currents within medium 2 is required by Ohm's law, i.e., $\mathbf{J} = \sigma\mathbf{E}$. These currents will in turn induce magnetic fields, as dictated by Ampère's Law, $\nabla \times \mathbf{H} = \mathbf{J} = \sigma\mathbf{E}$. This inductive mechanism is very important for generation of anomalous responses for conductive bodies embedded in less conductive backgrounds (e.g., metallic sulfide ore bodies) due to the generation of strong electric currents within the body parallel to the interface, but is less important for targets that are resistive relative to their backgrounds (Um and Alumbaugh, 2007; Um, 2011). Now let us consider the galvanic interaction between two adjacent regions.

Galvanic coupling between two regions of different conductivity results from currents passing normal to the boundary. In the absence of extrinsic sources, i.e., $\nabla \cdot \mathbf{J} = 0$, the continuity of the normal component of current density $\mathbf{J}$, i.e., $J_1^N = J_2^N$, requires, by Ohm's

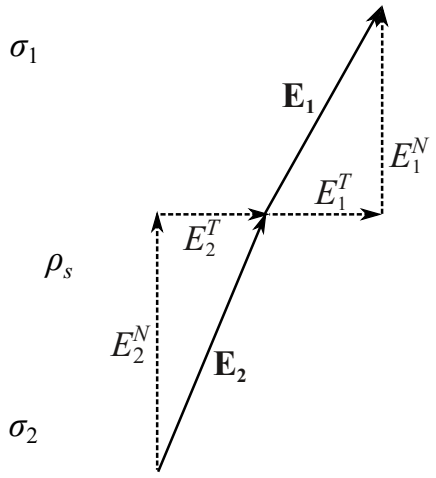

Figure 3.3. Decomposition of the electric field at a boundary into normal and tangential components. After Wilkinson (2011).

law, that

$$\sigma_1 E_1^N = \sigma_2 E_2^N, \tag{3.2}$$

and therefore generally $E_1^N \neq E_2^N$ (Chave and Jones, 2012). In order to satisfy the continuity of the normal component of the current density across a boundary, a surface charge builds up at that boundary. The normal component of the electric displacement field $\mathbf{D}$ is discontinuous across a boundary by the surface charge density ρ_s, i.e.,

$$D_1^N - D_2^N = \rho_s, \tag{3.3}$$

where ρ_s is in units of C/m^2. If we make substitutions using the constitutive relation $\mathbf{D} = \varepsilon\mathbf{E}$, and further make the assumption that $\varepsilon_1 = \varepsilon_2 = \varepsilon$ (i.e., permittivity does not vary between media), we can rewrite this boundary condition as

$$\varepsilon\left(E_1^N - E_2^N\right) = \rho_s. \tag{3.4}$$

As we have established, $J_1^N = J_2^N = J^N$, and so considering Ohm's law, $\mathbf{J} = \sigma\mathbf{E}$, we may

write

$$\rho_s = \varepsilon \left(E_1^N - E_2^N \right) = \varepsilon J_n \left(\frac{1}{\sigma_1} - \frac{1}{\sigma_2} \right). \tag{3.5}$$

This equation indicates that where there exists a component of current density or electric field normal to a conductivity boundary, a surface charge accumulates. The phenomenon of surface charge accumulation may alternatively be approached starting from Maxwell's equations rather than the derived boundary conditions. Outside of extrinsic sources, i.e., $\nabla \cdot \mathbf{J} = 0$, Gauss's law, $\nabla \cdot \mathbf{D} = \rho$, states that the electric charge density is equal to (Chave and Jones, 2012):

$$\rho = \varepsilon \nabla \cdot \mathbf{E} = \varepsilon \nabla \cdot (\mathbf{J}/\sigma) = \varepsilon \mathbf{J} \cdot \nabla (1/\sigma), \tag{3.6}$$

where the product rule $\nabla \cdot (\mathbf{J}/\sigma) = 1/\sigma \, (\nabla \cdot \mathbf{J}) + \mathbf{J} \cdot (\nabla (1/\sigma))$ has been employed. Equation (3.6) indicates that charge accumulation only occurs at places where the current density $\mathbf{J}$ has a component parallel to the conductivity gradient $\nabla\sigma$. Evaluating the dot product of equation (3.6) results in equation (3.5).

Surface charge accumulation gives rise to secondary electric fields which have the effect of decreasing the total electric field in the more conductive (less resistive) region and increasing the total electric field in the less conductive (more resistive) region. Consider the simple 1D model illustrated in Figure 3.4, which consists of two adjacent halfspaces with conductivities σ_1 and σ_2, divided by a vertical interface. The conductivity gradient is normal to the boundary between regions and there exists a component of $\mathbf{J}$ normal to the interface. In the case that $\sigma_2 < \sigma_1$, it is required by equation (3.5) that $E_2^N > E_1^N$. This is achieved by accumulation of a positive surface charge with associated electric field $\mathbf{E}_s$, which decreases E^N in region 1 and increases it in region 2 (Vozoff, 1991).

In a geophysical context, for a thin, resistive target that exhibits a large conductivity contrast relative to its background, charge accumulation can be significant if there exists a substantial component of the electric current density, or electric field, normal to the bound-

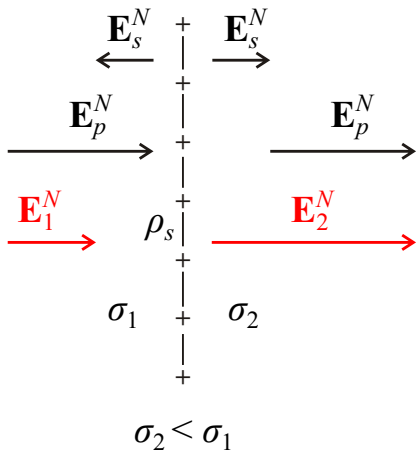

Figure 3.4. Charge accumulation at a conductivity boundary due to the requirement of continuity of the normal component of current density, $\mathbf{J}^N = \sigma \mathbf{E}^N$. The normal electric field $\mathbf{E}_s^N$ due to the surface charge distribution adds vectorially to the normal applied electric field $\mathbf{E}_p^N$ on either side of the interface, decreasing the net normal electric field $\mathbf{E}_1^N$ on the left and increasing the net normal electric field $\mathbf{E}_2^N$ on the right. After Vozoff (1991).

ary of the resistive target. The resultant galvanic perturbation in the measured electric field primarily accounts for the electric field amplitude anomaly produced by thin, horizontal resistors excited by a controlled HED source, as will be discussed in Section 3.2.3.

3.2.2 The resistive layer as a TM-mode waveguide

The description of the thin resistive layer as a TM-polarized 'leaky waveguide' stems from analysis of EM propagation in a layered earth model (e.g., Chave et al., 1990; Weidelt, 2007; Chave, 2009; Løseth, 2011; Swidinsky, 2015). In a 1D representation of the earth's subsurface, galvanic coupling between adjacent layers, and therefore resistive layer waveguiding, are strictly TM-mode phenomena (Eidesmo et al., 2002; Weidelt, 2007; Chave, 2009).

Consider a thin resistive layer with resistivity on the order of 10–100 times that of its halfspace background, overlain by a sea layer and in turn, an infinitely resistive air halfspace (i.e., a finite-water depth adaptation of the canonical oil field model discussed

in Section 2.2). In the TE mode, the electric field is polarized tangential to the resistive layer, i.e., there exists no electric field component normal to its boundary, and coupling between adjacent layers is exclusively inductive. A thin resistive layer has little impact on TE mode propagation since it may inductively couple across the resistive layer to the conductive halfspace below (Weidelt, 2007). By requisite of the continuity of the tangential (horizontal) electric field at the air-sea interface, the purely geometrical $1/r^3$ decay of the electric field in the air layer is imparted onto the electric field inside the water layer (Weidelt, 2007). In asymptotic limit (i.e., for sufficient source-receiver offset), the electric field inside the water layer is dominated by the $1/r^3$-decay 'air wave' contribution.

In the TM mode, the magnetic field is polarized tangential to the resistive layer, i.e., there exists no magnetic field component normal to its boundary, and coupling between adjacent layers is both inductive and galvanic. In the TM mode, the resistive layer, however thin, disrupts vertical current flow and generates galvanic perturbations in the EM fields (Eidesmo et al., 2002; Weidelt, 2007). The resistive layer guides the flow of EM energy laterally along its extent, with concomitant energy leakage to the more conductive overlying and underlying sediment layers (Eidesmo et al., 2002; Edwards, 2005; Chave, 2009; Swidinsky, 2015). Given the relatively low conductivity of the resistive layer as compared to its background, it serves as a low-attenuation pathway for TM-mode propagation. This guiding of EM energy or fields is often visualized through mapping of the real part of the Poynting vector, which represents the time-averaged energy flux (e.g., Chave et al., 1990; Weidelt, 2007; Key, 2012b; Chave, 2009) or in 2D, through mapping of the current stream function, which represents the magnetic field divided by magnetic permeability (e.g., Edwards, 2005; Swidinsky, 2015). The overall effect of the presence of the resistive layer is to modify current flow patterns in adjacent layers, thereby generating anomalous fields that may be detectable at the seafloor under appropriate conditions (Eidesmo et al., 2002; Chave, 2009; Swidinsky, 2015).

3.2.3 Source field geometry

The sensitivity of the CSEM method to a particular target depends on the electrical properties of the target and its orientation relative to excited current flow or electric field direction. For detection of thin, largely horizontal resistors such as hydrocarbon reservoirs, excitation of vertical currents is important for galvanic coupling. A HED excites both galvanically and inductively coupled modes of current flow in a stratified earth, but only in the direction inline with the dipole axis is there significant vertical current flow.

The relative sensitivity of different HED source-receiver configurations to the presence of thin resistive layers can be understood by examining the geometry of the source field in both the inline and broadside directions (Figure 3.5). In the direction inline with respect to the dipole axis, the electric field has a significant vertical component whose path may be interrupted by horizontal resistors to produce a galvanic distortion of the electric field amplitude that may be measured at the seafloor (Constable, 2010). In the direction broadside with respect to the dipole axis, the electric field is largely horizontal, meaning that coupling between source and tabular resistors is mainly inductive (MacGregor and Sinha, 2000; Constable, 2010). At the low frequencies used for CSEM acquisition, for a thin resistive layer, galvanic coupling (in addition to inductive coupling) in the inline configuration will produce a larger anomalous response than inductive coupling alone in the broadside configuration (Constable, 2010). The inline horizontal electric field is thus the most sensitive to thin, laterally extensive resistive targets.

The difference in sensitivity between the inline and broadside horizontal electric fields is well established and has been illustrated by numerous synthetic studies (e.g., Constable and Weiss, 2006; Um and Alumbaugh, 2007; Constable, 2010). Comparing the difference in 1D solutions for a two-halfspace model with and without a resistive reservoir layer, it can be seen that there is a greater difference in the horizontal electric field amplitude between

the two model variations for the inline configuration than for the broadside configuration (Figure 3.6). Note that the solutions are presented for a 1 Hz HED source, but that transmission frequencies employed in CSEM surveying may be much lower. As frequency decreases, inductive coupling becomes less significant and the discrepancy between the inline and broadside horizontal electric field sensitivities increases.

3.2.4 Inductive attenuation

The EM fields excited by a CSEM source decay in space via both geometric spreading, and more importantly in conductive media, inductive attenuation. The skin depth of a medium, $\delta = \sqrt{2/\omega\mu_0\sigma}$, defines the distance over which EM fields have decayed by $1/e$, or 37%, of their original amplitude. As conductivity and frequency increase, the skin depth of a homogeneous medium decreases. Given an earth system composed of regions of different conductivities, at a particular frequency, the tendency is that for a given source-receiver offset, propagation through one part of the earth system dominates the observed CSEM response (Constable and Srnka, 2007).

This effect is illustrated in Figure 3.7, where the 1 Hz inline horizontal electric field amplitude and phase are illustrated for the 1D canonical reservoir model: a 100 m-thick, 0.01 S/m (100 ohm-m) resistive layer buried at a depth of 1000 m in a 1 S/m (1 ohm-m) sediment halfspace, an overlying 1000 m-thick 3.3 S/m (0.3 ohm-m) sea layer, and an overlying air halfspace. For comparison, solutions for wholespaces having the same resistivities as the sea, sediment, and resistive layer are plotted alongside, as well as the 1D solution for the background model (resistive layer absent).

With reference to Figure 3.7, there are four major divisions of the 1D reservoir response as a function of source-receiver offset, characterized by gradual transitions from one skin depth or attenuation regime to another. From the near offset up to approximately 1 km offset, the 1D reservoir response is dominated by fields which have propagated di-

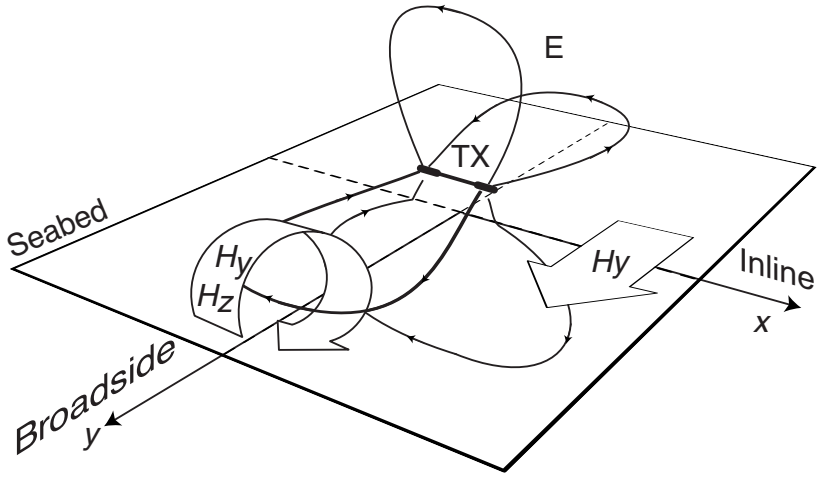

Figure 3.5. Geometry of the source field for an x-directed HED (TX) above a seabed (horizontal plane). For an inline geometry, only the x- and z-components of the electric field are present; the vertical component E_z couples galvanically with the underlying reservoir. For a broadside geometry, the electric field is largely horizontal and therefore can only induce a relatively weak inductive response in the resistive layer. As frequency decreases, the discrepancy between the inline and broadside horizontal electric field sensitivities increases. Modified from Weiss (2007).

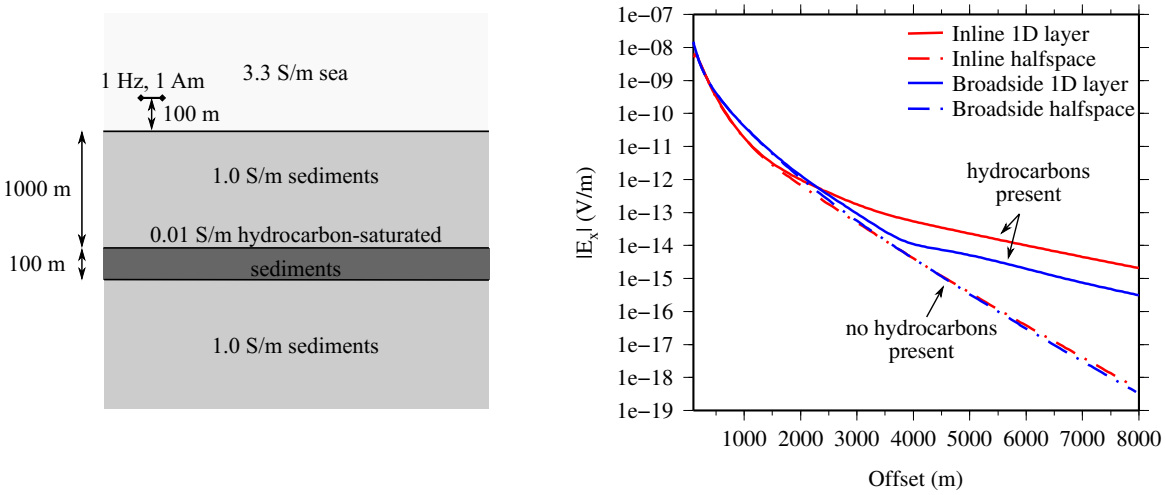

Figure 3.6. The inline and broadside horizontal electric field components for the 1D canonical reservoir model using a 1Hz, 1 Am HED source located at 100 m above the seafloor. The two-halfspace background response (dashed line) is also illustrated for comparison. In comparing the hydrocarbon-saturated reservoir responses to the background responses for both the inline and broadside configurations, it is evident that the inline horizontal electric field is more sensitive to the presence of the hydrocarbon-saturated reservoir than the broadside horizontal electric field.

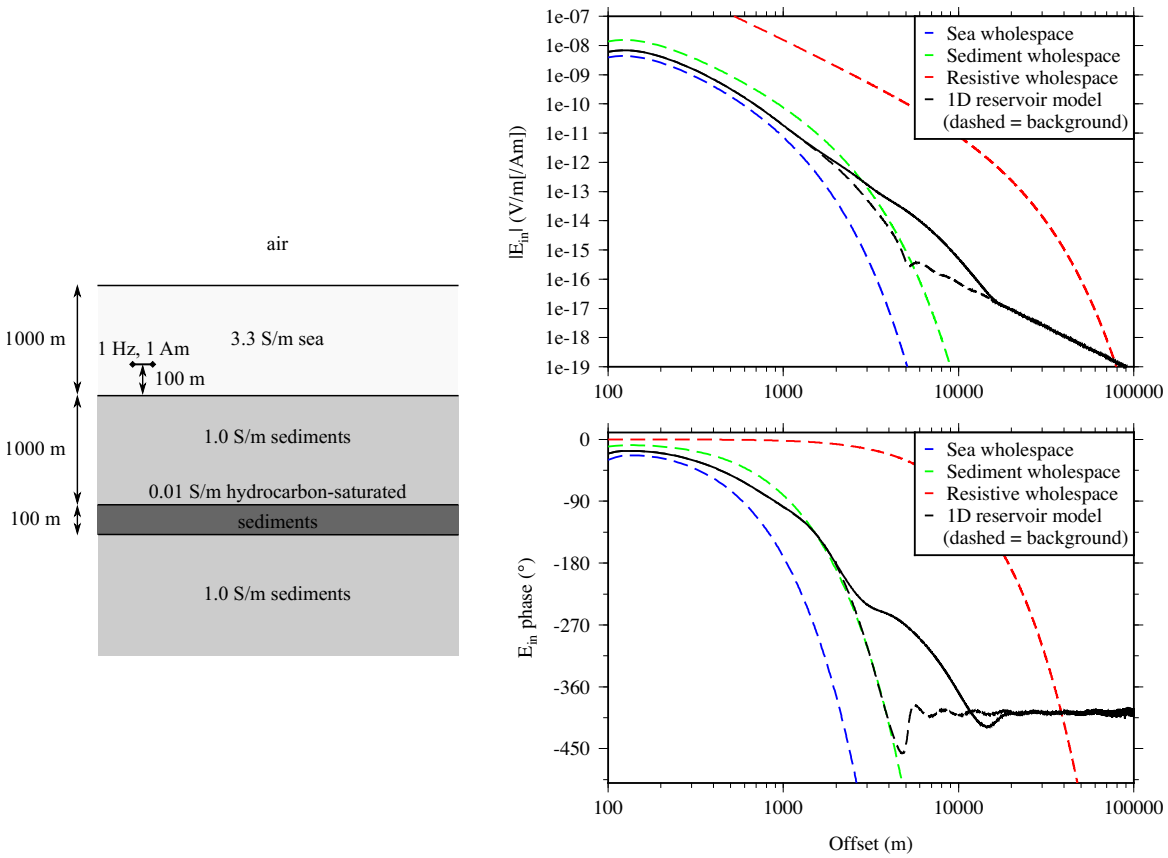

Figure 3.7. The inline horizontal electric field amplitude and phase (right, black solid line) for the 1D canonical reservoir model. Solutions are illustrated also for wholespaces having the same resistivities as the sea, sediment, and resistive layers (blue, green, and red dashed lines, respectively), as well as for the 1D background model, i.e., no reservoir present (black dashed line). Solutions are for a 1 Hz, 1 Am HED source simulated at a height of 100 m above the sea-sediment interface. At near offset, the 1D reservoir model response is dominated by fields which have travelled directly through the sea layer and the shallow sediment section. At intermediate offset, the response is dominated by fields which have travelled through the resistive layer, resulting in an increase in electric field amplitude. At large offset, the airwave becomes dominant with its characteristic $1/r^3$ dipole decay and infinite phase velocity.

rectly through the seawater; exponential attenuation parallels and is close to that for a sea wholespace, which has a skin depth of 277 m at 1 Hz. For offsets in the range of 1–2 km, the 1D reservoir response is dominated by fields which have propagated through the sediment subsurface; the 1D reservoir solution gradually merges with that for a sediment wholespace, which has a skin depth of 503 m at 1 Hz. The 1D background solution continues to follow that of the sediment wholespace up to an offset of approximately 5 km, at which point fields which have propagated above the air-sea interface (i.e., the airwave) begin to dominate the response. The visible onset of the airwave is characterized by amplitude decay principally via $1/r^3$ geometric spreading from a dipole source, that is, there is little inductive attenuation, and near-constant phase. As air is infinitely resistive, it has an infinite penetration depth and hence signal decay is via geometric spreading only while it travels along the air-sea interface. The flattening of the electric field phase indicates near-synchronous arrival of the dominant air signal across the receiver array and an apparent phase velocity comparable to the speed of light (Constable and Srnka, 2007). In the presence of a resistive layer, the visible onset of the airwave is delayed to farther offset. For offsets in the range of 10–20 km, the 1D reservoir response is dominated by fields which have propagated through the buried resistive layer, which has a skin depth of 5030 m at 1 Hz. For offsets greater than 20 km, propagation through the air dominates.

Um and Alumbaugh (2007) explain the dependence of the CSEM response on source-receiver offset generally:

> At small separations, the measured EM response can be thought of as the direct field generated by an HED source through seawater and shallow marine sediments. At an intermediate distance, the anomalous galvanic and inductive responses generated by the deeper structures become resolvable. At larger separations, the air-wave response becomes dominant.

Thus we conclude that at sufficient source-receiver offset, the response is dominated

by contributions from the subsurface and target that we are interested in imaging. This sensitivity to the subsurface becomes weaker with decreasing water depth as the visible onset of the airwave occurs at progressively shorter offsets (Constable and Srnka, 2007).

3.2.5 Water depth

The CSEM method behaves quite differently in the deep marine environment than it does in the terrestrial or shallow marine environments. In fact, early assessment of the CSEM method for offshore exploration in the 1980s foundered because exploration at the time was restricted to the shallow marine environment (Constable, 2006). This difference in behaviour inspired early advocates of the CSEM method for deepwater exploration to create entirely new names for the marine technology, namely *seabed logging* by Statoil and *remote reservoir resistivity mapping* by ExxonMobil (Constable, 2006).

The difference in nature of the CSEM response between the deep marine and shallow marine environments stems from the finite skin depth of the sea layer. For sufficient water depth, fields travelling to and/or from the air-sea interface will be attenuated such that the airwave will not appear until very far offset, but for increasingly shallow water, the filtering effect of the sea layer is lessened, and the airwave becomes dominant at progressively shorter offsets as water depth decreases. The result is that for water depth less than roughly 300 m, the resistor signature that would normally be apparent at intermediate offset is masked by the airwave (Weiss, 2007).

The use of the term ‘airwave’ for the atmospheric coupling or interaction observed in the marine CSEM method arose in analogy to the refracted airwave observed in the seismic reflection method (Andréis and MacGregor, 2007). This is a simplistic interpretation of the airwave since it does not take into account the short-ranging reflections at the air-sea and sea-earth interfaces which result in coupling between the fields in the air and subsurface (Weidelt, 2007; Løseth, 2011). Through asymptotic expansion of the electric field in the

air, Weidelt (2007) illustrated that these reflections are significant at intermediate offsets, but that the leading term with $\sim 1/r^3$ decay is sufficient for description of the airwave in the far-field. This leading term is a strictly TE mode phenomenon and is independent of the parameters of the resistive layer (Weidelt, 2007).

The dominance of the airwave at shallow water depth is demonstrated in Figure 3.8, which illustrates 1D solutions for the canonical oil field model (e.g., Figure 3.7) with variable water depth. For shallow water depth, the difference between the resistor-present and resistor-absent solutions is minimal due to the onset of the airwave at short offset. The onset of the airwave is characterized by $1/r^3$ dipole decay since signal strength is reduced principally via geometric spreading only, with minimal inductive attenuation associated with travel through the sea section. The offset at which the airwave becomes dominant and overprints the signal from the subsurface, sometimes referred to as the *critical distance* (e.g., Um and Alumbaugh, 2007), is primarily controlled by water depth, or more specifically, the ratio of seawater skin depth to water depth. Source frequency is a secondary control on the critical distance since skin depth decreases as frequency increases.

For sufficiently deep water, the airwave does not appear in the CSEM response until offsets at which the signal strength is well below the EM noise floor. For shallow water however, the airwave is apparent at shorter offset. Since many hydrocarbon exploration targets lie in relatively shallow water, various mitigation schemes have been developed to reduce the masking effect of the airwave. Proposed mitigation schemes include: (1) data reduction, which aims to quantify and subtract the airwave signature so as to obtain a response corresponding exclusively to the seawater and subsurface (e.g., Amundsen et al., 2006; Weidelt, 2007; Chen and Alumbaugh, 2011); (2) mode decomposition, where the mode least affected by the interaction with the atmosphere is extracted and used in interpretation (e.g., Andréis and MacGregor, 2008); (3) optimal survey design, where acquisition parameters are chosen to maximize airwave attenuation and sensitivity to the target (e.g.,

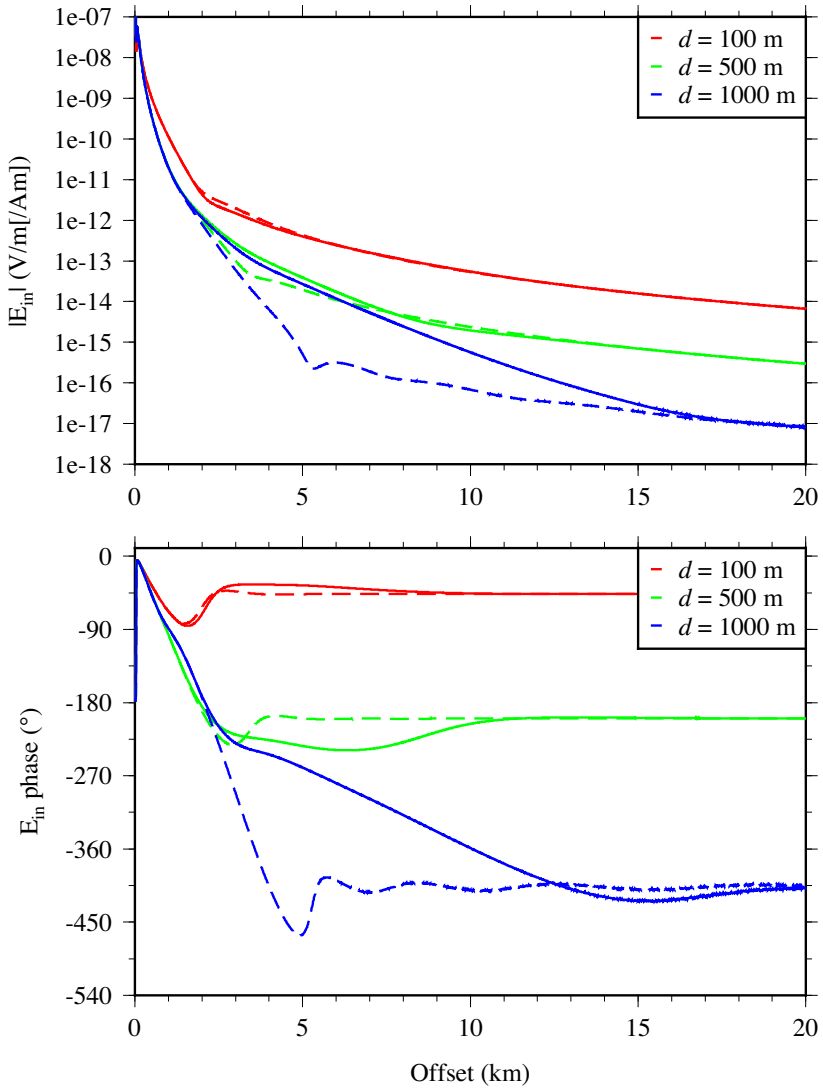

Figure 3.8. The inline horizontal electric field amplitude and phase for the 1D canonical reservoir model with variable water depth d. Solutions are illustrated for water depths of 100 m (red), 500 m (green), and 1000 m (blue), where the solid line indicates the resistor-present solution and the dashed line indicates the resistor-absent (background) solution. The source is a 1 Hz, 1 Am HED at a height of 100 m above the sea-sediment interface. As water depth decreases, it becomes more difficult to discern the presence of the resistive layer due to the dominance of the airwave at increasingly shorter offsets. The airwave is characterized by $1/r^3$ amplitude decay (geometric spreading only, no inductive attenuation) and near-constant phase as the arrival of the airwave is near-synchronous across receivers at far offset.

MacGregor et al., 2006); and (4) the usage of time-domain CSEM in shallow water (e.g., Andréis and MacGregor, 2007; Weiss, 2007; Andréis and MacGregor, 2008; Li and Constable, 2010; Connell and Key, 2013). If data are appropriately modelled to account for the air layer, mitigation schemes (1) and (2) are unneccessary (Constable, 2010). Further, although time-domain CSEM potentially offers greater sensitivity to resistive targets in shallow water (see Weiss, 2007), it has poorer signal-to-noise ratio than the frequency-domain CSEM method and still requires accurate modelling of atmospheric coupling due to the inseparability of target and airwave signatures.

3.2.6 Implications

Theoretically, at sufficient source-receiver offset, any horizontal resistive layer of sufficient lateral extent and sufficiently large transverse resistance (vertically integrated resistivity, or 1D resistivity-thickness product) is detectable via the marine CSEM method (Constable, 2006; Constable and Srnka, 2007). If this statement is vague, it is because it is difficult to articulate the conditions for detection in view of the numerous controls on sensitivity; this underscores the impracticality of attempting to predict or interpret the CSEM response without adequate modelling. Since the CSEM response measured at the seafloor is the cumulative response to an earth volume, the response to a target cannot be isolated. It is thus important in CSEM modelling to not only correctly model the electrical structure of the target, but also that of its background (MacGregor and Tomlinson, 2014).

Chapter 4

Methodology

The frequency-domain 3D CSEM finite-element forward code CSEM3DFWD (Ansari and Farquharson, 2011, 2013, 2014; Ansari, 2014; Ansari et al., 2015) was used in this project for simulation of marine CSEM data for a sequence of offshore earth conductivity models of increasing complexity. Simulations were performed for source parameters generally representative of marine CSEM surveys, i.e., a HED source located a short distance above the seafloor, with transmission frequencies in the range of 0.1–10 Hz. A monochromatic source was simulated here, although real-life CSEM acquisition typically employs a source with power concentrated in several harmonics across the 0.1–10 Hz frequency band. For all models, a source with unity dipole moment (1 Am) was used to obviate the need for normalization of the electric field amplitude by the dipole moment, since electric field amplitude is typically presented in units of V/Am^2 (V/m[/Am]). The fields were calculated at discrete points located a short distance (typically 0.0001 m) above the seafloor to simulate an inline receiver array placed at the seafloor; receiver spacings simulated in modelling were however denser than those typical of a marine CSEM survey to facilitate verification of solution accuracy against semi-analytic or other numerical solutions. Numerical results for simple, layered conductivity models were validated through comparison to 1D semi-

analytic Hankel transform solutions. The 1D marine HED code developed and employed in this study, named MARDIP1D, is outlined in Appendix A. For the 3D seafloor topography model, results were validated against numerical solutions existing in the literature. All three components of the electric and magnetic fields were computed using CSEM3DFWD, but results focussed on the inline horizontal electric field solution because of the particular sensitivity of the component to laterally extensive resistive bodies.

The basic procedure for numerical modelling of EM data involves: firstly, construction of a geoelectric model and subsequent subdivision or *discretization* of the model domain, i.e., meshing; and secondly, formulation of the EM boundary value problem, approximation of the governing equations by a discrete system, and solution of this discrete system. In the following Sections 4.1 and 4.2, procedures for geoelectric model construction and mesh generation will be reviewed. In Section 4.3, the methodology for the CSEM3DFWD code will be presented, including formulation of the CSEM boundary value problem, its discretization using the finite-element method, and solution of the resultant discrete system using iterative methods.

4.1 Geoelectric model construction

A geoelectric model represents a 3D domain over which electrical properties vary spatially; because the earth's structure is complex, its true physical structure is typically approximated by a simplified but reasonable earth model (Zhdanov, 2002). The geoelectric model must be described or summarized in a format that is compatible with mesh generation and numerical modelling software. In this work, models are defined as 3D polyhedral domains using *piecewise linear complexes* (PLCs). A piecewise linear complex is composed of a set of nodes, also known as vertices, and facets (connecting segments or polygonal surfaces) that may be summarized in .poly file format. The .poly file format is described in detail in the

documentation for mesh generation program TetGen (Si, 2006).

Generation of an appropriate .poly file for a simple 1D or 3D rectilinear model is relatively straightforward and can be done manually, but for more complex structure, manual definition becomes impractical. To facilitate .poly file generation for more complex models, in-house model-building software developed by Dr. Peter Lelièvre, as well as auxiliary programs for mesh manipulation and visualization, were employed. Of particular use was the graphical 3D model-building assistant FacetModeller 3D, developed by Dr. Peter Lelièvre and Gary Blades (Figure 4.1). This program allows users to graphically define a 3D polygonal domain using nodes and facets, as well as subdomains or regions to which physical attributes may later be assigned. The program has several additional features to facilitate model building, including built-in model viewing, import of previously defined node and facet data (e.g., topographical surfaces), and import and digitization of geological cross-sections. Once the polyhedral domain is constructed, the model may be exported in .poly file format for meshing using TetGen software (Si, 2006) and/or in .vtu format for visualization using Paraview software (Ayachit, 2015).

4.2 Mesh generation

4.2.1 Overview of TetGen software

Geoelectric models were meshed using release 1.4.3 of TetGen, a third-party, open-source software package (Si, 2006, 2009). TetGen generates unstructured tetrahedral meshes suitable for finite-element and finite-volume numerical modelling using a Delaunay refinement algorithm. The benefit of this discretization method to finite-element modelling is that the Delaunay criterion promotes generation of well-shaped tetrahedra with small aspect or radius-to-edge ratios over poorly shaped tetrahedra with large aspect or radius-to-edge ratios (Figure 4.2).

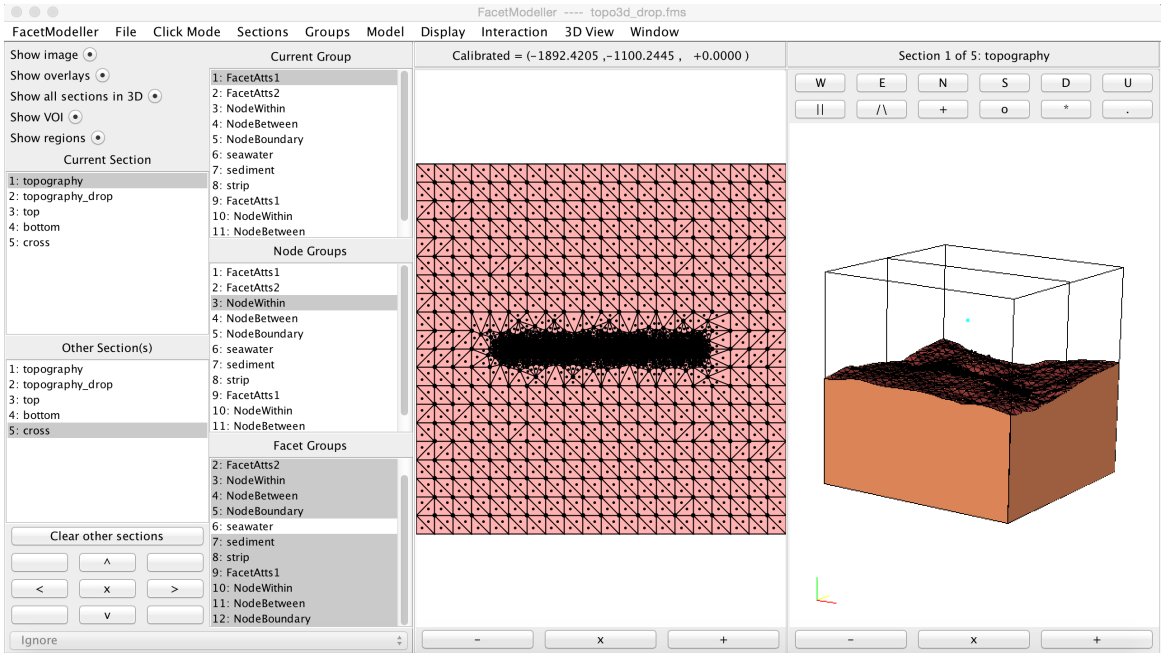

Figure 4.1. Screenshot of 3D graphical model-building software FacetModeller. The node and facet groups comprising the 3D model may be graphically defined and manipulated using this software.

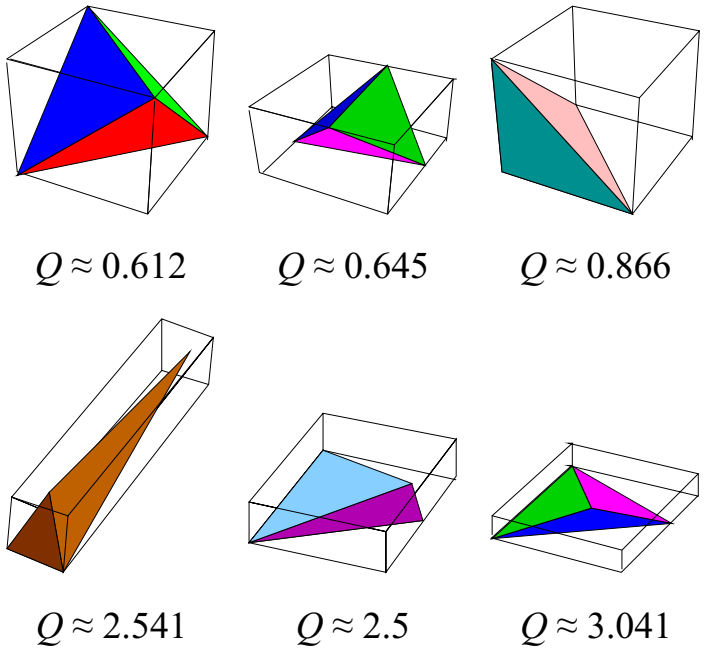

Figure 4.2. Examples of tetrahedra with different radius-to-edge ratios, Q. The top row of tetrahedra with $Q < 1$ are relatively well-shaped, while the bottom row of tetrahedra with $Q > 2$ are relatively badly shaped. From Si (2006).

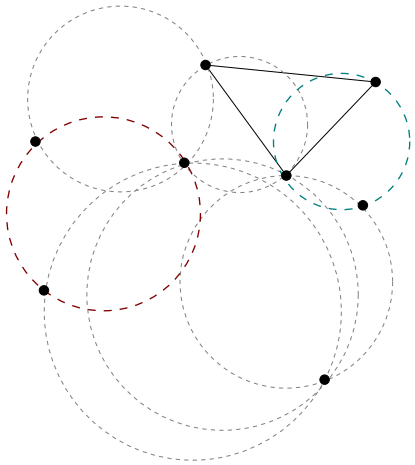

Figure 4.3. A planar Delaunay triangulation of a 2D point set. Two triangles and their corresponding circumcircles are shown in colour for example. Modified from Si (2013).

A Delaunay triangulation of a d-dimensional point set V is a d-dimensional simplicial complex $\mathscr{D}$ that satisfies the criterion that every simplex (e.g., tetrahedron for $d = 3$) in $\mathscr{D}$ has a circumsphere whose inside contains no other vertex of V and whose underlying space, the union of all simplices, forms the convex hull of V (Figure 4.3; Si, 2015). A Delaunay refinement algorithm generates and maintains a Delaunay triangulation while adding nodes to eliminate poorly shaped elements (Cheng et al., 2012). In two dimensions, Delaunay triangulation provides mathematical guarantees on mesh quality based on maximization of the minimum angle within triangles. Generalized to higher dimensions, Delaunay triangulation still maintains advantageous geometric properties, but the minimum angle, whether considering face angles (i.e., the angle between two edges) or dihedral angles (i.e., the angle between the edge intersection of two faces and a plane perpendicular to that edge), is not maximized (Cheng et al., 2012). In this manner, Delaunay tetrahedralizations are not quite as effective as planar Delaunay triangulations for generation of quality meshes.

Delaunay tetrahedralizations can be further characterized by how they handle domain boundaries (*constrained* tetrahedralization) and cell shape and size criteria (*quality* tetrahedralization; see Section 4.2.2). In *constrained* Delaunay tetrahedralization, both inner and

outer domain boundaries are respected, i.e., the tetrahedralization is boundary-conforming. The user may specify whether constraining boundaries are to remain completely unmodified or may be further subdivided to improve mesh quality (Si, 2015). If boundaries are permitted to be subdivided, the Delaunay criterion will hold locally for tetrahedra away from boundaries, that is, for tetrahedra whose facets are not on the boundary (Si, 2009). Some badly shaped tetrahedra may still result in proximity to sharp features where two constraining surfaces meet at an acute dihedral angle (Si, 2015).

Given an input .poly file for an earth model, TetGen generates as output four files which describe the domain tetrahedralization and are required as input for CSEM3DFWD; these include a .node file, an .ele file, a .face file, and a .neigh file, which respectively contain a list of nodes, a list of tetrahedra, a list of triangular faces, and a list of neighbours (i.e., tetrahedra adjacent to a given tetrahedron) for the mesh. For 2D triangular meshing of topographic surfaces within the model domain, such as the seafloor or stratal interfaces, Triangle meshing software (Shewchuk, 1996) was employed; this software is also based on a Delaunay triangulation algorithm. The TetGen and Triangle software packages and accompanying documentation are available at `http://tetgen.berlios.de/plc.html` (accessed August 2015) and `https://www.cs.cmu.edu/~quake/triangle.html` (accessed August 2015).

4.2.2 Mesh quality and refinement

Generation of unstructured meshes of suitable quality for finite-element methods is a non-trivial problem, both in the theoretical development of meshing algorithms and in their application to discretization of partial differential equation (PDE) problems. Mesh quality is a complex function of several geometric features and has a significant effect on both the accuracy of the numerical solution in terms of discretization and interpolation errors, and the conditioning of the system matrix (Shewchuk, 2002; Du et al., 2009; Si, 2015).

Iterative solvers are typically implemented in finite-element methods over direct solvers because they are less restricted in terms of the size of problems they can handle, but an inherent shortcoming is that they are less robust to ill-conditioning associated with mesh geometry. For systems with a large condition number, iterative solvers will have slow performance and the solution may fail to converge. At present, construction of a mesh suitable for modelling may require more time and effort from the user or researcher than numerical solution of the PDE problem on the mesh (Cheng et al., 2012).

The two most important mesh quality criteria for finite-element methods are cell shape and size. In terms of cell shape, cells with very large (near 180°) or very small (near 0°) angles should generally be avoided since their presence negatively impacts the accuracy and convergence of the numerical solution (Si, 2013). Large angles cause interpolation errors which in turn lead to large differences between the approximated and true solution, and small angles exacerbate ill-conditioning of the system (Cheng et al., 2012). A common shape measure for cells is their aspect ratio. There are several definitions of aspect ratio, including the ratio of the maximum edge length to minimum height or altitude, or the ratio of the circumradius to the inradius (Si, 2013; Cheng et al., 2012); these definitions may be used equivalently in that a bound with respect to one measure results in a bound with respect to the other measure (Si, 2013). The aspect ratio as a quality measure for tetrahedra achieves the same objective as combined restrictions on both face angles and dihedral angles (Si, 2013).

A similar but weaker measure of cell shape is the circumradius-to-shortest-edge ratio (written for brevity as radius-to-edge ratio; Figure 4.4). The radius-to-edge ratio is a measure of the "roundness" of a tetrahedron, and can have values between ∞ and $\sqrt{6}/4\,(\doteq 0.612)$, which is the radius-to-edge ratio of an ideal equilateral tetrahedron (Cheng et al., 2012; Si, 2015). Most badly shaped tetrahedra with small or large angles have large radius-to-edge ratios, while most well-shaped tetrahedra have small radius-to-edge ratios (Figure 4.2). The

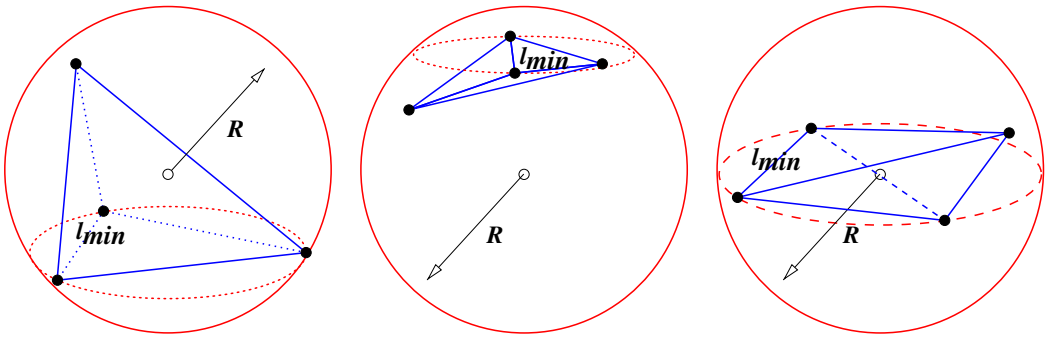

Figure 4.4. The circumradius-to-shortest-edge ratio of several tetrahedra. The radius-to-edge ratio is a suitable quality measure for most tetrahedra, with the exception of slivers (right). While most badly shaped cells have large radius-to-edge ratios, slivers can have radius-to-edge ratios as small as $1/\sqrt{2} \doteq 0.707$. Modified from Si (2013).

radius-to-edge ratio Q is related to the minimum face angle θ_{min} of a tetrahedron τ by the inequality relation (Si, 2015)

$$Q(\tau) = \frac{R}{l_{min}} \geq \frac{1}{2\sin\theta_{min}},$$

where R is the radius of the circumsphere, l_{min} is the minimum edge length, and $\sqrt{6}/4 \leq Q \leq \infty$. An upper bound on the radius-to-edge ratio enforces a lower bound on the minimum face angle. By bounding the radius-to-edge ratio, Delaunay refinement algorithms eliminate most badly shaped tetrahedra with small or large dihedral angles, with the exception of one class of badly shaped tetrahedra known as *slivers* (Cheng et al., 2012). A sliver is a type of flat, badly shaped cell that has a dihedral angle near 180° but has a radius-to-edge ratio as small as $1/\sqrt{2} \doteq 0.707$ (Figure 4.4, right). A second shape quality measure is required to eliminate this type of badly shaped cell.

In the *quality* Delauney tetrahedralization, the user may explicitly specify both/either an upper bound on the radius-to-edge ratio and/or a lower bound on dihedral angle (TetGen releases 1.4.3 and onward). This second quality criterion attempts to screen out slivers. Enforcement of quality criteria generally leads to good grading in the mesh, that is, transition from small to large cell size accomplished over a minimal distance while maintaining

quality, well-shaped tetrahedra (Cheng et al., 2012; Si, 2015). This is important because poor grading, or large local contrasts in cell size, can contribute to ill-conditioning of the system. In TetGen release 1.4.3, the default values for maximum radius-to-edge ratio and minimum dihedral angle are 2.0 and 5°, respectively. It should be noted that even with appropriate quality criteria, in a constrained tetrahedralization which respects domain boundaries, some badly shaped cells may persist in proximity to sharp, constraining features (e.g., where bounding surfaces meet at acute dihedral angles; Si, 2015). For all tetrahedral meshing performed in this study, a maximum radius-to-edge ratio of 1.2 and minimum dihedral angle of 5° were enforced. These quality criteria were assessed to provide a good balance between mesh refinement for accuracy and problem size, as controlled by the number of cells in the mesh.

In terms of cell size, small cell size offers greater accuracy, but a discretization with a large number of small cells costs more computationally than one with a small number of large cells (Cheng et al., 2012). Mesh generation must balance problem size, in terms of number of cells in the mesh, and accuracy in numerical solution. In practice, the mesh must be sufficiently refined to accurately represent: (1) the geometry of the earth's structure, and (2) spatial variations in the EM field solutions, particularly in proximity to the EM source, where the fields vary rapidly in space, and in proximity to the EM receivers, where a high accuracy in solution is desired (Plessix et al., 2007; Vieira da Silva et al., 2012). Further, in marine CSEM models, refinement at the receivers must be sufficient to capture the jump in electric field due to the discontinuity of its normal component across the sea-sediment (seafloor) conductivity boundary. While refinement is important for solution accuracy, having small cell size extend to the boundaries of the domain drastically increases the problem size, memory requirements, and convergence time of the iterative solver. For computational efficiency, the mesh is ideally fine near the centre, where the source is approximately located, and increasingly coarse toward the edges (Hohmann, 1988; Newman

and Alumbaugh, 1995; Streich, 2009).

Some numerical schemes attempt to automate the process of balancing refinement, problem size, and accuracy by using adaptive mesh refinement based on an a posteriori error estimate, where refinement is only added where necessary to improve the solution (e.g., Key, 2012c; Schwarzbach et al., 2011). The approach taken in this study for mesh refinement in the vicinity of the source and along receiver lines was manual insertion of rectangular regions or blocks which enforced refinement by virtue of their dimensions or proximity to constraining boundaries. For example, a block of dimensions 5 m $\times$ 5 m $\times$ 5 m might be inserted above or below the source, and a rectangular block of dimensions 10 m $\times$ 10 m $\times$ receiver line length might be inserted at z = 10 m above the seafloor, along the simulated receiver line. These blocks were assigned the resistivity of the background so that their presence did not modify the electrical structure of the model.

4.2.3 Domain boundaries

When enforcing Dirichlet boundary conditions of the first order (i.e., the values of the fields are fixed at the boundaries of the domain; see Section 4.3.1), we assume that the field values go to zero at the boundaries of the mesh. To ensure that this is a valid assumption, the boundaries of the volume must be placed far enough from the source that the field magnitudes become negligible at the boundaries. Placement of domain boundaries at sufficient distance from the source is also required to maintain the validity of the assumption of zero energy reflection at the boundaries of the domain (Newman and Alumbaugh, 1995). For marine CSEM, where the decay of the fields is dictated by skin depth, we require that the modelling domain extends several skin depths, ideally defined by the most resistive element of the earth system, beyond the source location. A practical guideline is to place the boundaries at approximately $8\delta_{ave}$ from the source location $\mathbf{r}' = (x', y', z')$, where δ_{ave} is the average skin depth of the system, or the skin depth of the most resistive background

component, e.g., the resistive sedimentary half-space of the marine two-halfspace model (SeyedMasoud Ansari, personal communication, 2013). This is only a general guideline, as placement of receivers as well as location and extent of anomalous bodies within the domain may dictate adjustment of the boundaries to improve the convergence of the iterative solver (SeyedMasoud Ansari, personal communication, 2013). Plessix et al. (2007) suggest a similar skin depth-based approach for defining mesh boundaries. In their automated gridding algorithm based on source location and frequency, grid dimensions are estimated as

$$\left[x' - r_x\delta_{ave}, x' + r_x\delta_{ave}\right] \times \left[y' - y_x\delta_{ave}, y' + r_y\delta_{ave}\right] \times \left[z_{air}, z' + r_z\delta_{ave}\right],$$

where r_x and r_y are constants between 4 and 8, depending on the location of receivers, r_z is around 4, z_{air} is the z-coordinate (depth) of the air-sea interface, and δ_{ave} is the average skin depth of the domain, which generally corresponds to the skin depth of a homogeneous sediment background. When considering the choice of constants r_x and r_y, for a homogeneous space, at four skin depths, the amplitudes of the EM fields have been reduced by 98%, and at eight skin depths, the amplitudes have been reduced by 99.97% (Plessix et al., 2007).

4.3 The CSEM3DFWD forward code

The CSEM3DFWD forward code (Ansari and Farquharson, 2011, 2013, 2014; Ansari, 2014; Ansari et al., 2015) was written by Dr. Seyedmasoud Ansari, former PhD student of the Department of Earth Sciences, Memorial University of Newfoundland and Labrador, St. John's, Newfoundland. The method is based on a scalar-vector potential formulation of the induction EM problem with finite-element discretization based on the Garlerkin variant of the method of weighted residuals. Decomposition of the electric field in terms of scalar and vector potentials allows, in theory, investigation of the inductive and galvanic contributions to the EM response, which in turn provides insight into the physical mechanisms

involved in generation of a specific anomalous response. The code allows simulation of various controlled-source configurations, including magnetic point sources, loop sources, and grounded wire or electric dipole sources in both horizontal and vertical orientations.

Development of the CSEM3DFWD code was ongoing during completion of this work and continues at present, with the result that two different versions of the code were used in the course of this study. The following methodology describes the ungauged, quasi-static code presented in Ansari and Farquharson (2014) and Ansari (2014), which was used for all models not containing an air layer. For all models containing an air layer, an ungauged version which extended application to non-quasi-static, damped wave behaviour was employed; modifications with respect to the previous quasi-static version are described in Section 4.3.4. A similar version of the non-quasi-static code, modified to include explicit gauge conditions for unique potentials, is described in Ansari et al. (2015).

4.3.1 Problem formulation

From Section 2.1.6, in the quasi-static limit (i.e., $\sigma \gg \varepsilon\omega$), Faraday's and Ampère's laws in the frequency-domain reduce to

$$\nabla \times \mathbf{E} + i\omega\mathbf{B} = 0 \tag{4.1}$$

and

$$\nabla \times \mathbf{H} - \mathbf{J} = \mathbf{J}_\mathbf{e}^\mathbf{s}, \tag{4.2}$$

and the electric field Helmholtz equation for a homogeneous region reduces to

$$\nabla \times \nabla \times \mathbf{E} + i\omega\mu_0\sigma\mathbf{E} = -i\omega\mu_0\mathbf{J}_\mathbf{e}^\mathbf{s}, \tag{4.3}$$

where we have made the assumption that $\mu = \mu_0$. For low frequencies characteristic of EM induction methods, equation (4.3) poses difficulties to numerical methods due to the instability of the numerical solution with vanishing conductivity term $i\omega\mu_0\sigma\mathbf{E}$ as $i\omega\mu_0\sigma \rightarrow 0$. The matrix system arising from discretization of equation (4.3) is ill-conditioned, and iterative methods may struggle or fail to converge (Sasaki and Meju, 2009; Ansari, 2014). To avoid numerical difficulties associated with a vanishing conductivity term, the electric field is decomposed in terms of a scalar potential $\phi(\mathbf{r}, \omega)$ and vector potential $\mathbf{A}(\mathbf{r}, \omega)$.

The Helmholtz theorem states that any 3D vector field $\mathbf{F}$ which is continuous and zero at infinity can be resolved as the sum of the gradient of a scalar potential ϕ and the curl of a vector potential $\mathbf{A}$, i.e., (Blakely, 1996)

$$\mathbf{F} = \nabla\phi + \nabla \times \mathbf{A}. \tag{4.4}$$

As a corollary to the Helmholtz theorem, since the divergence of the magnetic flux density $\mathbf{B}$ is zero, i.e., $\nabla \cdot \mathbf{B} = 0$, there exists some vector potential $\mathbf{A}$ such that

$$\mathbf{B} = \nabla \times \mathbf{A}. \tag{4.5}$$

Substituting equation (4.5) into equation (4.1), we obtain

$$\nabla \times (\mathbf{E} + i\omega\mathbf{A}) = 0. \tag{4.6}$$

Another corollary to the Helmholtz theorem states that since $\nabla \times (\mathbf{E} + i\omega\mathbf{A}) = 0$, there exists some scalar potential ϕ for which

$$\mathbf{E} + i\omega\mathbf{A} = -\nabla\phi.$$

Rearranging, we obtain an expression for the electric field $\mathbf{E}$ in terms of the vector potential $\mathbf{A}$ and scalar potential ϕ,

$$\mathbf{E} = -i\omega\mathbf{A} - \nabla\phi. \tag{4.7}$$

Substituting this expression for $\mathbf{E}$ into equation (4.3), we obtain

$$\nabla \times \nabla \times \mathbf{A} + i\omega\mu_0\sigma\mathbf{A} + \mu_0\sigma\nabla\phi = \mu\mathbf{J}_\mathbf{e}^\mathbf{s}. \tag{4.8}$$

This vector equation comprises three components in four unknowns: the three components of vector potential $\mathbf{A}$ as well as the scalar potential ϕ. An additional equation is thus required to solve for $\mathbf{A}$ and ϕ. To form a square system, we include the continuity equation,

$$\nabla \cdot \mathbf{J} = \begin{cases} -\nabla \cdot \mathbf{J}_\mathbf{e}^\mathbf{s} & \text{at source location, and} \\ 0 & \text{everywhere else,} \end{cases} \tag{4.9}$$

which we have shown, in Section 2.1, can be derived from Maxwell's equations by taking the divergence of Ampère's law and substituting Gauss's law, i.e., $\nabla \cdot \mathbf{D} = 0$. Using the constitutive relation $\mathbf{J} = \sigma\mathbf{E}$ and substituting equation (4.7) into (4.9) yields

$$-i\omega\nabla \cdot (\sigma\mathbf{A}) - \nabla \cdot (\sigma\nabla\phi) = -\nabla \cdot \mathbf{J}_\mathbf{e}^\mathbf{s}. \tag{4.10}$$

Equations (4.8) and (4.10) form a square system that is diagonally dominated by the vector and scalar potential terms (Ansari and Farquharson, 2014). Using the finite-element method of discretization, the system is solved for $\mathbf{A}$ and ϕ. In order to obtain a unique solution, boundary conditions must be applied to the boundaries of the computational domain. We introduce Ω for the computational domain volume and Γ as its outer boundary. Dirichlet

boundary conditions are applied at the outer boundary Γ of the form

$$(\mathbf{n} \times \mathbf{A})_\Gamma = 0, \tag{4.11}$$

and

$$\phi_\Gamma = 0. \tag{4.12}$$

4.3.2 Finite-element discretization

To discretize the PDE boundary-value problem outlined in Section 4.3.1, the Galerkin variant of the method of weighted residuals is used. In the method of weighted residuals, the solution of the boundary value problem is approximated by minimizing the weighted residual of the relevant equations over the entire domain. The original boundary value problem is then satisfied in a weak, weighted-integral (i.e., average) sense over the entire domain.

To apply the finite-element method, the computational domain is first subdivided into subdomains, also known as cells or *elements* (note however that the term finite element can also refer to the more primary elements of a cell, such as the nodes and edges; e.g., Schwarzbach et al., 2011). Unstructured tetrahedral meshes are employed because they are able to accurately represent curvilinear boundaries and allow for local refinement within the mesh. Within each element, the vector and scalar potentials are interpolated from values calculated at the edges and nodes of each element, respectively. The vector and scalar potentials are expressed as expansions in a finite number of vector and scalar basis functions associated with the element edges and nodes, i.e.,

$$\mathbf{A} = \sum_{j=1}^{n_A} A_j \mathbf{N}_j \tag{4.13}$$

and

$$\phi = \sum_{k=1}^{n_\phi} \phi_k N_k, \tag{4.14}$$

where $\mathbf{N}_j$ and N_k are edge-element and nodal-element basis functions, respectively. The expansion coefficients A_j and ϕ_k respectively represent the magnitude of the vector potential at the j^{th} edge and magnitude of the scalar potential at the k^{th} node and are the unknowns or degrees of freedom of the system. The upper summation bounds n_A and n_ϕ represent the number of edges and number of nodes within each tetrahedral element, i.e., $n_A = 6$ and $n_\phi = 4$.

The behaviour of edge- and nodal-element basis functions at the boundaries of an element make them a judicious choice for approximation of the vector and scalar potentials from a physical standpoint; continuity of the tangential component of the electric field is enabled by continuity of the tangential components of $\mathbf{N}$ and ∇N, and discontinuity of the normal component of the electric field is enabled by discontinuity of the normal component of ∇N (Figure 4.5). Further, since $\nabla \cdot \mathbf{N} = 0$ by construction, the divergence-free condition for the electric field, i.e., $\nabla \cdot \mathbf{E} = 0$, and the Coulomb gauge condition, $\nabla \cdot \mathbf{A} = 0$, are implicitly satisfied within a source-free element (Ansari and Farquharson, 2014).

To apply the method of weighted residuals, we require a weak formulation of the problem described by equations (4.8) and (4.10). To accomplish this, we form residuals that we require to be zero in a weak, weighted-average sense. A vector residual $\mathbf{r}$ is formed from equation (4.8),

$$\mathbf{r} = \nabla \times \nabla \times \tilde{\mathbf{A}} + i\omega\mu_0\sigma\tilde{\mathbf{A}} + \mu_0\sigma\nabla\tilde{\phi} - \mu_0\mathbf{J}_\mathbf{e}^\mathbf{s}, \tag{4.15}$$

where $\tilde{\mathbf{A}}$ and $\tilde{\phi}$ represent the approximated vector and scalar potentials. This vector residual is minimized by setting its inner product with vector weighting function $\mathbf{W}$ on the domain Ω to zero, i.e.,

$$R = \int_\Omega \mathbf{W} \cdot \mathbf{r} d\Omega = 0. \tag{4.16}$$

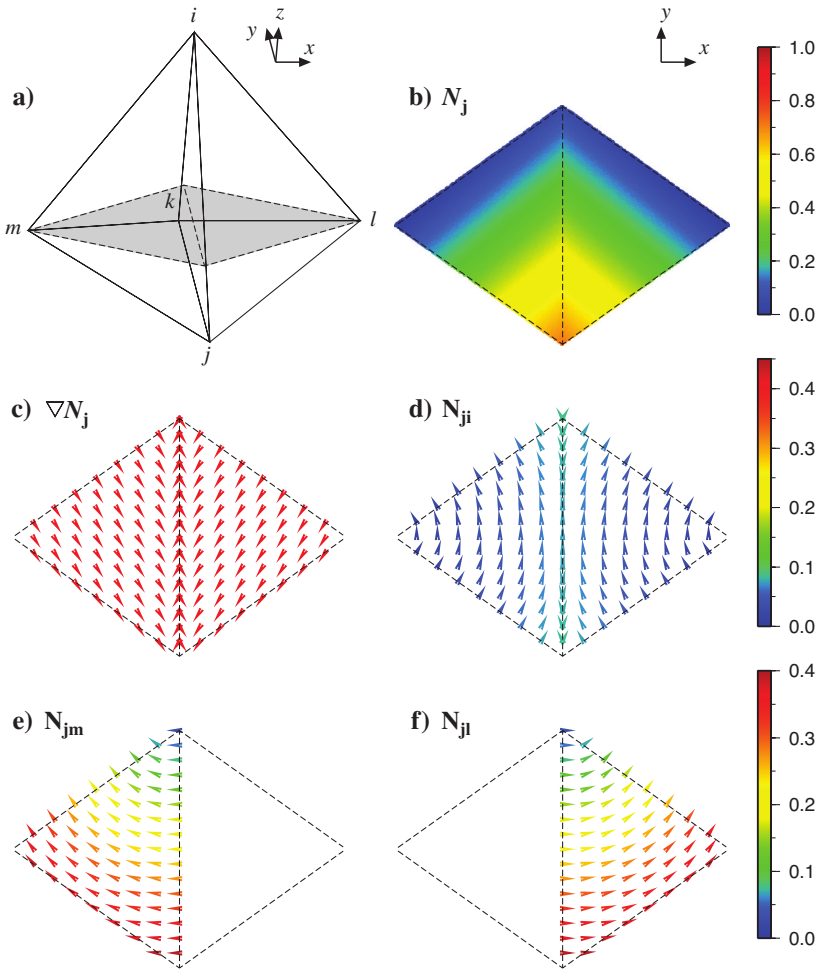

Figure 4.5. Illustration of the behaviours of vector edge-element and scalar nodal-element basis functions across two adjacent tetrahedra, (i, j, k, m) and (i, j, k, l), with shared face (i, j, k). Colour indicates magnitude of the plotted quantity and arrows indicate direction. Panel (a) illustrates the neighbouring tetrahedra and the grey-coloured plane on which the scalar and vector (arrow) plots of panels (b)-(f) are projected; panel (b) is a scalar plot of the basis function N_j; from the left to right cell, N_j is continuous. Panel (c) is a vector plot of the gradient of the scalar basis function, ∇N_j; the tangential component of ∇N_j is continuous across the shared face, while its normal component is discontinuous. Panel (d) is a vector plot of the vector basis function $\mathbf{N}_{ji}$; $\mathbf{N}_{ji}$ is purely tangential along and continuous across the shared face. Panels (e) and (f) are plots of additional vector basis functions $\mathbf{N}_{jm}$ and $\mathbf{N}_{jl}$ associated with edges that are not along the shared face; across the shared face, they are purely normal. From Ansari and Farquharson (2014).

If the residual $\mathbf{r}$ can be made to be orthogonal to $\mathbf{W}$, the inner product will be zero and an accurate solution will be obtained. By substituting (4.15) into (4.16) and applying integration by parts to the first inner product term, $\mathbf{W}\cdot\nabla\times\nabla\times\tilde{\mathbf{A}}$, we obtain the weighted PDE

$$\begin{aligned}&\int_{\Omega}(\nabla\times\mathbf{W})\cdot\left(\nabla\times\tilde{\mathbf{A}}\right)d\Omega-\int_{\gamma+\Gamma}\mathbf{W}\times\left(\nabla\times\tilde{\mathbf{A}}\right)\cdot\mathbf{n}dS\\&+i\omega\mu_0\int_{\Omega}\sigma\mathbf{W}\cdot\tilde{\mathbf{A}}d\Omega+\mu_0\int_{\Omega}\sigma\mathbf{W}\cdot\nabla\tilde{\phi}d\Omega=\mu_0\int_{\Omega}\mathbf{W}\cdot\mathbf{J}_{\mathbf{e}}^{\mathbf{s}}d\Omega,\end{aligned}\tag{4.17}$$

where γ denotes the inner boundaries (i.e., element interfaces) of the mesh. A scalar residual r is similarly constructed from equation (4.10),

$$r=-i\omega\nabla\cdot\left(\sigma\tilde{\mathbf{A}}\right)-\nabla\cdot\left(\sigma\nabla\tilde{\phi}\right)+\nabla\cdot\mathbf{J}_{\mathbf{e}}^{\mathbf{s}},\tag{4.18}$$

and is minimized by setting the integral of its product with scalar weighting function v over the domain Γ to zero, i.e.,

$$\rho=\int_{\Omega}vrd\Omega=0.\tag{4.19}$$

By substituting (4.18) into (4.19) and applying integration by parts to the volume integrals involving both potentials $\mathbf{A}$ and ϕ, we obtain

$$\begin{aligned}&i\omega\int_{\Omega}\nabla v\cdot\sigma\tilde{\mathbf{A}}d\Omega-i\omega\int_{\gamma+\Gamma}v\sigma\tilde{\mathbf{A}}\cdot\mathbf{n}dS\\&+\int_{\Omega}\nabla v\cdot\sigma\nabla\tilde{\phi}d\Omega-\int_{\gamma+\Gamma}v\sigma\nabla\tilde{\phi}\cdot\mathbf{n}dS=-\int_{\Omega}v\nabla\cdot\mathbf{J}_{\mathbf{e}}^{\mathbf{s}}d\Omega.\end{aligned}\tag{4.20}$$

The surface integral terms in equation (4.20) describe the behaviour of the normal current density contributions from $\mathbf{A}$ and ϕ. Using the relation $\tilde{\mathbf{J}}=\sigma\tilde{\mathbf{E}}=\sigma\left(-i\omega\tilde{\mathbf{A}}-\nabla\tilde{\phi}\right)$, the

surface integral terms can be combined into

$$i\omega \int_{\Omega} \nabla v \cdot \sigma \tilde{\mathbf{A}} d\Omega + \int_{\Omega} \nabla v \cdot \sigma \nabla \tilde{\phi} d\Omega + \int_{\gamma+\Gamma} v \tilde{\mathbf{J}} \cdot \mathbf{n} dS = -\int_{\Omega} v \nabla \cdot \mathbf{J}_{\mathbf{e}}^{\mathbf{s}} d\Omega. \tag{4.21}$$

With appropriate choice of weighting functions $\mathbf{W}$ and r, the surface integrals of equations (4.17) and (4.21) can be made to be zero at the inner mesh boundaries (shared cell faces) via mutual cancellation of terms in neighbouring cells. The surface integrals at the outer mesh boundary Γ are forced to zero to conform to the Sommerfeld boundary radiation condition that no energy reflects back from the infinite outer boundary. Regardless, the outer boundary Γ is chosen to be sufficiently far from the source to effectually satisfy this condition. In the Galerkin variant of the method of weighted residuals, the basis functions used to approximate the vector and scalar potentials are used as the weighting functions, i.e.,

$$\mathbf{W} = \mathbf{N} \tag{4.22}$$

and

$$r = N. \tag{4.23}$$

Using these basis functions for the weighting functions, substituting equations (4.13) and (4.14) into equations (4.17) and (4.21), and expanding over the entire tetrahedralized domain, we obtain the finite-element equations

$$\sum_{j=1}^{N_{edges}} \tilde{A}_j \int_{\Omega} (\nabla \times \mathbf{N}_i) \cdot (\nabla \times \mathbf{N}_j) \, d\Omega + i\omega\mu_0 \sum_{j=1}^{N_{edges}} \tilde{A}_j \int_{\Omega} \sigma \mathbf{N}_i \cdot \mathbf{N}_j d\Omega + \mu_0 \sum_{k=1}^{N_{nodes}} \tilde{\phi}_k \int_{\Omega} \sigma \mathbf{N}_i \cdot \nabla N_k d\Omega = \mu_0 \int_{\Omega} \mathbf{N}_i \cdot \mathbf{J}_{\mathbf{e}}^{\mathbf{s}} d\Omega \tag{4.24}$$

and

$$i\omega \sum_{j=1}^{N_{edges}} \tilde{A}_j \int_\Omega \nabla N_l \cdot \left(\sigma \mathbf{N}_j\right) d\Omega + \sum_{k=1}^{N_{nodes}} \tilde{\phi}_k \int_\Omega \nabla N_l \cdot \left(\sigma \nabla N_k\right) d\Omega = -\int_\Omega N_l \nabla \cdot \mathbf{J}_\mathbf{e}^\mathbf{s} d\Omega, \tag{4.25}$$

where $i = 1,...,N_{edges}$, $l = 1,...,N_{nodes}$, and N_{edges} and N_{nodes} are respectively the total number of edges and total number of nodes in the mesh. The system of equations formed by (4.24) and (4.25) is solved for the coefficients $\tilde{A}_j$ of the approximated vector potential and coefficients $\tilde{\phi}_k$ of the approximated scalar potential.

4.3.3 Solution of the discrete system

The discrete system formed by equations (4.24) and (4.25) can be represented in matrix form as:

$$\begin{pmatrix} \mathbf{C} + i\omega\mu_0\mathbf{D} & \mu_0\mathbf{F} \\ i\omega\mathbf{G} & \mathbf{H} \end{pmatrix} \begin{pmatrix} \tilde{\mathbf{A}} \\ \tilde{\phi} \end{pmatrix} = \begin{pmatrix} \mu_0 S_1 \\ S_2 \end{pmatrix}, \tag{4.26}$$

where **C**, **D**, **F**, **G**, and **H** are inner-product functionals defined by the left-hand side integrals of equations (4.24) and (4.25), i.e.,

$$\mathbf{C} = \mathscr{F}(\mathbf{N}), \tag{4.27a}$$

$$\mathbf{D} = \mathscr{F}(\sigma, \mathbf{N}), \tag{4.27b}$$

$$\mathbf{F} = \mathscr{F}(\sigma, \mathbf{N}, \nabla N), \tag{4.27c}$$

$$\mathbf{G} = \mathscr{F}(\sigma, \mathbf{N}, \nabla N), \quad \text{and} \tag{4.27d}$$

$$\mathbf{H} = \mathscr{F}(\sigma, \nabla N), \tag{4.27e}$$

or more specifically,

$$C_{ij} = \int_{\Omega} (\nabla \times \mathbf{N}_i) \cdot \left(\nabla \times \mathbf{N}_j\right) d\Omega, \tag{4.28a}$$

$$D_{ij} = \int_{\Omega} \sigma \mathbf{N}_i \cdot \mathbf{N}_j d\Omega, \tag{4.28b}$$

$$F_{ik} = \int_{\Omega} \sigma \mathbf{N}_i \cdot \nabla N_k d\Omega, \tag{4.28c}$$

$$G_{lj} = \int_{\Omega} \nabla N_l \cdot \left(\sigma \mathbf{N}_j\right) d\Omega, \quad \text{and} \tag{4.28d}$$

$$H_{lk} = \int_{\Omega} \nabla N_l \cdot (\sigma \nabla N_k) \, d\Omega, \tag{4.28e}$$

where $i, j = 1, ..., N_{edges}$ and $l, k = 1, ..., N_{nodes}$. Note that $\mathbf{G}$ is the transpose of $\mathbf{F}$. S_1 and S_2 are source terms defined by the right-hand side integrals of equations (4.24) and (4.25),

$$S_1 = \int_{\Omega} \mathbf{N}_i \cdot \mathbf{J}_{\mathbf{e}}^{\mathbf{s}} d\Omega \tag{4.29a}$$

and

$$S_2 = -\int_{\Omega} N_l \nabla \cdot \mathbf{J}_{\mathbf{e}}^{\mathbf{s}} d\Omega. \tag{4.29b}$$

The inner-product functionals of the coefficient matrix, (4.28a) – (4.28e), describe the interactions among the vector basis functions, among the nodal basis functions, and between the vector and nodal basis functions. The terms of the source vector, (4.29a) and (4.29b), describe the interactions between the basis functions and the source function. Given the choice of linear edge-element and nodal-element basis functions for the expansions of the approximated vector and scalar potentials, closed-form formulae can be derived for the integrals in equations (4.28) and (4.29).

Since options are limited for preconditioning of linear systems with complex coefficient matrices, the complex-valued system is converted to a real-valued system via decomposi-

tion into real and imaginary parts. Consider a system of the form

$$Au = b,$$

where A is a complex-valued matrix of order M, and $u, b \in \mathbb{C}^M$. Decomposing the system into real and imaginary parts i.e.,

$$(R + iS)(x + iy) = (\alpha + i\beta),$$

where R and S are real-valued matrices of order M and $x, y, \alpha, \beta \in \mathbb{R}^M$, the system can be rewritten in real-valued form as (Axelsson and Kucherov, 2000)

$$\begin{pmatrix} R & -S \\ S & R \end{pmatrix} \begin{pmatrix} x \\ y \end{pmatrix} = \begin{pmatrix} \alpha \\ \beta \end{pmatrix}.$$

Following this model, the complex matrix equation (4.26) can instead be solved in its equivalent real-valued form

$$\begin{pmatrix} \mathbf{C} & -\omega\mu_0\mathbf{D} & \mu_0\mathbf{F} & 0 \\ \omega\mu_0\mathbf{D} & \mathbf{C} & 0 & \mu_0\mathbf{F} \\ 0 & -\omega\mathbf{G} & \mathbf{H} & 0 \\ \omega\mathbf{G} & 0 & 0 & \mathbf{H} \end{pmatrix} \begin{pmatrix} \tilde{A}^R \\ \tilde{A}^I \\ \tilde{\phi}^R \\ \tilde{\phi}^I \end{pmatrix} = \begin{pmatrix} \mu_0 S_1 \\ 0 \\ S_2 \\ 0 \end{pmatrix}, \tag{4.30}$$

where $\tilde{A}^R$, $\tilde{A}^I$, $\tilde{\phi}^R$, and $\tilde{\phi}^I$ are the real and imaginary parts of the coefficients for the approximated vector and scalar potentials, respectively. Note that the real-valued coefficient matrix is twice the size of its complex equivalent, and so the system now has twice the number of unknowns.

In theory, to obtain a unique solution, the Dirichlet boundary conditions of equations

(4.11) and (4.12) must be implemented on Γ, the outer boundary of the mesh. In the finite-element discretization, on boundary Γ we have $\mathbf{n} \times \mathbf{A} = A_j$ and $\phi = \phi_k$, where subscripts j and k respectively denote all edges and all nodes on boundary Γ. To enforce the Dirichlet conditions that coefficients A_j and ϕ_k associated with boundary Γ must be zero, all elements of the rows of the coefficient matrix corresponding to the boundary edges and nodes, with the exception of those elements occurring on the diagonal, are set to zero. The elements in the corresponding rows of the source vector are also set to zero. In practice, it was found that elimination of these rows in the coefficient matrix and source vector is unnecessary (Ansari and Farquharson, 2014).

The matrix equation (4.30) is iteratively solved using the generalized minimum residual (GMRES) solver from SPARSKIT (Saad, 1994). To improve convergence, a dual-threshold incomplete LU factorization (ILUT) preconditioner, also from SPARSKIT, was employed. Representing the matrix equation symbolically as $Au = b$, GMRES provides an approximate solution that minimizes the residual norm $||Au - b||_2$. After each iteration, GMRES outputs the residual norm $||Au_m - b||_2$, where u_m is the approximate solution at iteration m. The residual norm can be plotted against the number of iterations to examine the convergence behaviour of the solution. Ideally, this curve exhibits an initial rapid decrease in the residual norm, followed by stabilization (i.e., convergence) at later iterations. For the explicitly ungauged $\mathbf{A} - \phi$ system presented here, it has been demonstrated that convergence associated with a decrease of 10 to 12 orders of magnitude in the residual norm is sufficient for the iterative solver to provide an accurate solution (Ansari and Farquharson, 2014; Ansari, 2014).

Once the matrix equation (4.30) is solved for the real and imaginary parts of the vector and scalar potential expansion coefficients, the electric field is calculated using equation (4.7), i.e.,

$$\mathbf{E} = -i\omega\mathbf{A} - \nabla\phi,$$

where $\mathbf{A}$ and ϕ are obtained using the basis function expansions defined in equations (4.13) and (4.14). Using equation (4.5), i.e., $\mathbf{B} = \nabla \times \mathbf{A}$, and substituting $\mathbf{H}$ for $\mathbf{B}$ using the constitutive relation $\mathbf{B} = \mu_0 \mathbf{H}$, the magnetic field is calculated as

$$\mathbf{H} = \frac{1}{\mu_0} \nabla \times \mathbf{A}. \tag{4.31}$$

4.3.4 Revisions for the non-quasi static regime

For non-quasi-static, damped wave behaviour, Ampère's law retains the displacement current term $i\varepsilon\omega\mathbf{E}$, i.e.,

$$\nabla \times \mathbf{H} - (\sigma + i\varepsilon\omega)\,\mathbf{E} = \mathbf{J}_\mathbf{e}^\mathbf{s}, \tag{4.32}$$

and the electric field Helmholtz equation consequently retains terms explicit in ε, i.e.,

$$\nabla \times \nabla \times \mathbf{E} + i\mu_0\omega\sigma\mathbf{E} - i\varepsilon\omega^2\mathbf{E} = -i\mu_0\omega\mathbf{J}_\mathbf{e}^\mathbf{s}. \tag{4.33}$$

Following the same process as done previously, we arrive at the decomposed system of equations

$$\nabla \times \nabla \times \mathbf{A} + \left(i\omega\mu_0\sigma + \omega^2\mu\varepsilon\right)\mathbf{A} + (\mu_0\sigma + i\omega\mu_0\varepsilon)\,\nabla\phi = \mu_0\mathbf{J}_\mathbf{e}^\mathbf{s} \tag{4.34}$$

and

$$-i\omega\nabla\cdot(\sigma\mathbf{A}) - \nabla\cdot(\sigma\nabla\phi) + \omega^2\varepsilon\nabla\cdot\mathbf{A} - i\omega\varepsilon\nabla\cdot\nabla\phi = -\nabla\cdot\mathbf{J}_\mathbf{e}^\mathbf{s}. \tag{4.35}$$

This system replaces the previous quasi-static system defined by equations (4.8) and (4.10). Finite-element discretization of the new system defined by equations (4.34) and (4.35)

yields a discrete system represented by the matrix equation

$$\begin{pmatrix} \mathbf{C} + i\omega\mu_0\mathbf{D} + \omega^2\mu_0\mathbf{D}' & \mu_0\mathbf{F} + i\omega\mu_0\mathbf{F}' \\ i\omega\mathbf{G} + \omega^2\mathbf{G}' & \mathbf{H} + i\omega\mathbf{H}' \end{pmatrix} \begin{pmatrix} \tilde{\mathbf{A}} \\ \tilde{\phi} \end{pmatrix} = \begin{pmatrix} \mu_0 S_1 \\ S_2 \end{pmatrix}, \tag{4.36}$$

where $\mathbf{C}$, $\mathbf{D}$, $\mathbf{D}'$, $\mathbf{F}$, $\mathbf{F}'$, $\mathbf{G}$, $\mathbf{G}'$, $\mathbf{H}$ and $\mathbf{H}'$ are inner-product functionals defined by the nodal-element basis functions, edge-element basis functions, and physical properties σ and ε,

$$C_{ij} = \int_\Omega (\nabla \times \mathbf{N}_i) \cdot \left(\nabla \times \mathbf{N}_j\right) d\Omega, \tag{4.37a}$$

$$D_{ij} = \int_\Omega \sigma \mathbf{N}_i \cdot \mathbf{N}_j d\Omega, \tag{4.37b}$$

$$D'_{ij} = \int_\Omega \varepsilon \mathbf{N}_i \cdot \mathbf{N}_j d\Omega, \tag{4.37c}$$

$$F_{ik} = \int_\Omega \sigma \mathbf{N}_i \cdot \nabla N_k d\Omega, \tag{4.37d}$$

$$F'_{ik} = \int_\Omega \varepsilon \mathbf{N}_i \cdot \nabla N_k d\Omega, \tag{4.37e}$$

$$G_{lj} = \int_\Omega \nabla N_l \cdot \left(\sigma \mathbf{N}_j\right) d\Omega, \tag{4.37f}$$

$$G'_{lj} = \int_\Omega \nabla N_l \cdot \left(\varepsilon \mathbf{N}_j\right) d\Omega, \tag{4.37g}$$

$$H_{lk} = \int_\Omega \nabla N_l \cdot (\sigma \nabla N_k)\, d\Omega, \quad \text{and} \tag{4.37h}$$

$$H'_{lk} = \int_\Omega \nabla N_l \cdot (\varepsilon \nabla N_k)\, d\Omega, \tag{4.37i}$$

where $i, j = 1, ..., N_{edges}$ and $l, k = 1, ..., N_{nodes}$. The discrete system represented by matrix equation (4.36) is solved iteratively as described in Section 4.3.3.

Chapter 5

Synthetic marine models

In this chapter, 3D finite-element solutions are presented for several simple marine models whose solutions are compared to 1D semi-analytic or 3D numerical solutions existing in the literature. Structural elements common to offshore exploration environments, such as topography, finite water depth, and thin, laterally finite resistive bodies were individually introduced in several simple synthetic models, which allowed modelling challenges associated with each element to be individually investigated and addressed. The suite of simple marine models permitted gradual familiarisation with model-building, meshing, and forward-modelling software, and served to validate the accuracy of the CSEM3DFWD code for simulation of CSEM data in marine environments. Further, results demonstrated the necessity of 3D modelling to account for the effect on the observed CSEM response of structure which varies in three dimensions, however simplistically. Convergence curves, i.e., plots of the residual norm versus the number of iterations, are presented for several examples to demonstrate the behaviour of the iterative solution. Convergence behaviour and solution smoothness together provide a gauge of the acceptability of a numerical solution, which is particularly important for models for which analytic or precedent numerical solutions do not exist. All finite-element solutions presented in this chapter were computed

on an Apple Mac Pro with 2 $\times$ 4-core 2.8 GHz Intel Xeon processors and 24 GB RAM, with the exception of the solutions for the finite-water depth model (Section 5.4), which were computed on a HP ProLiant SL250s Gen8 compute node with 2 x 8-core 2.6 GHz Intel Xeon processors and 96 GB RAM.

5.1 Marine halfspace model

The marine halfspace model is the most basic of marine models and consists of two conductive halfspaces: an upper 3.3 S/m (0.3 ohm-m) sea halfspace and a lower 1 S/m (1 ohm-m) sediment halfspace. Figure 5.1 illustrates the unstructured mesh for the model, which has a domain of $|x|, |y|, |z| \leq 10$ km. A 1 Hz, unity dipole moment (1 Am) HED was simulated at $(x, y, z) = (0, 0, 100)$ m. An x-directed receiver line was simulated for $|x| \leq 5$ km with 50 m receiver spacing. Cell volume in the mesh varied from 2.0088 m^3 to 2.3677×10^{10} m^3. The mesh was refined near the source, where the fields vary rapidly, and along the simulated receivers, which were located at a height of 0.0001 m above the seafloor, or sea-sediment interface. Refinement at source and receivers was achieved via insertion of blocks, or rectangular regions; these inserted blocks had the same conductivity as the regions in which they were inserted so as not to modify the conductivity structure of the earth model. Note how the mesh is highly refined near its centre, but that cells are allowed to increase in size toward the outer boundary of the model domain. This grading from small cells in the centre of the mesh to large cells at its boundaries is ideal for the conditioning of the system matrix and the convergence of the iterative solver.

The unstructured mesh consisted of 507,236 elements, 81,323 nodes, and 588,960 edges, making the total number of unknowns in the associated finite-element system 1,340,566. A Krylov subspace dimension of 200 was used for the GMRES solver and a fill-in factor of 3 was used for the ILUT precondritioner. The iterative solver had a computation time of

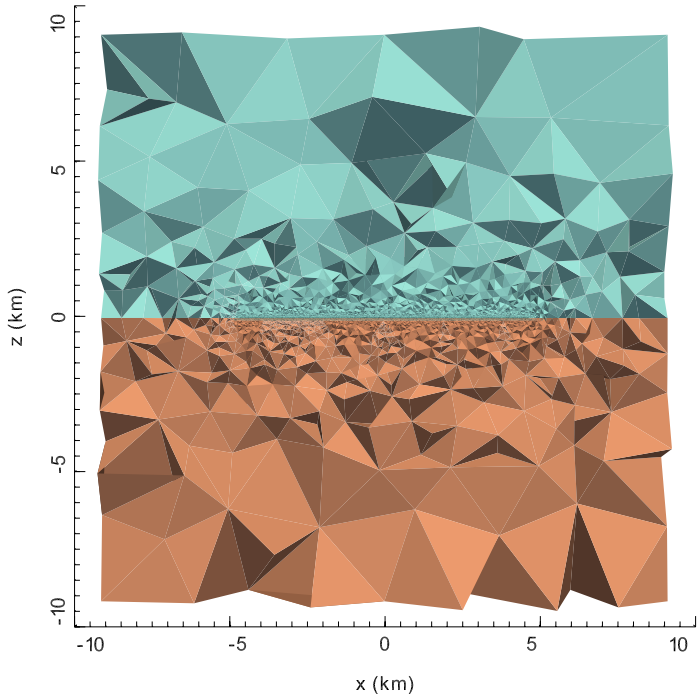

(a) *xz*-section of the full unstructured mesh.

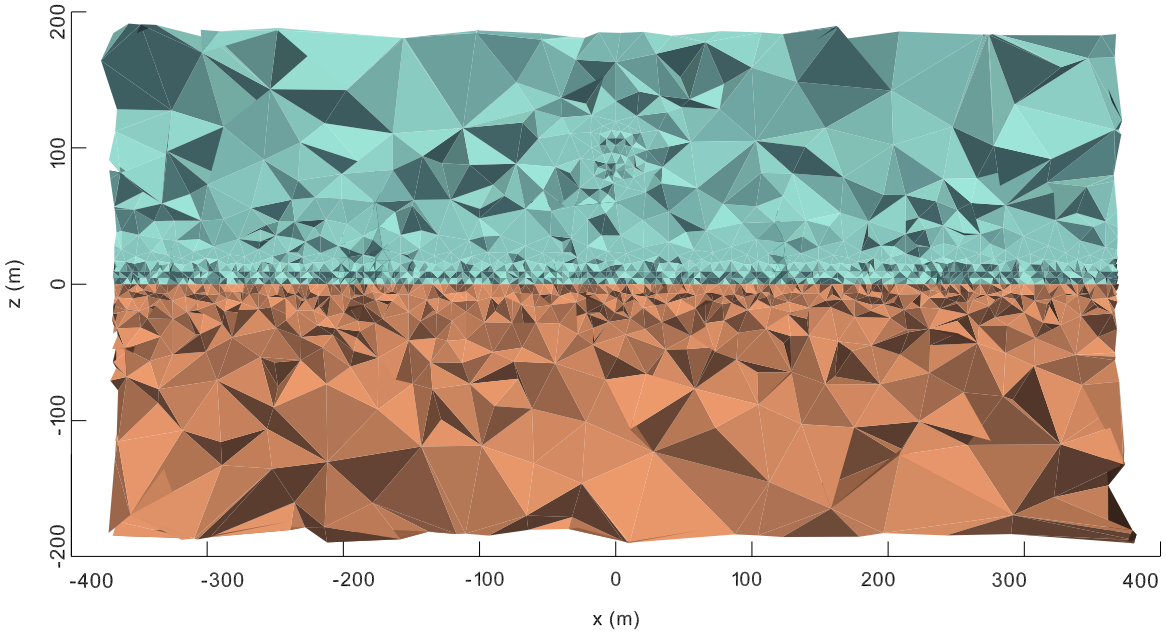

(b) Enlarged *xz*-section of the unstructured mesh for better illustration of the refinement at source and receivers.

Figure 5.1. *xz*-section for y = 0 km of the unstructured mesh for the marine halfspace model, consisting of a lower 1 S/m (1 ohm-m) sediment halfspace and upper 3.3 S/m (0.3 ohm-m) sea halfspace. The computational domain is $|x|, |y|, |z| \leq 10$ km. Refinement was manually enforced in the vicinity of the source, located at $(x, y, z) = (0, 0, 100)$ m, and along the receiver line, which extended to $|x| \leq 5$ km, by insertion of blocks having the same conductivity as their background.

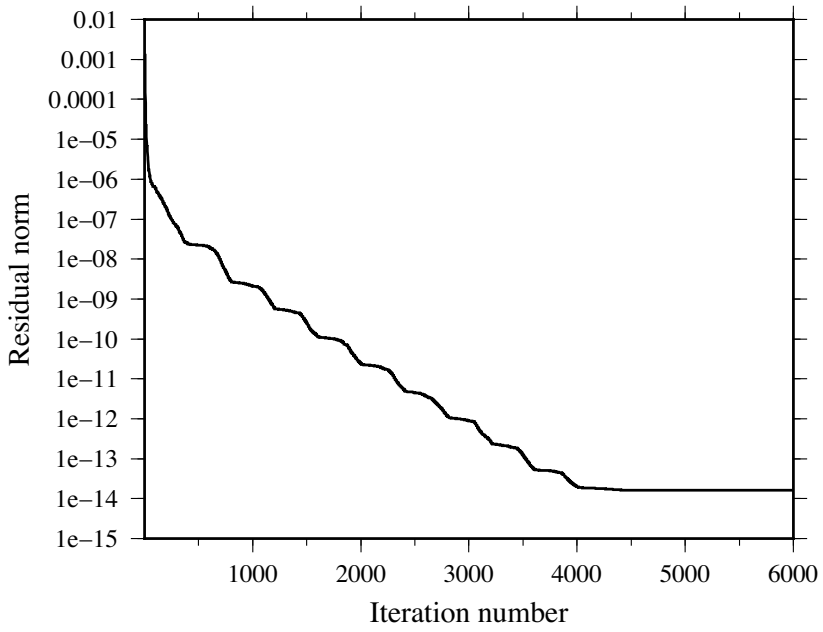

Figure 5.2. Residual norm versus number of iterations for the marine halfspace model with a simulated source frequency of 1 Hz. After approximately 4500 iterations, the iterative solution stabilized with a residual norm near 10^{-14}.

approximately 3130 s ($\sim$ 0.9 h) for 6000 iterations and required approximately 8 GB (7719 MB) of memory; the total run time for CSEM3DFWD was 8007 s ($\sim$ 2.2 h). Figure 5.2 illustrates the residual norm as a function of number of iterations. A residual norm of 10^{-14} was achieved after approximately 4500 iterations, which represents a decrease of 11 orders of magnitude.

Figure 5.3 illustrates the real and imaginary (in-phase and quadrature) parts of the finite-element solutions for the three non-vanishing inline field components, E_x, H_y, and E_z. 1D Hankel transform solutions, computed using the MARDIP1D code described in Appendix A, are plotted alongside the 3D finite-element numerical solutions to demonstrate the accuracy of the numerical solutions. It can be seen that the CSEM3DFWD solutions generally agree very well with the 1D Hankel transform solutions, with some misfit at offsets where the fields vary rapidly, e.g., at near offset in proximity to the source, and where the fields change sign (cusps in field amplitude plots of Figure 5.3). Marine CSEM data is typically

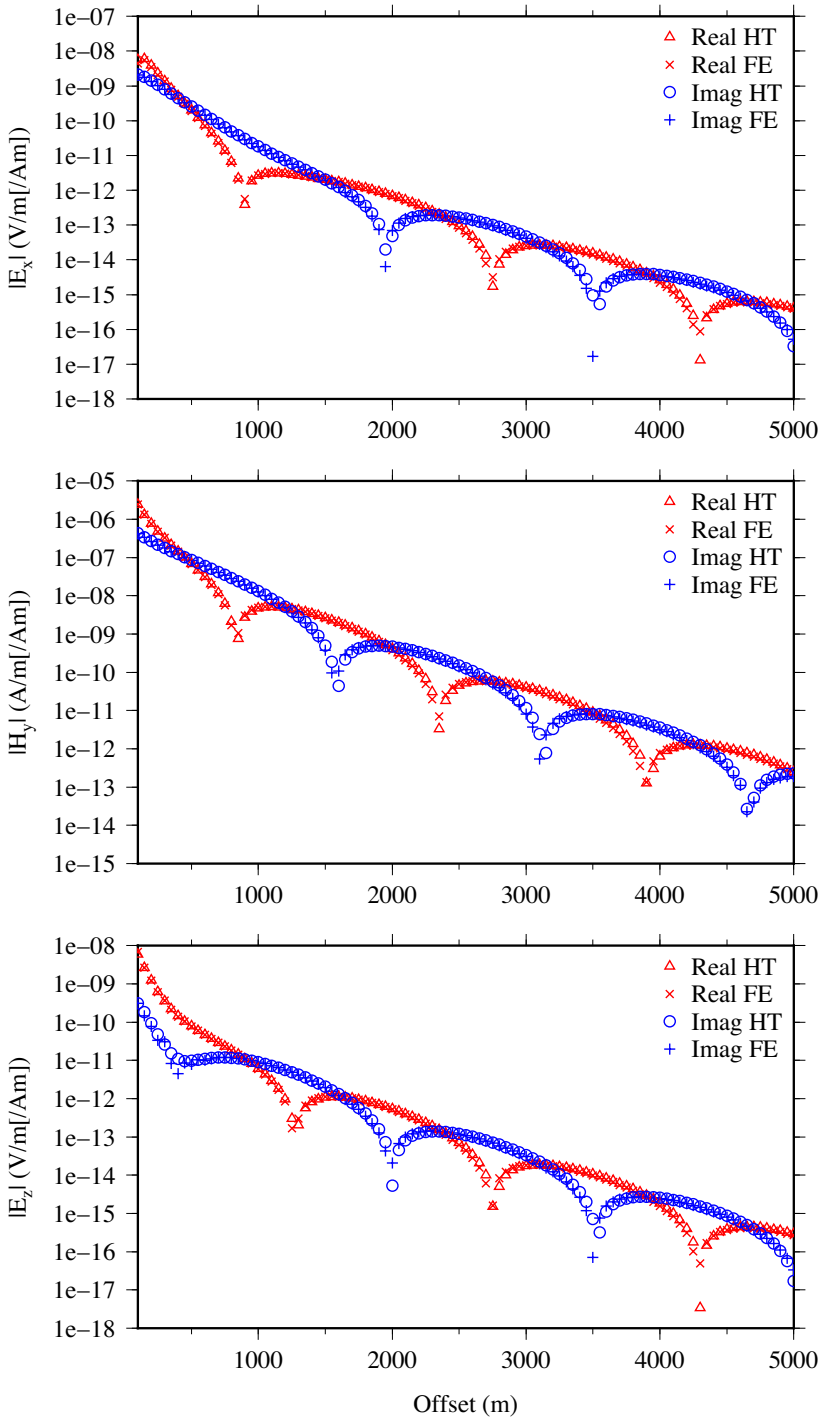

Figure 5.3. The real and imaginary parts for the non-vanishing inline field components E_x, H_y, and E_z for the marine halfspace model. 1D Hankel transform (HT) solutions are plotted alongside the 3D finite-element (FE) solutions to demonstrate the accuracy of the latter. The numerical solution matches the semi-analytic 1D solution very well, with some misfit where the fields vary rapidly, i.e., at near offset and where the fields change sign (cusps in above plots).

presented in amplitude-phase form to emphasize amplitude and phase anomalies arising from galvanic and inductive field interactions within the subsurface. Figure 5.4 presents the amplitude and phase for the inline horizontal electric field E_x.

5.2 Canonical disk model

The canonical disk model, first presented in Constable and Weiss (2006), and later in Weiss and Constable (2006), is a popular model for demonstration of 3D modelling schemes. The model is a 3D adaptation of the 1D canonical oil field model inspired by the Girassol oil field located offshore Angola, which was the site of the first CSEM field trial for industry (Ellingsrud et al., 2002; Constable, 2010). The baseline disk model consists of a 1 km-diameter, 100 m-thick, 0.01 S/m (100 ohm-m) disk buried at a depth of 1 km within a 1 S/m (1 ohm-m) halfspace, with an overlying 3.3 S/m (0.3 ohm-m) sea halfspace (Figure 5.5). The source parameters illustrated in Figure 5.5 correspond to the configuration used for the simulations presented in Figure 5.10.

Finite-element solutions were computed for the canonical disk model for various disk diameters to demonstrate the behaviour of the CSEM response to a resistive target of finite lateral extent. A 1 Hz, 1 Am HED was simulated above the edge of the disk at z = 100 m above seafloor, as illustrated in Figure 5.5. An x-directed receiver line was simulated to extend over the disk to a maximum offset of 8 km, with receiver spacing of 50 m. The receivers were positioned directly above the seafloor at z = 0.0001 m. Figure 5.6 illustrates sectional views of the unstructured mesh for the 2 km-diameter disk model. The full model domain had dimensions of 20 km $\times$ 20 km $\times$ 20 km, and was composed of 81,674 nodes, 589,923 edges, and 507,872 cells. Cell volumes ranged from 1.0125 m^3 to 2.1081×10^{10} m^3, with greater refinement around the source and receivers. The Krylov subspace dimension for GMRES was set to 200 and the fill-in factor for the ILUT preconditioner was set to

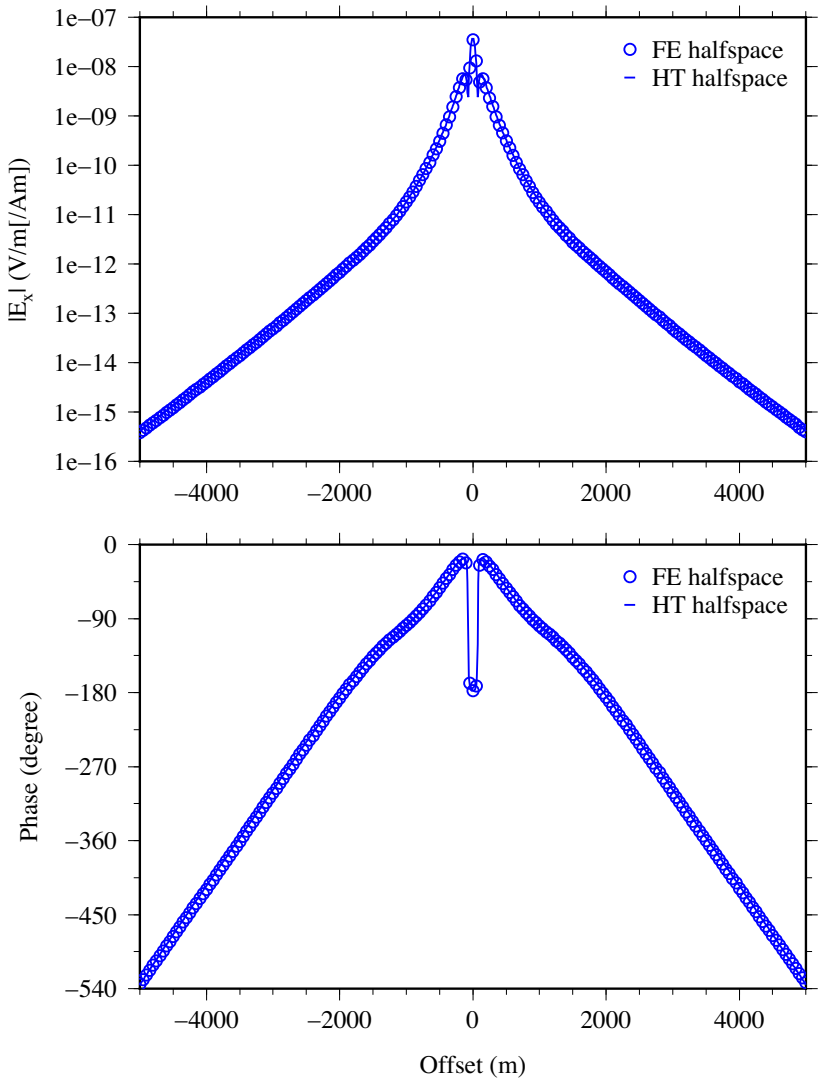

Figure 5.4. The amplitude and phase of the inline horizontal electric field E_x for the marine halfspace model. The 1D Hankel transform (HT) solution is plotted alongside the 3D finite-element (FE) solution to emphasize the accuracy of the latter.

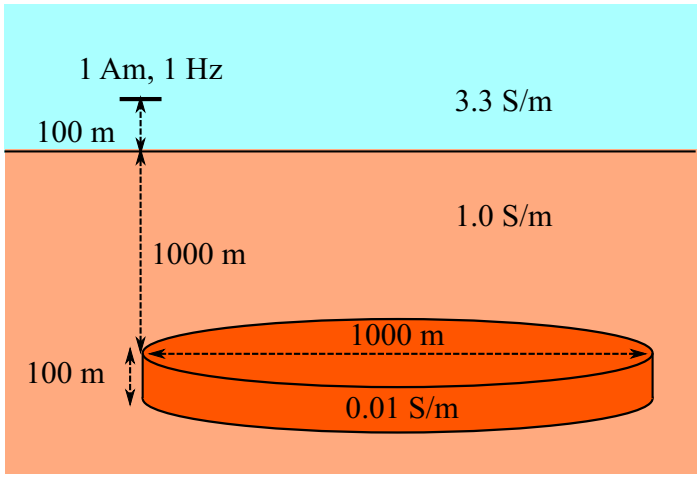

Figure 5.5. Schematic of the baseline canonical disk model, which consists of a 1 km-diameter, 100 m-thick, 0.01 S/m (100 ohm-m) disk buried at a depth of 1 km within a 1 S/m (1 ohm-m) halfspace, with an overlying 3.3 S/m (0.3 ohm-m) sea halfspace. The illustrated source parameters correspond to the configuration used for solutions presented in Figure 5.10.

3 for all examples. For the 2 km-diameter disk model, the iterative solution required 5950 s ($\sim$ 1.65 h) for 10,000 iterations and 7724 MB of memory. Convergence was achieved after 6000 iterations with a residual norm decrease of approximately 11 orders of magnitude (Figure 5.7).

Table 5.1 summarizes the mesh characteristics and iterative solution information for the different diameter disk models. The 3 km-diameter disk model was notable in that it required a greater number of cells in the unstructured mesh and that the solution did not converge in less than 10,000 iterations (Figure 5.8, compare to Figure 5.7). Because of its greater size, to attain an acceptable solution in a reasonable amount of time or iterations, the Krylov subspace dimension for GMRES was set to 400. The 3 km-diameter disk problem required 12 GB for solution and 10,161 s for 10,000 iterations, where convergence was achieved after approximately 8000 iterations (Figure 5.9).

The finite-element solutions for the inline electric field amplitude and phase for various disk diameters are illustrated in Figure 5.10, along with the 1D Hankel transform solutions for an infinite-extent resistive layer and a homogeneous sediment halfspace (i.e., no resistive

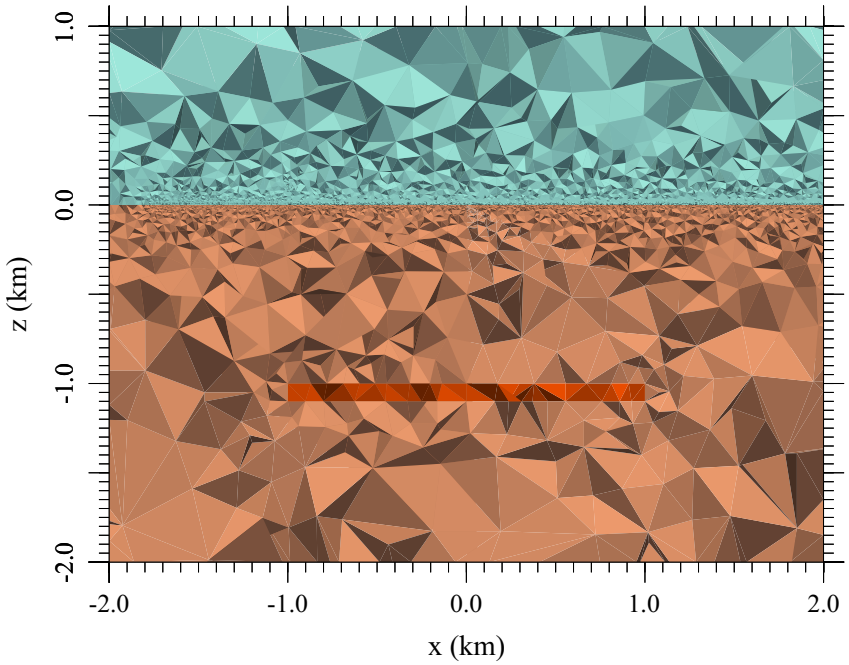

(a) Enlarged xz(cross)-section for $y = 0$ km.

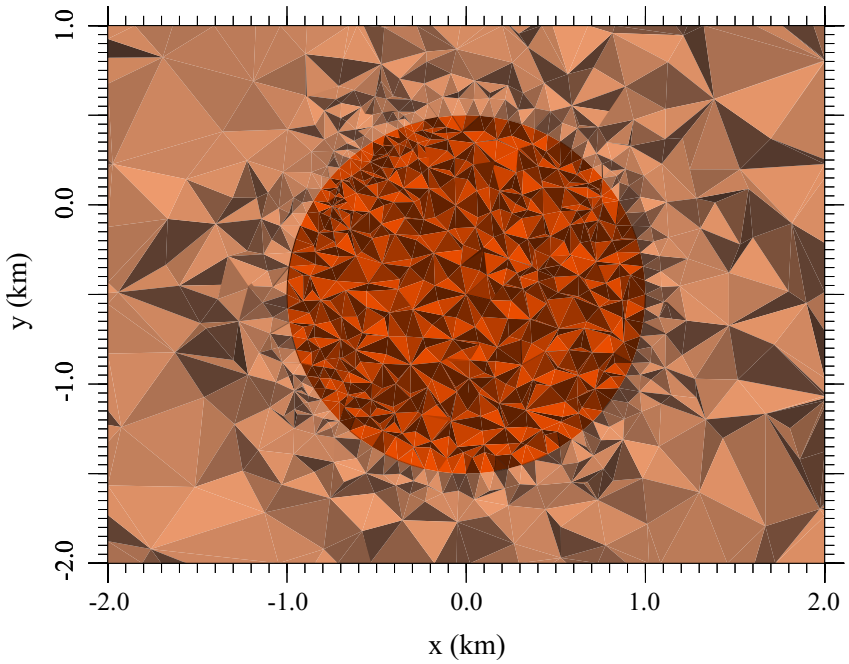

(b) Enlarged xy(depth)-section for $z = -1050$ km.

Figure 5.6. Unstructured mesh for the 2 km-diameter canonical disk model. The model consists of a 0.01 S/m (100 ohm-m), 100 m-thick, 2 km-diameter disk embedded at 1 km-depth within a 1 S/m (1 ohm-m) sediment lower halfspace, and with an overlying 3.3 S/m (0.3 ohm-m) sea upper halfspace. The full domain measures 20 km $\times$ 20 km $\times$ 20 km. Refinement was manually enforced in the vicinity of the 1 Hz, 1 Am HED source located at $(x, y, z) = (-1000, 0, 100)$ m, above the edge of the disk, and along the x-directed receiver line extending to offset of 8 km.

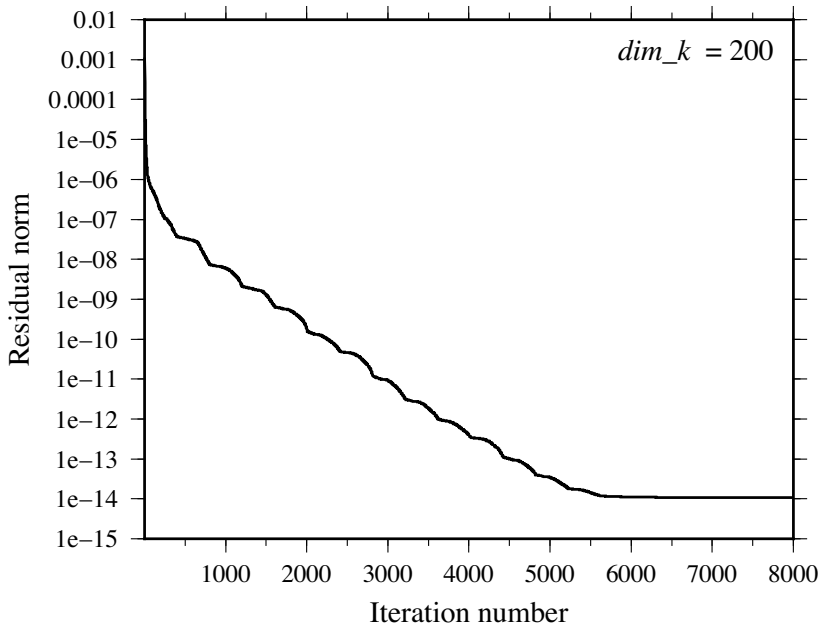

Figure 5.7. Residual norm versus number of iterations for the 2 km-diameter disk model. The dimension of the Krylov subspace (*dim_k*) for GMRES was set to 200. After approximately 6000 iterations, the iterative solution stabilized with a residual norm near 10^{-14}, which represents a decrease of 11 orders of magnitude from its initial value.

Table 5.1. Run information for the canonical disk model for different disk diameters, including total number of cells in the input mesh, iterative solver memory usage and run time, and total run time for CSEM3DFWD. The GMRES Krylov subspace dimension was set to 200 and the ILUT fill-in factor was set to 3 for all examples, with the exception of the 3 km-diameter disk model, which used a Krylov subspace dimension of 400.

Disk diameter (km)	**Total number of cells in mesh**	**GMRES memory usage (GB)**	**GMRES run time (h)**	**CSEM3DFWD total run time (h)**
1	453,660	7.2	1.2	2.3
2	507,872	7.7	1.7	3.0
3	656,189	12	2.8	4.9
4	458,859	7.2	1.2	2.3
5	488,547	7.5	1.3	2.5

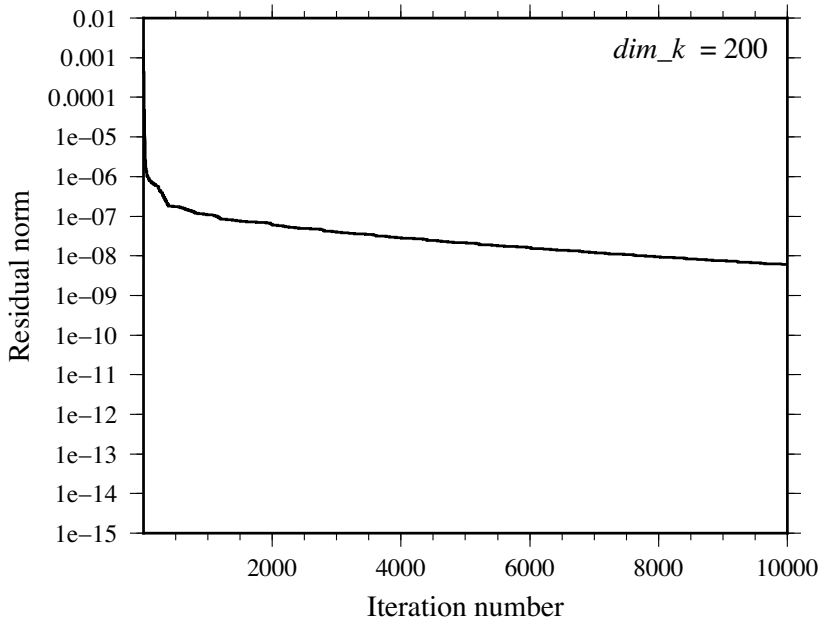

Figure 5.8. Residual norm versus number of iterations for the 3 km-diameter disk model, where the Krylov subspace dimension (*dim_k*) for GMRES was set to 200. Due to the larger problem size of the 3 km-diameter disk model, the solution did not converge in less than 10,000 iterations.

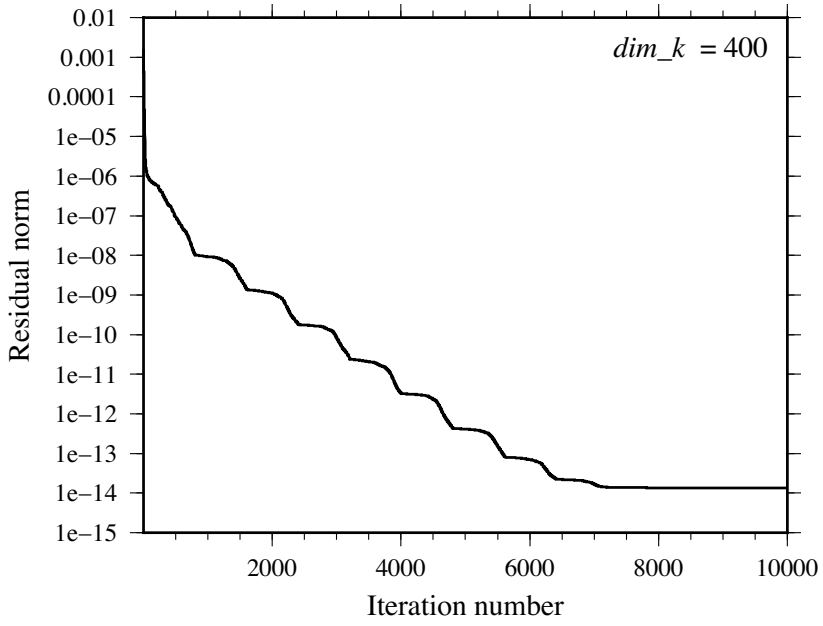

Figure 5.9. Residual norm versus number of iterations for the 3 km-diameter disk model, where the Krylov subspace dimension (*dim_k*) for GMRES was set to 400. The solution converged after approximately 8000 iterations.

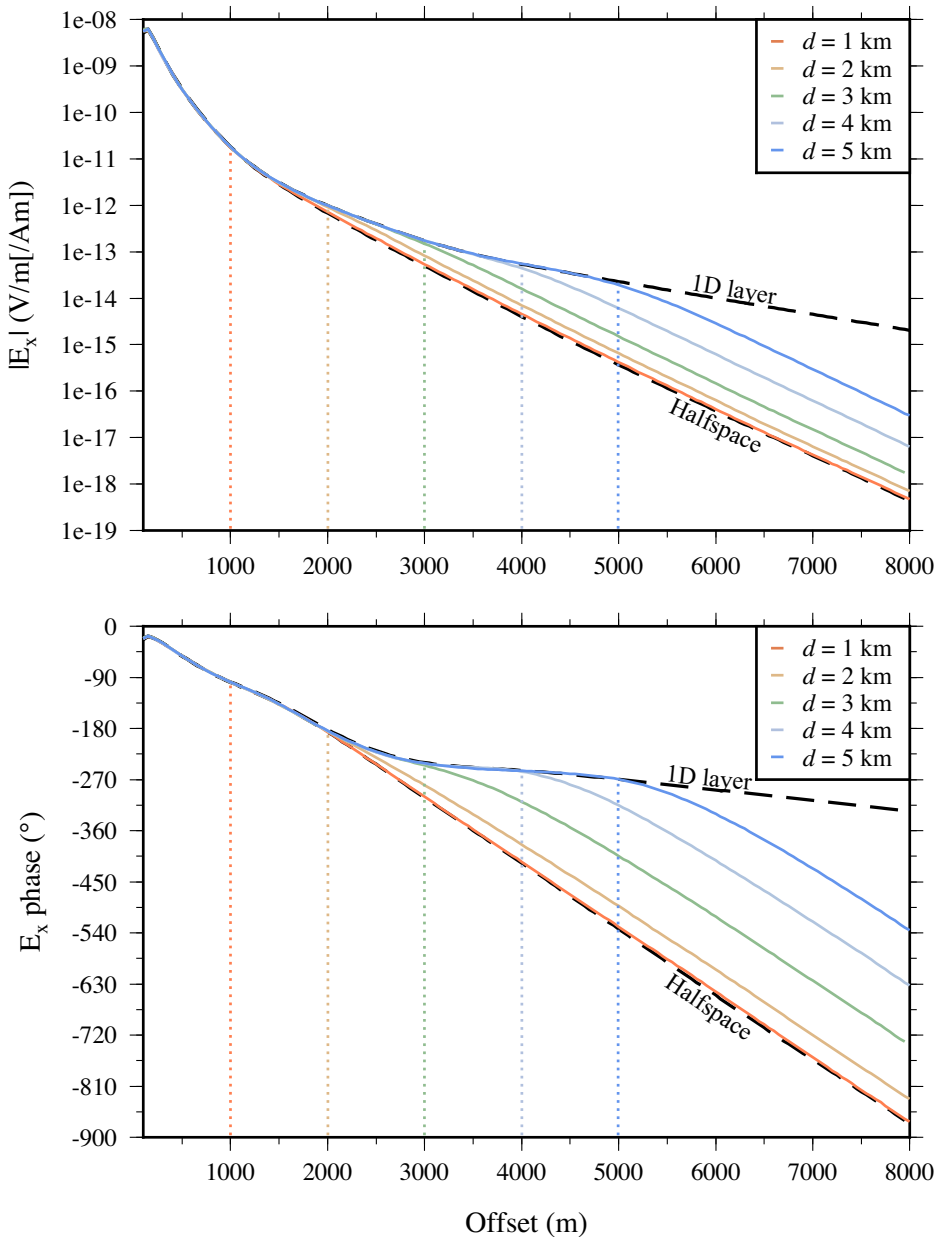

Figure 5.10. The inline horizontal electric field amplitude and phase for the canonical disk model for various disk diameters (d). The 1D Hankel transform solutions for the background marine halfspace model (i.e., no resistive layer present; lower dashed black line) and for the 1D analogue model featuring an infinite-lateral extent resistive layer of equivalent thickness and burial depth to the disk (upper dashed black line) are plotted for comparison.

layer present). The infinite-extent resistive layer is the 1D analogue to the 3D disk since the resistive layer has the same thickness and burial depth as the disk. The results demonstrate the edge effects of laterally finite layers on the CSEM response: for offsets less than the disk diameter, the 3D finite-element solution follows the 1D solution for an infinite-extent resistive layer, but for offsets greater than the disk diameter, the 3D solution falls below the 1D resistive layer solution and exhibits the same exponential decay rate as the halfspace solution. The 1 km-diameter disk is essentially invisible to the CSEM method with less than a 20% difference in amplitude relative to the homogeneous halfspace in its asymptotic limit. In this instance, 1D modelling provided a best case, upper estimate of the target response, but 3D modeling was required to properly account for the effects of finite target extent.

5.3 Seafloor topography model

Unstructured meshes are advantageous over rectilinear meshes in that they are able to accurately resolve surfaces with complex geometry without staircasing effects. To demonstrate the applicability of unstructured meshes and the finite-element method to modelling of realistic, complicated geometries, results are presented here for a seafloor topography model in which an irregular surface is introduced as the interface between a lower 1 S/m (1 ohm-m) sediment halfspace and an upper 3.3 S/m (0.3 ohm-m) sea halfspace.

The seafloor topography model presented here represents our first attempt to include irregular structural surfaces in a model. Irregular surfaces act as constraining features in the mesh tetrahedralization and therefore have the potential to interfere with generation of a quality mesh. In this instance, the challenge of generating a mesh of sufficient quality for iterative solution was further complicated by the requirement for refinement along an irregular surface; because of the irregularity of the seafloor, a different approach to receiver

refinement had to be taken instead of the usual approach for flat seafloor models, which was to insert rectilinear blocks in proximity to the seafloor.

The seafloor topography model was based on the 'mmal25pm' mesh available from the INRIA (Institut national de recherche en informatique et en automatique: French Institute for Research in Computer Science and Automation) Gamma Group 3D mesh research database (Figure 5.11). This mesh was previously incorporated in the seafloor topography model of Schwarzbach et al. (2011), for which a finite-element solution was presented; the aim in this study was to duplicate the results of Schwarzbach et al. (2011). The surface mesh has a regular, rectilinear node spacing of 25 m, and total dimensions of 4 km $\times$ 4 km. The nodal coordinates of the original mesh, as available from INRIA, were translated such that the center of the mesh corresponded to $(x,y,z) = (0,0,0)$ m. Transformation to relative coordinates facilitated manipulation of and reference to the mesh, and had also been done previously in Schwarzbach et al. (2011). An additional mesh, 'mmal200pm' (Figure 5.12), which represents the same topography as that of 'mmal25pm', but with a node spacing of 200 m instead of 25 m, was also used in the development of the final version of the seafloor topography mesh.

A 1 Am, 1 Hz, x-oriented HED source centered at $(x,y,z) = (0,0,100)$ m was simulated. The x- and y-directed receiver lines followed the topography of the seafloor, with a receiver spacing of 10 m and clearance of 0.0001 m. The receiver line was extended here to $|x| \leq$ 1 km, as compared to the shorter offset range of $|x| \leq 500$ m used in Schwarzbach et al. (2011), in the interest of having a greater range of offsets for comparison of the 3D finite-element seafloor topography solution to the 1D flat seafloor solution. Because a very high accuracy was desired for comparison to the solution of Schwarzbach et al. (2011), greater refinement was imposed in the vicinity of the source and along the near offset as compared to the degree of refinement that would typically be employed.

The seafloor topography model implemented a domain of $|x|, |y|, |z| \leq 2$ km to be com-

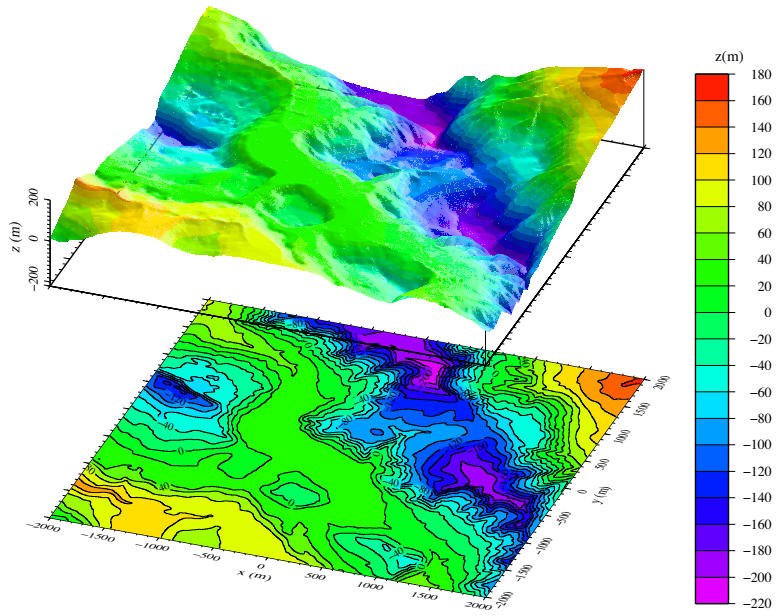

Figure 5.11. Seafloor topography mesh ‘mmal25pm’, available from the INRIA Gamma Group 3D mesh research database. The dimensions of the mesh are 4 km $\times$ 4 km, with a rectilinear node spacing of 25 m. The mesh coordinates have been translated such that the centre of the mesh corresponds to $(x, y, z) = (0, 0, 0)$ m. Topography z varies from -220 m to $+180$ m.

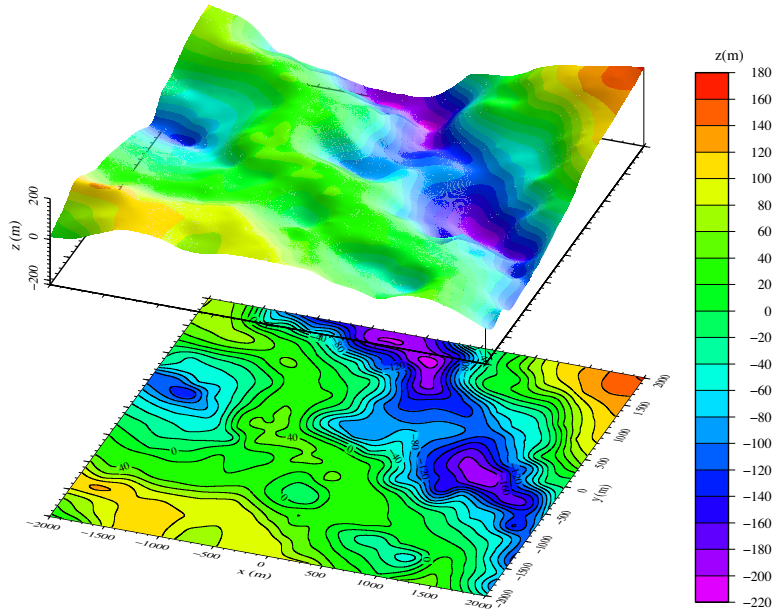

Figure 5.12. Seafloor topography mesh ‘mmal200pm’, available from the INRIA Gamma Group 3D mesh research database. The mesh contains the same topography as ‘mmal25pm’, but with a sampling, or node spacing, of 200 m.

parable to the domain dimensions of -2 km $\leq x, y \leq 2$ km, -1.5 km $\leq z \leq 2.5$ km used by Schwarzbach et al. (2011). Several iterations of the mesh design process were required before a mesh was obtained which was suitable for forward modelling. The first preliminary mesh used the original 'mmal25pm' seafloor node data, with node spacing of 25 m. Because this was a preliminary mesh trial, no attempt was made at the time to increase refinement along the receiver line. The resultant 3D mesh consisted of 494,126 cells, as compared to the 542,425 cells which composed the mesh of Schwarzbach et al. (2011), and is illustrated in Figure 5.13. The performance of the iterative solver for this mesh was poor, as demonstrated by the convergence curve in Figure 5.14. The system ill-conditioning may have been caused by the absence of grading to large cell size toward the boundaries of the mesh along the sea-sediment interface (see Figure 5.13), and/or by poor quality tetrahedra resulting from implementation of both a fine and regular node spacing, which would have constrained the tetrahedralization. A second mesh was constructed using the coarser 'mmal200pm' mesh, with the same domain boundaries. The resultant 3D mesh was very coarse, consisting of only 7,210 cells (Figure 5.15). While the residual norm of the iterative solution was rapidly reduced to a low value (Figure 5.16), the solution was not accurate due to the coarseness of the mesh.

The final mesh for the seafloor topography model was constructed using a hybrid mesh consisting of the 'mmal200pm' mesh as its base, with a 2200 m $\times$ 50 m rectangular section of the finer 'mmal25pm' mesh inserted and centred along the x-directed receiver line (Figure 5.17). This mesh provided a compromise between mesh quality and solution accuracy. To enforce refinement along the receiver line, the rectangular section of 'mmal25pm' was duplicated and translated -5 m in the z direction; the proximity of the two surfaces resulted in generation of cells on the order of (5 m)^3. The final mesh consisted of 32,757 nodes, 237,084 edges, and 203,809 cells. A similar mesh was constructed for a y-directed receiver line. For this model, the Krylov subspace dimension for GMRES was set to 200 and the

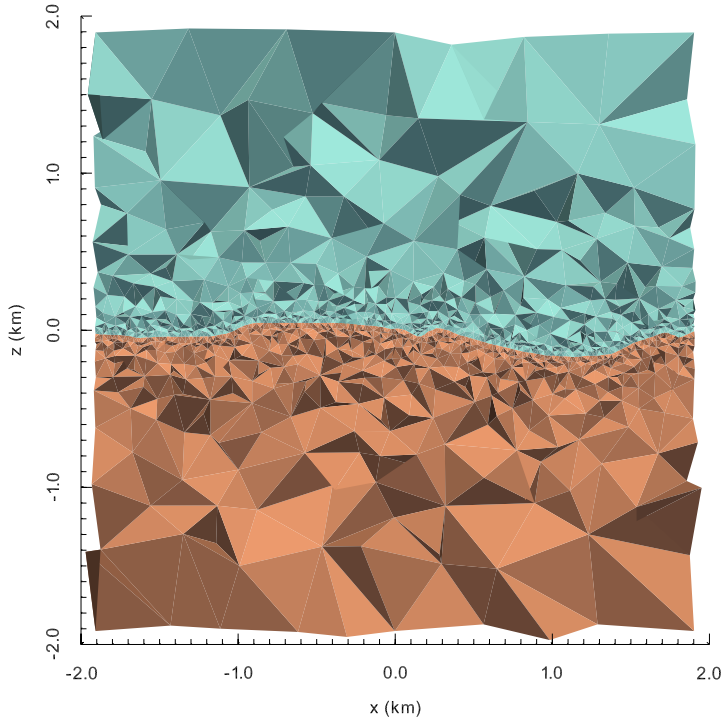

Figure 5.13. Preliminary mesh for the seafloor topography model that was based on the 'mmal25pm' node data. The model domain is $|x|, |y|, |z| \leq 2$ km. In this mesh, the seafloor surface node spacing was 25 m in both the x and y directions out to the boundaries of the domain.

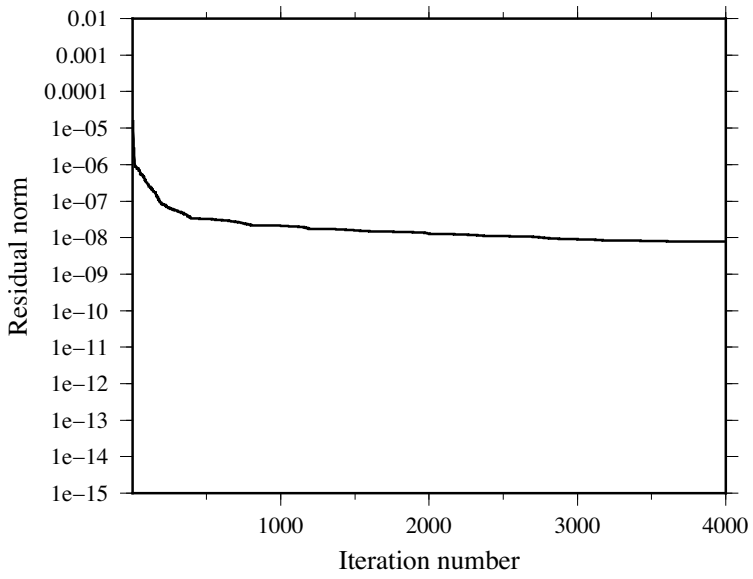

Figure 5.14. Residual norm versus number of iterations for the preliminary seafloor topography model whose mesh was based on the 'mmal25pm' node data (see Figure 5.13). The convergence behaviour of the iterative solution is poor, likely because of ill-conditioning due to inadequate cell grading and/or poor quality tetrahedra resulting from node constraints with fine (25 m) and regular spacing.

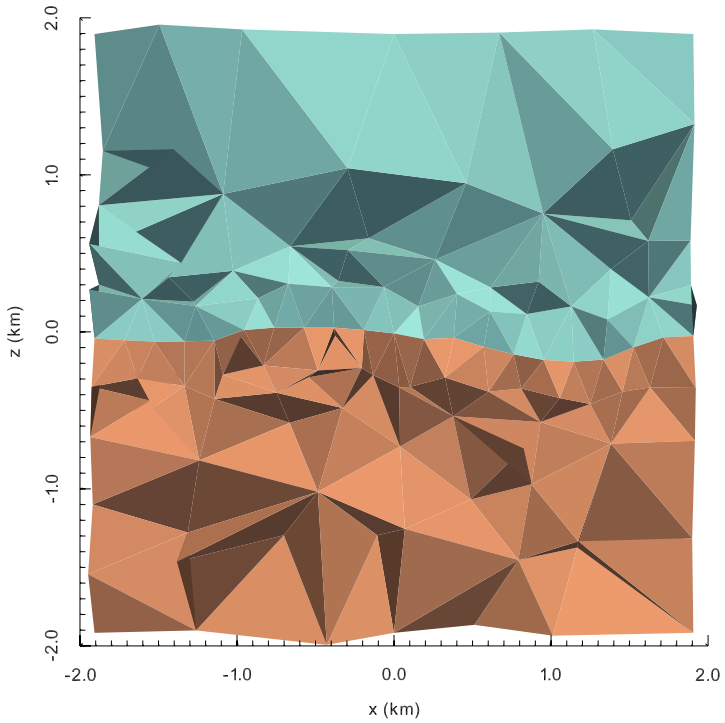

Figure 5.15. Preliminary unstructured mesh for the seafloor topography model which was based on the 'mmal200pm' node data. In this mesh, the seafloor surface node spacing was 200 m in both the x and y directions out to the boundaries of the domain.

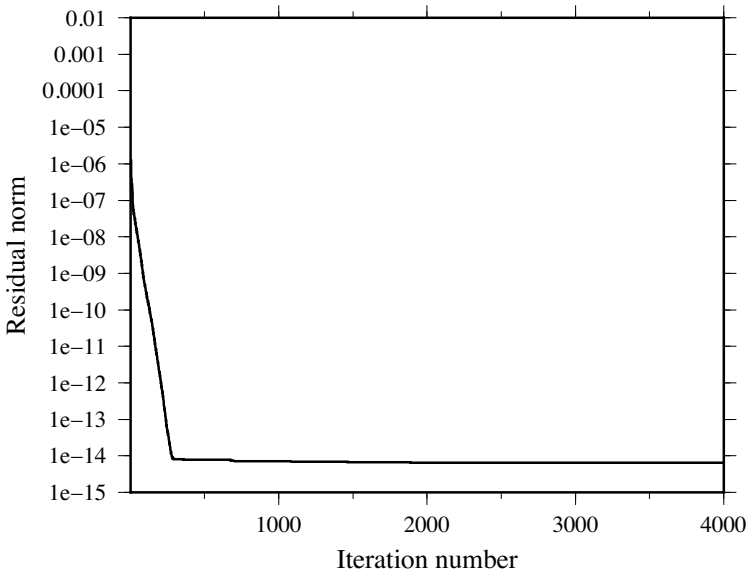

Figure 5.16. Residual norm versus number of iterations for the preliminary seafloor topography model whose mesh was based on the 'mmal200pm' node data (see Figure 5.15). While the residual norm was rapidly reduced, the solution was inaccurate due to the coarseness of the mesh.

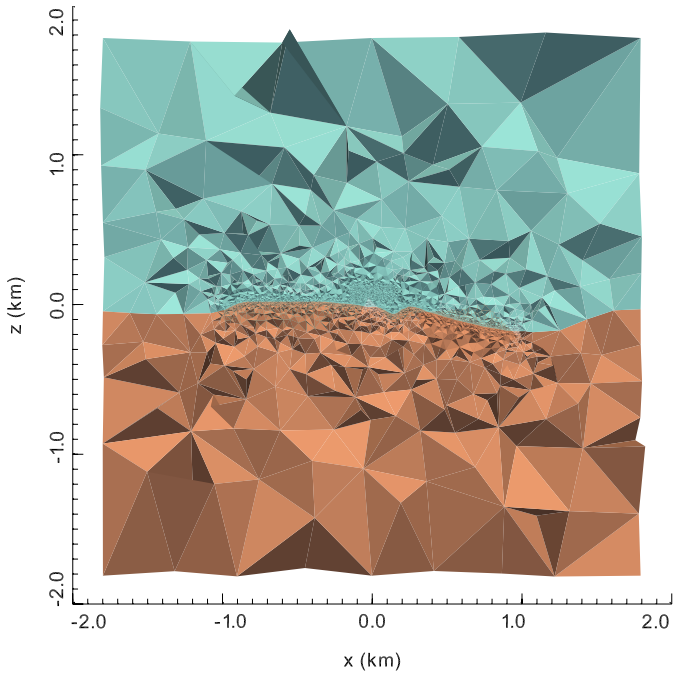

(a) *xz*-section of the final unstructured mesh for the seafloor topography model.

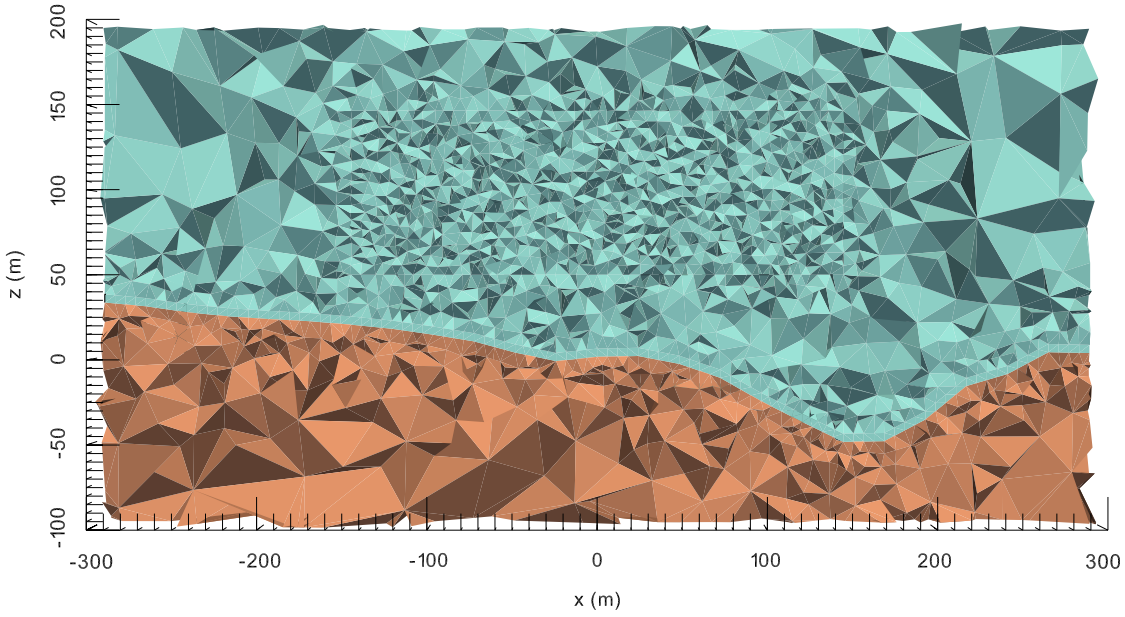

(b) Enlarged *xz*-section illustrating refinement at source and along near offset in detail.

Figure 5.17. *xz*-section of the final mesh for the seafloor topography model that uses the 'mmal200pm' mesh as its base with a 2200 m $\times$ 50 m rectangular section of 'mmal25pm' inserted and centred along the *x*-directed receiver line. This hybrid mesh provided a compromise between mesh quality and problem size.

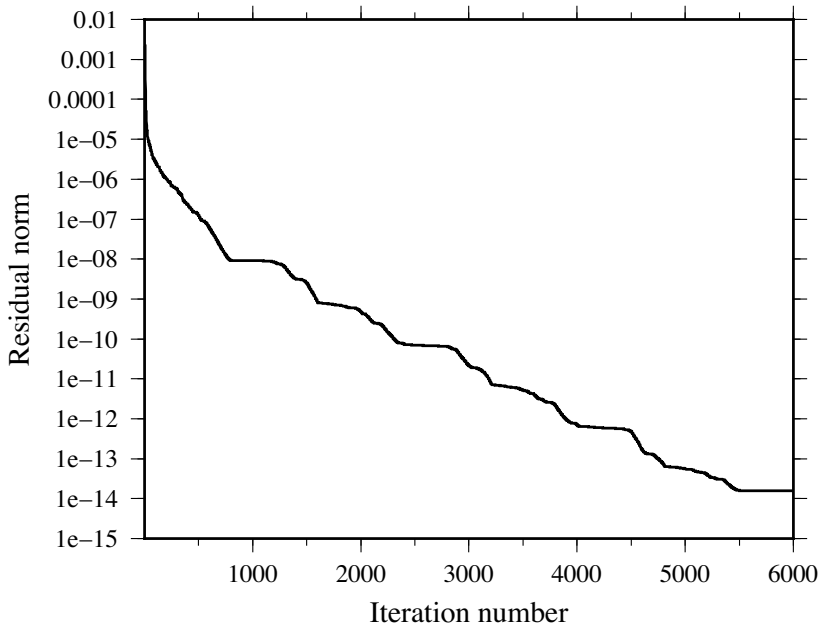

Figure 5.18. Residual norm versus number of iterations for the final seafloor topography model. The dimension of the Krylov subspace for GMRES was set to 200. A residual norm decrease of approximately 11 orders of magnitude was achieved after 6000 iterations.

ILUT fill-in factor was set to 3. The iterative solution required 5560 MB of memory and 1270 s ($\sim$ 21 min) computation time for 6000 iterations. A residual norm decrease of 11 orders of magnitude was achieved after approximately 6000 iterations (Figure 5.18).

Figure 5.19 illustrates the non-vanishing inline field amplitudes for the x-directed receiver line and Figure 5.20 illustrates the non-vanishing broadside field amplitudes for the y-directed receiver line. The finite-element solutions computed using CSEM3DFWD are in good agreement with those of Schwarzbach et al. (2011), which are also plotted in Figures 5.19 and 5.20. The 1D solutions for a flat seafloor model are also plotted in Figures 5.19 and 5.20 to illustrate how the seafloor topography solutions differ from the flat seafloor solutions. Results indicate that the CSEM response in presence of variable seafloor topography differs substantially from that observed in a flat seafloor environment due to significant lateral variations in resistivity at the surface. These results suggest that seafloor topography must be taken into account in modelling of real CSEM data to avoid misinterpretation.

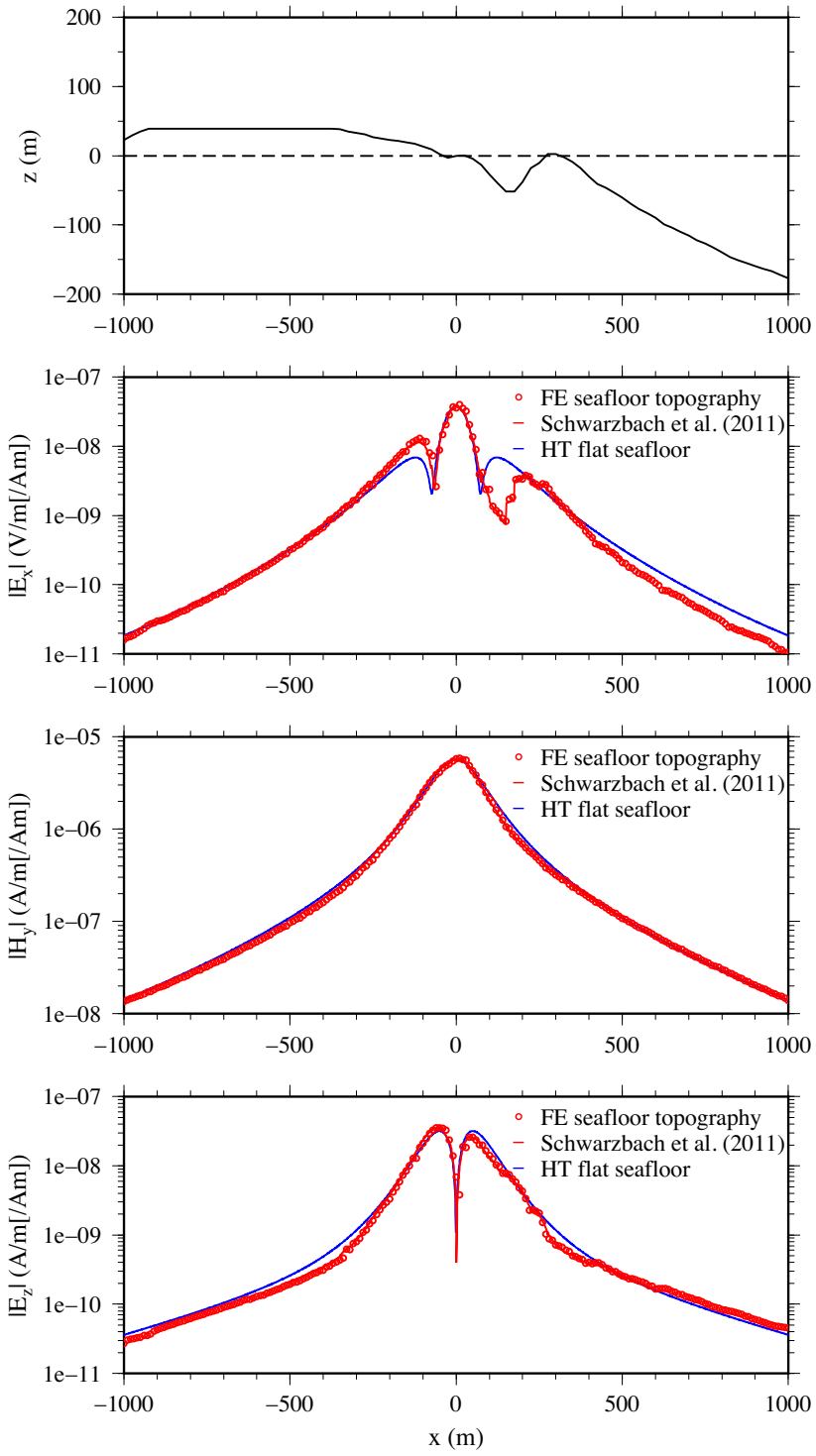

Figure 5.19. Inline field amplitudes for an x-profile of the seafloor topography model. The finite-element solution of Schwarzbach et al. (2011) (red line), which was computed for $|x| \leq 500$ m, as well as the 1D Hankel transform (HT) solution for a flat seafloor model (sea-sediment interface at $z = 0$; blue line), are plotted for comparison to the CSEM3DFWD finite-element (FE) solution (red circles).

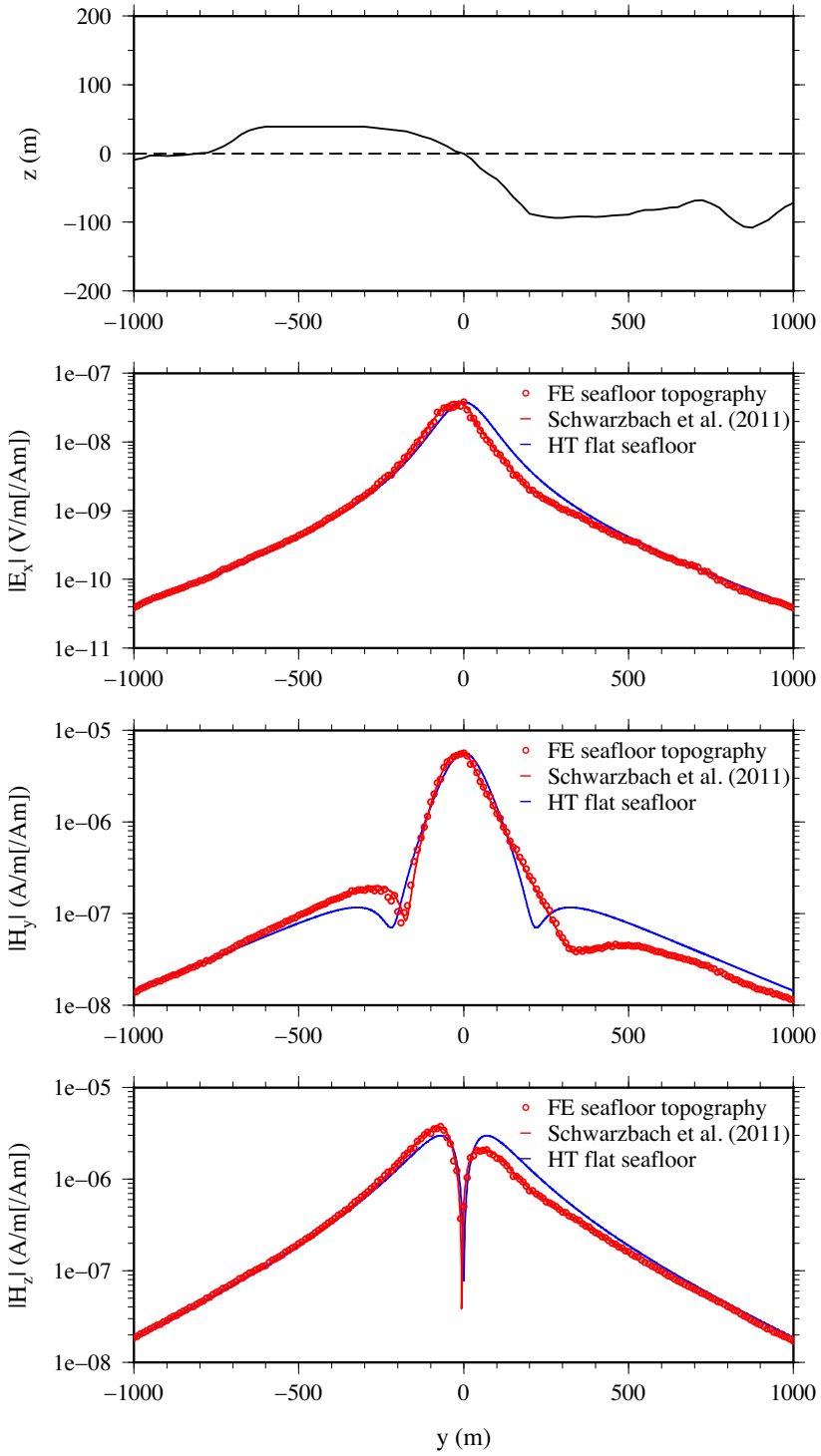

Figure 5.20. Broadside field amplitudes for a y-profile of the seafloor topography model. The finite-element solution of Schwarzbach et al. (2011) (red line), which was computed for $|y| \leq 500$ m, as well as the 1D Hankel transform (HT) solution for a flat seafloor model (sea-sediment interface at $z = 0$; blue line), are plotted for comparison to the CSEM3DFWD finite-element (FE) solution (red circles).

5.4 Marine halfspace model revisited: Finite water depth

To test the capability of the code in modelling an air layer, and to identify any difficulties therein, finite-element solutions for the electric and magnetic fields were computed for several simple models consisting of a lower 1.0 S/m (0.1 ohm-m) sediment halfspace, an overlying finite-thickness 3.3 S/m (0.3 ohm-m) sea layer, and an upper air halfspace, which was assigned a nominal conductivity of 10^{-8} S/m (10^{8} ohm-m). Water depths of 100 m and 500 m were modelled as examples of shallow and moderate water depths. The simulated source was a 1 Hz, 1 Am, x-directed HED located at $x, y, z = (0, 0, 50)$ m above the seafloor, and the simulated receiver line extended in the x-direction for $x \leq 5$ km with a receiver spacing of 50 m. Figure 5.21 illustrates the unstructured mesh for the finite-water depth model, which has total dimensions of $|x|, |y|, |z| \leq 12.5$ km and consists of 1,191,086 cells with volumes ranging from 0.0433 m^3 to 2.959 $\times 10^{10}$ m^3. Note that the lateral extent of the water layer was terminated at 6.5 km, well before the domain boundaries, to allow for grading to large cell size toward the boundaries of the domain; based on experience, this is required for acceptable iterative solver performance and convergence of the finite-element solution. With a Krylov subspace dimension of 600, the GMRES solver required approximately 23.5 GB for solution of the matrix system corresponding to this mesh.

Figure 5.22 illustrates the real and imaginary parts of the inline field components for a water depth of 100 m. The 3D finite-element solution for the horizontal electric field correlates well with the 1D solution, but the finite-element solutions for the horizontal magnetic and vertical electric fields deviate from the 1D solutions at far offset. Extension of the lateral boundaries of the sea layer to 9 km did not improve the accuracy of H_y or E_z at far offset, nor did extending the refinement 1.5 km beyond the end of the synthetic receiver line. Further, the accuracy of the solutions was not improved by assigning a conductivity corresponding to seawater to all cells with average z (calculated from node coordinates)

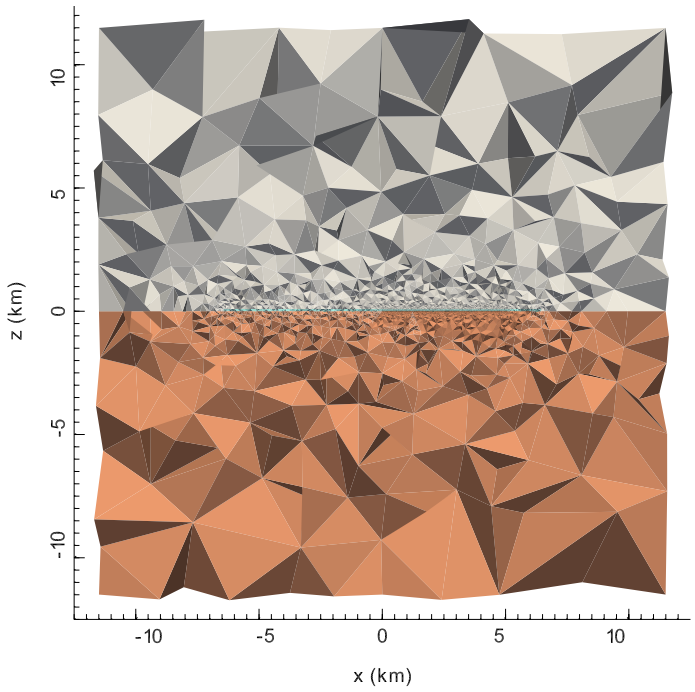

(a) *xz*-section of the full unstructured mesh for the 100 m-water depth model.

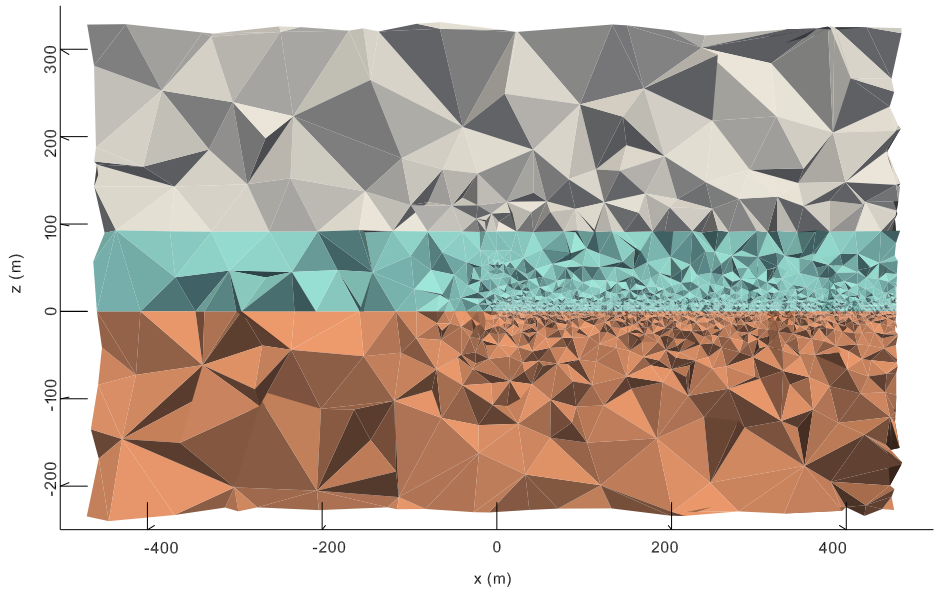

(b) Enlarged *xz*-section of the unstructured mesh exhibiting the refinement at source and receivers.

Figure 5.21. *xz*-section of the unstructured mesh for the marine halfspace model with finite water depth of 100 m, consisting of a 1 S/m (1 ohm-m) lower sediment halfspace, an overlying 100 m-thick 3.3 S/m (0.3 ohm-m) sea layer, and an upper air halfspace. The full domain is $|x|, |y|, |z| \leq 12.5$ km. Note the finite lateral extent of the sea layer, with $|x|, |y| \leq 6.5$ km. Refinement was manually enforced in the vicinity of the source, located at $(x, y, z) = (0, 0, 50)$ m, and along the receiver line, which extends to $x \leq 5$ km.

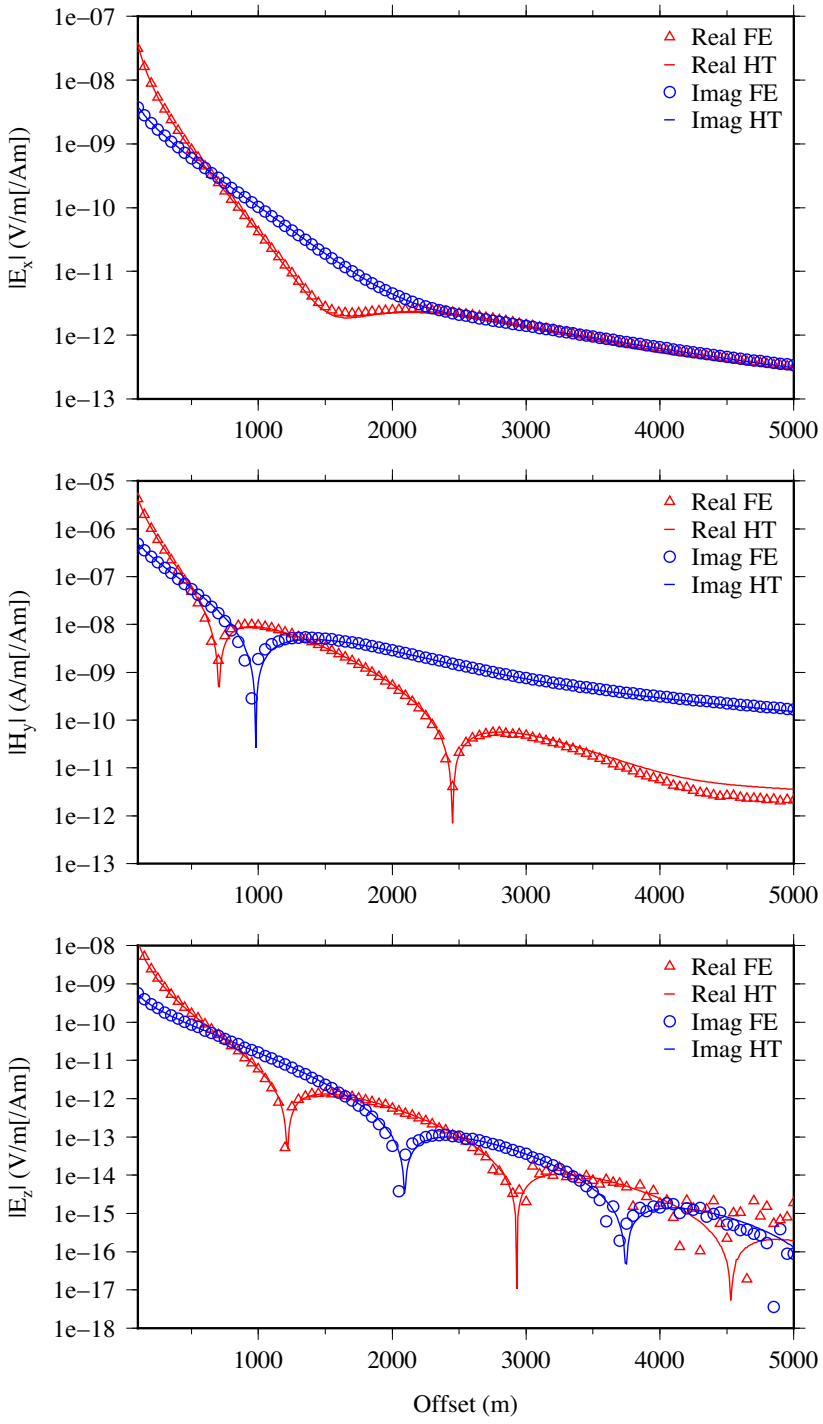

Figure 5.22. The real and imaginary parts for the non-vanishing inline field components E_x, H_y, and E_z for the marine halfspace model with finite water depth of 100 m. The 1D Hankel transform (HT) solutions are plotted alongside the 3D finite-element (FE) solutions to demonstrate the accuracy of the finite-element solutions. At far offset, the 3D finite-element solution for H_y deviates from its 1D counterpart. The finite-element solution for E_z is also inaccurate at far offset, but is much noisier.

within the depth range of the sea layer, i.e., σ = 3.3 S/m for all cells with ($0 < z_{av} < 100$) m, regardless of whether they were located within the bounds of the sea region. The motivation for trying this measure was to impose the electrical properties of the sea layer to cells within its depth range without imposing the regional boundaries that would prevent grading to large cell size toward the domain boundaries. Since none of these measures improved the accuracy of the finite-element solution for H_y and E_z at far offset, it appears that the solution inaccuracy is not related to the finite lateral extent of the sea layer.

Using the same lateral extent of 6.5 km for the sea layer, the finite-element solutions were computed for the same model but with a more moderate water depth of 500 m. The accuracy of the finite-element solutions for the horizontal magnetic and vertical electric fields at far offset was improved for increased water depth (Figure 5.23). For increased water depth, there is greater spatial separation between the high-contrast conductivity boundary of the air-sea interface and the lesser-contrast conductivity boundary of the sea-sediment interface. This suggests that the inaccuracy in H_y and E_z for a water depth of 100 m was related to the proximity of the air-sea interface to the observation or synthetic receiver locations near the sea-sediment interface (seafloor) for shallow water depth. It may then be that mesh refinement in the vicinity of the receivers was inadequate for proper modelling of the high conductivity contrasts. The vertical electric field component may have been particularly prone to discretization error since it is discontinuous across conductivity boundaries.

Of the three inline field components illustrated in Figure 5.22, the finite-element solution for the horizontal electric field is the smoothest and most accurate up to far offset. Figure 5.24 illustrates the inline horizontal electric field amplitude and phase for the marine halfspace model with finite water depth of 100 m. In Figure 5.24, two 1D solutions are plotted alongside the finite-element solution: the 1D solution computed using the MARDIP1D code described in Appendix A and employed throughout this thesis for 1D computations, and the 1D solution computed using the open-source DIPOLE1D

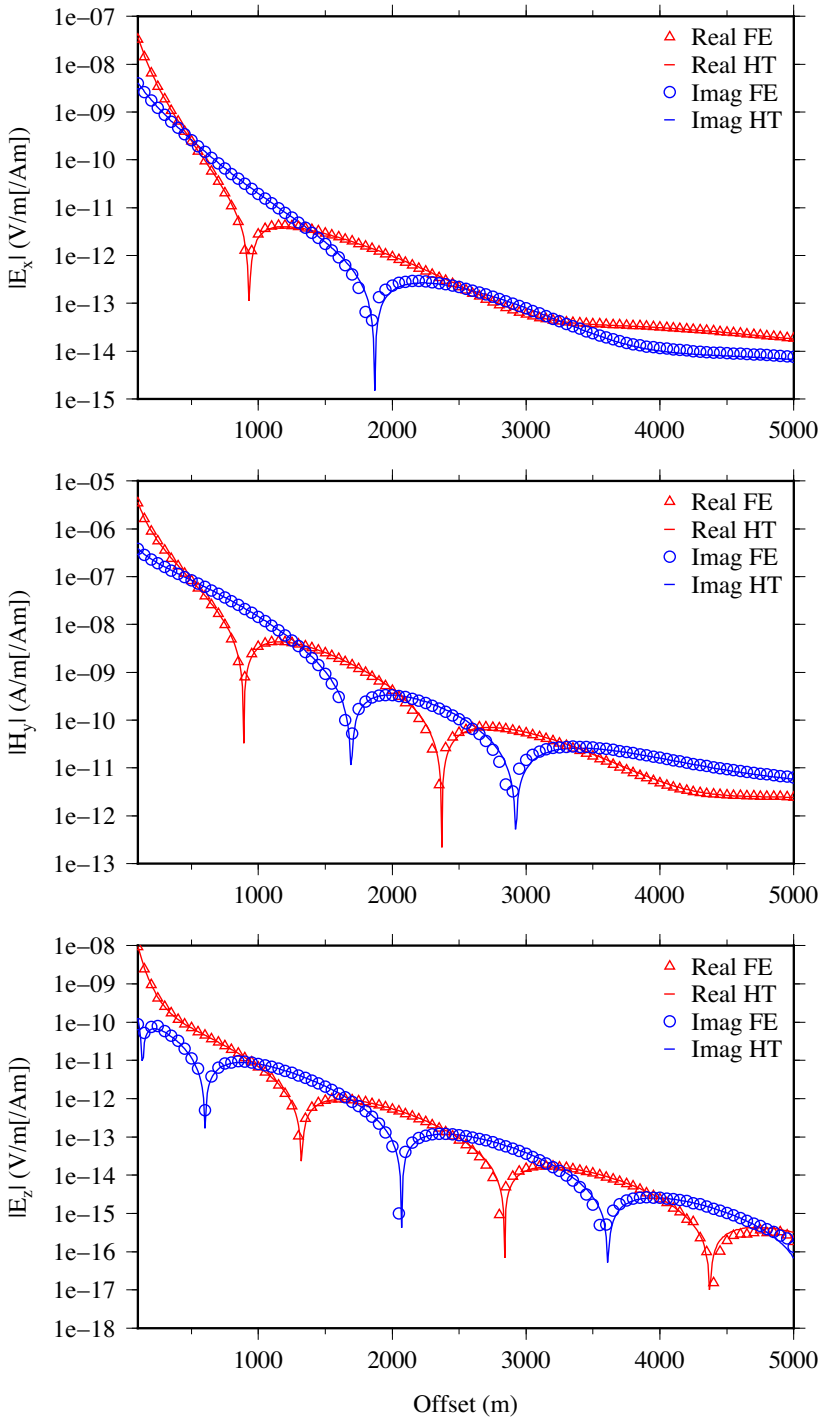

Figure 5.23. The real and imaginary parts for the non-vanishing inline field components E_x, H_y, and E_z for the marine halfspace model with finite water depth of 500 m. The 1D Hankel transform (HT) solutions are plotted alongside the 3D finite-element (FE) solutions to demonstrate the accuracy of the finite-element solution. Compared to those for a water depth of 100 m (Figure 5.22), the finite-element solutions for H_y and E_z are smoother and more accurate at far offset.

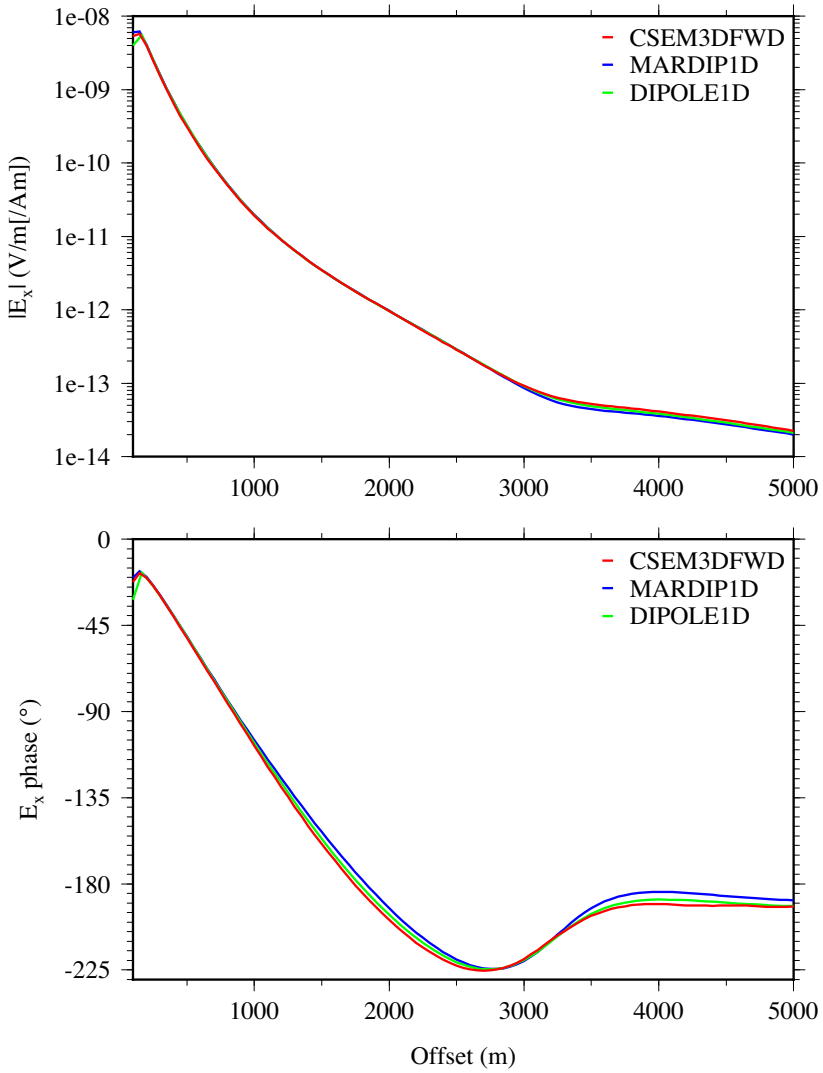

Figure 5.24. The inline horizontal electric field amplitude and phase for the marine halfspace model with water depth of 100 m. The 1D solutions computed using the MARDIP1D code described in Appendix A and the DIPOLE1D code of Key (2009) are illustrated alongside the 3D finite-element solution computed using CSEM3DFWD. There is some discrepancy between solutions in the far offset, particularly in phase, with the finite-element solution more closely matching the DIPOLE1D solution. The discrepancy between the two 1D solutions might be explained by different designs for the digital filter operator used in the numerical evaluation of the Hankel transform field expressions.

code of Key (2009), which is available online at `http://marineemlab.ucsd.edu/Projects/Occam/1DCSEM/`. It can be seen that there is some discrepancy at far offset between the finite-element solution and the 1D solutions, particularly in the phase, but that they generally agree well. Of the two 1D solutions, the finite-element solution more closely matches the DIPOLE1D solution. The discrepancy between the two 1D solutions, both of which are formulated in terms of Hankel transforms and evaluated using digital filter methods (e.g., Anderson, 1979), might be explained by different filter designs. The digital filter operators used for numerical evaluation of the Hankel transform integrals are characterized by the number, placement, spacing, and weighting of sampling points (Guptasarma and Singh, 1997). The fast Hankel transform routine of Anderson (1979) used to evaluate the Hankel transforms in the MARDIP1D code uses 283-fixed-point, fixed-spacing filters, while the DIPOLE1D code uses 201-point filters in which placement and spacing of the operator were chosen to optimize results (Key, 2009).

5.5 Summary

The CSEM3DFWD code has been demonstrated on and validated for several simple marine earth models. In general, the 3D finite-element solution agrees well with 1D semi-analytic solutions where available, with the exception of far offset fields for shallow water depths. For models with finite water depth, depending on the thickness of the water layer, greater mesh refinement than that employed in sea halfspace models may be required to reduce discretization errors arising in the vicinity of high conductivity contrasts, particularly at far offset where field amplitudes are attenuated. Unstructured tetrahedral meshes are demonstrated to conform well to curvilinear and irregular mesh boundaries, demonstrating the capability of unstructured meshes for accurate representation of realistic earth structure. In regards to mesh construction, cell size grading has been demonstrated to greatly influence

the conditioning of the system matrix and the convergence of the iterative solver; a transition from small cell size in the centre of the mesh to large cell size at its boundaries is ideal. This precludes extension of constraining boundaries or structure to the boundaries of the domain. For more complex models, constraining features which require high refinement for accurate geometric representation should be restricted to the inner mesh to allow for grading to larger cells at the outer boundary; in some instances, this may require artificial extension or padding of the model domain or employment of a coarser mesh discretization for structure located at a distance from the source-receiver line. For structure which varies arbitrarily in three dimensions, 3D modelling has been demonstrated to be necessary for accurate representation of the CSEM response, although 1D modelling may be accurate for tabular targets so long as source and receiver are located within the lateral extent of the target. In such instances, the off-target response exhibits an asymptotic slope characterized by the skin depth of the background. Significant seafloor topography has been illustrated to have a discernible effect on the CSEM response due to lateral variations in resistivity; it is therefore advisable that seafloor topography be properly resolved in models of marine environments where it is highly variable to account for its distortion of the CSEM response.

Chapter 6

Realistic reservoir model based on the North Amethyst oil field, Jeanne d'Arc Basin, offshore Newfoundland

6.1 Introduction

In this chapter, 1D and 3D modelling results are presented for a realistic earth model based on the North Amethyst oil field, located offshore Newfoundland. This model provided the opportunity to identify and attempt to address some of the challenges involved in modelling real-life earth structure with unstructured meshes, both in terms of accuracy in representation of structure and management of limited computational resources.

To provide context to the North Amethyst field, the tectonic evolution and stratigraphy of the region are briefly reviewed. 1D modelling results for 1D earth models based on well resistivity logs are subsequently presented; 1D modelling was performed as a precursor to 3D modelling to investigate how variations in electrical structure and survey parameters, specifically frequency and offset, affected the sensitivity of the marine CSEM method to

the target hydrocarbon reservoir. Finally, finite-element results are presented for 3D earth models where the reservoir structure was constructed from seismic horizon data. The 3D model represents the North Amethyst reservoir as a laterally finite resistive layer within a halfspace sediment background. A realistic model would ideally resolve background resistivity structure in detail since the CSEM response is a cumulative response to the entire earth volume, but this is infeasible given the region's structural complexity. Resolution of thin, structural layers such as shallow water, stratigraphic units, or fault-bounded hydrocarbon accumulations requires a large number of elements in the unstructured mesh and may lead to an ill-conditioned matrix system. Given the present unparallelized nature of the CSEM3DFWD modelling scheme, coupled with finite computational resources, the amount of structural detail that could be included in the model was limited.

6.2 Oil and gas exploration in offshore Newfoundland

The North Amethyst oil field is located approximately 350 km southeast of St. John's, Newfoundland and Labrador, in the prolific Jeanne d'Arc Basin. The Jeanne d'Arc Basin is part of a series of Mesozoic sedimentary basins located along Canada's east coast which are the focus of petroleum exploration and development activities due to the favourable association of hydrocarbon play elements: an organic-rich, oil-prone source rock, reservoir-quality sandstones, structural and/or stratigraphic traps, good migration pathways, and proper timing of hydrocarbon generation, migration, and trapping (McAlpine, 1990).

Figure 6.1 illustrates the Mesozoic and older basins located offshore Newfoundland, as well as offshore land tenure region and licence information based on the Canada Newfoundland & Labrador Offshore Petroleum Board's (C-NLOPB) scheduled land tenure system. Sectors, represented in purple in Figure 6.1, represent geographic areas nominated by industry that will become open to bidding in the next land tenure cycle (Call for Bids, Figure

6.1). Successful bidders are issued Exploration Licences, which may proceed to Significant Discovery Licences, and eventually Production Licences if the discovery is commercially viable. The Eastern Newfoundland region (Figure 6.1) is a region of particularly high industry activity, with both fine-grid 2D and massive 3D seismic and exploration drilling programs being planned for or having been executed in the deepwater Orphan and Flemish Pass basins (C-NLOPB, 2014). The Jeanne d'Arc region (Figures 6.1 and 6.2), which contains the shallow-water Jeanne d'Arc Basin, is characterized as mature because of its well-understood geology, a result of extensive drilling and geophysical programs, and the presence of multiple producing fields; exploration drilling and development activities continue in the region (C-NLOPB, 2014).

Industry activity in the northeast Grand Banks began in the 1960s with the acquisition of exploration permits by Pan American Petroleum (later Amoco, now part of BP) and Mobil Oil (now part of ExxonMobil). Initial drilling programs resulted in dry or uneconomic wells, and Amoco eventually allowed its lands to expire (Sinclair et al., 1992). After a period of no drilling and little seismic acquisition, several factors contributed to a rejuvenation of activity in the region. Firstly, under the 1977 amendments to the Canada Oil and Gas Land Regulations, renewal permits required at least one well to be drilled in each renewal permit land area over a four-year period, and secondly, Petro-Canada was allowed to acquire a 25% working interest in the lands (Sinclair et al., 1992). The first well drilled under the new regulations, Hibernia P-15, was spudded in May, 1979, by Chevron and its partners at the time and resulted in the discovery of Newfoundland and Labrador's first economic oil field, Hibernia (Sinclair et al., 1992).

Since then, over 400* exploration, delineation, and development wells have been drilled in the Newfoundland and Labrador offshore area. Twenty-four† significant discoveries have been made, and three major oil field areas are currently in production, all of which are

*417 total wells as of September 2, 2015, C-NLOPB.

†24 significant discovery areas as of January 26, 2015, C-NLOPB.

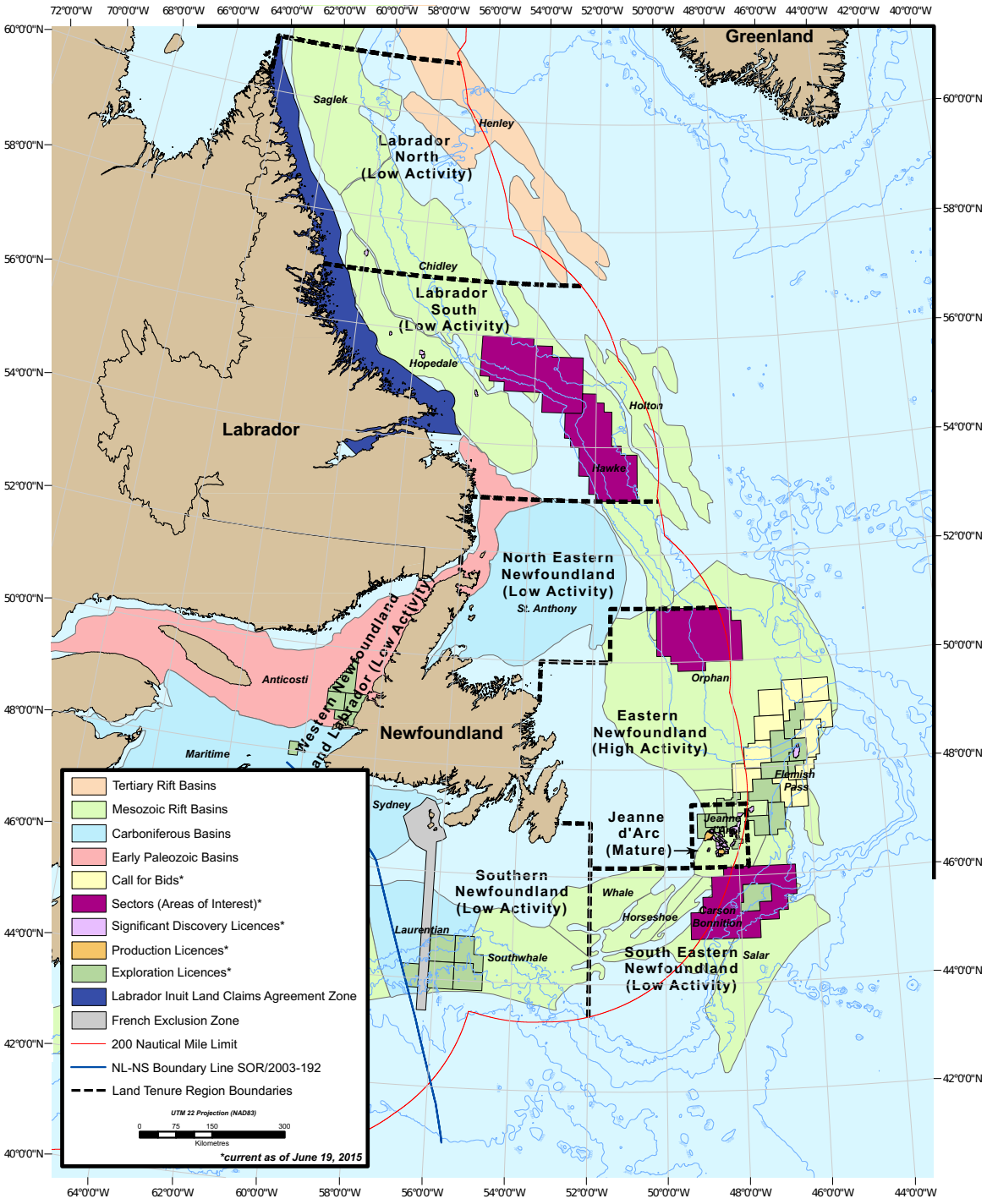

Figure 6.1. Newfoundland & Labrador offshore basins and licence information. The offshore area is divided into eight regions under the C-NLOPB's scheduled land tenure system. The North Amethyst field is located in the Jeanne d'Arc region. At present, all regions are classified as 'low activity' in terms of exploration and development with the exception of the Eastern Newfoundland region, which is classified as 'high activity', and the Jeanne d'Arc region, which is classified as 'mature'. Modified from C-NLOPB (2015b) and C-NLOPB (2015d).

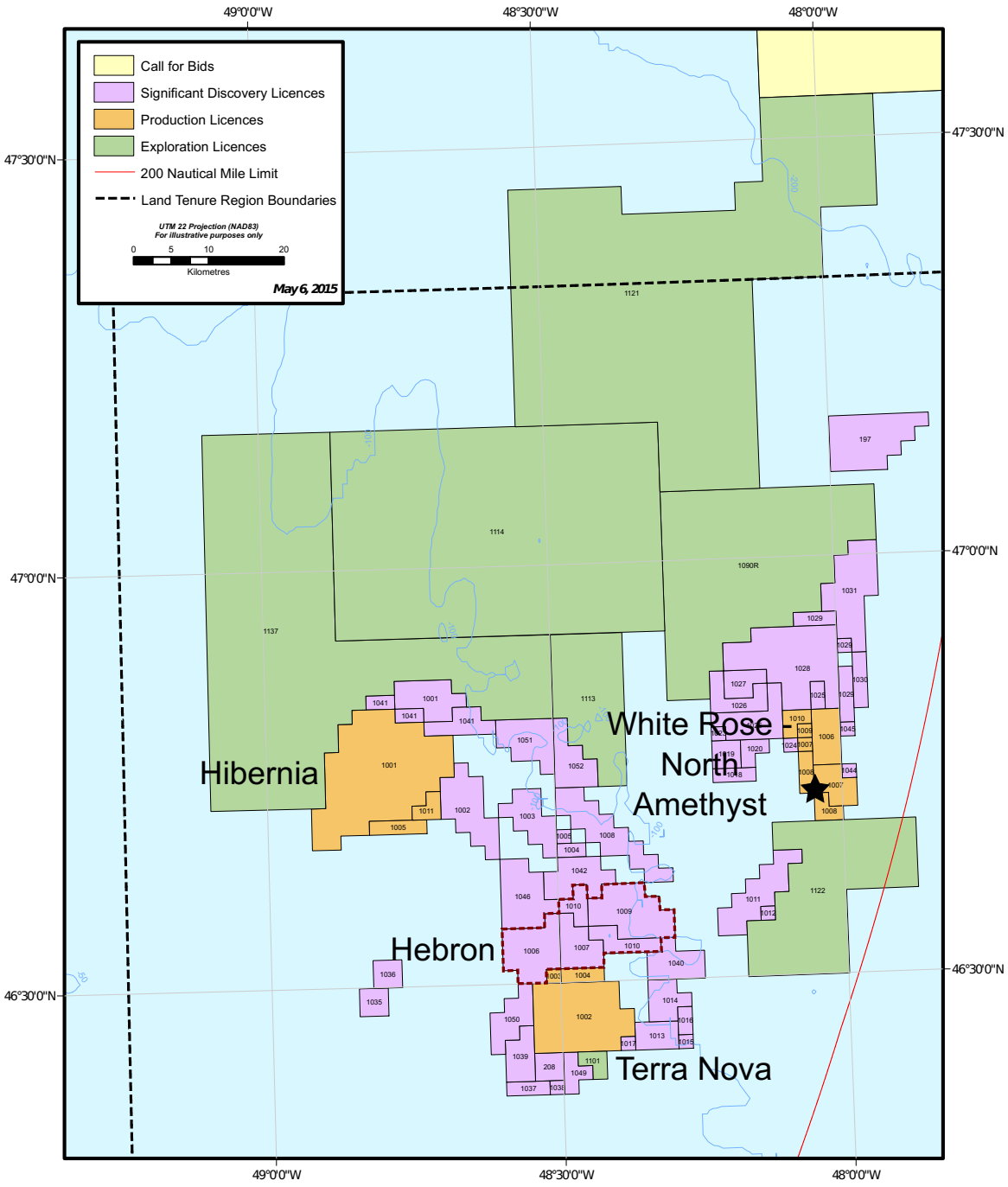

Figure 6.2. C-NLOPB licence information for the Jeanne d'Arc Basin. Production licences have been issued for the Hibernia, Terra Nova, and White Rose producing field areas. The approximate location of the North Amethyst Field is marked by the star. The Hebron asset contains three discovered fields and encompasses four Significant Discovery Licence areas (1006, 1007, 1009, 1010; dashed outline). Modified from C-NLOPB (2015a).

located in the Jeanne d'Arc Basin: Hibernia, Terra Nova, and White Rose, as well as its satellite expansion, North Amethyst (Figure 6.2). A fourth field, Hebron, which is also located in the Jeanne d'Arc Basin, is anticipated to produce its first oil by end of 2017 (Ayre, 2011). In total, these fields account for 3170 MMbbls (million barrels) of proven oil reserves, 1543 MMbbls of which have already been produced (C-NLOPB, 2015c). The North Amethyst field, the basis for this CSEM modelling study, is a relatively small field, with 75 MMbbls of proven reserves (C-NLOPB, 2015c).

6.3 Geological framework

6.3.1 Tectonic history of the continental margin of Newfoundland

The continental shelf of Newfoundland consists of a series of elongate, interconnecting Mesozoic sedimentary basins and troughs whose development was concomitant to the break-up of Pangea and opening of the present-day North Atlantic Ocean from Late Triassic to mid-Cretaceous (Sinclair et al., 1992). The basins are underlain by Late Proterozoic to Late Paleozoic basement of the northern Appalachian Orogen and are separated by elongate basement or sediment-covered ridges (McAlpine, 1990; Sinclair et al., 1992). The network of basins share a common evolutionary history as evidenced by the widespread occurrence of Late Triassic salt, mid and Late Jurassic carbonates, and Late Jurassic source rocks, although differences in structure and stratigraphy exist based on isolation in later stages of their evolution (Husky Oil Operations Limited, 2001; Enachescu, 2013). A major peneplanation surface known as the mid-Aptian or Avalon Unconformity, which formed during the second rift episode, truncates basin sedimentary strata and intervening basement highs (McAlpine, 1990; Sinclair et al., 1992). Overlying the mid-Aptian Unconformity are relatively undisturbed Upper Cretaceous and Tertiary strata (McAlpine, 1990).

Rifting associated with the opening on the Atlantic Ocean was accomplished in several

episodes, initiating south of the Grand Banks in the Late Triassic, propagating northward to east of the Grand Banks by mid-Cretaceous, and finally reaching the Labrador Sea by the end of the Cretaceous (Sinclair et al., 1992; Enachescu, 2013). Three main rift stages or phases can be identified to have affected the continental margin of Newfoundland: the Tethys phase (Late Triassic–Early Jurassic), the North Atlantic phase (Late Jurassic–Early Cretaceous) and the Iberia-Labrador phase (mid–Late Cretaceous; Husky Oil Operations Limited, 2001). The Grand Banks area was mainly affected by the Tethys and North Atlantic rifting episodes, with the Iberia-Labrador phase being more important for the northern Grand Banks and Labrador Sea basins (Enachescu, 2013). Crustal extension and salt tectonics resulted in generation of large anticlinal and structural-stratigraphic traps in which preserved Mesozoic sandstone reservoirs were able to become hydrocarbon-charged (Enachescu, 2013).

The Tethys phase was the most important rifting episode in determining the size and configuration of the present-day Grand Banks basins. The main northeast-southwest-trending basins were formed as half-grabens in the downthrow of a major crustal detachment (Husky Oil Operations Limited, 2001). Early basin syn-rift fill consisted of continental and lacustrine deposits. In the Early Jurassic, a major marine transgression inundated the failed-rift valley from the south, establishing a shallow marine environment from Early to Late Triassic in which marine evaporites and carbonates were deposited (McAlpine, 1990; Enachescu, 2013). Rifting stalled south of the Grand Banks in Early Jurassic. In the post-rift period, the epeiric basins deepened via thermal subsidence and developed significant accumulations of marine shales and carbonates (Enachescu, 2013). It was at the end of this period that the Late Jurassic (Kimmeridgian) Egret member was deposited, an organic-rich marine shale that would serve as the primary source rock for hydrocarbon pools in the Jeanne d'Arc Basin (Atkinson and Fagan, 2000).

Near the end of the Late Jurassic, rifting reinitiated to the east of the Grand Banks.

North-south-trending faults initiated separation of the Grand Banks from Iberia, formed new basins, and modified and enlarged previously formed basins (Atkinson and Fagan, 2000; Husky Oil Operations Limited, 2001). The intersecting northeast-southwest and north-south fault trends generated important fault-dependent traps throughout the Grand Banks basins (Enachescu, 2013). Rifting continued to advance northward, initiating separation of Labrador from Greenland in the Early Cretaceous. During this rift stage, the continental crust underlying the central Grand Banks was warped into a regional northwest-southeast-trending arch known as the Avalon Uplift (present-day south bank high) which extended from the Avalon Peninsula to the Newfoundland Ridge (McAlpine, 1990; Sinclair et al., 1992; Atkinson and Fagan, 2000). Coarse clastics that constitute some of the main hydrocarbon-bearing reservoirs, including the Jeanne d'Arc and Hibernia Formations, were deposited in marginal marine and fluvio-deltaic settings during this time (Atkinson and Fagan, 2000; Enachescu, 2013). Another episode of post-rift thermal subsidence followed, during which marine clastics and carbonates were deposited.

The Iberia-Labrador rifting phase initiated mid-Cretaceous and heavily influenced the development of the Orphan and Labrador Sea basins, although the Grand Banks were only weakly influenced by this episode (Enachescu, 2013). Northwest-southeast-trending faulting further fragmented the existing basins and intervening ridges, leading to new sources of sedimentation (Atkinson and Fagan, 2000; Husky Oil Operations Limited, 2001). The main reservoir rocks at the North Amethyst Field, including sandstones of the Ben Nevis/Avalon (BNA) Formation, were deposited during this rift episode. Sediments were derived from rift shoulders and uplifted intra-basinal ridges, with some evidence of sediment-recycling from earlier clastics (Enachescu, 2013). By Late Cretaceous, rifting and continental separation were complete, and lithospheric cooling led to subsidence of the entire margin as a relatively intact block which was later covered by Upper Cretaceous and Tertiary strata which have remained relatively undisturbed (Sinclair et al., 1992).

6.3.2 Stratigraphy of the Jeanne d'Arc Basin

The Jeanne d'Arc Basin is the deepest of the offshore Mesozoic basins, with an estimated stratal thickness of about 20 km at its depocentre, and contains the most complete stratigraphic record of the tectonic evolution of the Grand Banks area (McAlpine, 1990; Sinclair et al., 1992). The basin is situated completely within the continental plate and lies in relatively shallow water, with producing fields having water depths of approximately 90 to 130 m (Atkinson and Fagan, 2000; Enachescu, 2013). Other Mesozoic basins, such as the Orphan and Flemish Pass basins (Figure 6.1) extend from the continental margin to the continent-ocean boundary and are in comparatively deep water. For comparison, the Orphan Basin has variable water depth spanning from 200 to 4000 m, with the more prospective East Orphan Basin having water depths ranging from 1500 to 3500 m (Enachescu et al., 2004). The Flemish Pass Basin lies in intermediate to deep water with 500 to 1500 m depth, with most of the its large structural plays situated in water depths between 800 to 1200 m (Enachescu, 2014). These basins were restricted during early rifting but opened oceanward upon completion of continental separation (Enachescu, 2013).

Mesozoic and Cenozoic sedimentation and stratigraphy in the Jeanne d'Arc Basin was strongly controlled by regional tectonic events that occurred in relation to the opening of the North Atlantic Ocean and Labrador Sea, as described in the previous section (McAlpine, 1990). Major sedimentary sequences have been identified in the Jeanne d'Arc Basin which can be correlated to pre-rift (referred to as 'onset warp'; characterized by subsidence with little faulting), syn-rift, and post-rift deposition (Figure 6.3). During the Tethys rift phase (Late Triassic–Early Jurassic), syn-rift sedimentation within a northeast-trending graben commenced with deposition of Eurydice Formation red beds in the Triassic under arid continental conditions. This was followed by deposition of Argo Formation evaporites and carbonate-dominated Iroquois Formation in the Early Jurassic under restricted inner-

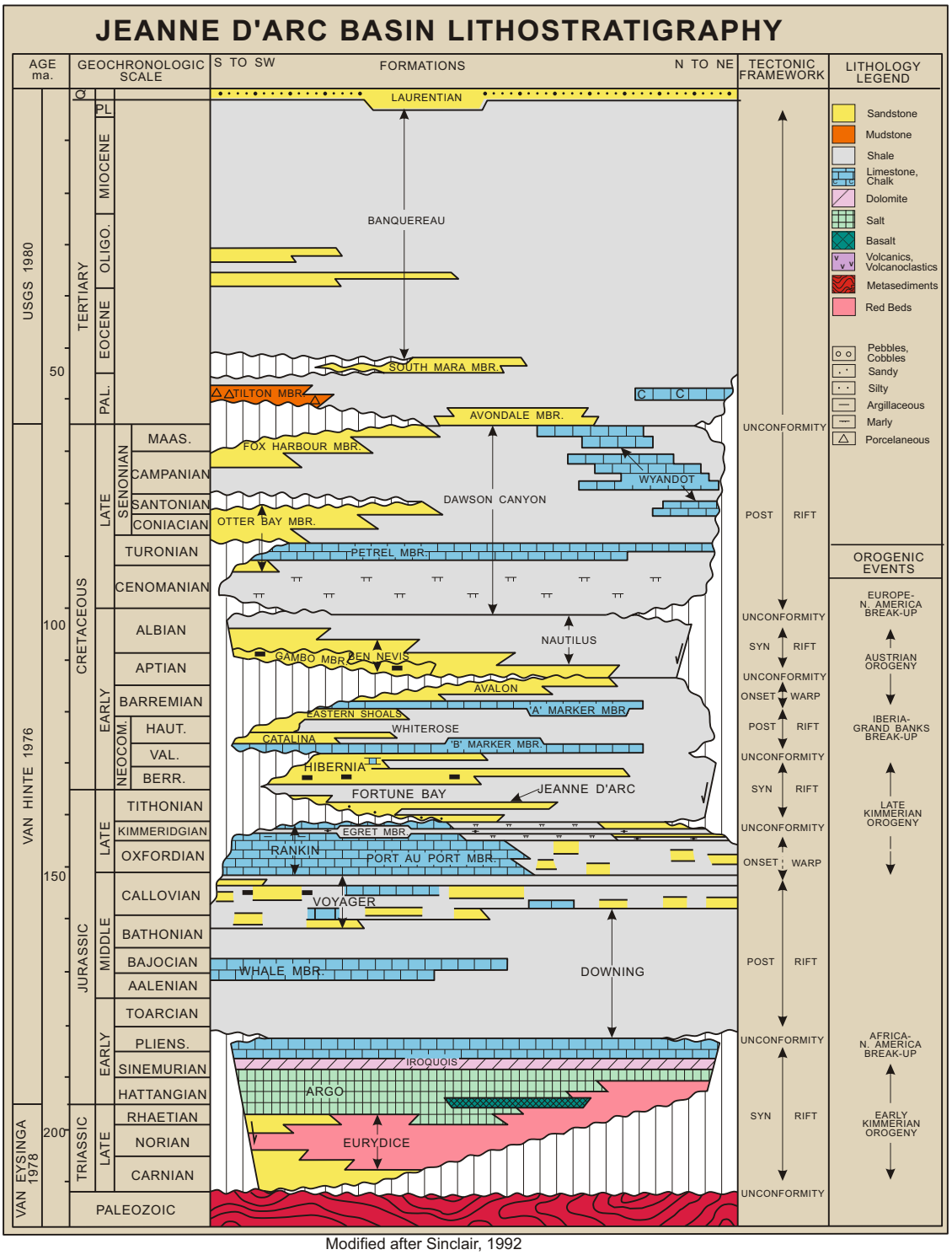

Modified after Sinclair, 1992

Figure 6.3. The lithostratigraphy of the Jeanne d'Arc Basin. Sedimentation was strongly controlled by regional tectonic events related to the opening of the present-day Atlantic Ocean and can be divided into pre-rift (onset warp), syn-rift, and post-rift depositional phases. From C-NLOPB (2015e).

shelf and shallow marine conditions which developed due to gradual marine transgression (McAlpine, 1990; Husky Oil Operations Limited, 2001). In the Middle Jurassic post-rift period, subsidence, progressive deepening, and transition to a more open marine shelf environment was associated with deposition of marine shales and carbonates of the Downing Formation (McAlpine, 1990; Husky Oil Operations Limited, 2001). Interbedded sandstones, shales, and limestones of the Voyager Formation prograde over upper Downing Formation and represent transition to a shallow or marginal marine-deltaic environment during a period of marine regression (McAlpine, 1990). Prior to renewed rifting in the Late Jurassic, interbedded limestones, shales, marlstones and minor sandstones of the Rankin Formation were deposited, including the organic-rich Egret Member which served as the primary source rock for hydrocarbon systems in the Jeanne d'Arc Basin. The fine-grained, laminated character of the Egret Member and its high organic content suggest a low-energy, restricted depositional environment, such as a deepwater anoxic basin (McAlpine, 1990). The upper boundary of the Rankin Formation is marked by the mid-Kimmeridgian (Late Jurassic) Unconformity associated with uplift and onset of the second phase of rifting in the Grand Banks.

Above the mid-Kimmeridgian Unconformity, syn-rift, sandstone-dominated fluvial, estuarine, and deltaic sediments of the Jeanne d'Arc and Hibernia formations were deposited in the south of the basin (McAlpine, 1990). The fluvial sandstones and conglomerates of the Jeanne d'Arc Formation graded basinward (northward) into the distal-equivalent shales of the Fortune Bay Formation (C-NLOPB, 2008). Braidplain and deltaic sandstones of the Hibernia Formation were deposited until Early Cretaceous, after which a period of post-rift subsidence and basin deepening prevailed in which the high seismic impedence 'A' and 'B' Marker limestones, the Catalina Formation marines sandstones, and the Whiterose Formation shales were deposited (C-NLOPB, 2008).

During the final rift phase, which commenced mid-Cretaceous, proximal fluvial and

shallow to deep estuarine sandstones of the BNA Formation and distal shales of the Nautilus Formation were deposited (C-NLOPB, 2008). BNA sandstones serve as the principal reservoir in the White Rose and North Amethyst oil fields. In the post-rift, passive margin period from Late Cretaceous through Tertiary, the basin experienced thermal subsidence and deepening during which fluvio-deltaic and open shelf clastics and minor limestones of the Dawson Canyon and Banquereau Formations were deposited.

6.3.3 The White Rose oil field and its satellite North Amethyst

The White Rose field area, discovered in 1984, is located on the eastern margin of the Jeanne d'Arc Basin, approximately 350 km east of St. John's, Newfoundland. The field area consists of a complex of rotated fault blocks within the hanging wall of the Voyager Fault Zone, which abuts the field to the east; the field is bounded to the north and west by the basinward-dipping flanks of the White Rose Diapir, and to the south by the uplifted Terrace block (Figure 6.4; Husky Oil Operations Limited, 2001). Northeast-southwest-, north-south-, and northwest-southeast-trending faults associated with different rifting episodes segment the field area. Figure 6.4 illustrates the time structure of the White Rose Complex. Because there is no single seismic marker that is continuous over the entire White Rose Complex, time structure mapping was done using a composite seismic marker constructed from the 'A' Marker in the west, the Base BNA seismic marker in the central area, and the mid-Kimmeridgian to Base Tertiary Unconformity seismic marker in the east (Husky Oil Operations Limited, 2001). The major structural elements of the field include structural highs associated with the White Rose Diapir in the north, the Amethyst Ridge in the south, and the rotated blocks adjacent to the Voyager Fault Zone, and structural lows associated with the Trave Syncline in the northeast and Grand Bruit Low in the southeast (Husky Oil Operations Limited, 2001). Structure was heavily influenced by salt movement during the third rifting episode, during which salt migrated into the White Rose Diapir and Amethyst

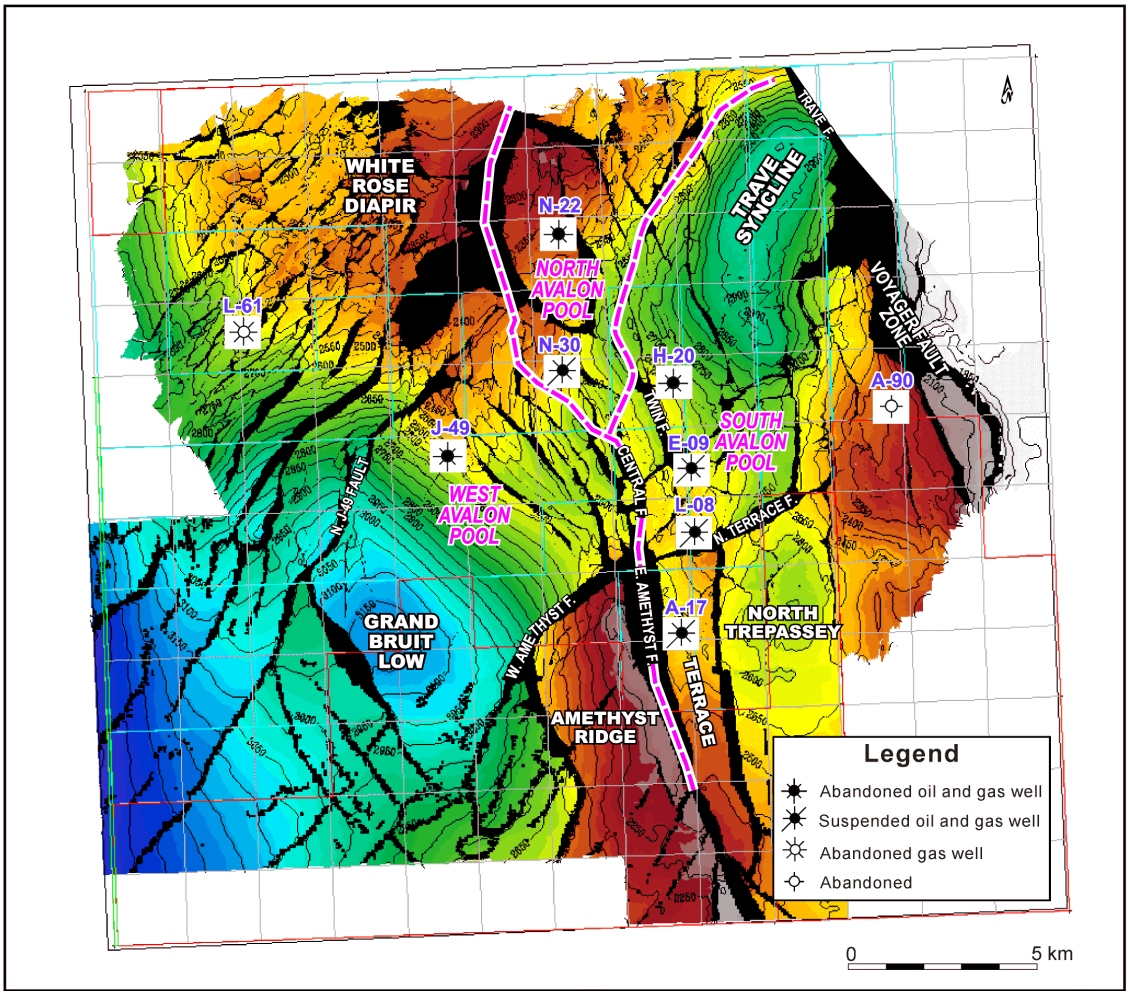

Figure 6.4. Regional composite marker time structure map of the White Rose Complex, where colour mapping reflects structural highs as red and structural lows as blue. The composite seismic marker is constructed from the 'A' Marker in the west, the Base BNA seismic marker in the central area, and the mid-Kimmeridgian to Base Tertiary Unconformity seismic marker in the east. The major structural elements of the field include highs (red/orange) associated with the White Rose Diapir in the north, the Amethyst Ridge in the south, and the rotated block directly adjacent to the Voyager Fault Zone, and lows (blue/green) associated with the Trave Syncline in the northeast and Grand Bruit Low in the southeast. From C-NLOPB (2001).

Ridge from the saddle area in between the two features, forming the Trave and Grand Bruit synclines (Husky Oil Operations Limited, 2001). Previous to this episode, the White Rose Diapir and salt-cored Amethyst Ridge formed a continuous salt-cored structural high to the west of the Voyager Fault Zone. The main hydrocarbon accumulations in the White Rose area are associated with structural traps generated by salt diapirism.

The North Amethyst field is located within the northwest-southeast-oriented Amethyst Ridge, a rotated fault block which is delineated by major faults to the north and east and borders the Terrace portion of the White Rose South Avalon pool (Figure 6.4). Oil and gas trapping is associated with the northwest-southeast-trending structural high near the eastern boundary fault of the ridge (Figure 6.5). The main reservoir interval is the westward-dipping BNA Formation, which consists of shallow-marine, fine-grained sandstones. The North Amethyst field and adjacent South Avalon Pool have similar reservoir thicknesses, but reservoir porosity and permeability are higher in the North Amethyst field because of its shallower burial depth and diagenetic history (Figure 6.6).

6.4 1D sensitivity analysis

1D modelling was performed for the North Amethyst field prior to 3D modelling in order to determine whether the CSEM method was likely to be sensitive to the BNA reservoir target, and if so, to estimate the optimal offset and frequency for generation of a CSEM anomalous response. Variations on a baseline 1D model were also used to study the effect of simplifications in stratigraphy and variations in water and reservoir burial depths on the CSEM response. The 1D marine HED code described in Appendix A was used to compute the 1D inline horizontal electric field solutions presented here. Because 1D modelling is computationally less demanding than 3D modelling, several variations of the baseline reservoir model could be analysed in a short period of time. There is no single approach to

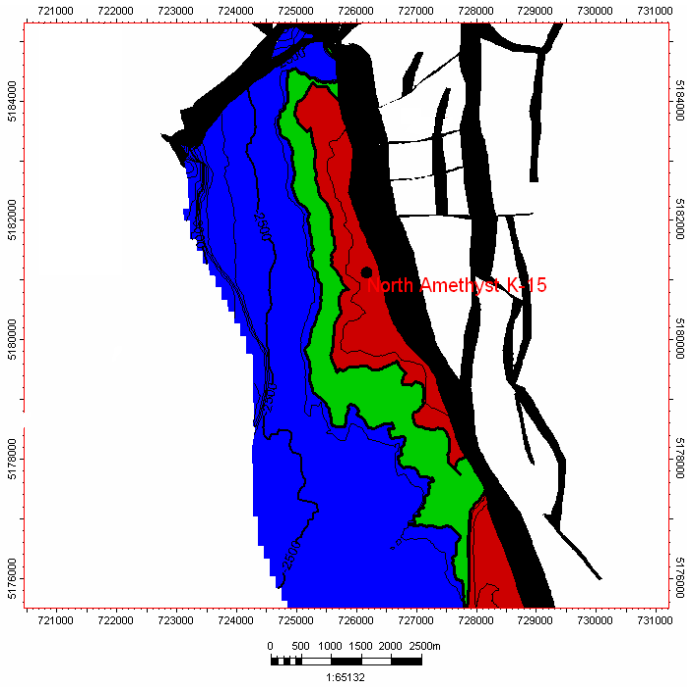

Figure 6.5. Map of the top reservoir surface for the BNA Formation, with fluid contacts as well as the location of well K-15 illustrated. Red, green, and blue represent gas-saturated, oil-saturated, and water-saturated reservoir, respectively. Heavy black lines indicate interpreted faults. Modified from C-NLOPB (2008).

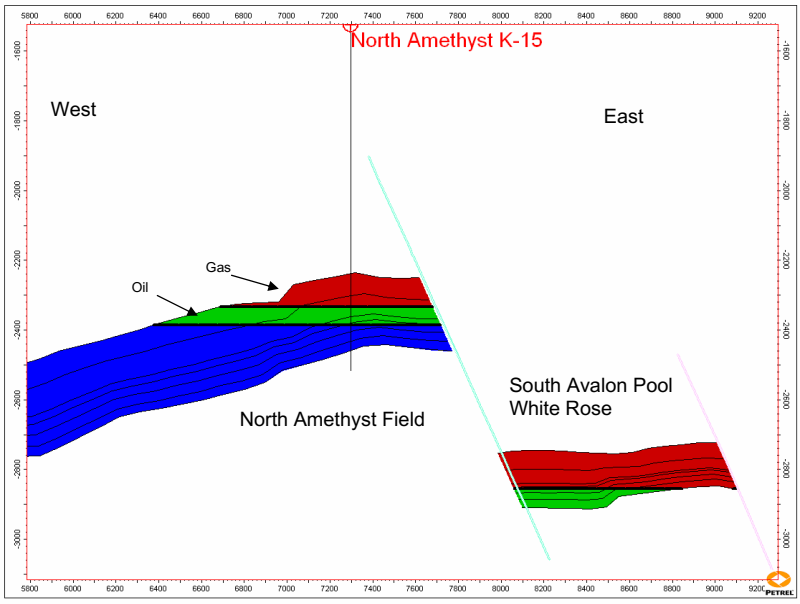

Figure 6.6. West to east structural cross-section through the BNA reservoir interval in the North Amethyst field and adjacent White Rose South Avalon Pool, with fluid contacts as well as the path of well K-15 illustrated. From C-NLOPB (2008).

simplification of 3D structure to one dimension for construction of a 1D earth model; in this study, the baseline 1D model was based primarily on a single well resistivity log exhibiting a strong anomalous response due to the presence of hydrocarbons within the BNA reservoir. Comparison of 1D results to 3D results in Section 6.5.3 emphasizes the limitations of 1D models in accurately representing 3D resistivity structure.

6.4.1 Resistivity model construction

The 1D models presented here were derived from analysis of resistivity logs for the North Amethyst exploration well K-15, and for the North Amethyst delineation wells E-17 and H-14, all of which were drilled in water depths of approximately 120 m (Figures 6.7 and 6.8). The stratigraphic top picks, i.e., stratigraphic boundaries inferred from well logs, illustrated in Figures 6.7 and 6.8 may be correlated to the lithostratigraphy of the Jeanne d'Arc Basin, previously illustrated in Figure 6.3. The principal BNA reservoir interval is marked at the top by the Ben Nevis Formation top pick, and at the base by the mid-Aptian Unconformity. The high resistivity signature of the BNA reservoir interval in well log K-15 is due to hydrocarbon-bearing reservoir.

The resistivity logs employed in this study consisted primarily of wireline induction measurements; the well log mnemonic AT/AHT90[‡] represents the deep-reading (i.e., large penetration depth) induction resistivity measurement made using Schlumberger's array induction imager tool (AIT). The mechanism of induction tools is based on generation of eddy currents within the formation via a coil transmitting in the kilohertz range and measurement of the resultant signal at a receiver coil. In an array induction tool, several arrays of mutually balanced coils are employed whose signals are combined post-acquisition to produce responses of variable reading depth and vertical resolution. Additional resistivity logs consisted of logging-while-drilling (LWD) propagation measurements; the well log

[‡]AT/AHT90 = array induction resistivity with 2 ft. vertical resolution, 90 in. depth of penetration

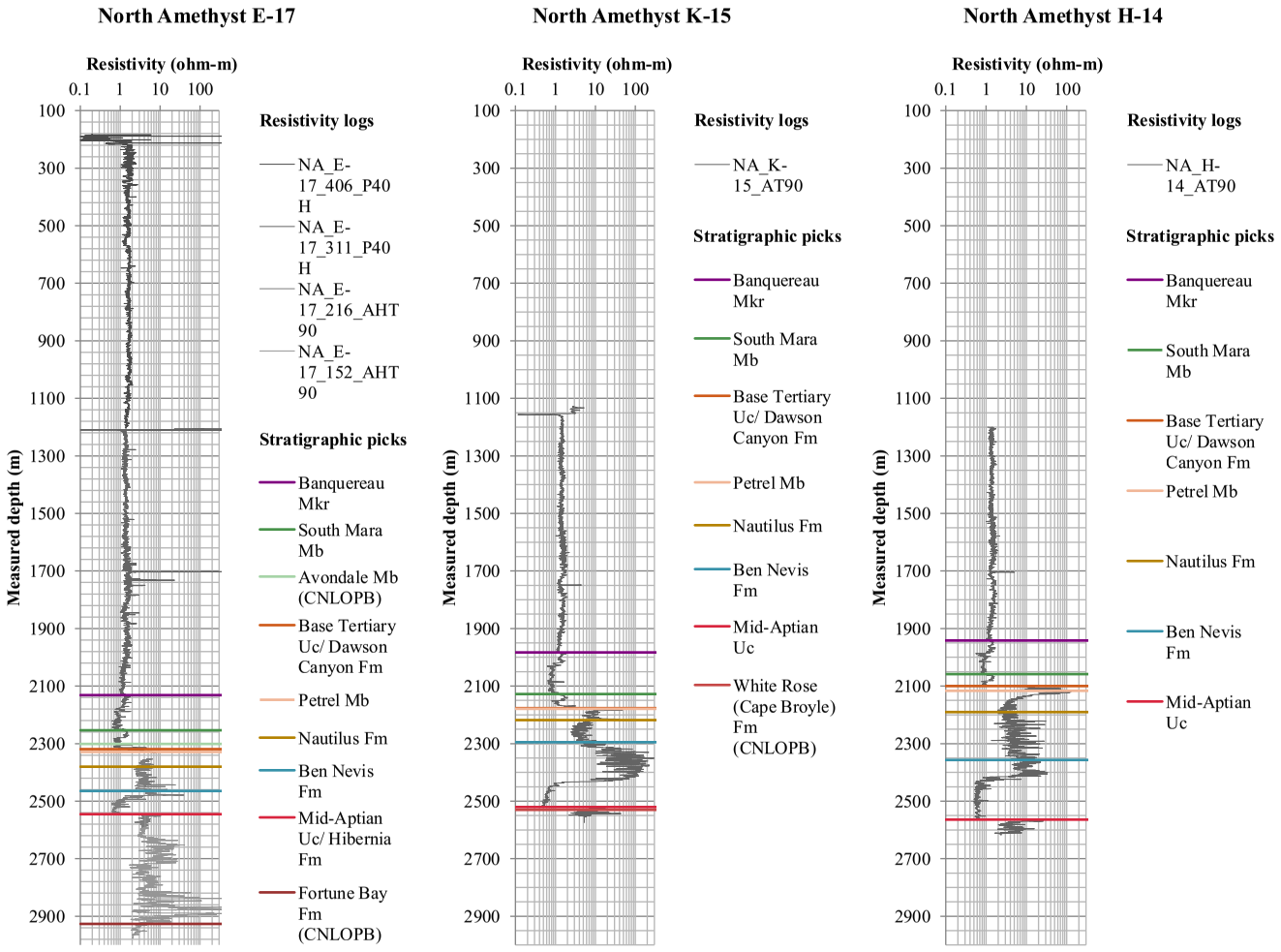

Figure 6.7. Complete resistivity logs for North Amethyst wells E-17, K-15, and H-14, with overlain stratigraphic top picks (sourced from the C-NLOPB's Schedule of Wells, where indicated); these may be correlated to the Jeanne d'Arc Basin lithostratigraphy illustrated in Figure 6.3. Depth is plotted in measured depth (m), that is, the depth measured along the borehole or well path. The BNA reservoir interval is marked at the top by the Ben Nevis Formation top pick, and at the base by the mid-Aptian Unconformity. Abbreviations: Mkr = Marker; Mb = Member; Fm = Formation; Uc = Unconformity.

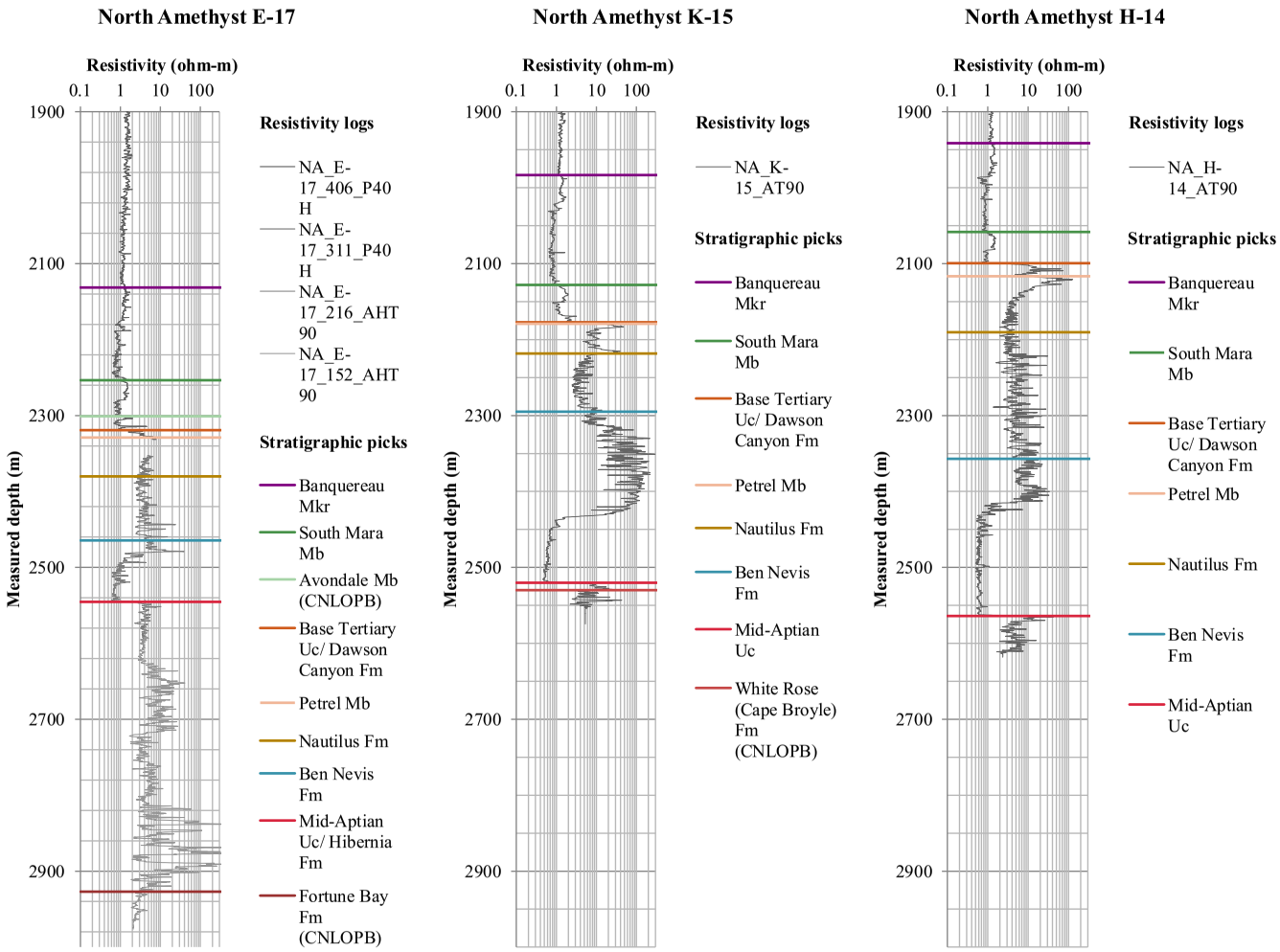

Figure 6.8. Enlarged sections of the resistivity logs for North Amethyst wells K-15, E-17, and H-14, illustrating the pre-Tertiary stratigraphy of interest, including the reservoir-bearing BNA and Hibernia Formations. The high resistivity signature of the BNA reservoir interval in well log K-15 is an indication of hydrocarbon-bearing reservoir. Abbreviations: Mkr = Marker; Mb = Member; Fm = Formation; Uc = Unconformity.

mnemonic P40H[§] represents the deep-reading propagation resistivity measurement made using Schlumberger's array resistivity compensated (ARC) tool. LWD tools employ a transmitter-receiver coil array where differences in measured phase (phase shift) and amplitude (attenuation) between two receivers are converted into two independent measurements of apparent resistivity.

To produce simplified models, the resistivity logs were visually sectioned into blocks based on perceived low-frequency resistivity variations. Each block, typically corresponding to a major formation, was assigned a single resistivity value based on visual estimate of the mid-range resistivity for the interval, excluding geologically insignificant outliers or spikes. This log-blocking procedure, while admittedly subjective, was judged adequate for the purpose of constructing a 1D model, which inherently requires a certain degree of approximation in earth structure. The corresponding stratigraphic units were identified using previously picked formation tops (see Figures 6.7 and 6.8).

The resistivity log of exploration well K-15 was ultimately chosen as the basis for the 1D North Amethyst model since it exhibits the strongest high-resistivity signature associated with hydrocarbon-saturated BNA reservoir, which has a baseline resistivity of approximately 75 ohm-m (see Figure 6.8). This choice models the hydrocarbon-bearing reservoir interval at a thickness of about 120 m and at a burial depth of about -2270 m true vertical depth subsea (TVDss). The true thickness of hydrocarbon-bearing BNA Formation is structurally controlled in the North Amethyst field and varies laterally from a minimum of 0 m to a maximum of 160 m, with an average thickness of 50–60 m[¶] where present. Maximum reservoir thickness occurs at the minimum reservoir burial depth of -2226 m TVDss. The 1D solution presented here thus approaches the best-case, upper estimate of the possible 3D response, which would result from simplication of the hydrocarbon-bearing reservoir

[§]P40H = phase shift resistivity at 2 MHz, 40-in. transmitter-receiver spacing

[¶]Estimated by taking the difference in depth between the triangulated top reservoir surface for the 3D model (Section 6.5.1), which has a near-regular node spacing of about 76 m, and the oil-water contact at -2386 m TVDss.

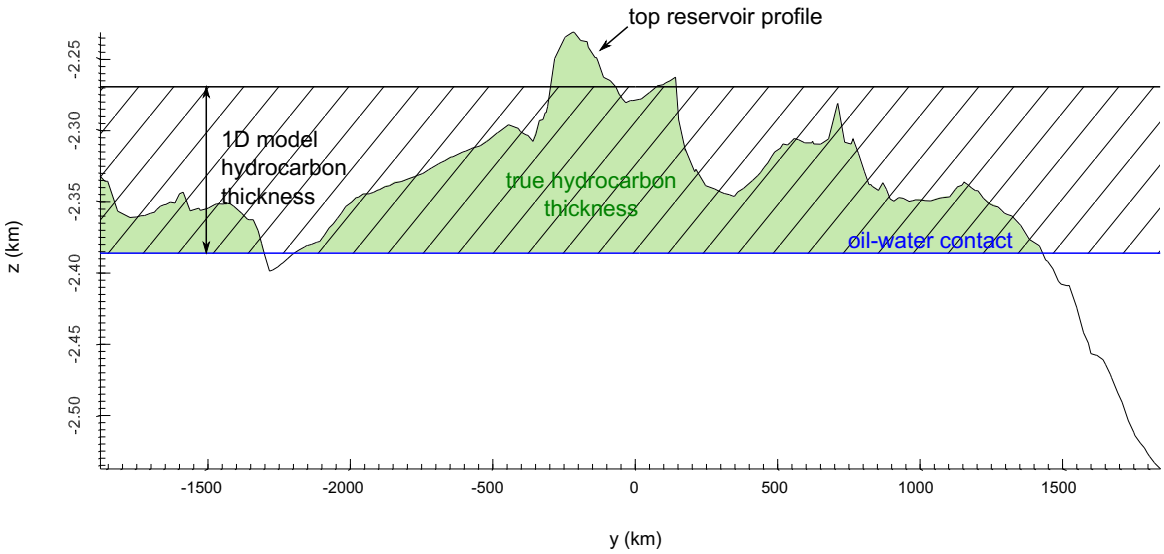

Figure 6.9. North-south cross-section through the eastern structural high of the Amethyst Ridge, illustrating the difference between the true, variable hydrocarbon thickness (green) and the constant, 1D-modelled hydrocarbon thickness (hatching) for the BNA reservoir. y corresponds to the north-south direction and z corresponds to true vertical depth subsea. The profile of the BNA reservoir top is outlined in black, and the oil-water contact is indicated in blue.

interval to maximum thickness and minimum burial depth. Figure 6.9 illustrates the difference between the true, variable hydrocarbon thickness and the constant, 1D-modelled hydrocarbon thickness in a north-south cross-section through the eastern structural high of the North Amethyst Ridge.

The baseline 1D model featuring the BNA reservoir is presented in Figure 6.10 and summarized in Table 6.1. Although the BNA reservoir contains both gas and oil, the gas-oil contact at -2334 m TVDss is only weakly manifest in the resistivity log (Figure 6.10), and so the gas- and oil-bearing zones were modelled as a combined hydrocarbon-bearing zone. The oil-water contact is easily identified as the abrupt transition from a baseline resistivity of approximately 75 ohm-m, associated with hydrocarbon-saturated BNA reservoir, to a baseline resistivity of approximately 0.7 ohm-m, associated with water-saturated BNA reservoir, at -2386 m TVDss (Figure 6.10). For 1D modelling, the oil-water contact was rounded to -2390 m TVDss for simplification. A sea layer was included in the 1D model

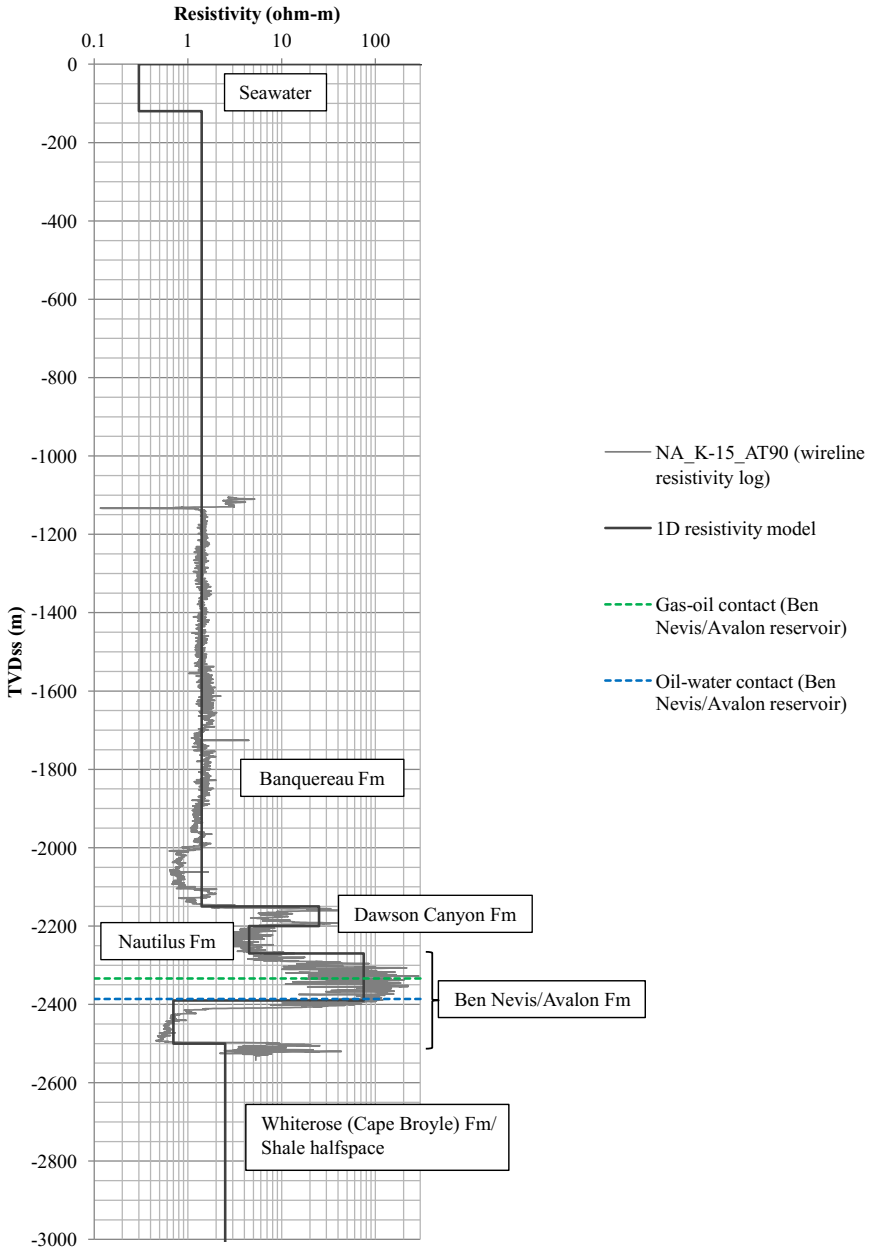

Figure 6.10. The 1D North Amethyst model featuring the hydrocarbon-bearing BNA reservoir. The model was derived mainly from resistivity log K-15, which exhibits a high resistivity signature associated with hydrocarbon-saturated BNA reservoir. Gas-oil and oil-water contacts for the BNA reservoir are at -2334 m and -2386 m, respectively. Correlations between resistivity blocks and major stratigraphy were inferred from well top stratigraphic picks (illustrated in Figures 6.7 and 6.8). Depth is in true vertical depth subsea (TVDss).

Table 6.1. Parameters for the 1D North Amethyst model featuring the BNA reservoir.

Top TVDss (m)	Resistivity (ohm-m)	Stratigraphy	Lithology	Comments
–	1.00E8	Air		Infinitely resistive; modelled as a halfspace
0.00	0.30	Sea		
−120.00	1.40	Banquereau Formation	Shale with sandstone or siltstone at base	South Mara Member sandstone often present at base
−2150.00	25.00	Dawson Canyon Formation	Marl and calcareous shale	Base Tertiary Unconfirmity marks top; Petrel Member argillaceous limestone often present at top
−2200.00	4.50	Nautilus Formation	Siltstone and calcareous shale with minor sandstone	
−2270.00	75.00	BNA Formation	Sandstone, siltstone, and shale	Reservoir quality, hydrocarbon-saturated
−2390.00	0.70	BNA Formation	Sandstone, siltstone, and shale	Reservoir quality, water-saturated
−2500.00	2.00	Whiterose (Cape Broyle) Formation	Siltstone and shale	Modelled as a halfspace

with thickness corresponding to the average water depth of the North Amethyst field area, 120 m. The burial depth of the BNA reservoir was modelled at 2150 m below seafloor, or −2270 m TVDss. The air top-halfspace was assigned an arbitrarily large resistivity for computations.

Variations on this model were tested where water depth and burial depth were modified to observe the effect of these changes on the CSEM response. Burial depth was modified by varying the thickness of the Tertiary Banquereau Formation; all other formation thicknesses were maintained. Finally, an even further simplified 1D model was prepared as a 1D analogue to the eventual 3D model that would be tested: a hydrocarbon-bearing reservoir embedded in a shale halfspace, with an overlying finite-thickness sea layer and air halfspace (Figure 6.11). The shale background was assigned the resistivity of the dominant Banquereau Formation.

A second 1D model including the deeper Hibernia Formation reservoir was constructed using a combination of resistivity log data from wells K-15 and E-17, with well K-15 representing stratigraphy to the base of the BNA Formation and well E-17 representing stratigraphy of the Hibernia Formation and below (Figure 6.12; Table 6.2). Well E-17 exhibits the resistivity response of hydrocarbon-bearing Middle and Basal Hibernia Formation, which have baseline resistivities of approximately 10 and 25 ohm-m, respectively. Basal Hibernia is the target for production in the northern portion of the North Amethyst field, and represents the Hibernia reservoir referenced here. The baseline resistivity for water-saturated Basal Hibernia Formation is approximately 1–2.5 ohm-m; a value of 2.5 ohm-m was chosen for 1D modelling.

In both 1D models, stratigraphy below the reservoir intervals was modelled as a shale halfspace and assigned a representative resistivity value of 2 ohm-m. Simplification of stratigraphy below the resistive reservoir intervals to a shale halfspace was deemed appropriate since deeper stratigraphy is not expected to contribute significantly to the CSEM

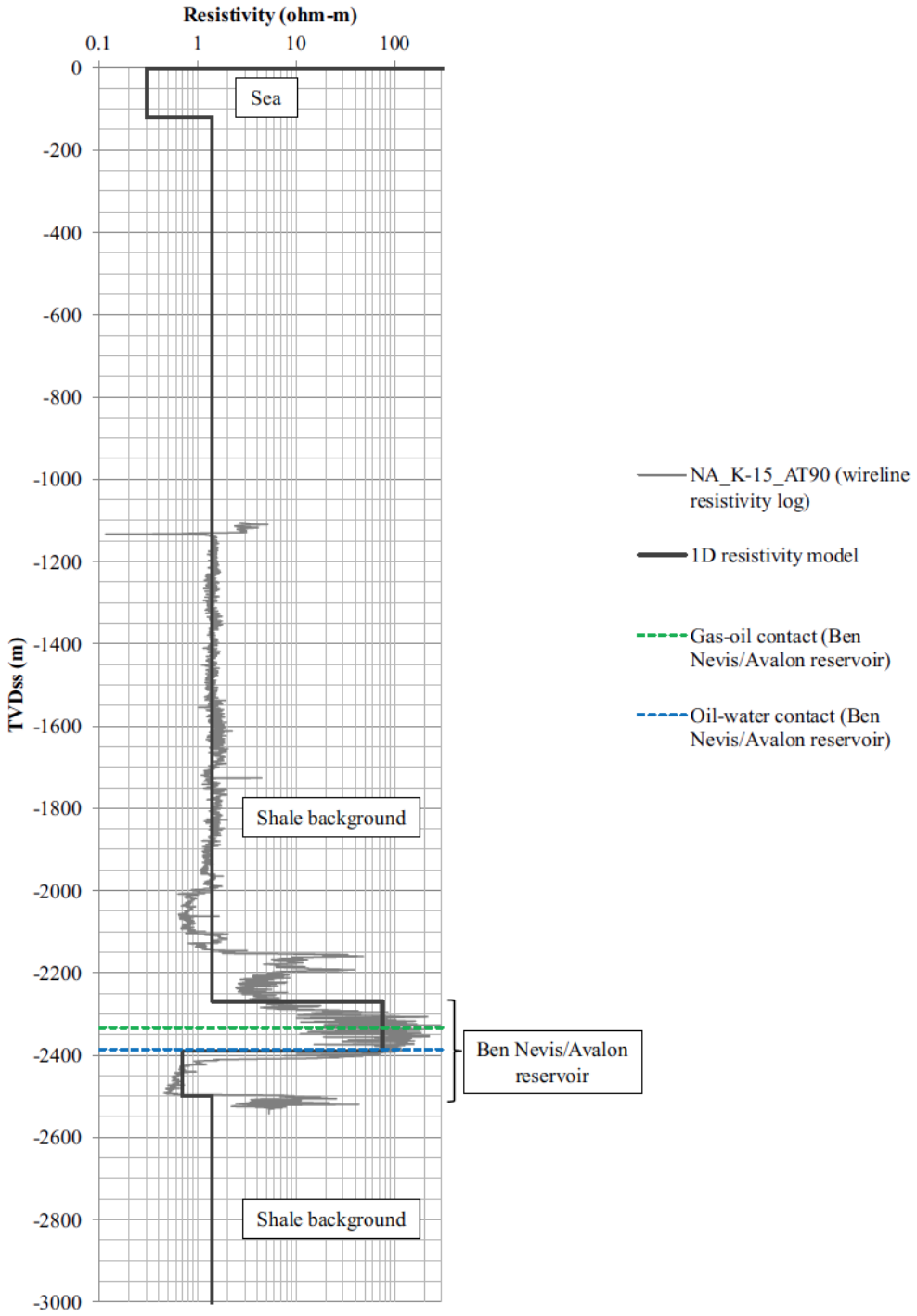

Figure 6.11. Simplified 1D resistivity model that served as an analogue to the 3D North Amethyst BNA reservoir model. The model represents a hydrocarbon-bearing reservoir embedded in a 1.4 ohm-m shale halfspace background, with an overlying finite-thickness 0.3 ohm-m sea layer and air top-halfspace.

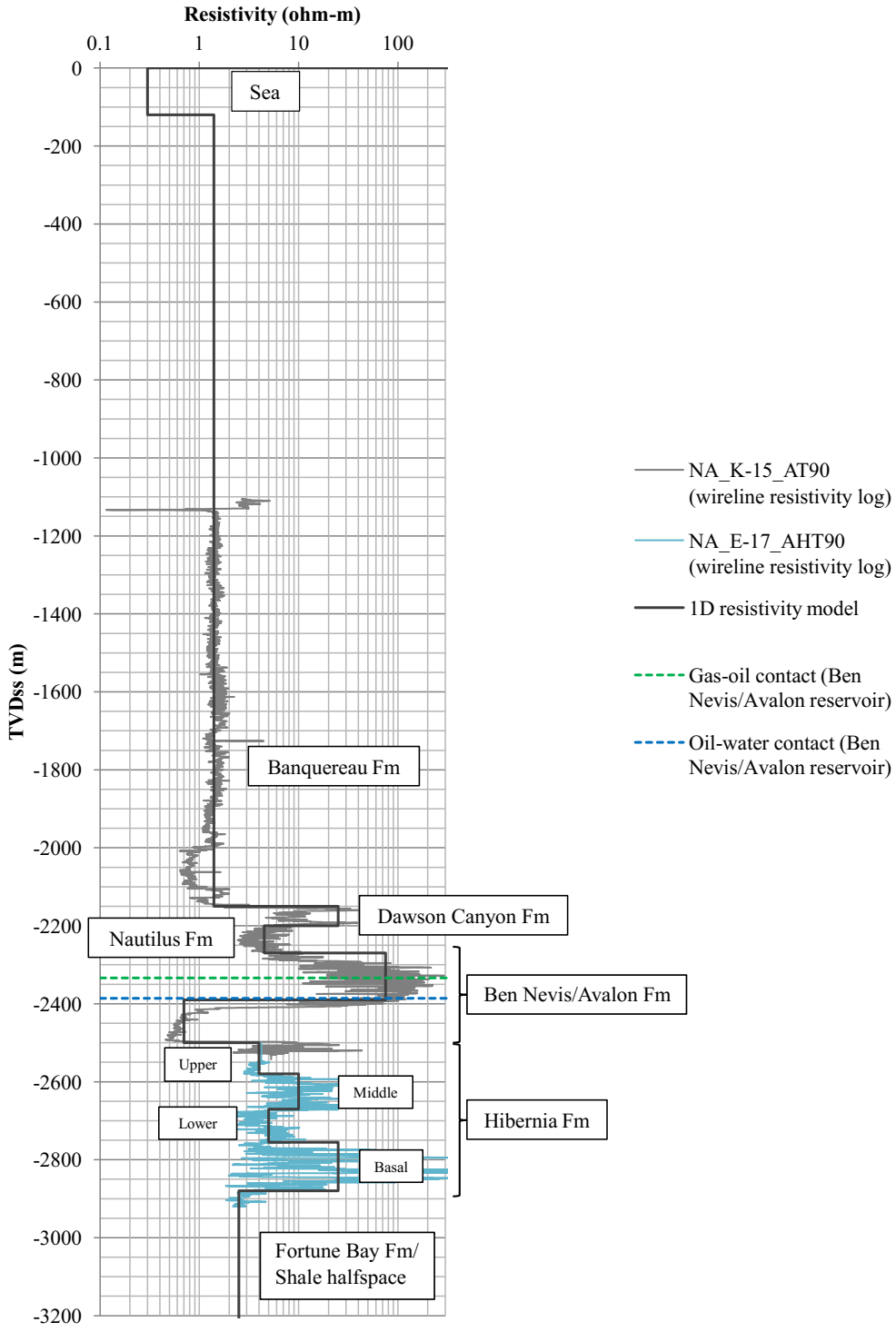

Figure 6.12. 1D North Amethyst resistivity model featuring both the primary BNA and secondary Hibernia hydrocarbon-bearing reservoirs. The model was derived from a combination of the K-15 and E-17, with well K-15 representing stratigraphy up to the base of the BNA Formation and well E-17 representing the Hibernia Formation and below. Well E-17 exhibits the resistivity response of the hydrocarbon-bearing Middle and Basal Hibernia units in the northern portion of the North Amethyst field. Depth is plotted in true vertical depth sub-sea (TVDss).

Table 6.2. Parameters for the 1D North Amethyst model featuring both the primary BNA and secondary Hibernia reservoirs.

Top TVDss (m)	Resistivity (ohm-m)	Stratigraphy	Lithology	Comments
–	1.00E8	Air		Infinitely resistive; modelled as a halfspace
0.00	0.30	Sea		
−120.00	1.40	Banquereau Formation	Shale with sandstone or siltstone at base	South Mara Member sandstone often present at base
−2150.00	25.00	Dawson Canyon Formation	Marl and calcareous shale	Base Tertiary Unconfirmity marks top; Petrel Member argillaceous limestone often present at top
−2200.00	4.50	Nautilus Formation	Siltstone and calcareous shale with minor sandstone	
−2270.00	75.00	BNA Formation	Sandstone, siltstone, and shale	Reservoir quality, hydrocarbon-saturated
−2390.00	0.70	BNA Formation	Sandstone, siltstone, and shale	Reservoir quality, water-saturated
−2500.00	4.00	Upper Hibernia Formation	Coarsening-upward cycles of shale and sandstone	Reservoir quality
−2580.00	10.00	Middle Hibernia Formation	Coarsening-upward cycles of shale and sandstone	Reservoir quality
−2670.00	5.00	Lower Hibernia Formation	Sandstone and shale	Poor reservoir quality
−2755.00	25.00	Basal Hibernia Formation	Fining-upward successions of sandstone	Reservoir quality; production target
−2880.00	2.00	Fortune Bay Formation	Shale and siltstone	Modelled as a halfspace

response measured at the seafloor. Further, from regional lithostratigraphy of the Jeanne d'Arc Basin (Figure 6.3), shale is the predominant lithology below the hydrocarbon-bearing sandstones of the BNA and Hibernia Formations. Furthermore, since well logs and seismic interpretation for the North Amethyst field area do not extend much deeper than the reservoir intervals of interest, assumptions must be made regarding the lithostratigraphy underlying these intervals based on regional studies.

6.4.2 Results

6.4.2.1 Variable water depth and reservoir burial depth

The 1D BNA reservoir model was analysed in terms of inline horizontal electric field anomaly for a suite of different reservoir burial and water depths. The inline horizontal electric field anomaly due to the presence of hydrocarbon-bearing reservoir was computed as the percentage difference in the inline horizontal electric field amplitude, $|E_x|$, between the hydrocarbons-present and hydrocarbons-absent scenarios, normalized by the hydrocarbons-absent amplitude (Figure 6.13). The resistivity for the hydrocarbons-present scenario, 75 ohm-m, was determined from the oil-saturated BNA Formation resistivity log signature, and the resistivity for the hydrocarbons-absent scenario, 0.70 ohm-m, was determined from the water-saturated BNA Formation resistivity log signature.

The results of the analysis are summarized in contour plots of the inline horizontal electric field anomaly as a function of both frequency and source-receiver offset in Figure 6.14. The three illustrated burials depths of 2150 m, 1120 m, and 620 m below seafloor are associated with Banquereau Formation thickness of 2030 m (true thickness), 1000 m, and 500 m, respectively. A conservative threshold for anomaly detection in real data is a 20% difference in the inline horizontal electric field amplitude, as suggested in MacGregor and Tomlinson (2014). Contours of the normalized inline horizontal electric field amplitude for the

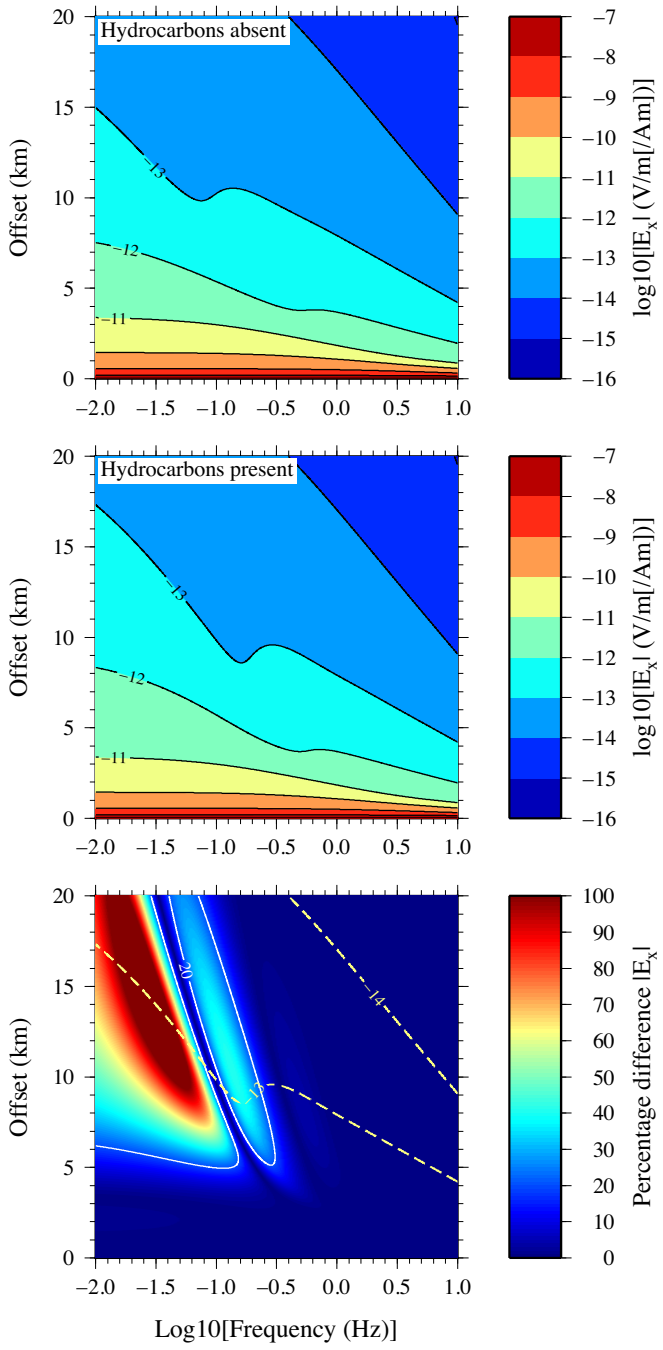

Figure 6.13. Colour contour plots of the logarithm of the normalized inline horizontal electric field amplitude $|E_x|$ for the baseline North Amethyst BNA reservoir model (see Figure 6.10), with a water depth of 120 m and a burial depth of 2150 m, for the hydrocarbons-present and hydrocarbons-absent scenarios. The $|E_x|$ anomaly (bottom) is expressed as the absolute percentage difference in the inline horizontal electric field amplitude $|E_x|$ between the two scenarios, normalized by the hydrocarbons-absent amplitude. The solid white contour indicates the 20% difference detectable anomaly threshold. Contours of the logarithm of the hydrocarbons-present amplitude are superimposed as dashed yellow lines on the anomaly contour plot to facilitate comparison of the signal strength at a given anomaly magnitude to typical EM noise floor values (Table 6.3).

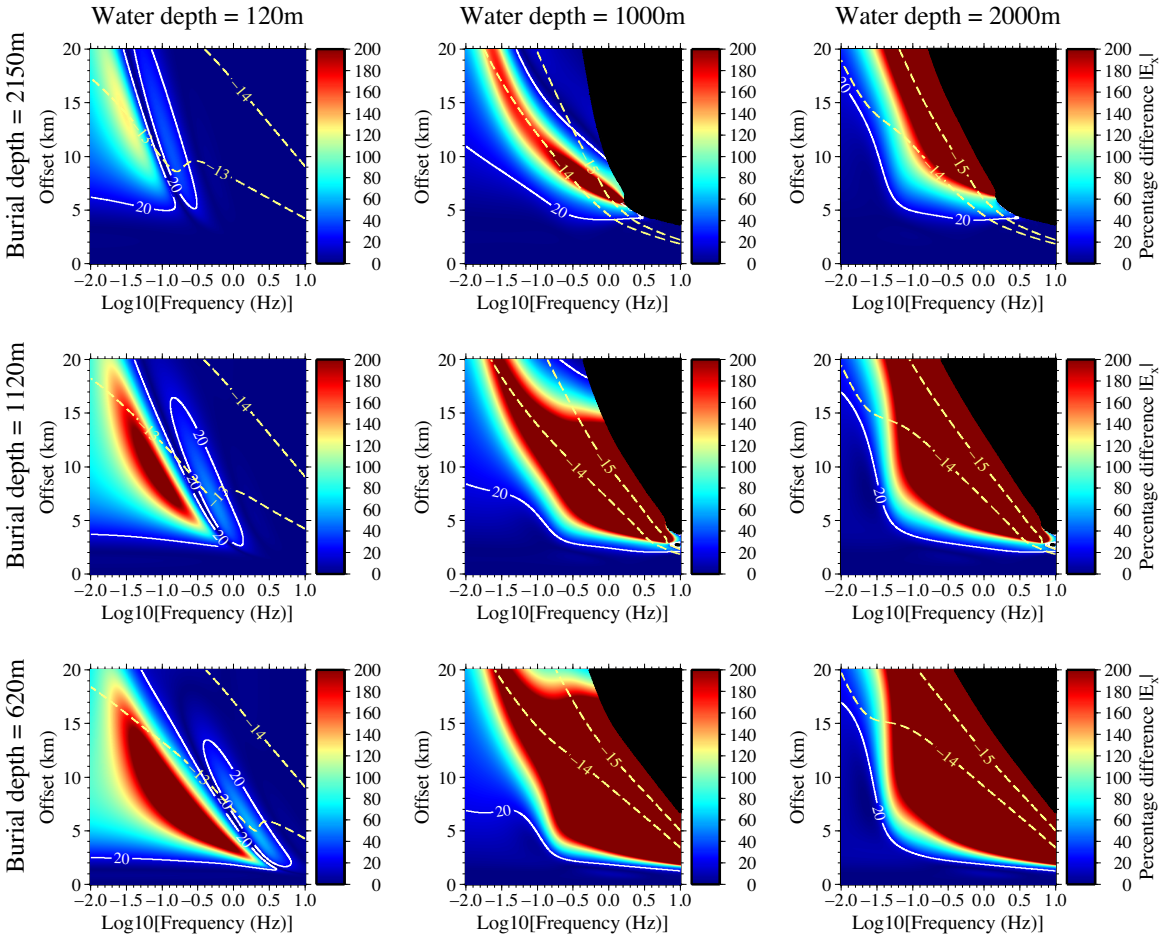

Figure 6.14. Reservoir burial depth versus water depth contour plot matrix of the normalized inline horizontal electric field anomaly due to the presence of hydrocarbons within the BNA reservoir, expressed as the absolute percentage difference in $|E_x|$, as a function of source-receiver offset and source frequency (0.01–10 Hz). The solid white contour indicates the 20% difference anomaly threshold. The dashed yellow lines are superimposed contours of the logarithm of the horizontal electric field amplitude, $\log_{10}\left[|E_x|\left(\mathrm{V/Am^2}\right)\right]$, for the hydrocarbons-present scenario. A portion of the plot is muted, as coloured in black, where the electric field amplitude falls below the accuracy threshold of the Hankel transform computation, approximately 10^{-16} V/Am^2.

Table 6.3. Summary of typical EM noise floor estimates for different water depths, compiled from various sources. The general trend is that noise increases as water depth decreases.

Water depth (m)	EM noise floor $\left(\mathrm{V/Am^2}\right)$	Source
2000	5×10^{-16}	Mittet and Morten (2013)
1500	10^{-15}	MacGregor and Tomlinson (2014)
1000	10^{-16}	Ellis and Keirstead (2011)
1000	10^{-16}	Constable and Weiss (2006)
500	10^{-15}	Ellis and Keirstead (2011)
330	10^{-14}	Ellis and Keirstead (2011)
300	3×10^{-15}	Mittet and Morten (2013)
100	7×10^{-15}	Mittet and Morten (2013)
100	10^{-13}	Ellis and Keirstead (2011)
40	1.5×10^{-14}	Mittet and Morten (2013)

hydrocarbons-present scenario are superimposed on the plots of inline horizontal electric field anomaly to facilitate comparison of anomaly magnitude to signal magnitude. In real life acquisition and interpretation of CSEM data, there is a trade-off between anomaly magnitude and signal-to-noise ratio. Real-life acquisition takes place in environments where the EM noise floor is on the order of 10^{-16} to 10^{-14} V/Am^2, depending on water depth (Table 6.3). Thus, while an anomaly may theoretically be detectable at a given frequency and offset based on modelling, it may not be detectable in practice.

Results indicate that for the true burial depth of 2150 m and true water depth of 120 m (Figure 6.13 and upper-left plot of Figure 6.14), the offset-frequency field in which the hydrocarbon-bearing reservoir exhibits a detectable anomaly is restricted to relatively low frequency and large source-receiver offset. 1D results thus suggest that the CSEM method will be sensitive to the presence of the hydrocarbon-bearing BNA reservoir at sufficiently low frequency and sufficiently large offset, for frequencies in the range of roughly 0.01–0.1 Hz and offsets greater than roughly 5 km. As water depth increases and/or burial depth

decreases relative to the true values for the North Amethyst BNA reservoir model, the frequency-offset field for anomaly detection expands, with a 20% difference anomaly appearing at shorter offset and higher frequency (Figure 6.14).

The expansion of the frequency-offset field as water depth increases and burial depth decreases may be understood in terms of the physical thicknesses of the water and conductive overburden in relation to their skin depths. As the thickness of the water layer increases relative to its skin depth, signal travelling to and from the sea-air interface is increasingly attenuated; the result is that the offset at which the air signal begins to dominate the target response increases, such that the offset range for anomaly detection also increases. As overburden thickness decreases relative to its average skin depth, signal travelling to and from the resistive reservoir target is less attenuated; the result is that the anomaly magnitude at a given offset increases, which in turn has the effect of decreasing the minimum offset for anomaly detection. Further, as overburden thickness decreases, the frequency range for anomaly detection extends to higher frequencies for which cumulative signal attenuation would have previously been too severe for detection of an anomaly. One must keep in mind however that at high frequency, signal is rapidly attenuated to near or below the noise threshold and that signal-to-noise ratio may be insufficient in practice.

Note also that for shallow water depth (i.e., water depth = 120 m in Figure 6.14), there are two distinct anomaly peaks in frequency-offset space: a stronger peak at nearer offset and a weaker peak at farther offset. The absolute percentage difference is presented in Figures 6.13 and 6.14, but the stronger peak at nearer offset is a positive anomaly, and the weaker peak at farther offset is a negative anomaly. For a given frequency, the stronger and nearer-offset positive anomaly is associated with an increase in the inline horizontal electric field measured at the seafloor due to signal which has been guided along the resistive target layer with less attenuation than signal travelling directly through the water layer or through the conductive overburden. The second weaker and farther-offset negative anomaly, which

is less prominent at greater water depth, is possibly associated with deconstructive interference of signal that has interacted with the resistive target and signal that has interacted with the air layer (see Key, 2012b).

6.4.2.2 Inclusion of the secondary Hibernia reservoir

The hydrocarbon-bearing BNA Formation reservoir interval is the main production target for the North Amethyst field, with the Basal Hibernia Formation being a secondary production target in the northern E-17 well block of the field. Many stratigraphy simplications were made in the design of the 3D North Amethyst BNA reservoir model, one of which was omission of the Basal Hibernia reservoir. Simplification of earth structure is necessary in modelling, but may impact the accuracy of the synthetic or forward-modelled solution in approximating real-life geophysical observations. To understand how inclusion or exclusion of a secondary, lower, hydrocarbon-bearing reservoir affects the CSEM response, the inline horizontal electric field anomaly was computed for a 1D model including stratigraphy below the BNA reservoir, as illustrated in Figure 6.12, for the hydrocarbons-present and hydrocarbons-absent scenarios for the Basal Hibernia reservoir.

Figure 6.15 illustrates the inline horizontal electric field anomalies and their difference for the two scenarios. The presence of hydrocarbons in the Basal Hibernia Formation has little effect on the frequency-offset field for detection of an inline horizontal electric field anomaly, but its presence increases the magnitude of the anomaly. This result is consistent with the view that the sensitivity of the marine CSEM method to thin resistive layers is largely (but not entirely) galvanic, and exhibits behaviour that is similar to the transverse resistance-equivalence observed in DC resistivity methods, at least at relatively low frequency (Constable and Weiss, 2006; Constable, 2010; MacGregor and Tomlinson, 2014). The presence of the Hibernia oil-bearing reservoir increases the transverse resistance of the resistive layer interval, thereby increasing the magnitude of the electric field anomaly.

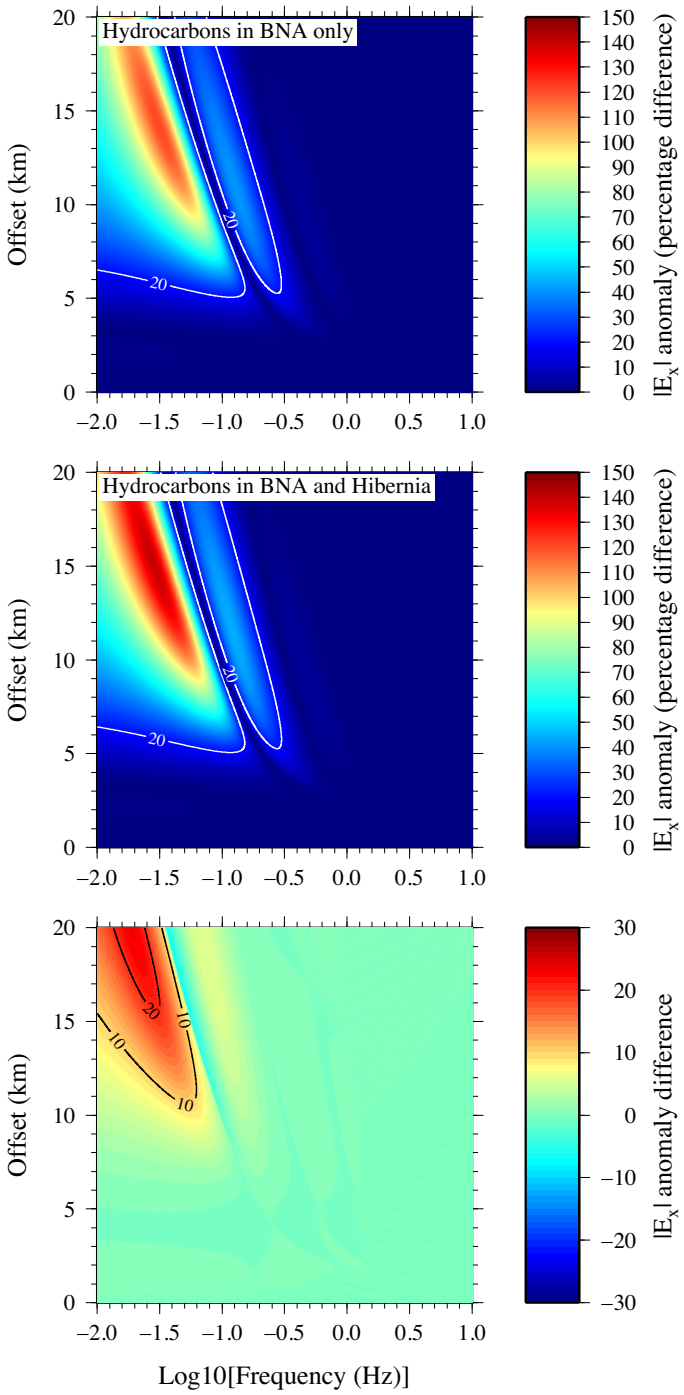

Figure 6.15. The normalized inline electric field anomaly for the 1D North Amethyst model including both the BNA and Hibernia reservoirs (see Figure 6.12), with and without hydrocarbons present in the Basal Hibernia reservoir. The difference in anomaly due to the presence of hydrocarbons in the Basal Hibernia reservoir in addition to the BNA reservoir is illustrated in the lower plot. The presence of hydrocarbons in the lower Hibernia reservoir has the effect of increasing the magnitude of the inline horizontal electric field anomaly as much as 20%, but does not appreciably impact the frequency-offset field for detection of the anomaly.

6.4.2.3 Simplification of stratigraphy: 1D analogue for the 3D model

The 3D North Amethyst reservoir model simplifies stratigraphy of the field area to a shale halfspace with resistivity of 1.4 ohm-m, the baseline resistivity of the Tertiary Banquereau Formation. Figure 6.11 illustrates the 1D analogue of this model, which consists of a hydrocarbon-bearing reservoir embedded in a 1.4 ohm-m shale halfspace. Compared to the detailed stratigraphy of the baseline 1D BNA reservoir model illustrated in Figure 6.10, most notable is the absence of the Dawson Canyon and Nautilus Formations, both of which partially consist of calcareous shale, accounting for their relatively high baseline resistivities of 25 ohm-m and 4.5 ohm-m, respectively.

Figure 6.16 demonstrates how the inline horizontal electric field anomaly changes with simplification of background stratigraphy to a shale halfspace. The most noticeable effect is an increase in the magnitude of the inline horizontal electric field anomaly, which is principally a galvanic, or TM-mode, effect (see Section 3.2). Resistive layers act as waveguides for low-attenuation propagation of EM fields and reduce penetration of the TM mode, or vertical current, to deeper, underlying conductive sediments. Removal of the relatively resistive Dawson Canyon and Nautilus Formations thus leads to greater current flow to the resistive reservoir and a corresponding increase in anomaly magnitude. A more subtle effect of omission of the Dawson Canyon and Nautilus Formations is a slight shift of peak anomaly to lower frequency, which is possibly an inductive effect associated with skin depth. In the absence of the Dawson Canyon and Nautilus Formations, that is, in a relatively more conductive background, lower frequencies are better able to penetrate to and interact with the reservoir than more heavily attenuated higher frequencies.

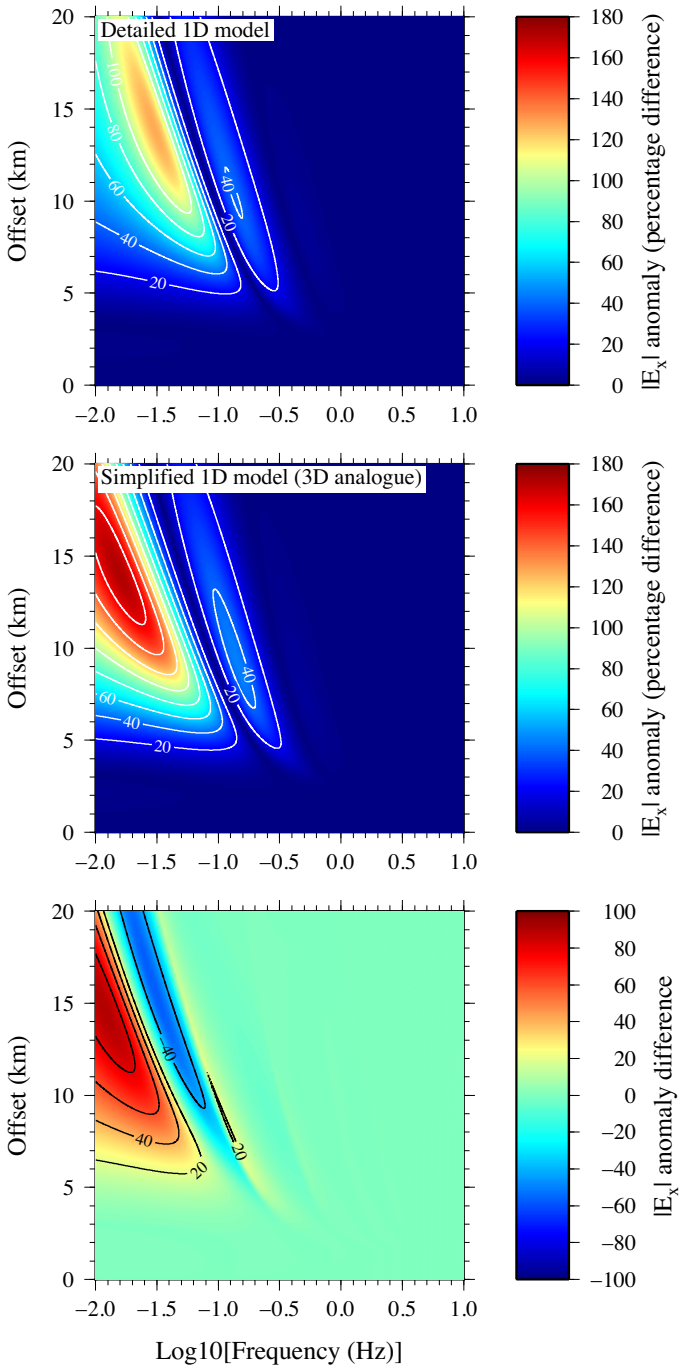

Figure 6.16. Comparison of and difference between the normalized inline horizontal electric field anomalies for the 1D North Amethyst BNA reservoir model with detailed stratigraphy (see Figure 6.10) and with simplified stratigraphy (see Figure 6.11). The main difference between the two models is the omission of the more resistive Dawson Canyon and Nautilus Formations (resistivities of 25 and 4.5 ohm-m, respectively), which leads to simplification of the model to a laterally finite hydrocarbon-bearing reservoir embedded in a 1.4 ohm-m shale halfspace. The difference in anomaly due to these simplifications is illustrated in the bottom plot. The overall effect of omission of these resistive formations is an increase in anomaly magnitude and a subtle shift of peak anomaly to lower frequency.

6.4.3 Summary and discussion

Simplification of background stratigraphy in the North Amethyst field to a homogeneous halfspace does not appear to significantly alter the frequency-offset field for detection of an inline horizontal electric field anomaly, but does modify the magnitude of the expected anomaly. The 1D solution for the simplified 3D analogue model suggests that sensitivity to the reservoir target will be greatest for frequencies in the range of 0.01–0.1 Hz and for offsets greater than 5 km. 1D modelling assumes an infinite lateral extent, uniform thickness reservoir, whereas the true dimensions of the North Amethyst field are approximately 4 km by 7 km, and hydrocarbon accumulation is not uniform but instead controlled by reservoir structure. It is thus unclear whether the 3D solution will be comparable to the 1D solution given the edge effects of laterally finite bodies on the CSEM response. 3D modelling results for the canonical disk model would suggest that when both source and receiver are located laterally within the limits of a resistive target, the 3D solution is well approximately by the 1D solution. The lateral dimensions of the BNA reservoir target do not however extend far beyond the minimal offset required for manifestation and detection of an inline electric field anomaly, as predicted by 1D modelling. An increase in water depth and/or decrease in burial depth would however appear to increase the frequency-offset field for detection of an anomaly.

6.5 3D modelling

6.5.1 Resistivity model construction

The 3D North Amethyst reservoir model simplifies true stratigraphy and structure to a hydrocarbon-bearing, laterally finite reservoir embedded in a shale halfspace, with an overlying finite-depth sea layer and upper air halfspace. Simplification of background structure was required since accurate representation of the region's structural complexity would have led to an unmanageable problem in view of present capabilities. Preliminary 1D modelling indicates that simplification of background stratigraphy and associated resistivity structure to a shale halfspace does not significantly modify the frequency-offset field for detection of an inline horizontal electric field anomaly, but that it does result in overestimation of anomaly magnitude. While there are many other hydrocarbon pools within the White Rose field area, compared to the main North Amethyst reservoir interval, these bodies are located at a greater distance both laterally and vertically from the simulated source-receiver line, which is positioned above the North Amethyst field on a regional structural high; for example, equivalent reservoir in the adjacent South Avalon Pool is positioned approximately 600 m deeper than the BNA reservoir in the North Amethyst field (see Figure 6.6). Hydrocarbon accumulations within adjacent blocks should thus contribute little to the cumulative CSEM response measured at a receiver above the North Amethyst field.

The shale halfspace was assigned the 1.4 ohm-m baseline resistivity of the Tertiary Banquereau Formation, which is the dominant lithostratigraphic unit overlying the BNA reservoir in terms of thickness; it accounts for 2030 m of the 2150 m-burial depth of the reservoir below seafloor. Resistivity values for hydrocarbon-saturated and water-satured BNA reservoir, 75 ohm-m and 0.7 ohm-m, respectively, were also derived from the 1D resistivity logs. Seawater was assigned a resistivity of 0.3 ohm-m, and air was assigned a

resistivity of 10^8 ohm-m.

The structure of the BNA reservoir was constructed from 3D seismic horizon data for the top and base reservoir surfaces, clipped within the fault-delimited bounds of the Amethyst Ridge structure. Original surface data were in point or node format, with x and y as UTM coordinates (m) and z as true-vertical-depth-sub-sea (TVDss; m). To simplify model construction, the UTM x, y-coordinates were translated to relative coordinates using the formulae:

$$x_{rel}(i) = x_{utm}(i) - \left[\min(x_{utm}) + \frac{|\max(x_{utm}) - \min(x_{utm})|}{2}\right]$$

and

$$y_{rel}(i) = y_{utm}(i) - \left[\min(y_{utm}) + \frac{|\max(y_{utm}) - \min(y_{utm})|}{2}\right],$$

where x, y_{utm} represent the UTM coordinates, and x, y_{rel} represent the relative, translated coordinates. With this transformation, the origin of the model and mesh now lies at the centre of the rectangle defined by the maximum lateral dimensions of the reservoir.

Generation of the reservoir surface meshes from the original seismic horizon node data is summarized graphically in Figure 6.17 for the top reservoir surface. The reservoir top and base surfaces were triangulated from node data using the 2D unstructured mesh generator Triangle. The original node data for the top and base reservoir were unsuitable for direct input to Triangle because of their high density and irregular spacing (Figure 6.17a). Polygons defining only the lateral extent of the top and base reservoir were instead used as input. Triangle's Delaunay refinement algorithm only allows nodes to be added, and not destroyed, when attempting to improve the quality of a mesh. By constraining triangulation only by the lateral extent of the reservoir, and not imposing the original node density, generation of a good quality mesh composed of well-shaped, equilateral triangles was promoted. Polygons outlining the top and base reservoir were manually defined in FacetModeller using the

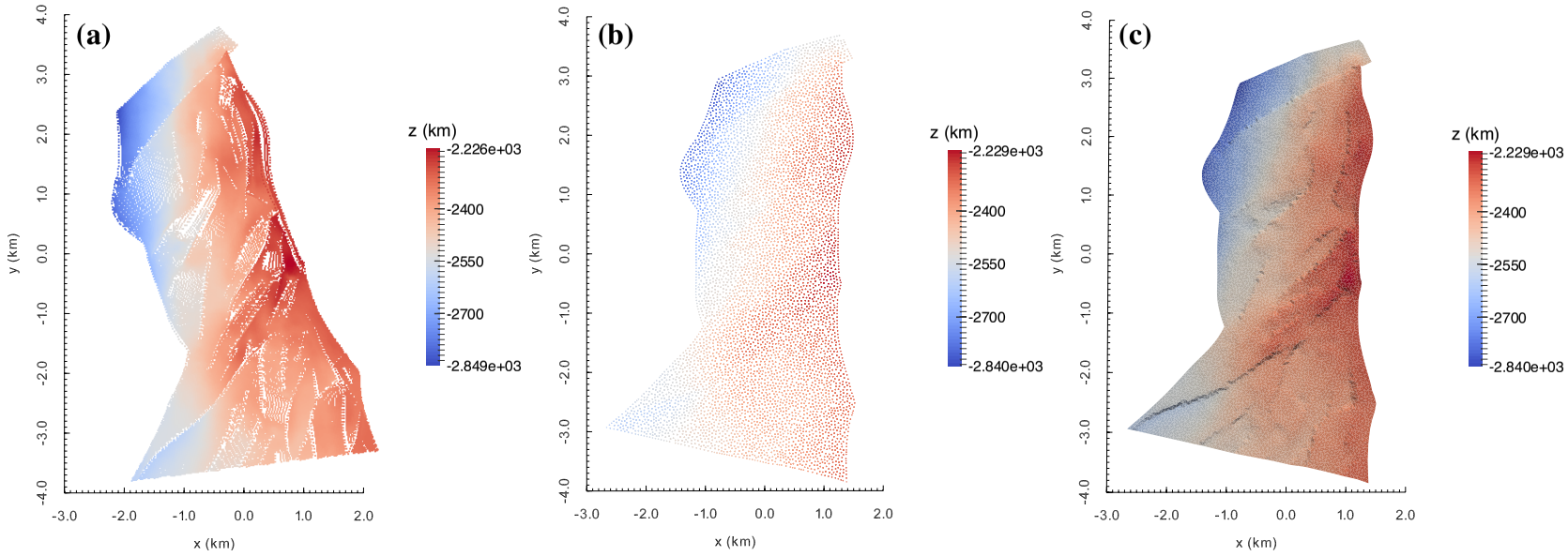

Figure 6.17. Resampling, rotation, and meshing of the top reservoir surface for the 3D North Amethyst BNA reservoir model. The base reservoir surface was similarly modified and meshed. **(a)** The original top reservoir node data from seismic horizons. Fault traces are emphasized by sharp changes in z and the absence of node data since fault planes are defined as separate surfaces. **(b)** The resampled, rotated ($-20°$), and x-translated ($+400$ m) top reservoir node data. Resampling was effectuated by providing Triangle with a polygon outlining the top reservoir to mesh, and interpolating depth (z) for the output node dataset from the original node dataset. Node spacing is approximately 76 m due to the enforcement of a maximum triangle area of 2500 m^2. Resampling has led to smoothed topography where fault displacement is now only weakly expressed in the reservoir surface. **(c)** The complete unstructured triangular mesh (nodes and cells) generated for the top reservoir surface using Triangle.

original node datasets as guidelines. To ensure adequate node density to capture large-scale variations in surface topography, a maximum triangle area of 2500 m^2 was imposed during meshing, which corresponds to the area of a 76 m-edge length equilateral triangle, thus enforcing a node spacing of roughly 76 m. After the Delaunay-constrained triangulation in x, y was generated for the reservoir surfaces, the z-coordinate for each output node was interpolated from the original node data. The effective resampling of the reservoir surface resulted in a smoothed topography retaining only subtle expressions of fault displacement (Figures 6.17b and 6.17c). Considering our present capabilities, this was advantageous since accurate representation of fault displacement would necessitate poorly shaped, elongate cells and/or greater node density, and thus greater refinement, in the vicinity of faults; neither was desirable due to the adverse effects on mesh quality and problem size. To facilitate definition of along-strike receiver lines in the coordinate system, the reservoir surfaces were rotated -20° in space to orient the strike of the eastern ridge, which serves as the hydrocarbon trap for the field (see Figures 6.5 and 6.6), with north-south. The data were also translated $+400$ m in the x-direction so that the eastern ridge was aligned parallel to the y-axis and centered at x = 1 km. An along-strike, y-directed receiver line was later defined to be centered at x = 1 km (Section 6.5.2).

In FacetModeller, the meshed reservoir surfaces were imported into the full 30 km $\times$ 30 km $\times$ 30 km model domain composed of a 1.4 ohm-m lower shale halfspace, an overlying 0.3 ohm-m, 120 m-thick sea layer, and a 10^8 ohm-m upper air halfspace (Figure 6.18). The dimensions of the sea layer were 22 km $\times$ 22 km $\times$ 120 m. The model was exported from FacetModeller in .poly file format and meshed using TetGen. A utility program was developed by Peter Lelièvre which cycles through the cells of the mesh and identifies those cells which fall within the lateral and vertical limits of any two input surfaces, in this instance, the top and base reservoir surfaces. Identified cells may then be assigned an attribute or physical property value based on their average z value. In this instance, cells falling above the

oil-water contact at -2386 m TVDss were assigned the baseline resistivity of hydrocarbon-saturated reservoir, 75 ohm-m, and cells falling below the oil-water contact were assigned the baseline resistivity of water-saturated reservoir, 0.7 ohm-m.

The final 3D unstructured mesh for the baseline North Amethyst BNA reservoir model is illustrated in various perspectives in Figures 6.19 through 6.21. Figures 6.19 and 6.20 illustrate yz-sections of the unstructured mesh in normal and rotated view, respectively, along a y-directed receiver line at $x = 1$ km. Figure 6.21 illustrates the unstructured mesh for the BNA reservoir interval in isolation. Hydrocarbon accumulation within the reservoir interval is associated with the fault-bounded, eastern structural high. Refinement was manually enforced in the vicinity of the source and along the simulated receiver line via insertion of rectangular blocks which were assigned the resistivity of the background so that their presence did not modify the electrical structure of the model. The final 30 km $\times$ 30 km $\times$ 30 km mesh consisted of 1,267,510 cells, 202,977 nodes, and 1,471,838 edges.

Variations of the baseline 3D resistivity model in hydrocarbon saturation, burial depth, and water depth were tested. Specifically, modelling was performed for both the true reservoir hydrocarbon content, as defined by the oil-water contact, and for the scenario where the reservoir interval was entirely hydrocarbon-saturated. These two scenarios roughly equate to an average oil thickness of 60 m and 190 m[‖], respectively, although they represent drastically different lateral oil extents. Six different combinations of water depth and burial depth were modelled, based on the true water depth of 120 m, increased water depths of 1000 m and 2000 m, the true burial depth of approximately -2500 m TVDss average, and a decreased burial depth of approximately -1500 m TVDss average. The increased water depths of 1000 m and 2000 m are more comparable to water depths encountered in the adjacent Orphan and Flemish Pass basins than in the relatively shallow Jeanne d'Arc Basin.

[‖]Estimated as the average difference in depth between the top reservoir and base reservoir triangulated surfaces, where the base reservoir depth was interpolated at the (x,y) coordinates of the top reservoir nodes.

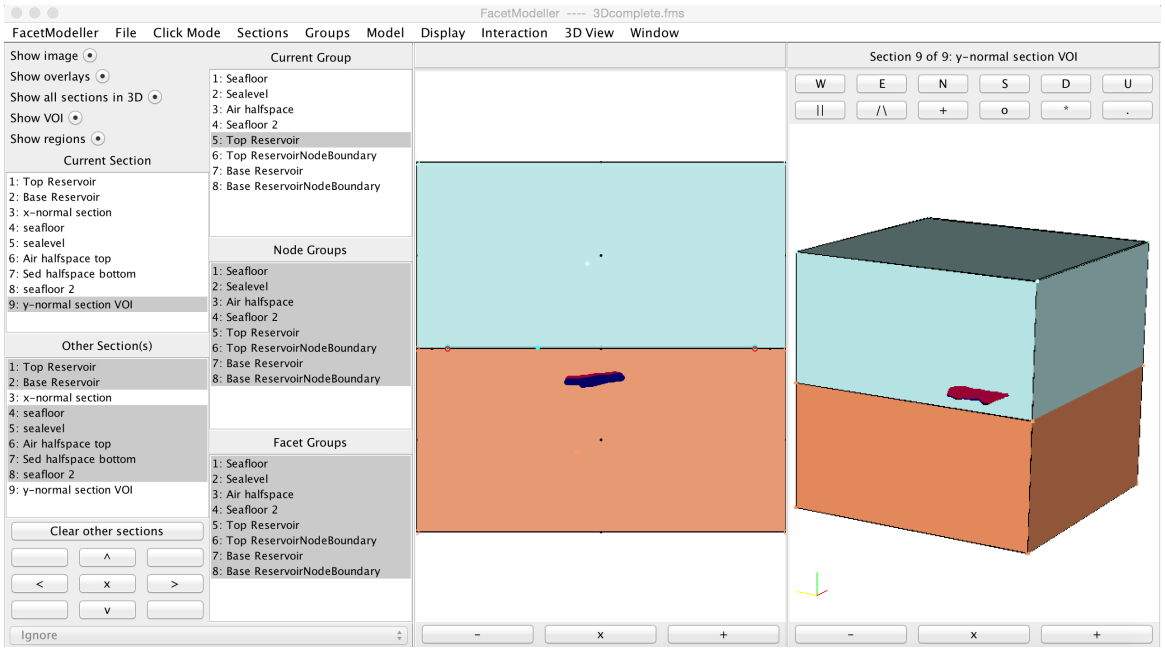

Figure 6.18. Screenshot of the 3D North Amethyst BNA reservoir model construction in FacetModeller. The 3D model consists of a laterally finite reservoir (red = top; base = dark blue) embedded in a lower shale halfspace (brown), with an overlying 120 m-thick sea layer (thin; poorly visible) and upper air halfspace (light blue).

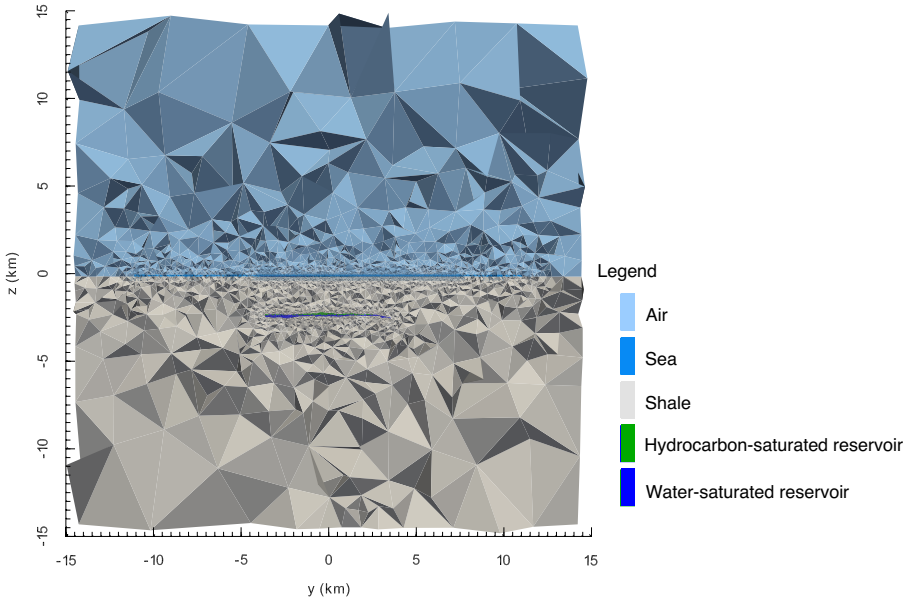

(a) *yz*-section of the full unstructured mesh for $x = 1$ km.

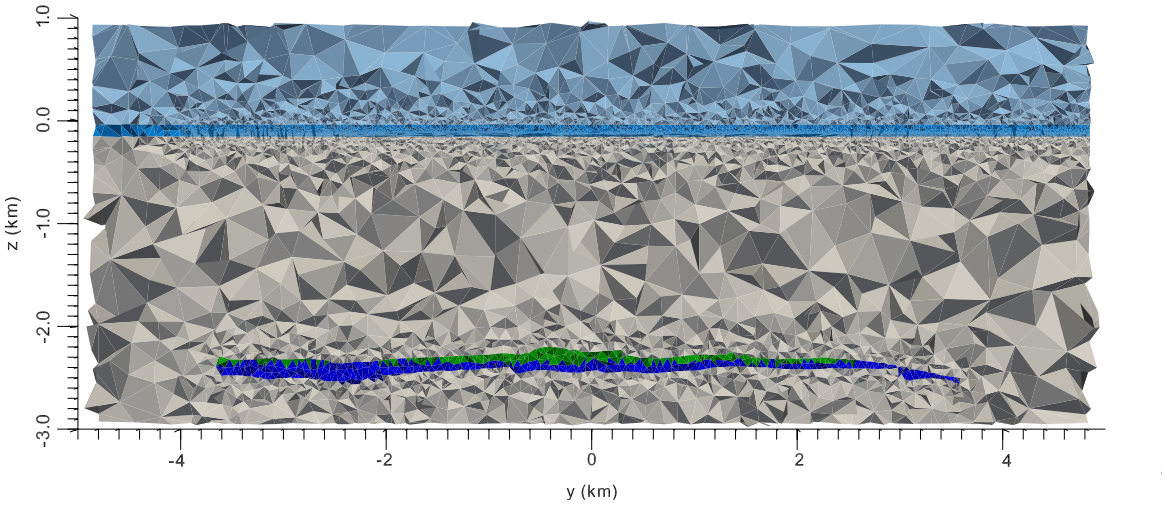

(b) Enlarged *yz*-section of the unstructured mesh for $x = 1$ km, illustrating the sea layer and BNA reservoir in greater detail.

Figure 6.19. Normal *yz*-section of the unstructured mesh for the 3D North Amethyst BNA reservoir model, along a *y*-directed receiver line at $x = 1$ km. Refinement was manually enforced in the vicinity of the dipole source location and along the receiver line by insertion of blocks having the same resistivity as their background.

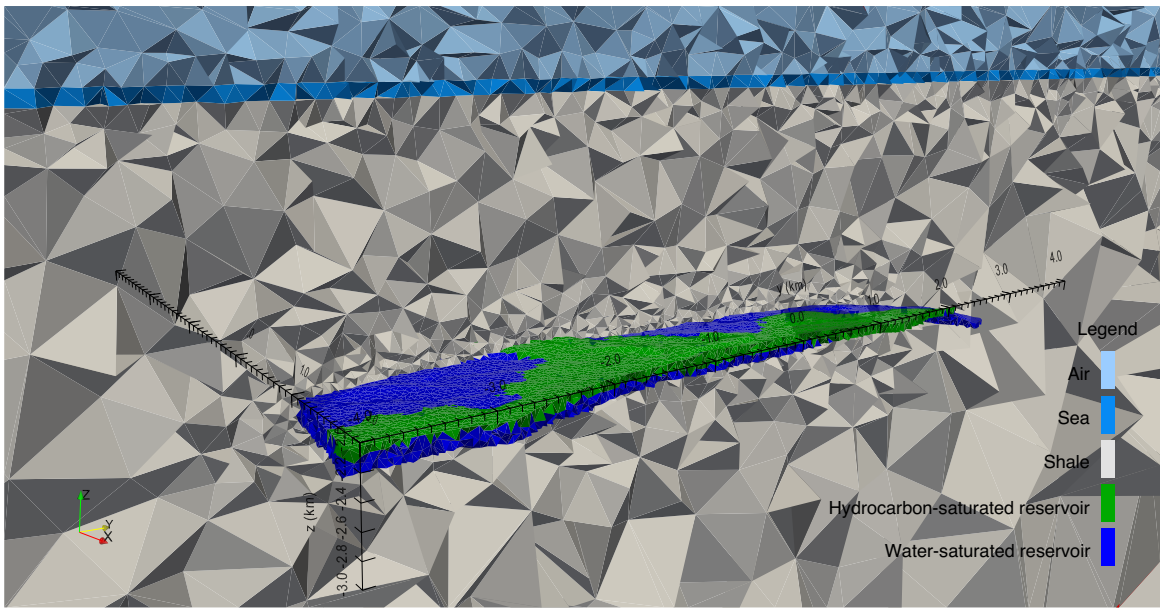

Figure 6.20. Perspective (rotated) section of the unstructured mesh for the 3D North Amethyst BNA reservoir model. The background is yz-sectioned at $x = 2$ km, but the full xyz-extent of the reservoir interval is illustrated for $x > 2$ km.

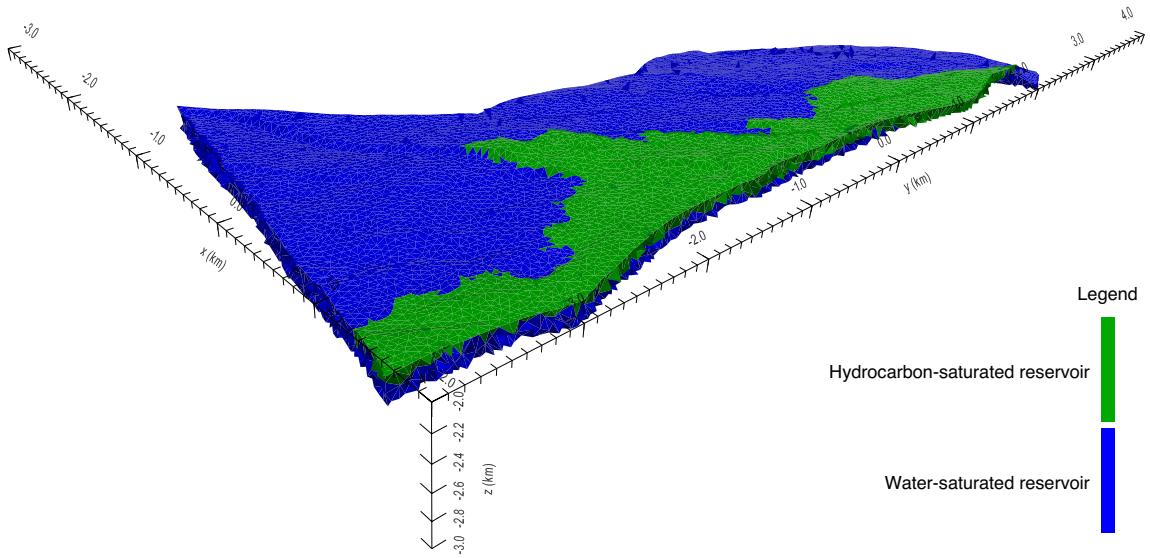

Figure 6.21. The unstructured mesh for the isolated 3D BNA reservoir. Hydrocarbon accumulation is associated with the fault-bounded, structural high on the eastern ($+x$) limit of the ridge. The oil-water contact is at -2386 m TVDss. Tetrahedra with average $z > -2386$ m TVDss were assigned the resistivity value of hydrocarbon-saturated reservoir, while tetrahedra with average $z < -2386$ m TVDss were assigned the resistivity value of water-saturated reservoir.

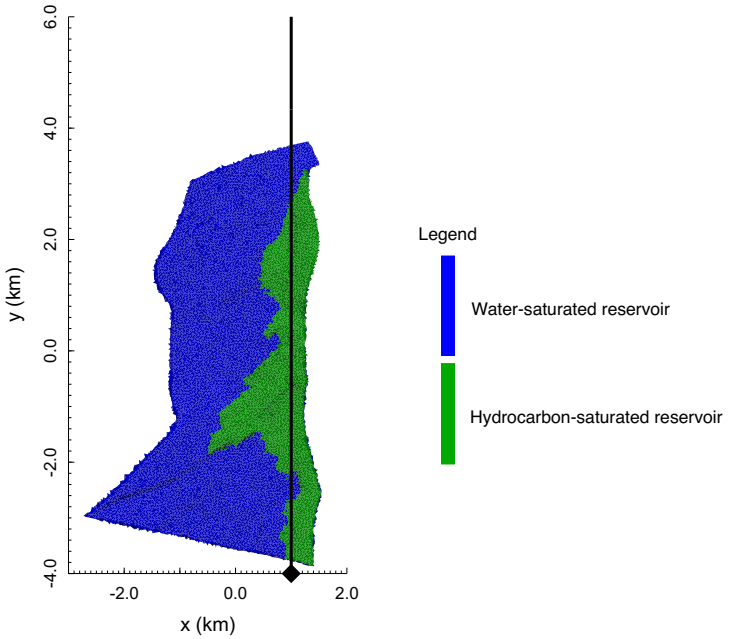

Figure 6.22. The y-directed, inline source-receiver geometry simulated for the 3D North Amethyst model. The source-receiver array is oriented along the strike of the eastern structural high of the North Amethyst ridge, which serves as a trap for hydrocarbon accumulation in the field area. The diamond indicates the location of the y-directed, 1 Am-moment HED source, which is centered at (x,y) = (1 km, -4 km) at a height of 50 m above seafloor. The simulated receiver line extends from y = -4 km to y = 6 km and is centered at x = 1 km.

6.5.2 Along-strike, inline source-receiver geometry

For the 3D North Amethyst reservoir model, the source was simulated as a 1 Am, y-directed HED centered at $(x,y) = (1000,-4000)$ m and $z = \{-70,-950,-1950\}$ m TVDss, which corresponded to a height of 50 m above seafloor for water depth = $\{120,1000,2000\}$ m TVDss, respectively. As discussed previously, the reservoir surface data were rotated so that the hydrocarbon trend was aligned parallel to the y-axis and centered at x = 1 km. The along-strike, inline, y-directed receiver line extended from (x,y) = $(1000,-4000)$ m to (x,y) = $(1000,6000)$ m, with $z = \{-119.9999,-999.9999,-1999.9999\}$ m TVDss, which corresponded to a height of 0.0001 m above seafloor for water depth = $\{120,1000,2000\}$ m TVDss, respectively. Figure 6.22 illustrates this inline source-receiver geometry against the top reservoir surface. Simulated transmission frequencies were 0.025 Hz, which falls mid-

Table 6.4. Run information for the different 3D North Amethyst reservoir model variations, including total number of cells in the input mesh, iterative solver memory usage, and total run time for CSEM3DFWD. Memory and run time correspond to the true hydrocarbon content scenario, i.e., hydrocarbons only present above the oil-water contact in the reservoir, and a simulated source frequency of 0.5 Hz. The GMRES Krylov subspace dimension was 400 for all examples, and the ILUT fill-in factor was 3.

Water depth (m)	**Average burial depth** (m)	**Total number of cells in mesh**	**GMRES memory usage** (dim_k **= 400;** $lfil$ **= 3)** (GB)	**CSEM3DFWD total run time** (h)
120*	2416*	1,267,510	25	18.7
120	1416	1,237,772**	24	19.4
1000	2416	1,060,080	20.9	15.7
1000	1416	1,212,530	21.6	16.2
2000	2416	1,085,818	21	15.8
2000	1416	908,189	17.9	14.4

*True earth parameters **Employed coarser receiver refinement to minimize problem size

optimal frequency range for anomaly detection based on 1D modelling, and 0.5 Hz, which falls mid-range of the typical frequencies employed in CSEM acquisition (0.01–10 Hz) and serves as a comprise between target sensitivity at low frequency and structural resolution at high frequency in view of real-life acquisition and interpretation of marine CSEM data.

6.5.3 Results

CSEM3DFWD run information for the different 3D North Amethyst reservoir model variations, including total number of cells in the input unstructured mesh, iterative solver (GMRES) memory usage, and total run time for the program, are summarized in Table 6.4 for reference. Note that memory and run time correspond to the true hydrocarbon content scenario, i.e., hydrocarbons only present above the oil-water contact in the reservoir, and a simulated frequency of 0.5 Hz; modifications to source frequency and electrical properties (e.g., to simulate a completely hydrocarbon-filled reservoir) result in modifications to the

matrix system which may in turn result in modifications to program run time and memory usage. The number of cells required in the mesh generally increased as water depth decreased and burial depth decreased owing to the increased proximity of mesh-constraining structural features, e.g., the air-sea, seafloor, and reservoir boundaries. For all runs, the GMRES Krylov subspace dimension was set to 400, and the fill-in factor was set to 3. All simulations were completed on a HP ProLiant SL250s compute node with 2×8-core Intel Xeon 2.6 GHz processors and 96 GB RAM.

6.5.3.1 True earth parameters

Figures 6.23 and 6.24 illustrate the 0.025 Hz and 0.5 Hz finite-element solutions, respectively, for the real and imaginary parts of the inline field components E_y, H_x, and E_z for the true North Amethyst BNA reservoir model. Hydrocarbon content was defined by the oil-water contact at -2386 m TVDss, the water depth was 120 m, and the average reservoir burial depth was -2416 m TVDss. In comparing the finite-element solutions for 0.025 Hz and 0.5 Hz, it is interesting to note that for 0.5 Hz (Figure 6.24), the solutions for H_y, and particularly, for E_z, become increasingly noisy as offset increases and as field amplitude decreases. It appears that mesh refinement was insufficient for the 0.5 Hz case to provide resolution of such small field amplitudes. For the E_z component, the shortcoming in refinement is likely exacerbated by the thinness of the sea layer, which places the high conductivity contrast sea-air interface in close proximity to the high conductivity contrast sea-sediment interface at which receivers are simulated. While the components E_y and H_x are continuous across conductivity boundaries, E_z is discontinuous, and mesh refinement must be sufficient to capture the rapid spatial variation in E_z for a smooth and accurate solution. Since the inline horizontal electric field component E_y is smooth and any additional refinement would result in a larger problem size, the mesh was not modified to improve the accuracy of the horizontal magnetic and vertical electric field components.

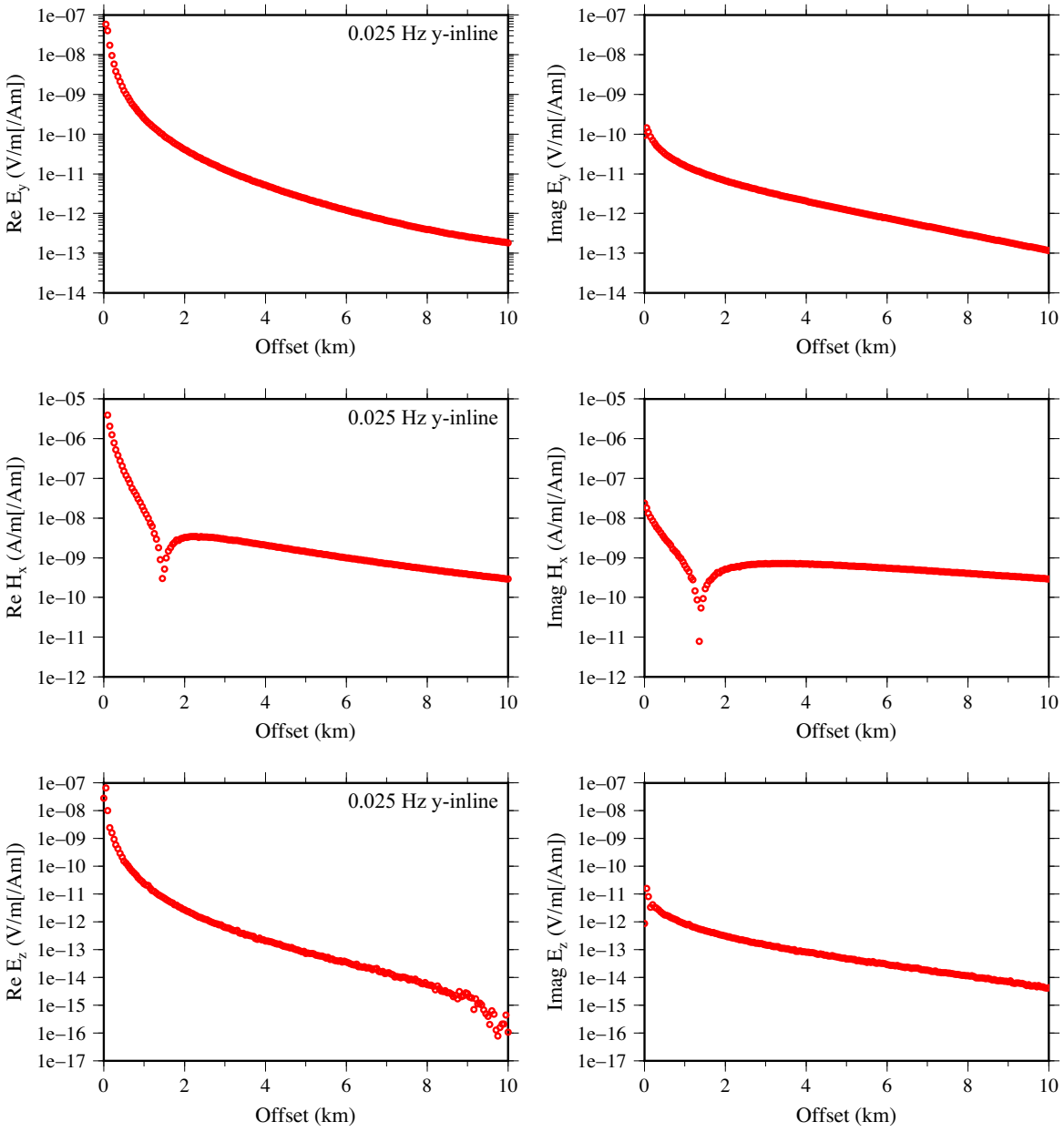

Figure 6.23. The 0.025 Hz solutions for the real and imaginary parts of the field components E_y, H_x, and E_z for the 3D North Amethyst BNA reservoir model with true hydrocarbon content as defined by the oil-water contact at -2386 m TVDss, true water depth of 120 m, and true burial depth of -2416 m TVDss average. The source is a y-directed HED centered 50 m above the seafloor at $y = -4$ km, and the inline receiver array extends from $y = -4$ km to $y = +6$ km. Offset, i.e., source-receiver separation, is displayed on the x-axis.

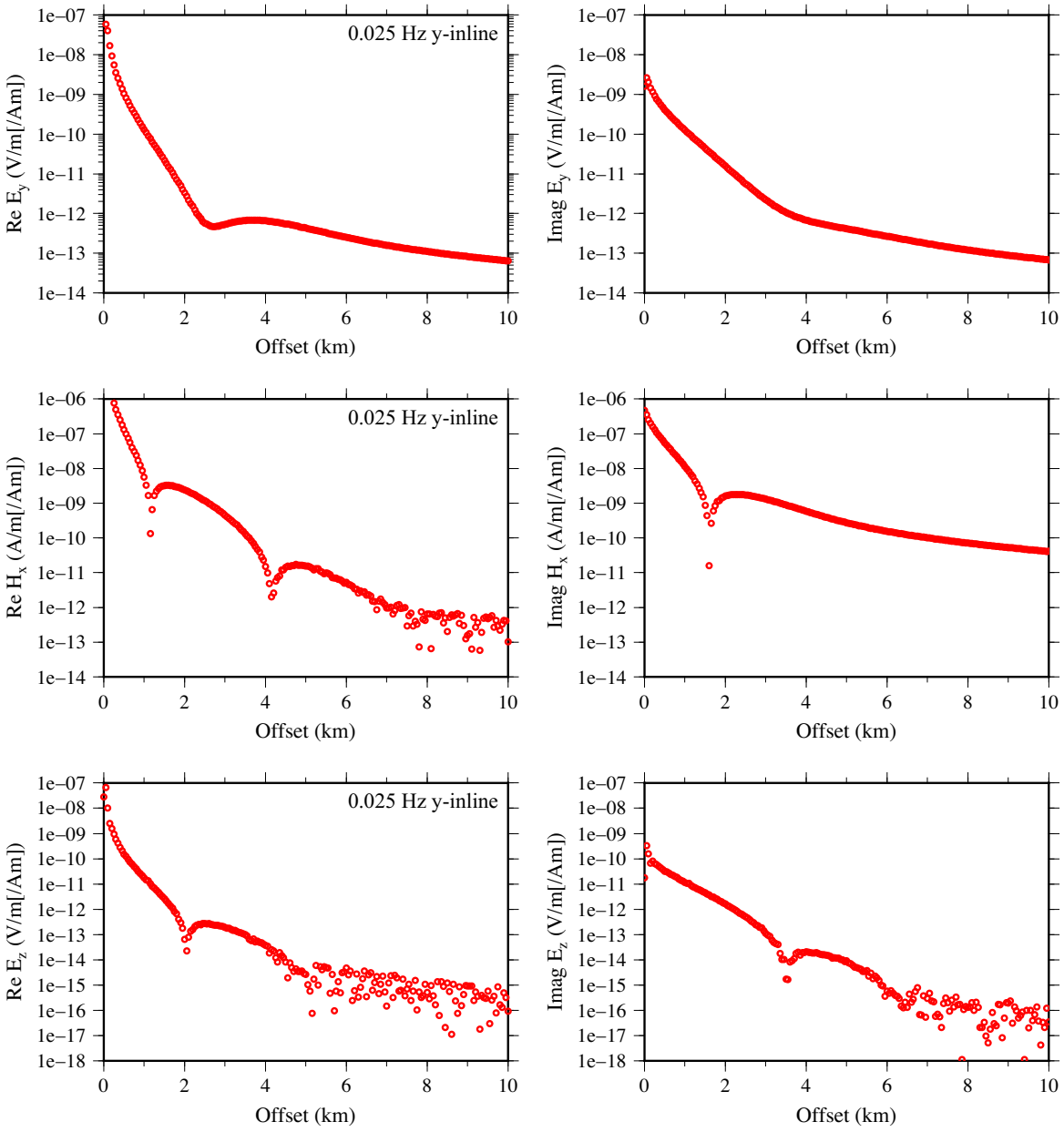

Figure 6.24. The 0.5 Hz solutions for the real and imaginary parts of the field components E_y, H_x, and E_z for the 3D North Amethyst BNA reservoir model with true hydrocarbon content as defined by the oil-water contact at -2386 m TVDss, true water depth of 120 m, and true burial depth of -2416 m TVDss average. The source is a y-directed HED centered 50 m above the seafloor at $y = -4$ km, and the inline receiver array extends from $y = -4$ km to $y = +6$ km. Offset, i.e., source-receiver separation, is displayed on the x-axis.

The inline horizontal electric field anomalies for the true 3D North Amethyst BNA reservoir model for source frequencies of 0.025 Hz and 0.5 Hz, respectively, are presented in Figures 6.25 and 6.26. For 0.025 Hz, the maximum inline horizontal electric field anomaly was about 1.21% at 6500 m offset**, drastically less than that predicted by 1D modelling (see Figure 6.16). For offset less than 10 km, 1D modelling predicted a maximum anomaly of 106.73% at 9760 m offset. The 1D anomaly corresponding to the offset for maximum 3D anomaly was 56.03%. For 0.5 Hz, the maximum inline horizontal electric field anomaly was negligible, although this frequency is outside of the optimal frequency range, as determined by 1D modelling, for CSEM sensitivity to target. The maximum 3D 0.5 Hz inline horizontal electric field anomaly was 0.11% at 5450 m offset, whereas the maximum 1D 0.5 Hz anomaly for offset less than 10 km was 10.31% at 6300 m; a 1D 0.5 Hz anomaly of 8.66% occurred at 5450 m offset, the offset associated with maximum 3D anomaly.

That the inline horizontal electric field anomalies were substantially less than those predicted by 1D modelling was not unexpected given that firstly, the lateral dimensions of the target do not extend far beyond the minimum offset for a 20% difference anomaly based on 1D modelling, approximately 5 km. The 1D model assumed an infinite-extent reservoir, whereas the maximum y-extent of the reservoir in the 3D model was approximately 7 km. Secondly, the 1D model assumed a constant-thickness, constant-burial depth hydrocarbon-bearing interval, whereas true thickness and burial depth vary laterally due to structural control (see Figure 6.9). Since the CSEM method is sensitive to transverse resistance, overestimation of thickness would result in overestimation of the inline horizontal electric field anomaly. Given the high lateral variability in hydrocarbon thickness, 1D modelling was inadequate for prediction of the 3D CSEM response.

**Recall that receiver, or observation point, spacing is 50 m, and so offset is defined in 50 m increments.

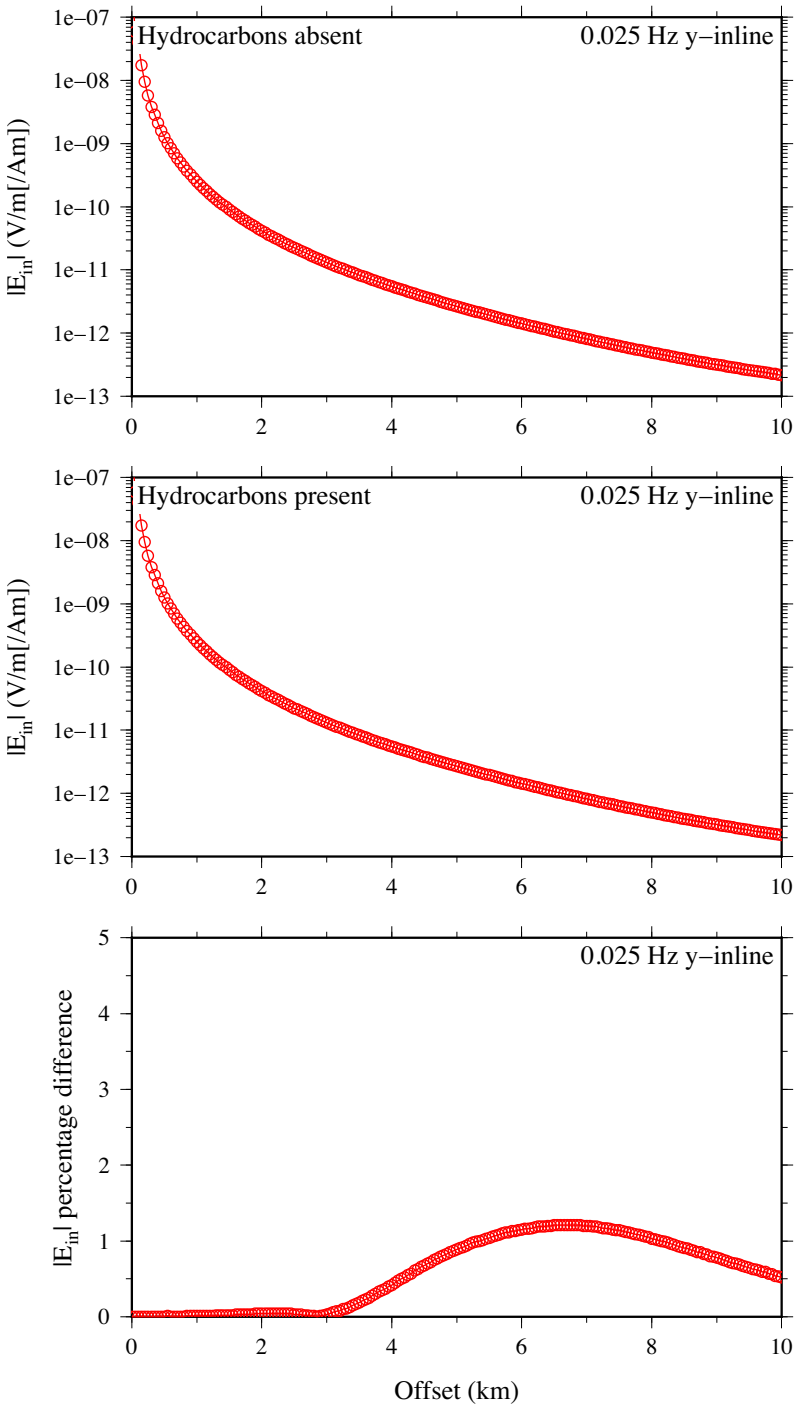

Figure 6.25. The 0.025 Hz inline horizontal electric field anomaly ($E_{in} = E_y$) for the true 3D North Amethyst BNA reservoir model. The top and middle panels illustrate the inline horizontal electric field solutions for the hydrocarbons-absent and hydrocarbons-present scenarios, respectively, and the bottom panel illustrates the inline horizontal electric field anomaly, calculated as the percentage difference between the hydrocarbons-absent and hydrocarbons-present amplitudes, normalized by the hydrocarbons-absent amplitude The maximum inline electric field anomaly is approximately 1%, drastically less than that predicted by 1D modelling for offset less than 10 km.

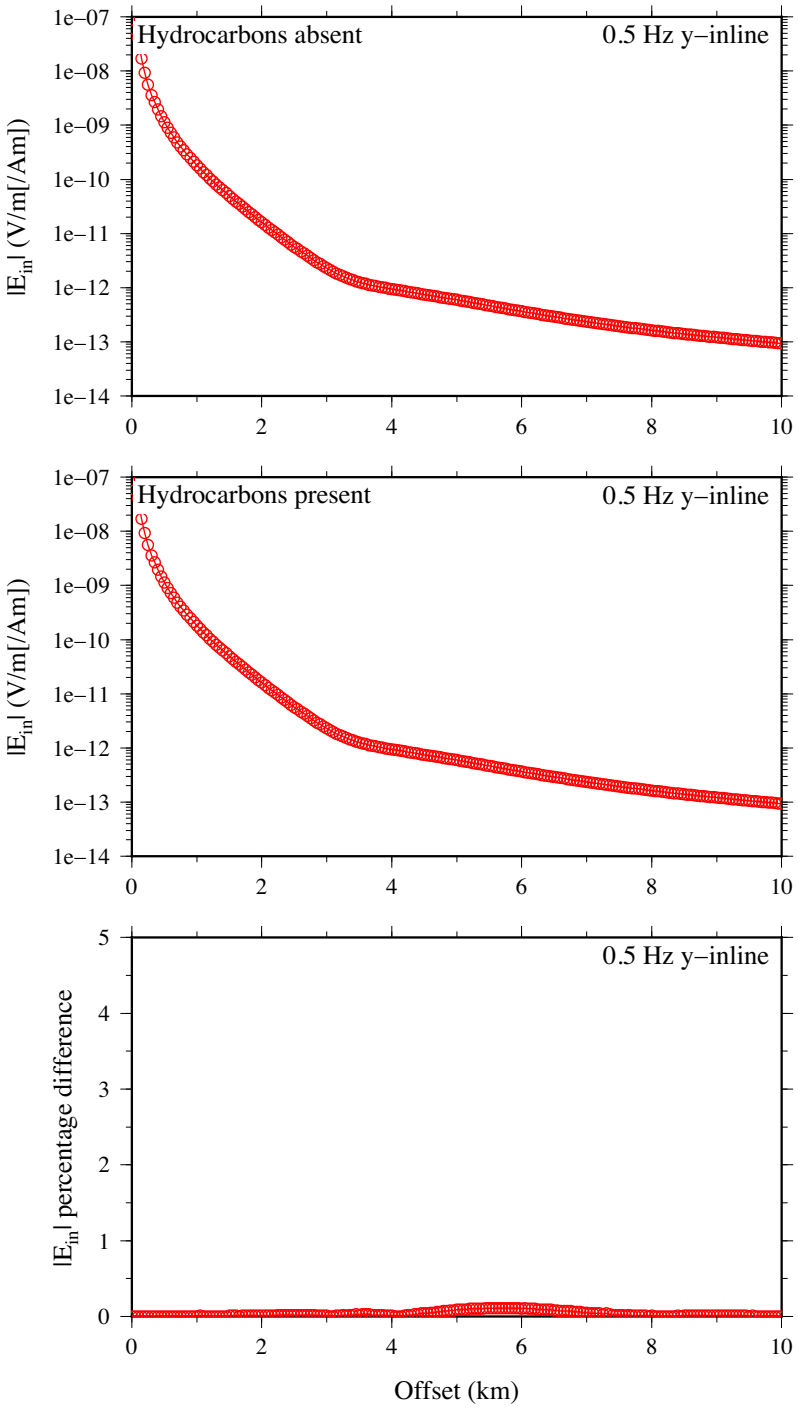

Figure 6.26. The 0.5 Hz inline horizontal electric field anomaly ($E_{in} = E_y$) for the true 3D North Amethyst BNA reservoir model. The inline electric field anomaly is negligible at 0.5 Hz, although this frequency falls outside of the optimal frequency range for target sensitivity and detection, as predicted by 1D modelling.

6.5.3.2 Variable hydrocarbon content, burial depth, and water depth

To understand what conditions would enable detection of the hydrocarbon target, 3D modelling was extended to variations of the baseline (true) model in terms of water depth, reservoir burial depth, and hydrocarbon content. The source frequency was simulated at the more moderate 0.5 Hz in view of the typical range of frequencies employed in CSEM acquisition (0.1–10 Hz). Based on 1D modelling, a transmission frequency of 0.5 Hz is non-optimal for the true earth parameters, but provides sufficient sensitivity ($>$20% anomaly) to the reservoir target for decreased burial depth and/or increased water depth (see Figure 6.14). Further, 0.5 Hz provides a better compromise between depth penetration at low frequency and structural resolution at high frequency than 0.025 Hz, the 1D-predicted optimal frequency for anomaly detection in the true earth model.

Figures 6.27 and 6.28 illustrate the 0.5 Hz inline horizontal electric field anomalies for variations on the baseline (true) 3D North Amethyst BNA reservoir in terms of water depth and reservoir burial depth for a reservoir with true hydrocarbon content, i.e., hydrocarbons present only above the oil-water contact (Figure 6.27), and for a reservoir completely filled by hydrocarbons, i.e., hydrocarbons present throughout the reservoir interval (Figure 6.28). Plots illustrating the hydrocarbons-present and hydrocarbons-absent inline horizontal electric field amplitudes corresponding to the inline horizontal electric field anomalies presented in Figures 6.27 and 6.28 may be found in Appendix B; these plots are useful for comparison of anomaly magnitude to electric field amplitude when considering the strength of the signal-to-noise ratio.

The inline electric field anomaly generally increased with decreased reservoir burial depth and/or increased water depth, and was manifest at nearer offset with decreased burial depth, as consistent with 1D modelling results. Of note is that for the true hydrocarbon content (Figure 6.27), for an average burial depth of 1416 m, the maximum anomaly is greater

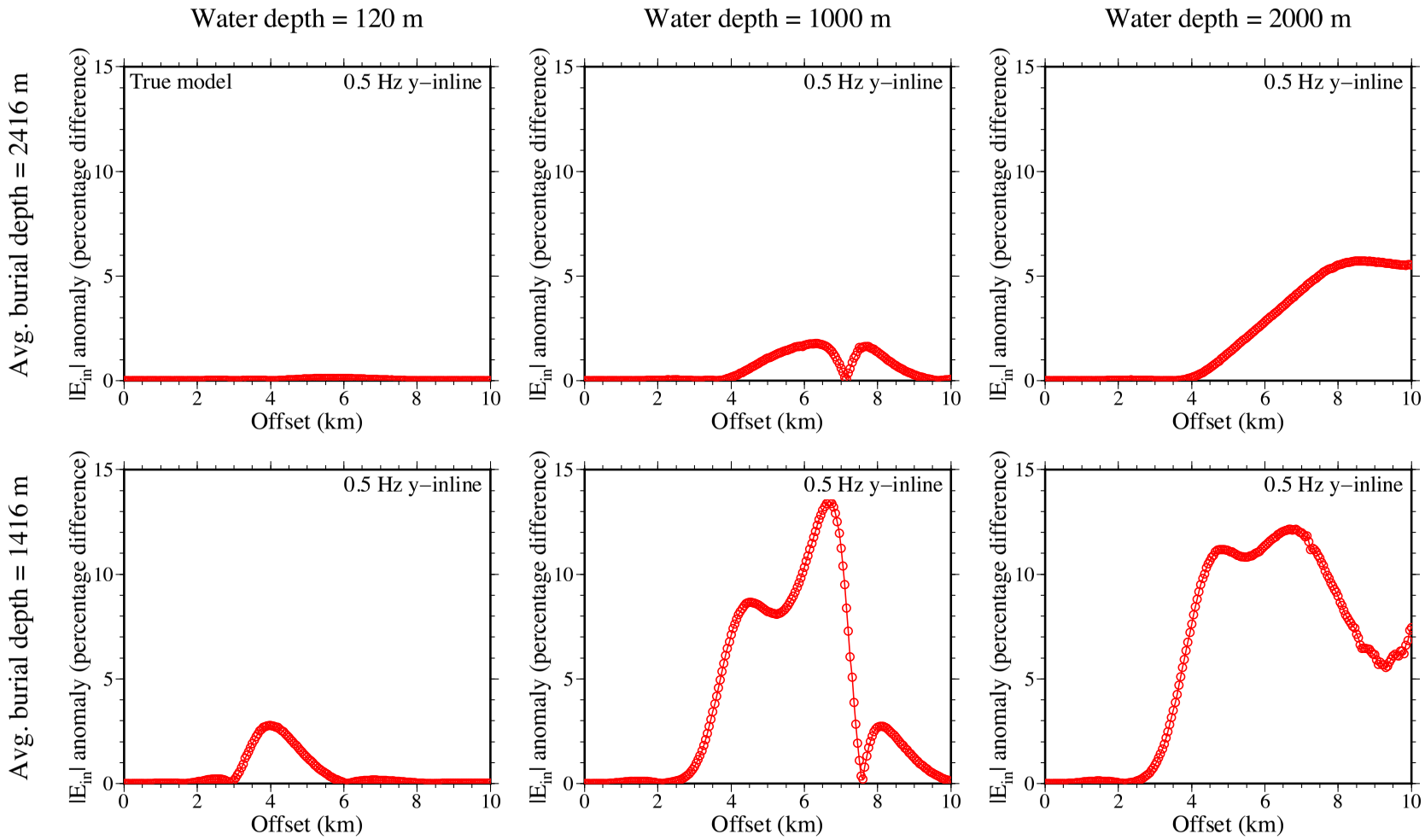

Figure 6.27. The 0.5 Hz inline horizontal electric field anomaly (E_{in} = E_y) for variations of the baseline (true) 3D North Amethyst BNA reservoir model in terms of water depth and reservoir burial depth for the scenario of true hydrocarbon content, i.e., hydrocarbons above the oil-water contact only.

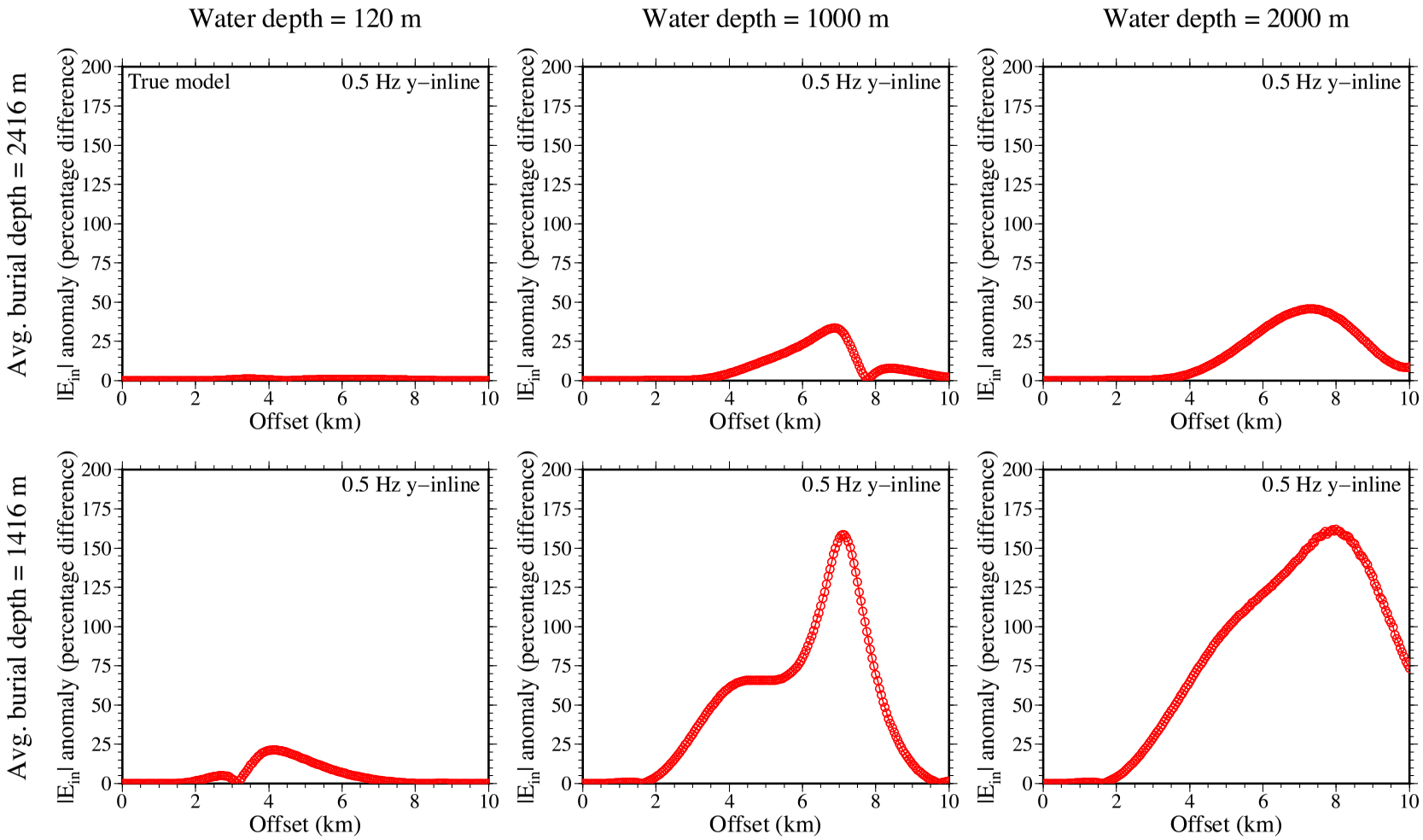

Figure 6.28. The 0.5 Hz inline horizontal electric field anomaly (E_{in} = E_y) for variations of the baseline (true) 3D North Amethyst BNA reservoir model in terms of water depth and reservoir burial depth for the scenario of the reservoir interval being completely hydrocarbon-filled. Note the change in scale from 0–15% in Figure 6.27 to 0–200% here.

for a water depth of 1000 m than for a water depth of 2000 m; the mean anomaly (or integrated anomaly over all offsets) is however greater for a water depth of 2000 m than for a water depth of 1000 m. Comparing between the plots of Figures 6.27 and 6.28, for a given water depth and reservoir burial depth, the inline electric field anomaly is approximately 10–20 times greater with increased oil thickness. These results again highlight the sensitivity of the marine CSEM method to transverse resistance. Recall that the true hydrocarbon thickness was approximately 60 m on average whereas a completely hydrocarbon-filled reservoir corresponds to an average thickness of approximately 190 m; the lateral extent of hydrocarbons was also much greater in the latter scenario.

6.5.4 Summary and discussion

1D modelling can lead to gross anomaly overestimation for targets of limited lateral extent or with significant lateral variation in thickness, particularly when the lateral dimensions of the target are less than or border the minimum offset required for detection. 1D modelling remains however a good starting point for analysis of the frequency-offset field for anomaly generation and detection because of the large range of frequencies and offsets that may be considered in a trivial amount of time. By contrast, 3D modelling presented in this chapter only considers single frequencies and a limited range of source-receiver offsets, and requires considerable computational resources.

A deficiency of the 3D results presented here is that they are not representative of a 3D survey since they consider only a single line orientation across the target. For simulation of a 3D survey, many meshes, each specific to a particular source-receiver geometry, would be required, or a single mesh with extensive refinement to accommodate many source-receiver geometries; the latter approach may however lead to unmanageable problems in terms of size and/or ill-conditioning. Such simulations may require several days, or even weeks, for computation. Based on memory usage-scaling, which is roughly linear with problem size

(refer to Table 6.4), for a Krylov subspace dimension of 400 for GMRES, making full use of the 96 GB available on select compute nodes, a maximum mesh size of approximately 4,800,000 cells might be manageable. Whether the solution would converge in a reasonable number of iterations is however unknown, since system ill-conditioning may increase or be exacerbated as problem size increases. Lastly, it should be noted that forward modelling presented here only addresses the detectability, not the recoverability, of targets from marine CSEM data; no attempt has been made to complete a resolution or recoverability analysis to predict the accuracy with which true electrical structure may be recovered from CSEM data.

For the specific scenario of the North Amethyst reservoir modelled here, CSEM data would suggest that based on true, or, as accurately modelled as possible, hydrocarbon content and distribution, the BNA reservoir does not present a favourable target for detection. It has been demonstrated however that with increased water depth and or decreased burial depth, anomaly generation is more substantial. The nearby Orphan and Flemish Pass basins may be more prospective or favourable environments for acquisition of marine CSEM data due to their greater water depths. Given regional lithostratigraphy, the prospect of hydrocarbon targets with substantially shallower burial depth is poor within the Jeanne d'Arc Basin. The other major reservoir-bearing intervals in the Jeanne d'Arc Basin, including the Hibernia and Jeanne d'Arc Formations, occur at greater burial depths than the BNA Formation. For example, in the Hebron field, which includes Ben Nevis, Hibernia, and Jeanne d'Arc reservoirs, average reservoir depths in TVDss are 1900 m, 2950 m, and 2900–4400 m, respectively (ExxonMobil Canada Properties, 2011). Based on simulations presented here, it is conjectured that hydrocarbon anomaly generation at these burial depths would require accumulations of greater lateral extent and/or resistivity-thickness product than the North Amethyst hydrocarbon-bearing BNA interval.

On a final note, the North Amethyst field model presented here considers the hydrocarbon-

bearing BNA interval in isolation, despite the presence of other hydrocarbon pools in lateral and vertical proximity. The possible implications of omission of these bodies in the resistivity model has been briefly discussed (Sections 6.4.2.2 and 6.5.1). In the future, should modelling capabilities permit, it would be of interest to perform simulations for models including hydrocarbon accumulations on a regional rather than local scale to observe the effect on the measured CSEM response.

Chapter 7

Conclusions

3D CSEM data has been simulated for several simple marine models existing in the literature as well as a realistic reservoir model using the CSEM3DFWD finite-element code in conjunction with unstructured meshes. 3D finite-element simulations have demonstrated that the CSEM response to resistivity structure with substantial lateral variability can deviate significantly from 1D predictions; 3D simulation tools are therefore required for reliable interpretation of CSEM data. The CSEM3DFWD code has been demonstrated to accurately simulate CSEM data for models having finite-depth water and infinite air layers, scenarios that had not previously been tested.

Unstructured meshes have been demonstrated to be able to accurately represent complex resistivity structure arising from topography and stratigraphy, as in the seafloor topography and North Amethyst reservoir models. The implementation of finite-element schemes on unstructured meshes can however be challenging, as elaborated below. To the author's knowledge, the North Amethyst reservoir model presented here represents one of the few examples in the 3D EM modelling literature of discretization of a realistic 3D model using unstructured tetrahedral meshes. Modelling completed for the North Amethyst model does not comprise a full CSEM feasibility study, but does contribute to our understanding of the

conditions for CSEM hydrocarbon detection in the given regional stratigraphic setting.

In our opinion, the most significant impediment to modelling of more realistic, detailed earth models is design and generation of the unstructured mesh, or further, understanding how different parameters such as cell size, grading, and boundaries ultimately affect the quality of the mesh and behaviour of the solution. Iterative solutions remain susceptible to ill-conditioning, and thus are very much tied to the quality of the mesh. Experience with fairly simple earth models has exposed multiple areas of difficulty related to unstructured mesh design, in particular for models which feature thin layers and/or fine structural detail. Ad hoc, user-overseen design of meshes of suitable quality for finite-element modelling has proven to be cumbersome, requiring a great amount of time and input from the user. This work has underscored the importance of improving mesh design and refinement procedures to facilitate extension of modelling using unstructured meshes to more realistic, and by requisite more complicated, earth models.

In view of mesh quality and system conditioning, mesh design best practice is to allow adequate grading of the mesh from small cell size at the domain interior to large cell size at its boundaries; this may require artificial extension of the mesh or coarsening of structure away from the source-receiver line. Constraining features, while required for accurate geometric representation of geoelectric structure, should generally be kept to a minimum or coarsened where possible (e.g., background structure located far from the source-receiver line) so as not to interfere any more than necessary with the quality tetrahedralization of TetGen. Such measures not only improve conditioning of the system, but keep problem size in terms of cells, and hence nodes and edges, to a minimum. It is recognized however that this may not always be possible when high resolution of structural detail is required, such as for small or thin targets, or for significant lateral resistivity variations in proximity to source and receivers, e.g., where seafloor topography is highly variable or non-target resistive structures are present in the shallow subsurface. Further, as problem size increases,

ill-conditioning of the system may be compounded, such that mesh quality which was acceptable for a smaller mesh may no longer be acceptable for a larger mesh. It may be beneficial to explore alternative preconditioning measures in the future to further improve the condition number of the system matrix prior to iterative solution.

Two models in this study have featured irregular structural or stratigraphic surfaces, namely the seafloor topography model presented in Chapter 5 and the North Amethyst reservoir model presented in Chapter 6, although a different approach was taken for each in regards to surface meshing. In the former, a regular, rectilinear node spacing was provided as input to Triangle, while in the latter, only a polygon outlining the extent of the surface was provided. When constructing meshes featuring topographic surfaces derived from other data sets, it is suggested herein as best practice to supply to Triangle as input for triangulation only a polygon defining the lateral boundary of the surface instead of the original surface node data with arbitrary density and spacing. This allows Triangle to triangulate the surface with the least amount of constraints, thus allowing the best quality triangulation to be generated. The size of the cells can be controlled through implementation of an area constraint rather than an explicit node density. Depth, or the z-coordinate, can later be interpolated on the triangulated surface from the original node data.

Concerning mesh refinement to ensure solution accuracy at observation points and where the fields vary rapidly (e.g., at the source and near offset and in proximity to large conductivity contrasts), implementation of an adaptive mesh refinement strategy may be advantageous so as to only increase refinement where necessary to improve the solution (see Key, 2009; Schwarzbach et al., 2011). It is difficult for the user to discern, prior to solution, where and how much refinement is necessary for solution accuracy. Further, manual refinement via insertion of artificial structures is very problem-specific. Consider simulation of a full 3D CSEM survey requiring forward solutions for many source-receiver geometries and frequencies. Manual design of multiple meshes, each optimized for a given

source-receiver geometry, would be impractical. It may therefore be beneficial to explore schemes which automate and optimize mesh generation according to such factors as source frequency, source location, and source-receiver geometry (see Plessix et al., 2007; Commer and Newman, 2008).

As increasingly realistic and complicated models are addressed, accurate reproduction of geoelectric structure will necessitate a larger mesh in terms of cell size. Strategies for minimizing system ill-conditioning have been proposed which also act to minimize problem size, although they require user input. The attractiveness of iterative solutions stems from their more moderate memory requirements as compared to direct solutions, although it has been demonstrated herein that they may still be very high. The presently non-parallelized structure of the forward code, in combination with finite computational resources, dictate an upper limit on the problem size, and consequently the amount of structural detail, that can be handled at present. In the future, it may be advantageous to investigate domain decomposition procedures to reduce problem size and enable parallelization (see Puzyrev et al., 2013).

As a final comment, 3D forward modelling is limited in its application in and of itself; it would ultimately be desirable to implement CSEM3DFWD as the forward solve procedure in an inversion routine that may be used to invert real-life CSEM data to produce resistivity images of the subsurface which may be interpreted independently, or preferably, in conjunction with other geological or geophysical data.

References

Abubakar, A., T. M. Habashy, V. L. Druskin, L. Knizhnerman, and D. Alumbaugh, 2008, 2.5D forward and inverse modeling for interpreting low-frequency electromagnetic measurements: Geophysics, **73**, no. 4, F165–F177.

Alcocer, J. A. E., M. V. García, H. S. Soto, F. Roth, D. Baltar, P. T. Gabrielsen, and V. R. Paramo, 2012, Experience from using 3D CSEM in the Mexican deepwater exploration program: SEG Technical Program Expanded Abstracts, 1–5.

Alumbaugh, D. L., G. A. Newman, L. Prevost, and J. N. Shadid, 1996, Three-dimensional wideband electromagnetic modeling on massively parallel computers: Radio Science, **31**, no. 1, 1–23.

Amundsen, L., L. Løseth, R. Mittet, S. Ellingsrud, and B. Ursin, 2006, Decomposition of electromagnetic fields into upgoing and downgoing components: Geophysics, **71**, no. 5, G211–G223.

Anderson, W. L., 1979, Numerical integration of related Hankel-transforms of orders 0 and 1 by adaptive digital filtering: Geophysics, **44**, no. 7, 1287–1305.

———, 1982, Fast Hankel-transforms using related and lagged convolutions: ACM Transactions on Mathematical Software, **8**, no. 4, 344–368.

———, 1989, A hybrid fast Hankel transform algorithm for electromagnetic modeling: Geophysics, **54**, no. 2, 263–266.

Andréis, D., and L. MacGregor, 2007, Time domain versus frequency domain CSEM in

shallow water: SEG Technical Program Expanded Abstracts, 643–647.

———, 2008, Controlled-source electromagnetic sounding in shallow water: Principles and applications: Geophysics, **73**, no. 1, F21–F32.

Ansari, S., 2014, Three dimensional finite-element numerical modeling of geophysical electromagnetic problems using tetrahedral unstructured grids: PhD thesis, Memorial University of Newfoundland.

Ansari, S., and C. G. Farquharson, 2011, 3D finite-element simulation of electromagnetic data for inductive and galvanic components: SEG Technical Program Expanded Abstracts, 766–769.

———, 2013, Three-dimensional modeling of controlled-source electromagnetic response for inductive and galvanic components: Presented at the 5th International Symposium on Three-Dimensional Electromagnetics, SEGJ.

———, 2014, 3D finite-element modeling of electromagnetic data using vector and scalar potentials and unstructured grids: Geophysics, **79**, no. 4, E149–E165.

Ansari, S., C. G. Farquharson, and S. MacLachlan, 2015, Gauged vector finite-element schemes for the geophysical EM problem for unique potentials and fields: SEG Technical Program Expanded Abstract, 801–805.

Archie, G. E., 1942, The electrical resistivity log as an aid in determining some reservoir characteristics: Transactions of the AIME, **146**, no. 1, 54–62.

Aruliah, D. A., U. M. Ascher, E. Haber, and D. Oldenburg, 2001, A method for the forward modelling of 3-D electromagnetic quasi-static problems: Mathematical Models and Methods in Applied Sciences, **11**, no. 1, 1–21.

Atkinson, I., and P. Fagan, 2000, Sedimentary basins and hydrocarbon potential of Newfoundland and Labrador: Report 2000-01, Department of Mines and Energy, Government of Newfoundland and Labrador. (Available at `http://www.nr.gov.nl.ca/nr/publications/energy/sedimentarybasins.pdf` [Accessed Au-

gust 2015]).

Avdeev, D. B., 2005, Three-dimensional electromagnetic modelling and inversion from theory to application: Surveys in Geophysics, **26**, 767–799.

Axelsson, O., and A. Kucherov, 2000, Real valued iterative methods for solving complex symmetric linear systems: Numerical linear algebra with applications, **7**, no. 4, 197–218.

Ayachit, U., 2015, The ParaView Guide. (Available at `http://www.paraview.org/paraview-guide/` [Accessed August 2015]).

Ayre, M., 2011, Report of the Hebron Public Review Commissioner for the Hebron Development Application. (Available at `http://www.cnlopb.ca/pdfs/hebpubrev.pdf` [Accessed August 2015]).

Badea, E. A., M. E. Everett, G. A. Newman, and O. Biro, 2001, Finite-element analysis of controlled-source electromagnetic induction using Coulomb-gauged potentials: Geophysics, **66**, no. 3, 786–799.

Bassiouni, Z., 1994, Theory, measurement and interpretation of well logs: Society of Petroleum Engineers, volume **4** *of* SPE Textbook Series.

Blakely, R. J., 1996, Potential theory in gravity and magnetic applications: Cambridge University Press.

Börner, R.-U., O. G. Ernst, and K. Spitzer, 2008, Fast 3-D simulation of transient electromagnetic fields by model reduction in the frequency domain using Krylov subspace projection: Geophysical Journal International, **173**, no. 3, 766–780.

Bouchrara, S., L. MacGregor, J. Tomlinson, U. Strecker, J. Fan, X. Ran, and G. Yu, 2012, Integrated analysis of well log, seismic and CSEM data for prospect appraisal: A case study from West Africa: SEG Technical Program Expanded Abstracts, 1–5.

Boyce, T. T. M., 1996, Finite element modelling for marine electromagnetic petroleum exploration: Master's thesis, University of Manitoba, Winnipeg, Manitoba, Canada.

C-NLOPB, 2001, Decision Report 2001.01: White Rose Canada-Newfoundland Benefits

Plan and White Rose Development Plan. (Available at http://www.cnlopb.ca/news/pdfs/d01_01.pdf [Accessed August 2015]).

———, 2008, Decision Report 2008.03: Staff Analysis of the North Amethyst Satellite Tie-back Project. (Available at http://www.cnlopb.ca/news/pdfs/sadev.pdf [Accessed August 2015]).

———, 2014, Canada-Newfoundland & Labrador Offshore Petroleum Board (C-NLOPB) Scheduled Land Tenure. (Available at http://www.cnlopb.ca/pdfs/cfntechdoc.pdf [Accessed August 2015]).

———, 2015a, Canada-Newfoundland & Labrador Offshore Jeanne d'Arc Region Licence Information. (Available at http://www.cnlopb.ca/pdfs/maps/jda.pdf [Accessed August 2015]).

———, 2015b, Canada-Newfoundland & Labrador Offshore Licence Information. (Available at http://www.cnlopb.ca/pdfs/maps/nlol.pdf [Accessed August 2015]).

———, 2015c, Canada-Newfoundland & Labrador Offshore Petroleum Board (C-NLOPB) 2014–15 Annual Report. (Available at http://www.cnlopb.ca/pdfs/ar2015e.pdf [Accessed August 2015]).

———, 2015d, Canada-Newfoundland & Labrador Offshore Sedimentary Basins. (Available at http://www.cnlopb.ca/pdfs/maps/nlsb.pdf [Accessed August 2015]).

———, 2015e, Jeanne d'Arc Basin Lithostratigraphy. (Available at http://www.cnlopb.ca/pdfs/maps/xdb_lith.pdf [Accessed August 2015]).

Carazzone, J. J., O. M. Burtz, K. E. Green, and D. A. Pavlov, 2005, Three dimensional imaging of marine CSEM data: SEG Technical Program Expanded Abstracts, 575–578.

Carazzone, J. J., T. A. Dickens, K. E. Green, C. Jing, L. A. Wahrmund, D. E. Willen, M. Commer, and G. A. Newman, 2008, Inversion study of a large marine CSEM survey:

SEG Technical Program Expanded Abstracts, 644–647.

Chave, A. D., 1983, Numerical integration of related Hankel transforms by quadrature and continued fraction expansion: Geophysics, **48**, no. 12, 1671–1686.

———, 2009, On the electromagnetic fields produced by marine frequency domain controlled sources: Geophysical Journal International, **179**, no. 3, 1429–1457.

Chave, A. D., and C. S. Cox, 1982, Controlled electromagnetic sources for measuring electrical conductivity beneath the oceans: 1. Forward problem and model study: Journal of Geophysical Research, **87**, no. B7, 5327–5338.

Chave, A. D., A. H. Flosadóttir, and C. S. Cox, 1990, Some comments on the seabed propagation of VLF/ULF electromagnetic fields: Radio Science, **25**, no. 5, 825–836.

Chave, A. D., and A. G. Jones, 2012, The magnetotelluric method: Theory and practice: Cambridge University Press.

Chen, J., and D. L. Alumbaugh, 2011, Three methods for mitigating airwaves in shallow water marine controlled-source electromagnetic data: Geophysics, **76**, no. 2, F89–F99.

Cheng, S.-W., T. K. Dey, and J. R. Shewchuk, 2012, Delaunay mesh generation: CRC Press.

Colombo, D., G. McNeice, N. Raterman, M. Zinger, D. Rovetta, and E. S. Curiel, 2014, Exploration beyond seismic: The role of electromagnetics and gravity gradiometry in deep water subsalt plays of the Red Sea: Interpretation, **2**, no. 3, SH33–SH53.

Commer, M., and G. A. Newman, 2008, New advances in three-dimensional controlled-source electromagnetic inversion: Geophysical Journal International, **172**, no. 2, 513–535.

Commer, M., G. A. Newman, J. J. Carazzone, T. A. Dickens, K. E. Green, L. A. Wahrmund, D. E. Willen, and J. Shiu, 2008, Massively parallel electrical-conductivity imaging of hydrocarbons using the IBM Blue Gene/L supercomputer: IBM Journal of Research and Development, **52**, no. 1, 93–103.

Connell, D., and K. Key, 2013, A numerical comparison of time and frequency-domain marine electromagnetic methods for hydrocarbon exploration in shallow water: Geophysical Propsecting, **61**, no. 1, 187–199.

Constable, S., 2006, Marine electromagnetic methods—A new tool for offshore exploration: The Leading Edge, **25**, no. 4, 438–444.

———, 2010, Ten years of marine CSEM for hydrocarbon exploration: Geophysics, **75**, no. 5, 75A67–75A81.

———, 2013, Review paper: Instrumentation for marine magnetotelluric and controlled source electromagnetic sounding: Geophysical Prospecting, **61**, 505–532.

Constable, S., and L. J. Srnka, 2007, An introduction to marine controlled-source electromagnetic methods for hydrocarbon exploration: Geophysics, **72**, no. 2, WA3–WA12.

Constable, S. C., A. S. Orange, G. M. Hoversten, and H. F. Morrison, 1998, Marine magnetotellurics for petroleum exploration Part I: A sea-floor equipment system: Geophysics, **63**, no. 3, 816–825.

Constable, S. C., R. L. Parker, and C. G. Constable, 1987, Occam's inversion: A practical algorithm for generating smooth models from electromagnetic sounding data: Geophysics, **52**, no. 3, 289–300.

Constable, S. C., and C. J. Weiss, 2006, Mapping thin resistors and hydrocarbons with marine EM methods: Insights from 1D modeling: Geophysics, **71**, no. 2, G43–G51.

Danielsen, J., and R. Bekker, 2011, The future of marine CSEM: First Break, **29**, no. 4, 77–81.

Du, Q., D. Wang, and L. Zhu, 2009, On mesh geometry and stiffness matrix conditioning for general finite element spaces: Society for Industrial and Applied Mathematics Journal on Numerical Analysis, **47**, no. 2, 1421–1444.

Edwards, N., 2005, Marine controlled source electromagnetics: Principles, methodologies, future commercial applications: Surveys in Geophysics, **26**, no. 6, 675–700.

Eidesmo, T., S. Ellingsrud, L. M. MacGregor, S. Constable, M. C. Sinha, S. Johansen, F. N. Kong, and H. Westerdahl, 2002, Sea Bed Logging (SBL), a new method for remote and direct identification of hydrocarbon filled layers in deepwater areas: First Break, **20**, no. 3, 144–152.

Ellingsrud, S., T. Eidesmo, S. Johansen, M. C. Sinha, L. M. MacGregor, and S. Constable, 2002, Remote sensing of hydrocarbon layers by seabed logging (SBL): Results from a cruise offshore Angola: The Leading Edge, **21**, no. 10, 972–982.

Ellis, M., and R. Keirstead, 2011, Geological parameters effecting controlled-source electromagnetic feasibility: A North Sea sand reservoir example: SEG Technical Program Expanded Abstracts, 771–774.

Enachescu, M., S. Kearsey, J. Hogg, P. Einarsson, S. Nader, and J. Smee, 2004, Orphan Basin, offshore Newfoundland, Canada: Structural and tectonic framework, petroleum systems and exploration potential: SEG Technical Program Expanded Abstracts, 382–385.

Enachescu, M. E., 2013, Petroleum exploration opportunities in the Carson Basin, Newfoundland and Labrador offshore area: Call for Bids NL13-02, Area "C" – Carson Basin, Parcels 1 to 4. Government of Newfoundland Department of Natural Resources. (Available at `http://www.nr.gov.nl.ca/nr/invest/PetExOpCarsonNL1302.pdf` [Accessed August 2015]).

———, 2014, Petroleum exploration opportunities in the Flemish Pass Basin, Newfoundland and Labrador offshore area: Call for Bids NL13-01, Area "C" – Flemish Pass, Parcel 1. Government of Newfoundland Department of Natural Resources. (Available at `http://www.nr.gov.nl.ca/nr/invest/NL1301FlemishPassBasinEnachescu.pdf` [Accessed August 2015]).

Everett, M. E., and R. N. Edwards, 1993, Transient marine electromagnetics: the 2.5-D forward problem: Geophysical Journal International, **113**, no. 3, 545–561.

ExxonMobil Canada Properties, 2011, Consolidated Hebron Development Plan. (Available at http://www.cnlopb.ca/pdfs/conhebdevplan.pdf [Accessed August 2015]).

Flosadóttir, A. H., and S. Constable, 1996, Marine controlled source electromagnetic sounding 1: Modeling and experimental design: Journal of Geophysical Research, **101**, no. B3, 5507–5517.

Gist, G., A. Ciucivara, R. Houck, M. Rainwater, D. Willen, and J.-J. Zhou, 2013, Case study of a CSEM false positive - Orphan Basin, Canada: SEG Technical Program Expanded Abstracts, 805–809.

Grant, F. S., and G. F. West, 1965, Interpretation theory in applied geophysics: McGraw-Hill Book Company.

Green, K. E., O. M. Burtz, L. A. Wahrmund, C. Xia, G. Zelewski, T. Clee, I. Gallegos, A. A. Martinez, M. J. Stiver, C. M. Rodriguez, and J. Zhang, 2005, R3M case studies: Detecting reservoir resistivity in complex settings: SEG Technical Program Expanded Abstracts, 572–574.

Griffiths, D. J., 1999, Introduction to electrodynamics: Prentice-Hall.

Guptasarma, D., and B. Singh, 1997, New digital linear filters for Hankel J_0 and J_1 transforms: Geophysical Prospecting, **45**, no. 5, 745–762.

Haber, E., 2014, Computational methods in geophysical electromagnetics: Society of Industrial and Applied Mathematics.

Harrington, R. F., 1961, Time-harmonic electromagnetic fields: McGraw-Hill.

Hohmann, G. W., 1975, Three-dimensional induced polarization and electromagnetic modeling: Geophysics, **40**, no. 2, 309–324.

———, 1988, Numerical modeling for electromagnetic methods of geophysics, *in* Nabighian, M. N., ed., Electromagnetic Methods in Applied Geophysics: Society of Exploration Geophysicists, **1**, 313–363.

Hohmann, G. W., and A. P. Raiche, 1988, Inversion of controlled-source electromagnetic data, *in* Nabighian, M. N., ed., Electromagnetic Methods in Applied Geophysics: Society of Exploration Geophysicists, **2**, 469–503.

Hoversten, G. M., G. A. Newman, N. Geier, and G. Flanagan, 2006, 3D modeling of a deepwater EM exploration survey: Geophysics, **71**, no. 5, G239–G248.

Husky Oil Operations Limited, 2001, White Rose Development Application: Volume 2 - Development Plan. (Available at `http://www.cnlopb.ca/pdfs/wrda_vol2.pdf` [Accessed August 2015]).

Jin, J., 2002, The finite element method in electromagnetics: John Wiley & Sons.

———, 2014, The finite element method in electromagnetics, 3 ed.: John Wiley & Sons.

Kearey, P., M. Brooks, and I. Hill, 2002, An introduction to geophysical exploration, 3 ed.: Blackwell Publishing.

Keller, G. V., 1988, Rock and mineral properties, *in* Nabighian, M. N., ed., Electromagnetic Methods in Applied Geophysics: Society of Exploration Geophysicists, **1**, 13–51.

Key, K., 2003, Application of broadband marine magnetotelluric exploration to a 3D salt structure and a fast-spreading ridge: PhD thesis, University of California, San Diego, La Jolla, California, United States.

———, 2009, 1D inversion of multicomponent, multifrequency marine CSEM data: Methodology and synthetic studies for resolving thin resistive layers: Geophysics, **74**, no. 2, F9–F20.

———, 2012a, Is the Hankel transform faster than quadrature?: Geophysics, **77**, no. 3, F21–F30.

———, 2012b, Marine electromagnetic studies of seafloor resources and tectonics: Surveys in Geophysics, **33**, 135–167.

———, 2012c, Marine EM inversion using unstructured grids: a 2D parallel adaptive finite element algorithm: SEG Technical Program Expanded Abstracts, 1–5.

Key, K., and J. Ovall, 2011, A parallel goal-oriented adaptive finite element method for 2.5-D electromagnetic modeling: Geophysical Journal International, **186**, no. 1, 137–154.

Kong, F. N., S. E. Johnstad, T. Røsten, and H. Westerdahl, 2008, A 2.5D finite-element-modeling difference method for marine CSEM modeling in stratified anisotropic media: Geophysics, **43**, no. 1, F9–F19.

Li, Y., and S. Constable, 2007, 2D marine controlled-source electromagnetic modeling: Part 2—The effect of bathymetry: Geophysics, **72**, no. 2, WA63–WA71.

Li, Y., and K. Key, 2007, 2D marine controlled-source electromagnetic modeling: Part 1—An adaptive finite-element algorithm: Geophysics, **72**, no. 2, WA51–WA62.

Li, Y.-G., and S. Constable, 2010, Transient electromagnetic in shallow water: Insights from 1D modeling: Chinese Journal of Geophysics, **53**, no. 3, 737–742.

Løseth, L. O., 2011, Insight into the marine controlled-source electromagnetic signal propagation: Geophysical Prospecting, **59**, no. 1, 145–160.

Løseth, L. O., H. M. Pedersen, B. Ursin, L. Amundsen, and S. Ellingsrud, 2006, Low-frequency electromagnetic fields in applied geophysics: Waves or diffusion?: Geophysics, **71**, no. 4, W29–W40.

Løseth, L. O., and B. Ursin, 2007, Electromagnetic fields in planarly layered anisotropic media: Geophysical Journal International, **170**, no. 1, 44–80.

Lu, X., and L. J. Srnka, 2009, Logarithmic spectrum transmitter waveform for controlled-source electromagnetic surveying: U.S. Patent No. 7,539,279.

Lu, X., D. Willen, J. Z[hang], and I. Gallegos, 2006, Marine CSEM data processing techniques: SEG Technical Program Expanded Abstracts, 704–708.

Lu, X., and D. E. Willen, 2011, Electromagnetic data processing system: U.S. Patent No. 7,979,211.

MacGregor, L., D. Andréis, J. Tomlinson, and N. Barker, 2006, Controlled-source electromagnetic imaging on the Nuggets-1 reservoir: The Leading Edge, **25**, no. 8, 984–992.

MacGregor, L., and M. Sinha, 2000, Use of marine controlled-source electromagnetic sounding for sub-basalt exploration: Geophysical Prospecting, **48**, no. 6, 1091–1106.

MacGregor, L., M. Sinha, and S. Constable, 2001, Electrical resistivity structure of the Valu Fa Ridge, Lau Basin, from marine controlled-source electromagnetic sounding: Geophysical Journal International, **146**, no. 1, 217–236.

MacGregor, L., and J. Tomlinson, 2014, Marine controlled-source electromagnetic methods in the hydrocarbon industry: A tutorial on method and practice: Interpretation, **2**, no. 3, SH13–SH32.

Martinez, A., and A. P. Byrnes, 2001, Modeling dielectric-constant values of geologic materials: An aid to ground-penetrating radar data collection and interpretation: Current Research in Earth Sciences, **247**, no. 1, 1–16.

McAlpine, K. D., 1990, Mesozoic stratigraphy, sedimentary evolution, and petroleum potential of the Jeanne d'Arc Basin, Grand Banks of Newfoundland: Geological Survey of Canada Paper 89-17.

Mittet, R., and J. P. Morten, 2013, The marine controlled-source electromagnetic method in shallow water: Geophysics, **78**, no. 2, E67–E77.

Mittet, R., and T. Schaug-Pettersen, 2008, Shaping optimal transmitter waveforms for marine CSEM surveys: Geophysics, **73**, no. 3, F97–F104.

Myer, D., S. Constable, and K. Key, 2011, Broad-band waveforms and robust processing for marine CSEM surveys: Geophysical Journal International, **184**, 689–698.

Newman, G. A., 2014, A review of high-performance computational strategies for modeling and imaging of electromagnetic induction data: Surveys in Geophysics, **35**, no. 1, 85–100.

Newman, G. A., and D. L. Alumbaugh, 1995, Frequency-domain modelling of airborne electromagnetic responses using staggered finite differences: Geophysical Prospecting, **43**, 1021–1042.

———, 1997, Three-dimensional massively parallel electromagnetic inversion—I. Theory: Geophysical Journal International, **128**, 345–354.

Newman, G. A., M. Commer, and J. J. Carazzone, 2010, Imaging CSEM data in the presence of electrical anisotropy: Geophysics, **75**, no. 2, F51–F61.

Palacky, G. J., 1988, Resistivity characteristics of geologic targets, *in* Nabighian, M. N., ed., Electromagnetic Methods in Applied Geophysics: Society of Exploration Geophysicists, **1**, 52–129.

Plessix, R.-E., M. Darnet, and W. A. Mulder, 2007, An approach for 3D multisource, multifrequency CSEM modeling: Geophysics, **72**, no. 5, SM177–SM184.

Puzyrev, V., J. Koldan, J. de la Puente, G. Houzeaux, M. Vázquez, and J. M. Cela, 2013, A parallel finite-element method for three-dimensional controlled-source electromagnetic forward modelling: Geophysical Journal International, **193**, no. 2, 678–693.

Raiche, A. P., 1974, An integral equation approach to three-dimensional modelling: Geophysical Journal of the Royal Astronomical Society, **36**, no. 2, 363–376.

Saad, Y., 1994, SPARSKIT: A basic tool kit for sparse matrix computations (Version 2). (Available at `http://www-users.cs.umn.edu/~saad/software/SPARSKIT/` [Accessed January 2013]).

———, 2003, Iterative methods for sparse linear systems, 2 ed.: Society for Industrial and Applied Mathematics.

Sasaki, Y., and M. A. Meju, 2009, Useful characteristics of shallow and deep marine CSEM responses inferred from 3D finite-difference modeling: Geophysics, **74**, no. 5, F67–F76.

Schwarzbach, C., 2009, Stability of finite element solutions to Maxwell's equations in frequency domain: PhD thesis, Technische Universität Bergakademie Freiberg, Freiberg, Germany.

Schwarzbach, C., R.-U. Börner, and K. Spitzer, 2011, Three-dimensional adaptive higher order finite element simulation for geo-electromagnetics – a marine CSEM example:

Geophysical Journal International, **187**, no. 1, 63–74.

Sen, M., and P. L. Stoffa, 1995, Global optimization methods in geophysical inversion: Elsevier Science B.V., volume **4** *of* Advances in exploration geophysics.

Shewchuk, J. R., 1996, Triangle: Engineering a 2D quality mesh generator and Delaunay triangulator, *in* Lin, M. C., and D. Manocha, eds., Applied Computational Geometry: Towards Geometric Engineering: Springer-Verlag, volume **1148** *of* Lecture Notes in Computer Science, 203–222. (From the First ACM Workshop on Applied Computational Geometry).

———, 2002, What is a good linear finite element? Interpolation, conditioning, anisotropy, and quality measures: Technical Report, Department of Computer Science, University of California at Berkeley. (Available at `http://www.cs.berkeley.edu/~jrs/papers/elem.pdf` [Accessed August 2015]).

Si, H., 2006, TetGen: A quality tetrahedral mesh generator and three-dimensional Delaunay triangulator: Version 1.4 User's Manual. (Available at `http://wias-berlin.de/software/tetgen/files/tetgen-manual.pdf` [Accessed August 2015]).

———, 2009, TetGen: A quality tetrahedral mesh generator and a 3D Delaunay triangulator: Version 1.4.3. (Available at `http://wias-berlin.de/software/tetgen/tetgen143.html` [Accessed August 2015]).

———, 2013, TetGen: A quality tetrahedral mesh generator and 3D Delaunay triangulator: Version 1.5 User's Manual. (Available at `http://wias-berlin.de/software/tetgen/1.5/doc/manual/manual.pdf` [Accessed August 2015]).

———, 2015, TetGen, a Delaunay-based quality tetrahedral mesh generator: ACM Transactions on Mathematical Software, **41**, no. 2, article no. 11, 36 pages.

Sinclair, I. K., K. D. McAlpine, D. F. Sherwin, and N. J. McMillan, 1992, Part I: Geological framework, *in* Petroleum resources of the Jeanne d'Arc Basin and environs, Grand Banks, Newfoundland: Geological Survey of Canada Paper 92-8, 1–38.

Snieder, R., and J. Trampert, 1999, Inverse problems in geophysics, *in* Wirgin, A., ed., Wavefield inversion: Springer-Verlag, 119–190.

Srnka, L. J., J. J. Carazzone, M. S. Ephron, and E. A. Eriksen, 2006, Remote reservoir resistivity mapping: The Leading Edge, **25**, no. 8, 972–975.

Stamnes, J. J., 1986, Waves in focal regions: Adam Hilger.

Streich, R., 2009, 3D finite-difference frequency-domain modeling of controlled-source electromagnetic data: Direct solution and optimization for accuracy: Geophysics, **74**, no. 5, F95–F105.

Streich, R., M. Becken, and O. Ritter, 2011, 2.5D controlled-source EM modeling with general 3D source geometries: Geophysics, **76**, no. 6, F387–F393.

Swidinsky, A., 2015, On guided versus deflected fields in controlled-source electromagnetics: Geophysical Journal International, **201**, 1738–1742.

Telford, W. M., L. P. Geldart, and R. E. Sheriff, 1990, Applied geophysics, 2 ed.: Cambridge University Press.

Um, E. S., 2011, Three-dimensional finite-element time-domain modeling of the marine controlled-source electromagnetic method: PhD thesis, Stanford University, Stanford, California, United States.

Um, E. S., and D. L. Alumbaugh, 2007, On the physics of the marine controlled-source electromagnetic method: Geophysics, **72**, no. 2, WA13–WA26.

Um, E. S., J. M. Harrise, and D. L. Alumbaugh, 2010, 3D time-domain simulation of electromagnetic diffusion phenomena: A finite-element electric-field approach: Geophysics, **75**, no. 4, F115–F126.

Unsworth, M., and D. Oldenburg, 1995, Subspace inversion of electromagnetic data: application to mid-ocean-ridge exploration: Geophysical Journal International, **123**, no. 1, 161–168.

Unsworth, M. J., B. J. Travis, and A. D. Chave, 1993, Electromagnetic induction by a finite

electric dipole source over a 2-D earth: Geophysics, **58**, no. 2, 198–214.

Vieira da Silva, N., J. V. Morgan, L. MacGregor, and M. Warner, 2012, A finite element multifrontal method for 3D CSEM modeling in the frequency domain: Geophysics, **77**, no. 2, E101–E115.

Vozoff, K., 1991, The magnetotelluric method, *in* Nabighian, M. N., ed., Electromagnetic Methods in Applied Geophysics: Society of Exploration Geophysicists, **2**, 641–707.

Wait, J. R., 1962, Electromagnetic waves in stratified media: Pergamon Press.

Wannamaker, P. E., and G. W. Hohmann, 1982, Electromagnetic modeling of three-dimensional bodies in layered earths using integral equations: Report DOE/ID/12079-50; ESL-64, Earth Science Laboratory, University of Utah Research Institute. Prepared for the U.S. Department of Energy. (Available at `http://www.osti.gov/geothermal/servlets/purl/5349441` [Accessed December 2014]).

Wannamaker, P. E., G. W. Hohmann, and W. A. SanFilipo, 1984, Electromagnetic modeling of three-dimensional bodies in layered earths using integral equations: Geophysics, **49**, no. 1, 60–74.

Ward, S. H., and G. W. Hohmann, 1988, Electromagnetic theory for geophysical applications, *in* Nabighian, M. N., ed., Electromagnetic Methods in Applied Geophysics: Society of Exploration Geophysicists, **1**, 131–312.

Weidelt, P., 2007, Guided waves in marine CSEM: Geophysical Journal International, **171**, no. 1, 153–176.

Weiss, C. J., 2007, The fallacy of the “shallow-water problem" in marine CSEM exploration: Geophysics, **72**, no. 6, A93–A97.

———, 2013, Project APhiD: A Lorenz-gauged $\mathbf{A} - \phi$ decomposition for parallelized computation of ultra-broadband electromagnetic induction in a fully heterogeneous Earth: Computers & Geosciences, **58**, 40–52.

Weiss, C. J., and S. C. Constable, 2006, Mapping thin resistors and hydrocarbons with

marine EM methods, Part II — Modeling and analysis in 3D: Geophysics, **71**, no. 6, G321–G332.

Weiss, C. J., and G. A. Newman, 2002, Electromagnetic induction in a fully 3-D anisotropic earth: Geophysics, **67**, no. 4, 1104–1114.

Weitemeyer, K., 2008, Marine electromagnetic methods for gas hydrate characterization: PhD thesis, University of California, San Diego, La Jolla, California, United States.

Weitemeyer, K., and S. Constable, 2010, Mapping shallow geology and gas hydrate with marine CSEM surveys: First Break, **28**, no. 6, 97–102.

Weitemeyer, K., S. Constable, and M. Tréhu, 2011, A marine electromagnetic survey to detect gas hydrate at Hydrate Ridge, Oregon: Geophysical Journal International, **187**, no. 1, 45–62.

West, G. F., and J. C. Macnae, 1988, Physics of the electromagnetic induction exploration method, *in* Nabighian, M. N., ed., Electromagnetic Methods in Applied Geophysics: Society of Exploration Geophysicists, **2**, 5–45.

Wilkinson, A. J., 2011, EEE3055F - Module A: Electromagnetic Fields and Waves: 2011 Lecture Notes, Department of Electrical Engineering, University of Cape Town. (Available at `http://local.eleceng.uct.ac.za/courses/EEE3055F/` [Accessed July 2013]).

Yee, K. S., 1966, Numerical solution of initial boundary value problems involving Maxwell's equations in isotropic media: IEEE Transactions on Antennas and Propagation, **14**, no. 3, 302–307.

Zhdanov, M. S., 2002, Geophysical inverse theory and regularization problems: Elsevier Science B.V., volume **36** *of* Methods in geochemistry and geophysics.

———, 2009, Geophysical electromagnetic theory and methods: Elsevier B.V., volume **43** *of* Methods in geochemistry and geophysics.

Zonge, K. L., and L. J. Hughes, 1988, Controlled source audio-frequency magnetotellurics,

in Nabighian, M. N., ed., Electromagnetic Methods in Applied Geophysics: Society of Exploration Geophysicists, **2**, 713–809.

Appendix A

MARDIP1D: A 1D marine HED forward code

The 1D marine HED forward code used throughout this thesis, MARDIP1D, is based on closed-form Hankel transform expressions for the electric and magnetic fields due to an x-directed current element, i.e., a HED. The expressions were derived in Wannamaker and Hohmann (1982) and Wannamaker et al. (1984) for specification of the electric and magnetic tensor Green's functions for a time-harmonic electric dipole in a layered earth. Since we consider the special case of the observation points being located in the same earth layer as the source, as is true in the marine CSEM method, we require expressions for the fields only in the source layer. These expressions were numerically evaluated using a fast Hankel transform subroutine, the algorithm for which is described in Anderson (1979).

A.1 Theory

For an earth composed of n homogeneous layers, we wish to determine the electric and magnetic fields at some point $\mathbf{r} = (x, y, z)$ in layer j which contains a current element $\mathbf{J}_x dv'$

at $\mathbf{r}' = (x', y', z')$. For a homogeneous region containing sources, Maxwell's equations in the frequency domain take the inhomogeneous forms (e.g. Wannamaker et al., 1984; Ward and Hohmann, 1988)

$$\nabla \times \mathbf{E} + \hat{z}\mathbf{H} = -\mathbf{J}_m^s \tag{A.1a}$$

and

$$\nabla \times \mathbf{H} - \hat{y}\mathbf{E} = \mathbf{J}_e^s, \tag{A.1b}$$

where $\mathbf{J}_e^s$ and $\mathbf{J}_m^s$ are volume distributions of applied electric and magnetic current, respectively, the latter of which is a useful mathematical artifice, and where $\hat{z}$ and $\hat{y}$ are respectively the impedivity and the admittivity, defined as $\hat{z} = i\mu\omega$ and $\hat{y} = \sigma + i\varepsilon\omega$ (Ward and Hohmann, 1988).

It is often easier to solve an EM boundary value problem formulated in terms of potentials rather than solving for the electric and magnetic fields directly. A useful set of potentials for decomposition of the electric and magnetic fields in a space composed of homogeneous regions are the electric and magnetic Schelkunoff vector potentials $\mathbf{A}$ and $\mathbf{F}$ (see e.g., Harrington, 1961; Ward and Hohmann, 1988). For some homogeneous region containing sources, $\mathbf{A}$ and $\mathbf{F}$ satisfy the frequency-domain inhomogeneous Helmholtz equations (Wannamaker and Hohmann, 1982; Ward and Hohmann, 1988)

$$\left(\nabla^2 + k^2\right)\mathbf{A} = \mathbf{J}_e^s \tag{A.2a}$$

and

$$\left(\nabla^2 + k^2\right)\mathbf{F} = \mathbf{J}_m^s, \tag{A.2b}$$

where k is the wavenumber, defined such that (Ward and Hohmann, 1988)

$$k^2 = \mu\varepsilon\omega^2 - i\mu\sigma\omega = -\hat{z}\hat{y}. \tag{A.3}$$

Note that the vector potentials **A** and **F** have the same directions as their sources. Using this vector potential decomposition, the electric and magnetic fields may be expressed as (Wannamaker and Hohmann, 1982; Ward and Hohmann, 1988)

$$\mathbf{E} = -\nabla \times \mathbf{F} - \hat{z}\mathbf{A} + \frac{1}{\hat{y}}\nabla\nabla \cdot \mathbf{A} \tag{A.4a}$$

and

$$\mathbf{H} = \nabla \times \mathbf{A} - \hat{y}\mathbf{F} + \frac{1}{\hat{z}}\nabla\nabla \cdot \mathbf{F}. \tag{A.4b}$$

By expressing the dipole current source as an equivalent distribution of vertically oriented electric and magnetic current sources, there only exists vertical components of the Schelkunoff vector potentials, respectively designated ϕ and θ, which obey the scalar equations (Wannamaker and Hohmann, 1982)

$$\left(\nabla^2 + k^2\right)\phi = J_{ez}^{eq} \tag{A.5a}$$

and

$$\left(\nabla^2 + k^2\right)\theta = J_{mz}^{eq}, \tag{A.5b}$$

where J_{mz}^{eq} and J_{mz}^{eq} are the equivalent vertical electric and magnetic source distributions, respectively. Considering only vertical components of **A** and **F**, ϕ and θ, equation (A.4) becomes, in cartesian coordinates (Wannamaker and Hohmann, 1982; Wannamaker et al., 1984; Ward and Hohmann, 1988),

$$E_x = \frac{1}{\hat{y}}\frac{\partial^2\phi}{\partial x \partial z} - \frac{\partial\theta}{\partial y}, \qquad H_x = \frac{\partial\phi}{\partial y} + \frac{1}{\hat{z}}\frac{\partial^2\theta}{\partial x \partial z}, \tag{A.6a}$$

$$E_y = \frac{1}{\hat{y}}\frac{\partial^2\phi}{\partial y \partial z} + \frac{\partial\theta}{\partial x}, \qquad H_y = -\frac{\partial\phi}{\partial x} + \frac{1}{\hat{z}}\frac{\partial^2\theta}{\partial y \partial z}, \tag{A.6b}$$

$$E_z = \frac{1}{\hat{y}}\left(\frac{\partial^2}{\partial z^2} + k^2\right)\phi, \qquad \text{and} \qquad H_z = \frac{1}{\hat{z}}\left(\frac{\partial^2}{\partial z^2} + k^2\right)\theta. \tag{A.6c}$$

Since E_z and H_z are formulated exclusively in terms of ϕ and θ, respectively, this choice of potentials has separated the fields into TM and TE modes with respect to z. Now let us consider an earth composed of n homogeneous layers, with the source located in layer j. If we effect a 2D spatial Fourier transform of equation (A.5) using the Fourier transform pair (Wannamaker and Hohmann, 1982)

$$f(x,y,z) = \frac{1}{4\pi^2}\iint_{-\infty}^{\infty} F(k_x,k_y,z)\, e^{+i\left(k_x x + k_y y\right)} dk_x dk_y \tag{A.7a}$$

and

$$F(k_x,k_y,z) = \iint_{-\infty}^{\infty} f(x,y,z)\, e^{-i\left(k_x x + k_y y\right)} dx dy, \tag{A.7b}$$

a 1D scalar wave equation in z results whose general solution is composed of upward- and downward-propagating plane waves. For some arbitrary layer l, the solutions take the form (Wannamaker and Hohmann, 1982)

$${}^{-}\phi_l = {}^{-}\phi_l^{-} e^{+u_l(z-d_{l-1})} + {}^{-}\phi_l^{+} e^{-u_l(z-d_{l-1})} \tag{A.8a}$$

and

$${}^{-}\theta_l = {}^{-}\theta_l^{-} e^{+u_l(z-d_{l-1})} + {}^{-}\theta_l^{+} e^{-u_l(z-d_{l-1})}, \tag{A.8b}$$

for $z < z'$, i.e., above the source, and

$${}^{+}\phi_l = {}^{+}\phi_l^{-} e^{+u_l(z-d_l)} + {}^{+}\phi_l^{+} e^{-u_l(z-d_l)} \tag{A.9a}$$

and

$${}^{+}\theta_l = {}^{+}\theta_l^{-} e^{+u_l(z-d_l)} + {}^{+}\theta_l^{+} e^{-u_l(z-d_l)}, \tag{A.9b}$$

for $z > z'$, i.e., below the source, where u_l is defined such that

$$u_l^2 = k_x^2 + k_y^2 - k_l^2. \tag{A.10}$$

Note that in equations (A.8) and (A.9), the left-hand side superscripts $+$ and $-$ denote $z < z'$ (above the source) and $z > z'$ (below the source), respectively, and the right-hand side superscripts $+$ and $-$ denote downward- and upward-travelling waves, respectively. Under this 2D spatial Fourier transformation, relation (A.6) becomes

$$E_x = \frac{ik_x}{\hat{y}}\frac{\partial \phi}{\partial z} - ik_y\theta, \qquad H_x = ik_y\phi + \frac{ik_x}{\hat{z}}\frac{\partial \theta}{\partial z}, \tag{A.11a}$$

$$E_y = \frac{ik_y}{\hat{y}}\frac{\partial \phi}{\partial z} + ik_x\theta, \qquad H_y = -ik_x\phi + \frac{ik_y}{\hat{z}}\frac{\partial \theta}{\partial z}, \tag{A.11b}$$

$$E_z = \frac{\left(k_x^2 + k_y^2\right)}{\hat{y}}\phi, \quad \text{and} \quad H_z = \frac{\left(k_x^2 + k_y^2\right)}{\hat{z}}\theta. \tag{A.11c}$$

The upward- and downward-travelling waves of equations (A.8) and (A.9) are coupled through the reflection coefficients ${}^{-}R_l^{TM}$, ${}^{-}R_l^{TE}$, ${}^{+}R_l^{TM}$, and ${}^{+}R_l^{TE}$, as

$${}^{-}\phi_l^{+} = {}^{-}R_l^{TM}\,{}^{-}\phi_l^{-}, \tag{A.12a}$$

$${}^{-}\theta_l^{+} = {}^{-}R_l^{TE}\,{}^{-}\theta_l^{-}, \tag{A.12b}$$

$${}^{+}\phi_l^{-} = {}^{+}R_l^{TM}\,{}^{+}\phi_l^{+}, \tag{A.13a}$$

and

$${}^{+}\theta_l^{-} = {}^{+}R_l^{TE}\,{}^{+}\theta_l^{+}. \tag{A.13b}$$

The reflection coefficients are given by the formulae (Wannamaker and Hohmann, 1982; Wannamaker et al., 1984)

$${}^{-}R_l^{TM} = \frac{Z_l - {}^{-}\bar{Z}_{l-1}}{Z_l + {}^{-}\bar{Z}_{l-1}}, \tag{A.14a}$$

$$^{-}R_l^{TE} = \frac{Y_l - {}^{-}\bar{Y}_{l-1}}{Y_l + {}^{-}\bar{Y}_{l-1}}, \tag{A.14b}$$

$$^{+}R_l^{TM} = \frac{Z_l - {}^{+}\bar{Z}_{l+1}}{Z_l + {}^{+}\bar{Z}_{l+1}}, \tag{A.15a}$$

and

$$^{+}R_l^{TE} = \frac{Y_l - {}^{+}\bar{Y}_{l+1}}{Y_l + {}^{+}\bar{Y}_{l+1}}, \tag{A.15b}$$

with the recurrence relations (Wannamaker et al., 1984; Ward and Hohmann, 1988)

$$^{-}\bar{Z}_l = Z_l \frac{{}^{-}\bar{Z}_{l-1} + Z_l \tanh(u_l h_l)}{Z_l + {}^{-}\bar{Z}_{l-1} \tanh(u_l h_l)}, \tag{A.16a}$$

$$^{-}\bar{Y}_l = Y_l \frac{{}^{-}\bar{Y}_{l-1} + Y_l \tanh(u_l h_l)}{Y_l + {}^{-}\bar{Y}_{l-1} \tanh(u_l h_l)}, \tag{A.16b}$$

$$^{-}\bar{Z}_1 = Z_1, \tag{A.16c}$$

$$^{-}\bar{Y}_1 = Y_1, \tag{A.16d}$$

$$^{+}\bar{Z}_l = Z_l \frac{{}^{+}\bar{Z}_{l+1} + Z_l \tanh(u_l h_l)}{Z_l + {}^{+}\bar{Z}_{l+1} \tanh(u_l h_l)}, \tag{A.17a}$$

$$^{+}\bar{Y}_l = Y_l \frac{{}^{+}\bar{Y}_{l+1} + Y_l \tanh(u_l h_l)}{Y_l + {}^{+}\bar{Y}_{l+1} \tanh(u_l h_l)}, \tag{A.17b}$$

$$^{+}\bar{Z}_n = Z_n, \tag{A.17c}$$

and

$$^{+}\bar{Y}_n = Y_n, \tag{A.17d}$$

where Z_l is the impedance, $Z_l = u_l/\hat{y}_l$, Y_l is the admittance, $Y_l = u_l/\hat{z}_l$, and h_l is the height of the layer, $h_l = d_l - d_{l-1}$. Here Z_1, Y_1, Z_n, and Y_n represent the impedances and admittances of the top halfspace ($l = 1$) and the base halfspace ($l = n$). Equations (A.8) and (A.9) can

thus be expressed as

$$^{-}\phi_l = {}^{-}\phi_l^{-}\left[e^{+u_l(z-d_{l-1})} + {}^{-}R_j^{TM}e^{-u_l(z-d_{l-1})}\right], \tag{A.18a}$$

$$^{-}\theta_l = {}^{-}\theta_l^{-}\left[e^{+u_l(z-d_{l-1})} + {}^{-}R_l^{TE}e^{-u_l(z-d_{l-1})}\right], \tag{A.18b}$$

$$^{+}\phi_l = {}^{+}\phi_l^{+}\left[{}^{+}R_l^{TM}e^{+u_l(z-d_l)} + e^{-u_l(z-d_l)}\right], \tag{A.19a}$$

and

$$^{+}\theta_l = {}^{+}\theta_l^{+}\left[{}^{+}R_l^{TE}e^{+u_l(z-d_l)} + e^{-u_l(z-d_l)}\right]. \tag{A.19b}$$

For some layer $l \neq j$, the general solutions of equations (A.18) and (A.19) are constructed solely from source-free secondary potentials. For the source layer $l = j$, the general solutions for the potentials consist of both primary and secondary potentials, and so the coefficients may be decomposed into primary and secondary parts, i.e.,

$$^{-}\phi_j^{-} = {}^{P-}\phi_j^{-} + {}^{S}\phi_j^{-}, \tag{A.20a}$$

$$^{-}\theta_j^{-} = {}^{P-}\theta_j^{-} + {}^{S}\theta_j^{-}, \tag{A.20b}$$

$$^{+}\phi_j^{+} = {}^{P+}\phi_j^{+} + {}^{S}\phi_j^{+}, \tag{A.21a}$$

and

$$^{+}\theta_j^{+} = {}^{P+}\theta_j^{+} + {}^{S}\theta_j^{+}, \tag{A.21b}$$

where we have dropped the left-hand side $+$ and $-$ superscripts from the secondary coefficients since the upward- and downward-propagating secondary potentials are present throughout the layer, not just above or below the source. The primary solutions ${}^{P}\phi_j$ and

${}^{P}\theta_j$, which only arise in layer j containing the source, can be found by equating (A.11c) with the vertical components of the electric and magnetic fields for current element $\mathbf{J}_x dv'$ in a whole space of wavenumber k_j (e.g., Harrington, 1961, p. 80; Ward and Hohmann, 1988, p. 169). The resultant expressions for the primary potentials are (Wannamaker and Hohmann, 1982)

$$ {}^{P}\phi_j^x = \pm \frac{J_x i k_x}{2\left(k_x^2 + k_y^2\right)} e^{-i\left(k_x x' + k_y y'\right)} e^{-u_j |z - z'|} \tag{A.22a} $$

and

$$ {}^{P}\theta_j^x = -\frac{J_x \hat{z}_j i k_y}{2u_j\left(k_x^2 + k_y^2\right)} e^{-i\left(k_x x' + k_y y'\right)} e^{-u_j |z - z'|}. \tag{A.22b} $$

The secondary potentials can be determined by expanding equations (A.18) and (A.19) using the primary-secondary decomposition defined in (A.20) and (A.21), and subsequently matching equivalent terms in $z < z'$ and $z > z'$ spaces. For example, the downgoing primary potential reflected at the top boundary (now secondary) and the downgoing secondary potential reflected at the top boundary, both present in $z < z'$ space, are equivalent to the downgoing secondary potential incident at the base boundary, present in $z > z'$ space. Only one of the two quantities are required to define the total potential since they are equivalent, and hence redundant. By matching equivalent terms for $z < z'$ and $z > z'$ spaces, the downgoing secondary potential coefficients are determined to be (Wannamaker and Hohmann, 1982)

$$ {}^{S}\phi_j^- = \frac{\left[{}^{P+}\phi_j^+ + {}^{P-}\phi_j^- {}^{-}R_j^{TM}\right] {}^{+}R_j^{TM} e^{-2u_j h_j}}{1 - {}^{+}R_j^{TM} {}^{-}R_j^{TM} e^{-2u_j h_j}} \tag{A.23a} $$

and

$$ {}^{S}\theta_j^- = \frac{\left[{}^{P+}\theta_j^+ + {}^{P-}\theta_j^- {}^{-}R_j^{TE}\right] {}^{+}R_j^{TE} e^{-2u_j h_j}}{1 - {}^{+}R_j^{TE} {}^{-}R_j^{TE} e^{-2u_j h_j}}. \tag{A.23b} $$

The coefficients ${}^{P-}\phi_j^-$, ${}^{P+}\phi_j^+$, ${}^{P-}\theta_j^-$, and ${}^{P+}\theta_j^+$ depend on the source. For an x-directed

current source, from equation (A.22) (Wannamaker and Hohmann, 1982),

$$ {}^{P-}\phi_j^{-x} = -e^{-2u_j\left(z'-d_{j-1}\right)}\,{}^{P+}\phi_j^{+x}, \tag{A.24a} $$

$$ {}^{P-}\theta_j^{-x} = -e^{-2u_j\left(z'-d_{j-1}\right)}\,{}^{P+}\theta_j^{+x}, \tag{A.24b} $$

$$ {}^{P+}\phi_j^{+x} = \frac{-s_x ik_x}{\left(k_x^2+k_y^2\right)} e^{+u_j\left(z'-d_{j-l}\right)}, \tag{A.24c} $$

and

$$ {}^{P+}\theta_j^{+x} = \frac{-s_x \hat{z}_j ik_y}{u_j\left(k_x^2+k_y^2\right)} e^{+u_j\left(z'-d_{j-l}\right)}, \tag{A.24d} $$

where we have defined $s_x = \frac{1}{2}J_x e^{-i\left(k_x x'+k_y y'\right)}$. From equations (A.18), (A.20), (A.22), (A.23), and (A.24), for an x-directed current element, the total potentials in source layer j are (Wannamaker and Hohmann, 1982; Wannamaker et al., 1984)

$$ \begin{aligned} \phi_j^x = \frac{s_x ik_x}{\left(k_x^2+k_y^2\right)} \Big\{ &\left[\pm e^{-u_j|z-z'|} + {}^{-}R_j^{TM} e^{-u_j\left(z+z'-2d_{j-1}\right)} \right] \\ &+ {}^{x}A_j^{TM} \left[e^{+u_j\left(z-d_{j-1}\right)} + {}^{-}R_j^{TM} e^{-u_j\left(z-d_{j-1}\right)} \right] \Big\} \end{aligned} \tag{A.25a} $$

and

$$ \begin{aligned} \theta_j^x = \frac{-s_x \hat{z}_j ik_y}{u_j\left(k_x^2+k_y^2\right)} \Big\{ &\left[e^{-u_j|z-z'|} + {}^{-}R_j^{TE} e^{-u_j\left(z+z'-2d_{j-1}\right)} \right] \\ &+ {}^{x}A_j^{TE} \left[e^{+u_j\left(z-d_{j-1}\right)} + {}^{-}R_j^{TE} e^{-u_j\left(z-d_{j-1}\right)} \right] \Big\}. \end{aligned} \tag{A.25b} $$

The electric and magnetic fields in (k_x, k_y) space in layer j for an x-directed current element, also located in layer j, are obtained by substituting (A.25) into relation (A.11) and evaluating the expressions. The electric and magnetic fields can be expressed in Cartesian coordinates by applying the reverse Fourier transform defined in (A.7). To facilitate numerical evaluation of the electric and magnetic field expressions, we convert the double Fourier transforms with circularly symmetric integral kernels to Hankel transforms using

the relation (Wannamaker and Hohmann, 1982; Ward and Hohmann, 1988)

$$\iint_{-\infty}^{\infty} F\left(k_x^2+k_y^2\right) e^{i\left(k_x x+k_y y\right)} dk_x dk_y = 2\pi \int_0^{\infty} F\left(\lambda\right) \lambda J_0\left(\lambda\rho\right) d\lambda, \tag{A.26}$$

where $\lambda^2 = k_x^2 + k_y^2$, $\rho^2 = (x-x')^2 + (y-y')^2$, and $J_0(\lambda\rho)$ is the zeroth order Bessel function of the first kind. The primary electric field components ${}^P E_{xj}$ arising from the primary or particular potential solutions are (Wannamaker and Hohmann, 1982; Wannamaker et al., 1984)

$${}^P E_{xxj} = \frac{J_x}{4\pi\hat{\mathbf{y}}_j} \left\{ \left[\frac{(x-x')^2}{R^2} \right] {}^P\gamma_{1j}^E - {}^P\gamma_{2j}^E + k_j^2 {}^P\gamma_{3j}^E \right\}, \tag{A.27a}$$

$${}^P E_{yxj} = \frac{J_x}{4\pi\hat{\mathbf{y}}_j} \left\{ \left[\frac{(x-x')(y-y')}{R^2} \right] {}^P\gamma_{1j}^E \right\}, \tag{A.27b}$$

and

$${}^P E_{zxj} = \frac{J_x}{4\pi\hat{\mathbf{y}}_j} \left\{ \left[\frac{(x-x')(z-z')}{R^2} \right] {}^P\gamma_{1j}^E \right\}, \tag{A.27c}$$

where the first subscript (i.e., x, y, and z) denotes the component direction, $R = |\mathbf{r}-\mathbf{r}'|$, and we have defined

$${}^P\gamma_{1j}^E = \frac{e^{-ik_j R}}{R} \left[\frac{3}{R^2} + \frac{3ik_j}{R} - k_j^2 \right], \tag{A.28a}$$

$${}^P\gamma_{2j}^E = \frac{e^{-ik_j R}}{R} \left[\frac{1}{R^2} + \frac{ik_j}{R} \right], \tag{A.28b}$$

and

$${}^P\gamma_{3j}^E = \frac{e^{-ik_j R}}{R}. \tag{A.28c}$$

The secondary electric field components ${}^S E_{xj}$ arising from the secondary or complementary potential solutions are (Wannamaker and Hohmann, 1982; Wannamaker et al., 1984)

$${}^S E_{xxj} = \frac{J_x}{4\pi\hat{y}_j} \left\{ \left[\frac{2(x-x')^2}{\rho^3} - \frac{1}{\rho} \right] {}^S\gamma_{1j}^E - \left[\frac{(x-x')^2}{\rho^2} \right] {}^S\gamma_{2j}^E + k_j^2 {}^S\gamma_{3j}^E \right\}, \tag{A.29a}$$

$$ {}^{s}E_{yxj} = \frac{J_x}{4\pi\hat{y}_j}\left\{\left[\frac{2\,(x-x')\,(y-y')}{\rho^3}\right]{}^{s}\gamma^{E}_{1j} - \left[\frac{(x-x')\,(y-y')}{\rho^2}\right]{}^{s}\gamma^{E}_{2j}\right\}, \tag{A.29b} $$

and

$$ {}^{s}E_{zxj} = \frac{J_x}{4\pi\hat{y}_j}\left\{\left[\frac{-(x-x')}{\rho}\right]{}^{s}\gamma^{E}_{4j}\right\}, \tag{A.29c} $$

with Hankel transforms

$$ \begin{aligned} {}^{s}\gamma^{E}_{1j} = \int_0^\infty \Bigg\{ & \left[u_j\,{}^{x}A^{TM}_{j} + \frac{k_j^2}{u_j}\,{}^{x}A^{TE}_{j}\right] e^{+u_j\left(z-d_{j-1}\right)} \\ & - \left[u_j\left(e^{-u_j\left(z'-d_{j-1}\right)} + {}^{x}A^{TM}_{j}\right){}^{-}R^{TM}_{j}\right. \\ & \left. - \frac{k_j^2}{u_j}\left(e^{-u_j\left(z'-d_{j-1}\right)} + {}^{x}A^{TE}_{j}\right){}^{-}R^{TE}_{j}\right] e^{-u_j\left(z-d_{j-1}\right)} \Bigg\} J_1(\lambda\rho)\,d\lambda, \end{aligned} \tag{A.30a} $$

$$ \begin{aligned} {}^{s}\gamma^{E}_{2j} = \int_0^\infty \Bigg\{ & \left[u_j\,{}^{x}A^{TM}_{j} + \frac{k_j^2}{u_j}\,{}^{x}A^{TE}_{j}\right] e^{+u_j\left(z-d_{j-1}\right)} \\ & - \left[u_j\left(e^{-u_j\left(z'-d_{j-1}\right)} + {}^{x}A^{TM}_{j}\right){}^{-}R^{TM}_{j}\right. \\ & \left. - \frac{k_j^2}{u_j}\left(e^{-u_j\left(z'-d_{j-1}\right)} + {}^{x}A^{TE}_{j}\right){}^{-}R^{TE}_{j}\right] e^{-u_j\left(z-d_{j-1}\right)} \Bigg\} \lambda J_0(\lambda\rho)\,d\lambda, \end{aligned} \tag{A.30b} $$

$$ \begin{aligned} {}^{s}\gamma^{E}_{3j} = \int_0^\infty \frac{1}{u_j}\Big\{ & \left[{}^{x}A^{TE}_{j}\right] e^{+u_j\left(z-d_{j-1}\right)} \\ & + \left[\left(e^{-u_j\left(z'-d_{j-1}\right)} + {}^{x}A^{TE}_{j}\right){}^{-}R^{TE}_{j}\right] e^{-u_j\left(z-d_{j-1}\right)}\Big\} \lambda J_0(\lambda\rho)\,d\lambda, \end{aligned} \tag{A.30c} $$

and

$$ \begin{aligned} {}^{s}\gamma^{E}_{4j} = \int_0^\infty \lambda^2\Big\{ & \left[{}^{x}A^{TM}_{j}\right] e^{+u_j\left(z-d_{j-1}\right)} \\ & + \left[\left(e^{-u_j\left(z'-d_{j-1}\right)} + {}^{x}A^{TM}_{j}\right){}^{-}R^{TM}_{j}\right] e^{-u_j\left(z-d_{j-1}\right)}\Big\} J_1(\lambda\rho)\,d\lambda, \end{aligned} \tag{A.30d} $$

and additional coefficients

$$ {}^{x}A^{TM}_{j} = \frac{{}^{+}R^{TM}_{j} e^{-2u_j h_j} e^{+u_j\left(z'-d_{j-1}\right)}\left[{}^{-}R^{TM}_{j} e^{-2u_j\left(z'-d_{j-1}\right)} - 1\right]}{1 - {}^{+}R^{TM}_{j}\,{}^{-}R^{TM}_{j} e^{-2u_j h_j}} \tag{A.31a} $$

and

$$ {}^{x}A_j^{TE} = \frac{{}^{+}R_j^{TE} e^{-2u_j h_j} e^{+u_j\left(z'-d_{j-1}\right)} \left[{}^{-}R_j^{TE} e^{-2u_j\left(z'-d_{j-1}\right)} + 1 \right]}{1 - {}^{+}R_j^{TE}\,{}^{-}R_j^{TE} e^{-2u_j h_j}}. \tag{A.31b} $$

Similarly, the primary magnetic fields arising from the particular potential solutions are (Wannamaker and Hohmann, 1982; Wannamaker et al., 1984)

$$ {}^{P}H_{xxj} = 0, \tag{A.32a} $$

$$ {}^{P}H_{yxj} = \frac{-1}{4\pi}\left(z-z'\right) {}^{P}\gamma_{1j}^{H}, \tag{A.32b} $$

and

$$ {}^{P}H_{zxj} = \frac{1}{4\pi}\left(y-y'\right) {}^{P}\gamma_{1j}^{H}, \tag{A.32c} $$

where

$$ {}^{P}\gamma_{1j}^{H} = \frac{e^{-ik_j R}}{R}\left[\frac{1}{R^2} + \frac{ik_j}{R}\right]. \tag{A.33} $$

The secondary magnetic fields arising from the complementary potential solutions are (Wannamaker and Hohmann, 1982; Wannamaker et al., 1984)

$$ {}^{S}H_{xxj} = \frac{J_x}{4\pi}\left\{\left[\frac{2\left(x-x'\right)\left(y-y'\right)}{\rho^3}\right] {}^{S}\gamma_{1j}^{H} - \left[\frac{\left(x-x'\right)\left(y-y'\right)}{\rho^2}\right] {}^{S}\gamma_{2j}^{H}\right\}, \tag{A.34a} $$

$$ {}^{S}H_{yxj} = \frac{J_x}{4\pi}\left\{-\left[\frac{2\left(x-x'\right)^2}{\rho^3} - \frac{1}{\rho}\right] {}^{S}\gamma_{1j}^{H} + \left[\frac{\left(x-x'\right)^2}{\rho^2}\right] {}^{S}\gamma_{2j}^{H} + {}^{S}\gamma_{3j}^{H}\right\}, \tag{A.34b} $$

and

$$ {}^{S}H_{zxj} = \frac{J_x}{4\pi}\left\{\left[\frac{\left(y-y'\right)}{\rho}\right] {}^{S}\gamma_{4j}^{H}\right\}, \tag{A.34c} $$

with Hankel transforms

$$
\begin{aligned}
{}^{S}\gamma_{1j}^{H} = \int_0^{\infty} \Big\{ & \left[{}^{x}A_j^{TM} - {}^{x}A_j^{TE} \right] e^{+u_j\left(z-d_{j-1}\right)} \\
& + \left[\left(e^{-u_j\left(z'-d_{j-1}\right)} + {}^{x}A_j^{TM} \right) {}^{-}R_j^{TM} \right. \\
& \left. + \left(e^{-u_j\left(z'-d_{j-1}\right)} + {}^{x}A_j^{TE} \right) {}^{-}R_j^{TE} \right] e^{-u_j\left(z-d_{j-1}\right)} \Big\} J_1\left(\lambda\rho\right) d\lambda,
\end{aligned}
\tag{A.35a}
$$

$$
\begin{aligned}
{}^{S}\gamma_{2j}^{H} = \int_0^{\infty} \Big\{ & \left[{}^{x}A_j^{TM} - {}^{x}A_j^{TE} \right] e^{+u_j\left(z-d_{j-1}\right)} \\
& + \left[\left(e^{-u_j\left(z'-d_{j-1}\right)} + {}^{x}A_j^{TM} \right) {}^{-}R_j^{TM} \right. \\
& \left. + \left(e^{-u_j\left(z'-d_{j-1}\right)} + {}^{x}A_j^{TE} \right) {}^{-}R_j^{TE} \right] e^{-u_j\left(z-d_{j-1}\right)} \Big\} \lambda J_0\left(\lambda\rho\right) d\lambda,
\end{aligned}
\tag{A.35b}
$$

$$
\begin{aligned}
{}^{S}\gamma_{3j}^{H} = \int_0^{\infty} \Big\{ & \left[{}^{x}A_j^{TE} \right] e^{+u_j\left(z-d_{j-1}\right)} \\
& - \left[\left(e^{-u_j\left(z'-d_{j-1}\right)} + {}^{x}A_j^{TE} \right) {}^{-}R_j^{TE} \right] e^{-u_j\left(z-d_{j-1}\right)} \Big\} \lambda J_0\left(\lambda\rho\right) d\lambda,
\end{aligned}
\tag{A.35c}
$$

and

$$
\begin{aligned}
{}^{S}\gamma_{4j}^{H} = \int_0^{\infty} \frac{\lambda^2}{u_j} \Big\{ & \left[{}^{x}A_j^{TE} \right] e^{+u_j\left(z-d_{j-1}\right)} \\
& + \left[\left(e^{-u_j\left(z'-d_{j-1}\right)} + {}^{x}A_j^{TE} \right) {}^{-}R_j^{TE} \right] e^{-u_j\left(z-d_{j-1}\right)} \Big\} J_1\left(\lambda\rho\right) d\lambda.
\end{aligned}
\tag{A.35d}
$$

A.2 Algorithm

The algorithm for MARDIP1D, which requires computation of the electric and magnetic fields in a layered earth due to a HED, where the observation points and source are both located in the same layer, is summarized in Algorithm A.1, with reference to the pertinent equations introduced in the previous section. The Hankel transform expressions were evaluated using the fast Hankel transform subroutine of Anderson (1979).

Algorithm A.1 Part I: MARDIP1D forward solve procedure for the electric and magnetic fields in a layered earth due to a HED, with both source and observation points located in the same layer

Input: Earth model $\{\sigma_l, \varepsilon_{rl}, h_l\}$ for $l = 1, .., n$, where n is the number of earth layers
Set of observation points $\{\mathbf{r}_i\}$ for $i = 1, .., n_{obs}$, where n_{obs} is the number of observation points, and $\mathbf{r}_i = (x_i, y_i, z_i)$
Source parameters ω, I, dx, and $\mathbf{r}' = (x', y', z')$

Output: Electric and magnetic fields $\mathbf{E}_j(\mathbf{r})$, $\mathbf{H}_j(\mathbf{r})$ for layer j containing the source

procedure MARDIP1D($\{\sigma_l, \varepsilon_{rl}, h_l\}$, $\{\mathbf{r}_i\}$, ω, I, dx, $\mathbf{r}'$)
  for $i = 1, n_{obs}$ **do** ▷ For all observation points
    Compute ρ_i, R_i
    Evaluate the primary electric field ${}^P\mathbf{E}_j(\mathbf{r}_i)$ using (A.27) and (A.28)
    Evaluate the primary magnetic field ${}^P\mathbf{H}_j(\mathbf{r}_i)$ using (A.32) and (A.33)
    for all secondary field Hankel transforms defined in (A.30) and (A.35) **do**
      call HANKEL*(ρ_i, *nord*, HFUNC) to evaluate the Hankel transform of order *nord* with kernel function HFUNC
    end for
    Evaluate the secondary electric field ${}^S\mathbf{E}_j(\mathbf{r}_i)$ using (A.29), (A.30), and (A.31)
    Evaluate the secondary magnetic field ${}^S\mathbf{H}_j(\mathbf{r}_i)$ using (A.34), (A.35), and (A.31)
    Sum the primary and secondary fields to obtain the total electric and magnetic fields $\mathbf{E}_j(\mathbf{r}_i)$ and $\mathbf{H}_j(\mathbf{r}_i)$
  end for
end procedure

*Hankel subroutine developed by Anderson, 1979.

Algorithm A.1 Part 2: Secondary field Hankel transform kernels and reflection coefficients for source layer

function HFUNC(λ) ▷ Representative kernel function, defined for each Hankel transform

call LAYERS(λ)

Evaluate the kernel of the secondary field Hankel transform, as defined in (A.30) or (A.35), for a particular value of λ

end function

procedure LAYERS(λ)

for $l = 1, n$ **do** ▷ For all layers, including source layer j

Compute admittivity $\hat{y}_l$ and impedivity $\hat{z}_l$

Compute wavenumber k_l

Compute u_l, $u_l = \sqrt{\lambda^2 - k_l^2}$

Compute admittance Y_l and impedance Z_l

end for

Assign $\bar{Y}_1 = Y_1$, $\bar{Y}_n = Y_n$, $\bar{Z}_1 = Z_1$, and $\bar{Z}_n = Z_n$

for $l = 1, j-1, 1$ **do** ▷ For layers above the source layer

Compute $\bar{Y}_l$ and $\bar{Z}_l$ using the recurrence relations defined in equation (A.16)

end for

for $l = n-1, j+1, -1$ **do** ▷ For layers below the source layer

Compute $\bar{Y}_l$ and $\bar{Z}_l$ using the recurrence relations defined in equation (A.17)

end for

Compute source layer j reflection coefficients ${}^{-}R_j^{TM}$, ${}^{-}R_j^{TE}$, ${}^{+}R_j^{TM}$, and ${}^{+}R_j^{TE}$ using equations (A.14) and (A.15)

Compute coefficients ${}^{x}A_j^{TM}$ and ${}^{x}A_j^{TE}$ using equation (A.31)

end procedure

Appendix B

Supplementary plots for the 3D North Amethyst reservoir model

The hydrocarbons-present and hydrocarbons-absent solutions used for computation of the inline horizontal electric field amplitude anomalies presented in Figures 6.27 and 6.28 for variations of the 3D North Amethyst BNA reservoir model in terms of water depth, burial depth, and hydrocarbon content are included in this appendix for reference.

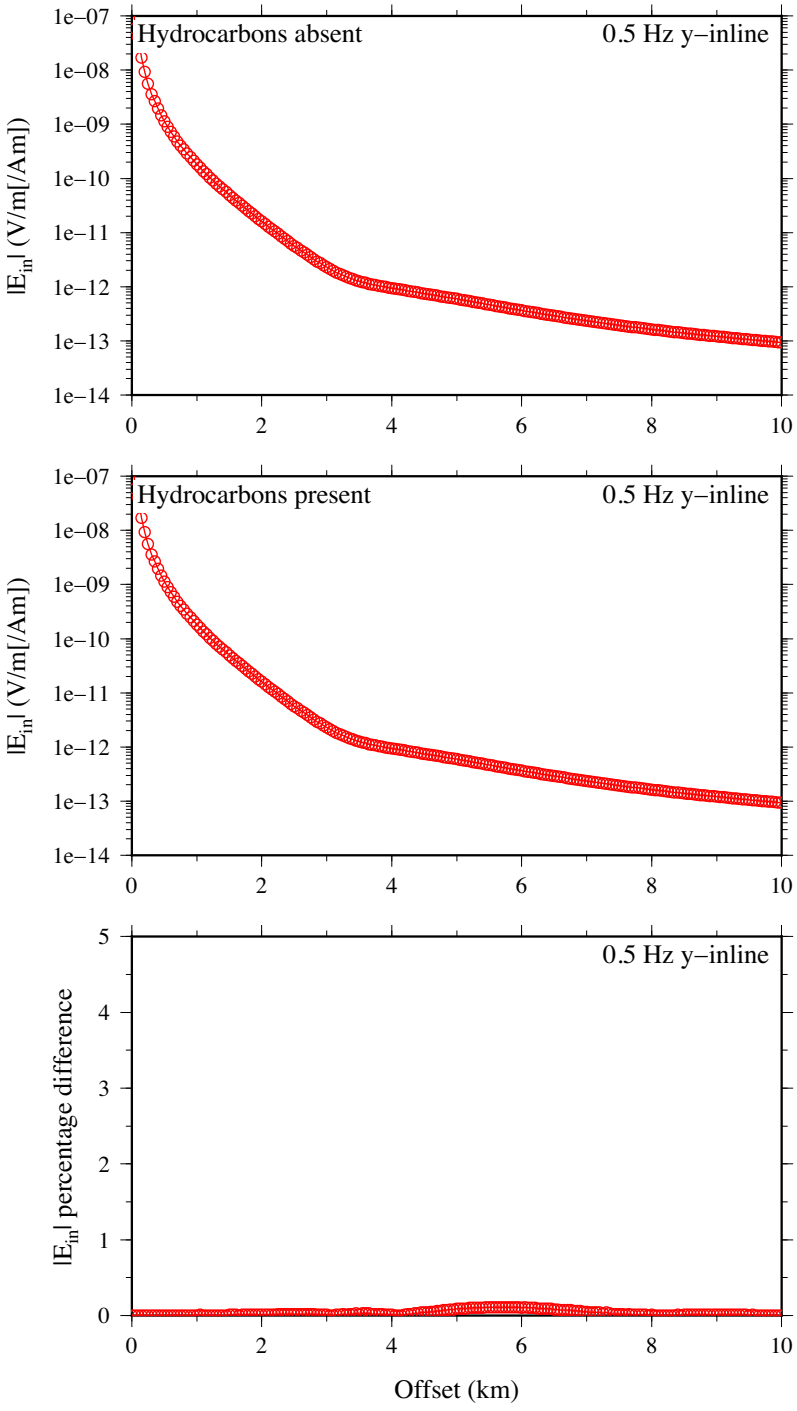

Figure B.1. The 0.5 Hz inline horizontal electric field and associated anomaly for the 3D North Amethyst BNA reservoir model with water depth = 120 m, average burial depth = 2416 m, and true hydrocarbon content, i.e., hydrocarbons present only above the oil-water contact in the reservoir.

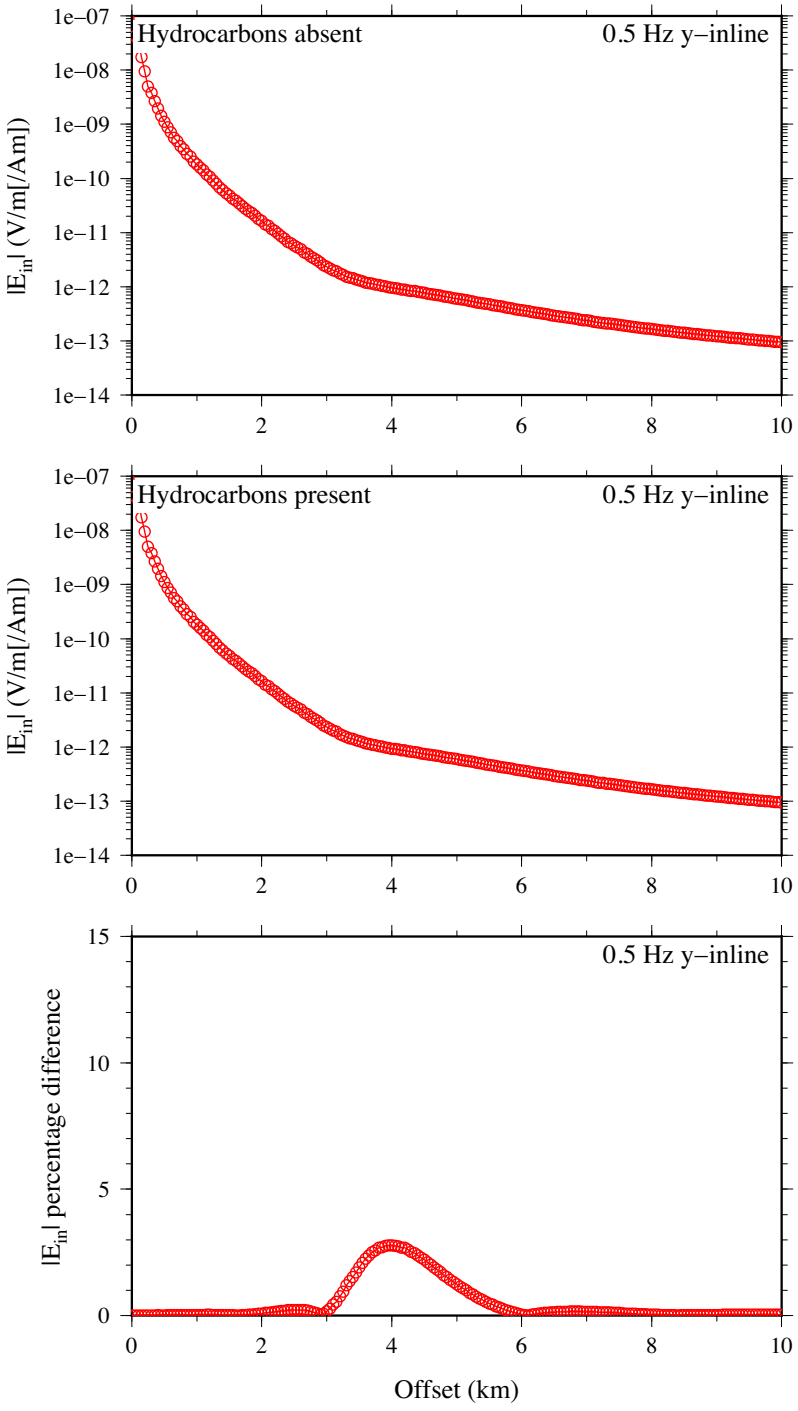

Figure B.2. The 0.5 Hz inline horizontal electric field and associated anomaly for the 3D North Amethyst BNA reservoir model with water depth = 120 m, average burial depth = 1416 m, and true hydrocarbon content, i.e., hydrocarbons present only above the oil-water contact in the reservoir.

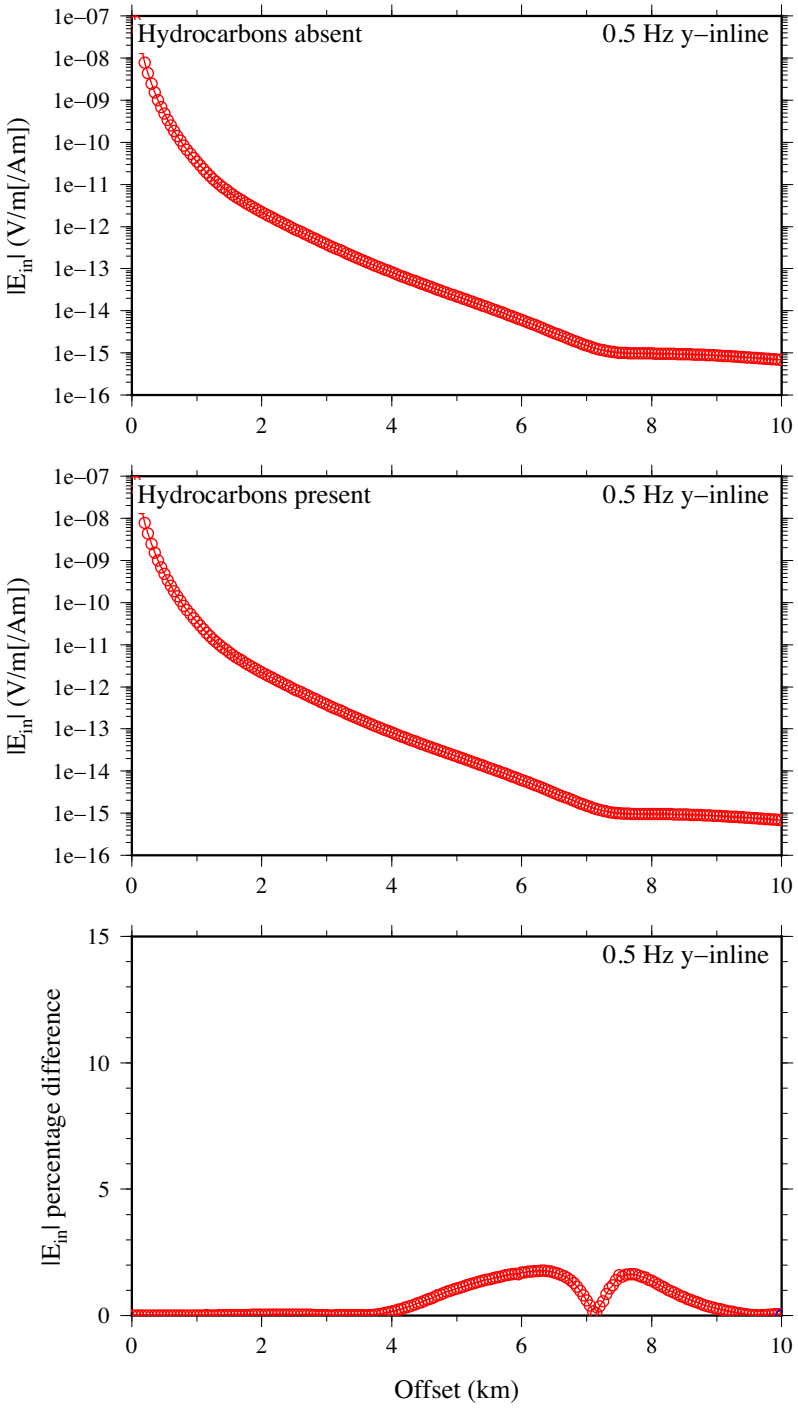

Figure B.3. The 0.5 Hz inline horizontal electric field and associated anomaly for the 3D North Amethyst BNA reservoir model with water depth = 1000 m, average burial depth = 2416 m, and true hydrocarbon content, i.e., hydrocarbons present only above the oil-water contact in the reservoir.

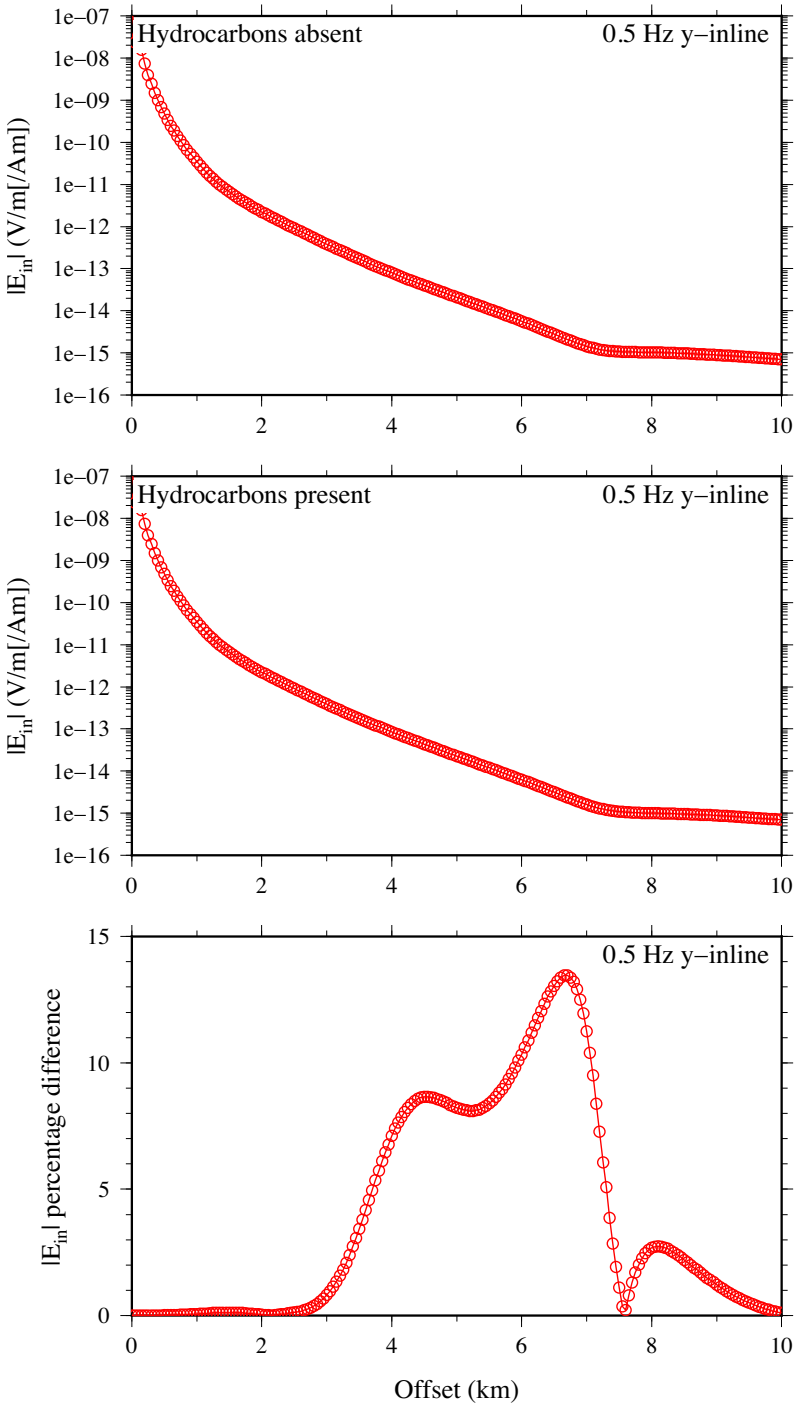

Figure B.4. The 0.5 Hz inline horizontal electric field and associated anomaly for the 3D North Amethyst BNA reservoir model with water depth = 1000 m, average burial depth = 1416 m, and true hydrocarbon content, i.e., hydrocarbons present only above the oil-water contact in the reservoir.

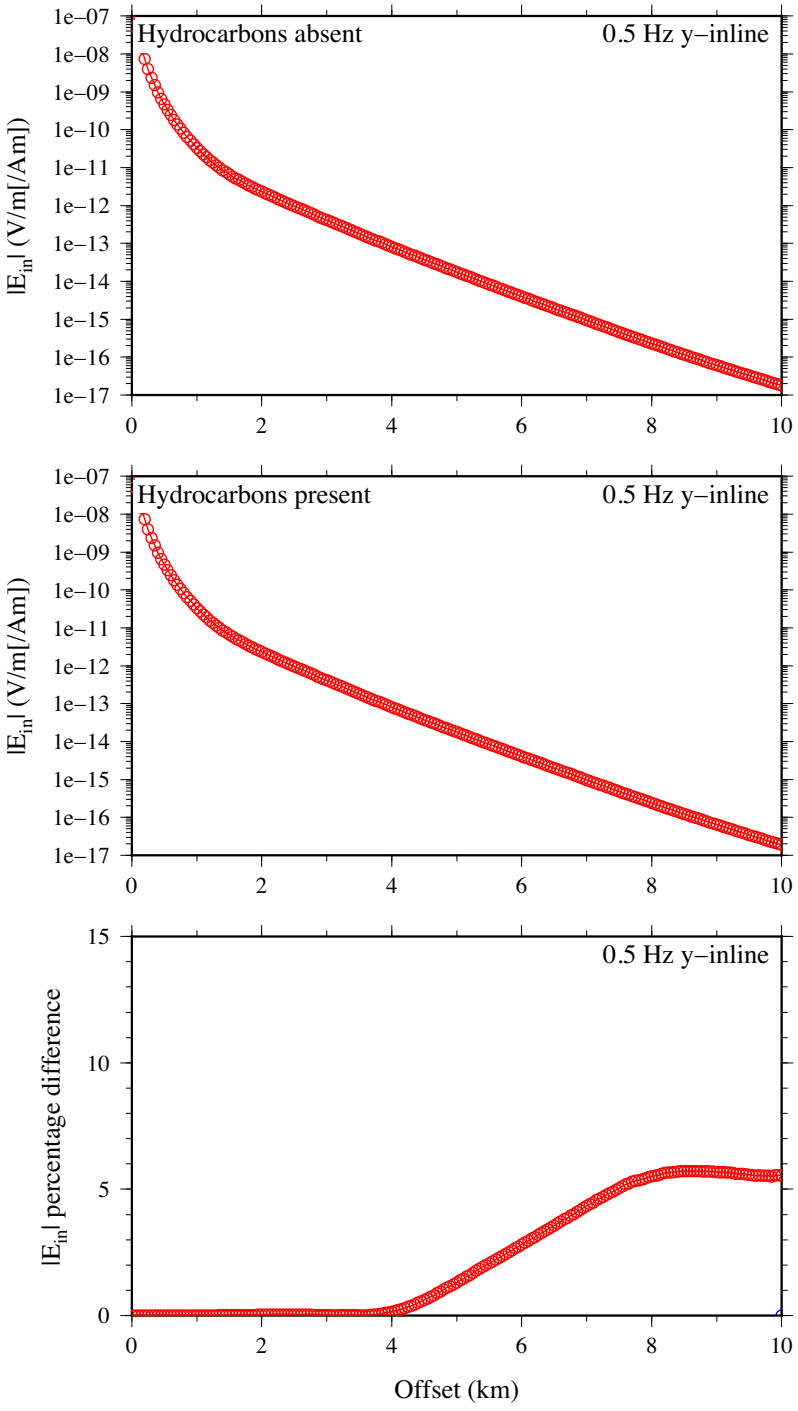

Figure B.5. The 0.5 Hz inline horizontal electric field and associated anomaly for the 3D North Amethyst BNA reservoir model with water depth = 2000 m, average burial depth = 2416 m, and true hydrocarbon content, i.e., hydrocarbons present only above the oil-water contact in the reservoir.

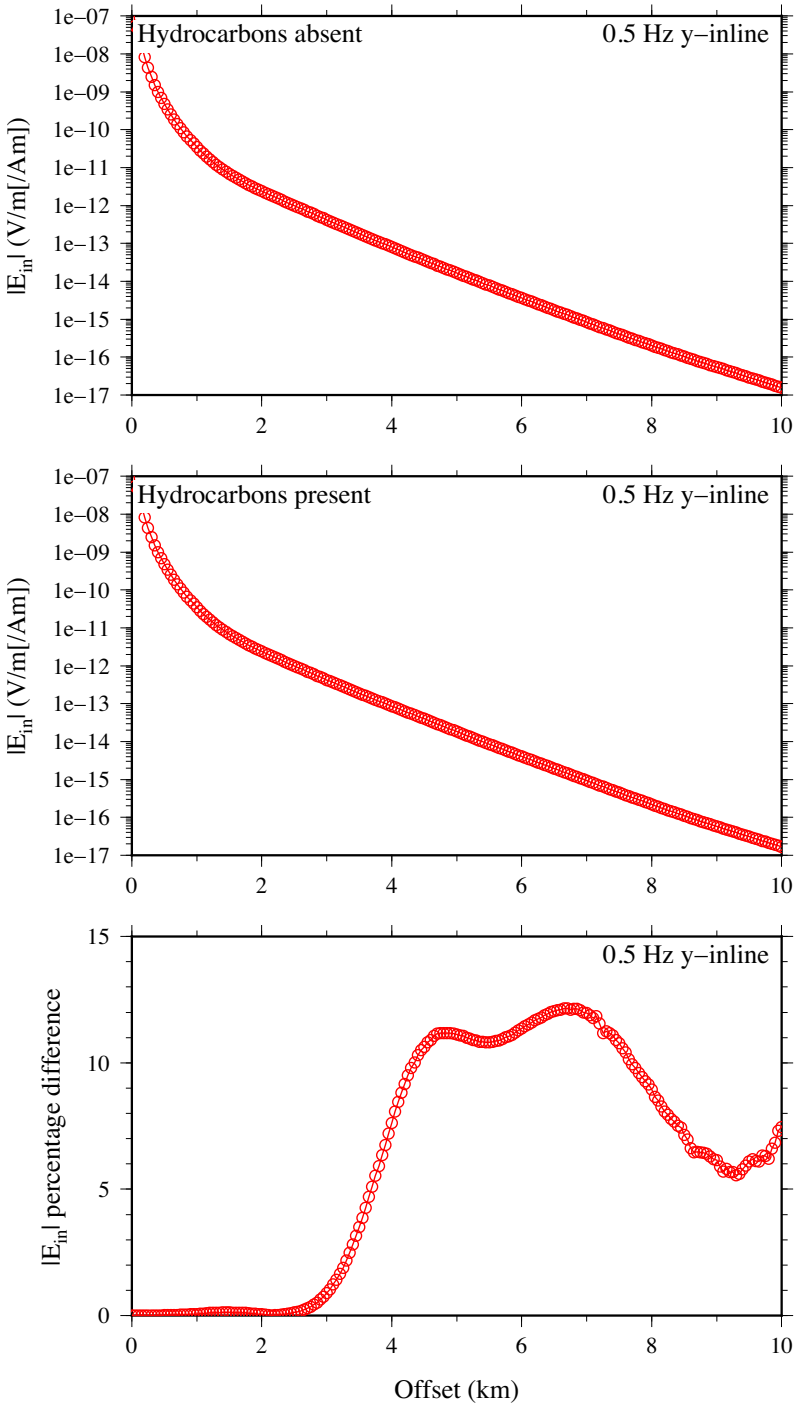

Figure B.6. The 0.5 Hz inline horizontal electric fields and associated anomaly for the 3D North Amethyst BNA reservoir model with water depth = 2000 m, average burial depth = 1416 m, and true hydrocarbon content, i.e., hydrocarbons present only above the oil-water contact in the reservoir.

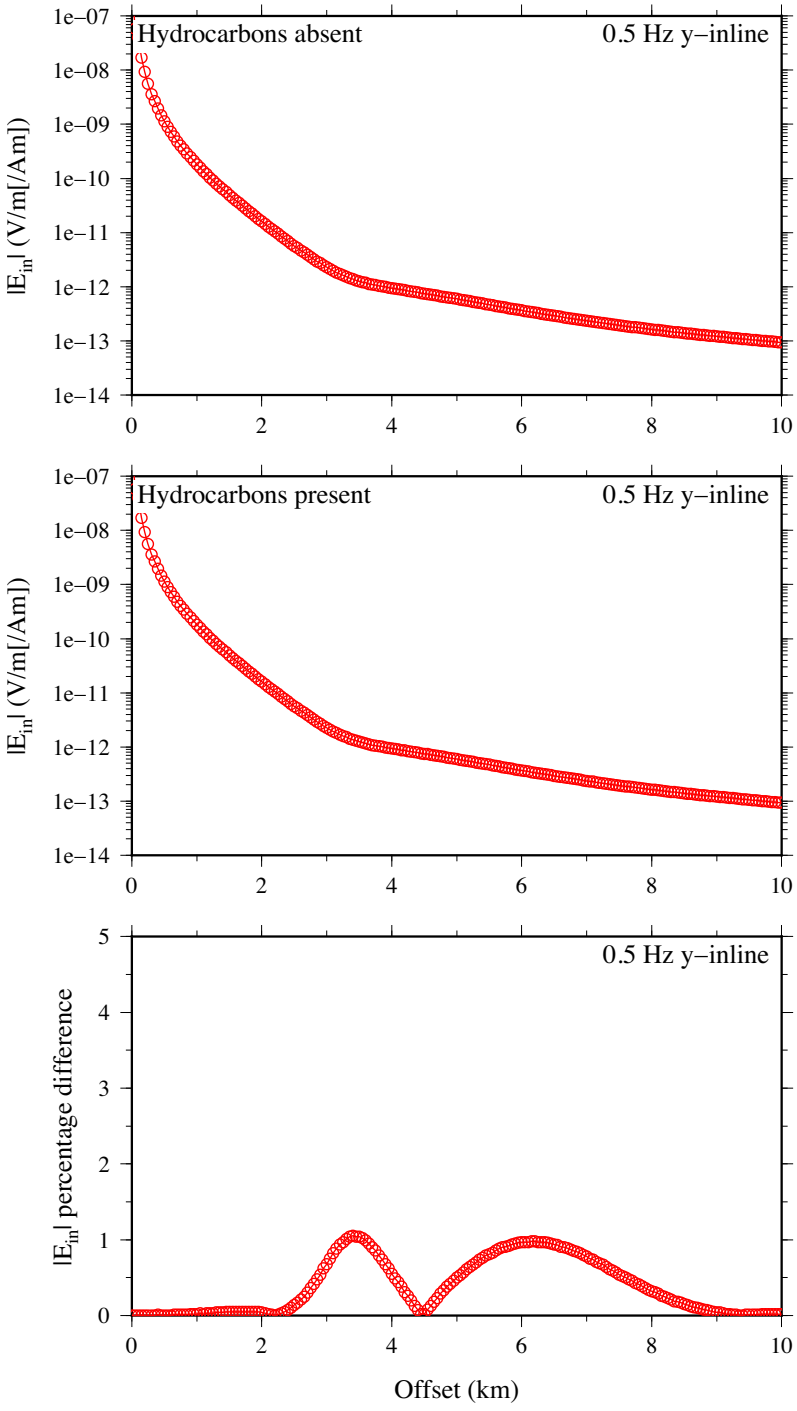

Figure B.7. The 0.5 Hz inline horizontal electric fields and associated anomaly for the 3D North Amethyst BNA reservoir model with water depth = 120 m, average burial depth = 2416 m, and the reservoir interval completely hydrocarbon-filled.

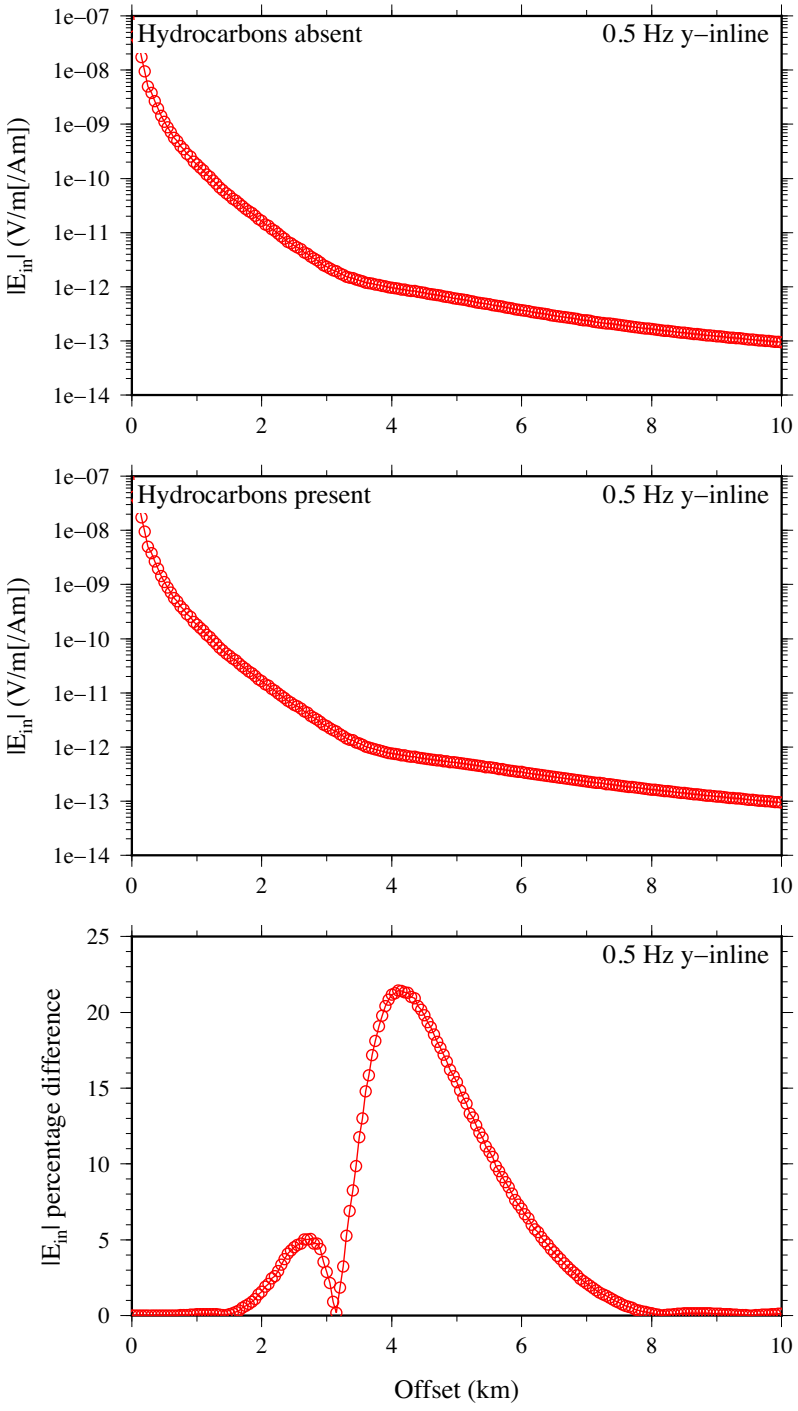

Figure B.8. The 0.5 Hz inline horizontal electric fields and associated anomaly for the 3D North Amethyst BNA reservoir model with water depth = 120 m, average burial depth = 1416 m, and the reservoir interval completely hydrocarbon-filled.

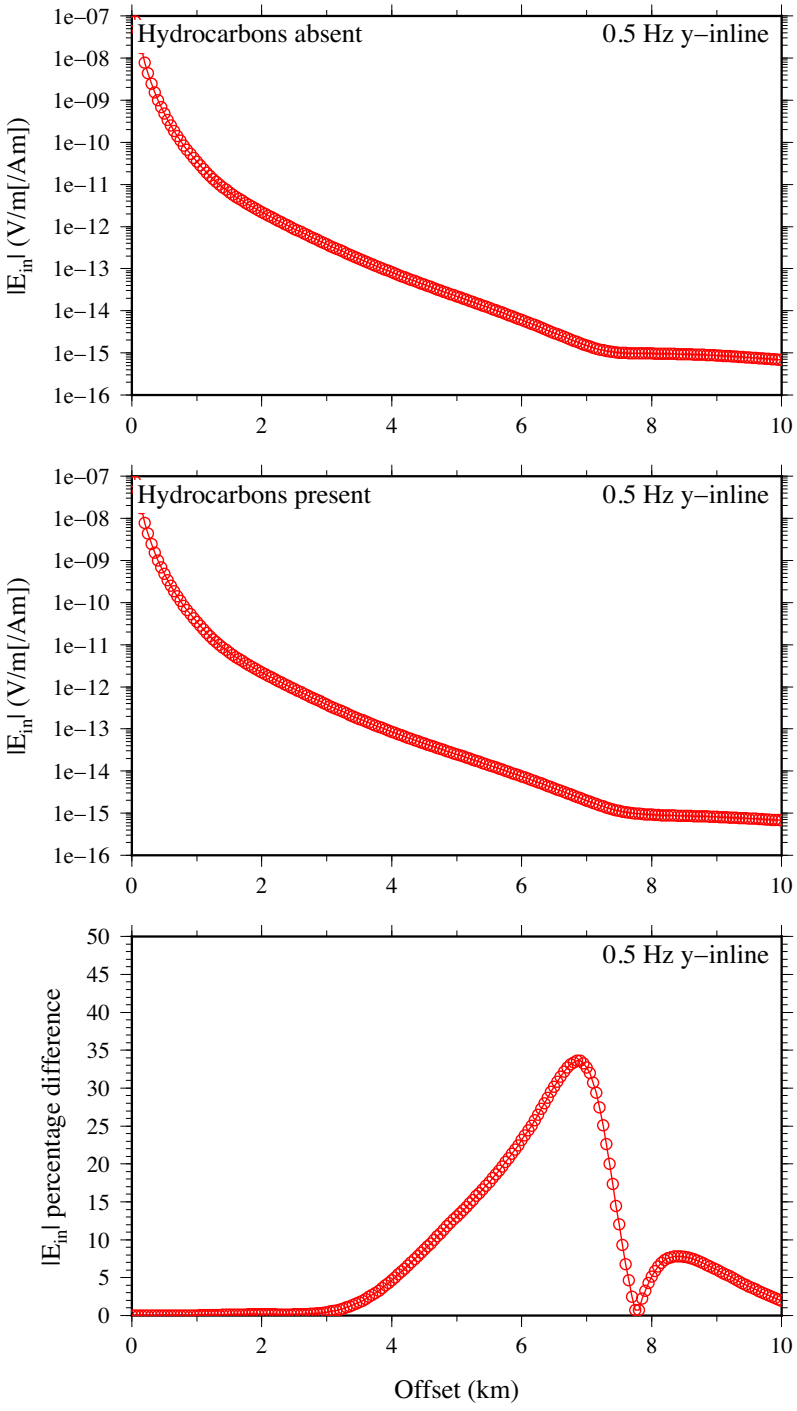

Figure B.9. The 0.5 Hz inline horizontal electric fields and associated anomaly for the 3D North Amethyst BNA reservoir model with water depth = 1000 m, average burial depth = 2416 m, and the reservoir interval completely hydrocarbon-filled.

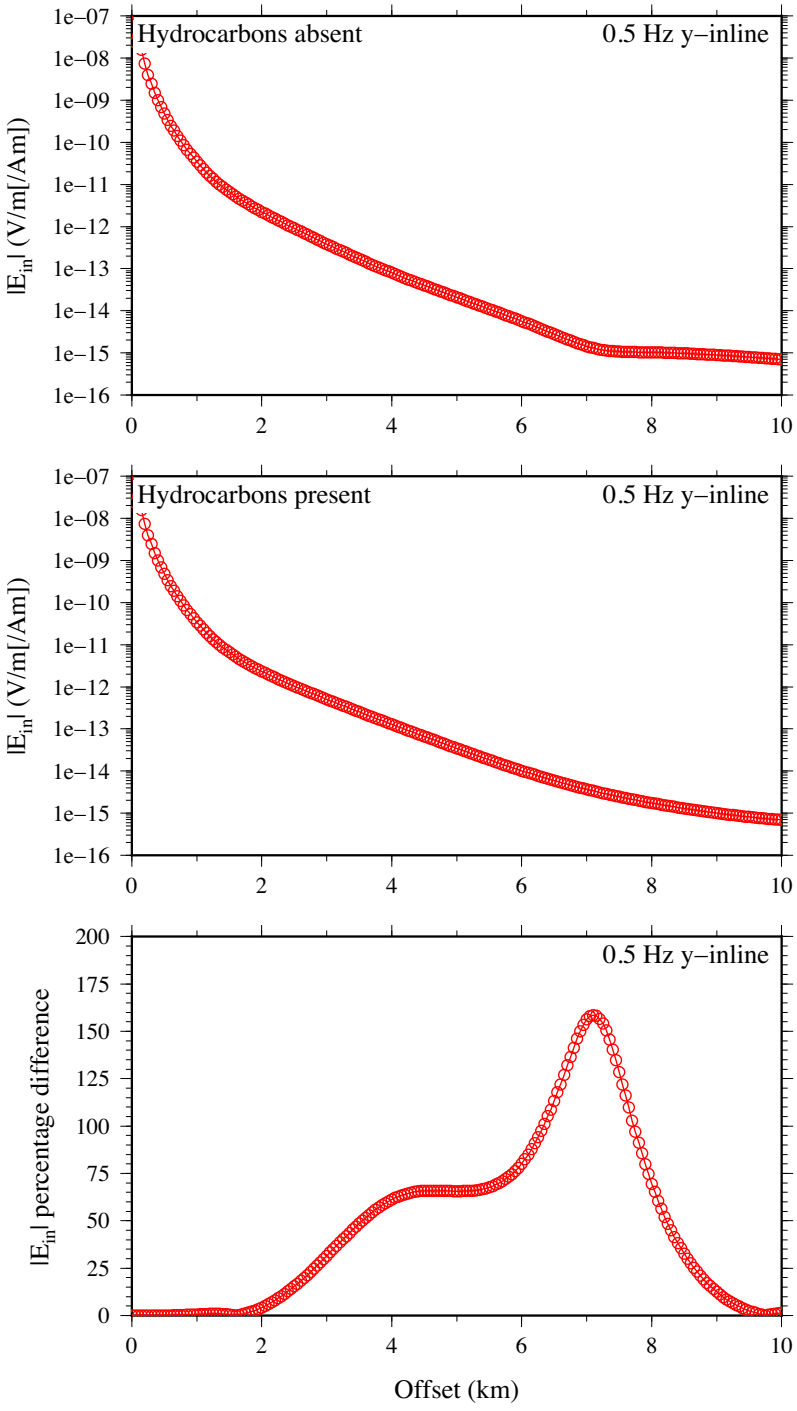

Figure B.10. The 0.5 Hz inline horizontal electric fields and associated anomaly for the 3D North Amethyst BNA reservoir model with water depth = 1000 m, average burial depth = 1416 m, and the reservoir interval completely hydrocarbon-filled.

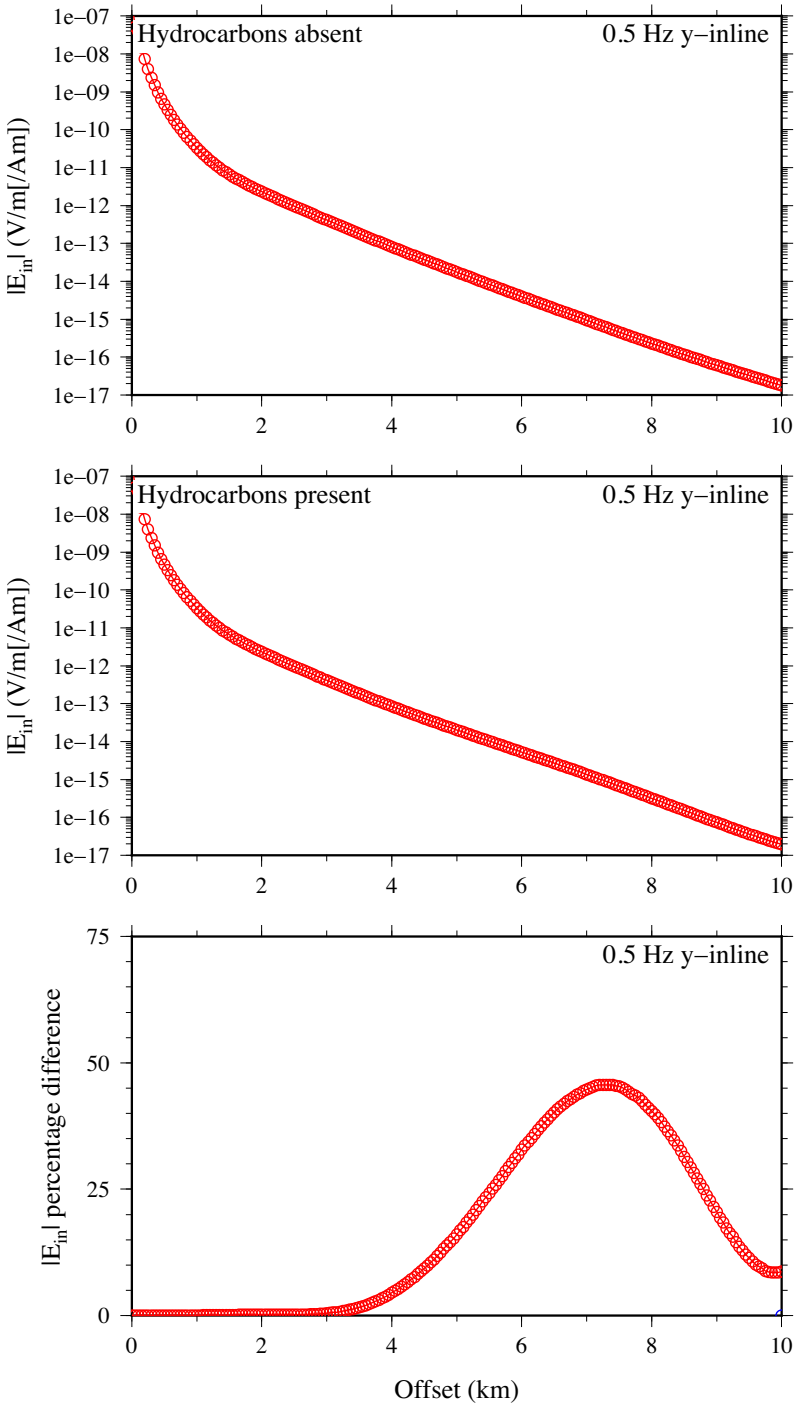

Figure B.11. The 0.5 Hz inline horizontal electric fields and associated anomaly for the 3D North Amethyst BNA reservoir model with water depth = 2000 m, average burial depth = 2416 m, and the reservoir interval completely hydrocarbon-filled.

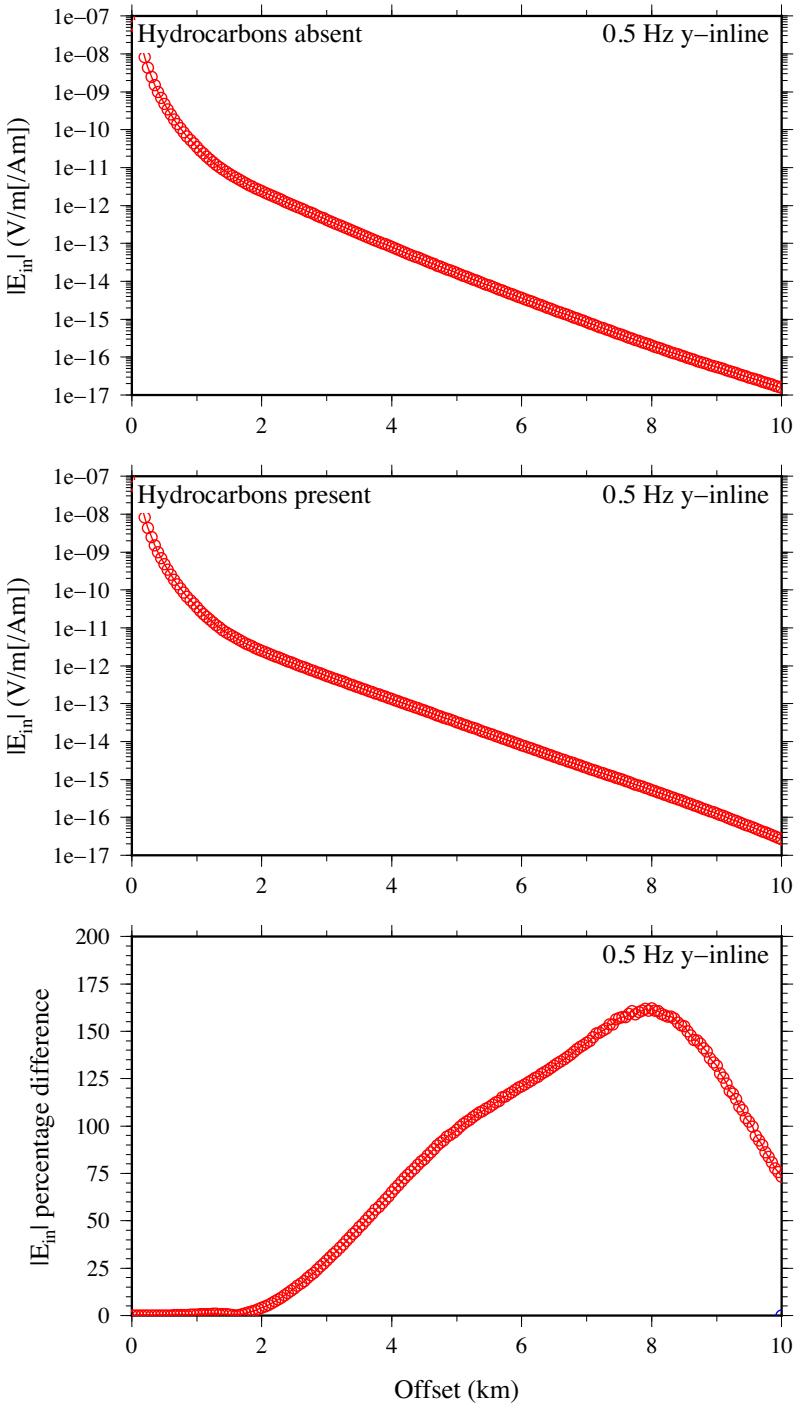

Figure B.12. The 0.5 Hz inline horizontal electric fields and associated anomaly for the 3D North Amethyst BNA reservoir model with water depth = 2000 m, average burial depth = 1416 m, and the reservoir interval completely hydrocarbon-filled.